Herschel Studies of Infrared Dark Clouds and Cores in the Hi-GAL Survey

by

Lucy A. Wilcock

A thesis submitted to

Cardiff University

for the degree of

Doctor of Philosophy

May 2012

DECLARATION

This work has not previously been accepted in substance for any degree and is not being concurrently submitted in candidature for any degree.

Signed ..... Date .....

STATEMENT 1

The work presented in this thesis is all my own work carried out under the supervision of Prof. D. Ward-Thompson as part of the Hi-GAL team with the exception of the following: *Herschel* observations of the Galactic Plane were taken as part of the *Herschel* Infrared Galactic Plane Survey (Hi-GAL) and were reduced and calibrated by the Hi-GAL team. *Spitzer* observations were taken as part of the *Spitzer* Galactic Legacy Infrared Mid-Pane Survey Extraordinaire (GLIMPSE) and were reduced and calibrated by the GLIMPSE consortia. PHAETHON was created by Dr D. Stamatellos and Prof. A. Whitworth, Cardiff University. The IRDCs used here are based on those found in previous surveys by Dr. R. Simon and Prof. G. Fuller and Dr. N. Peretto. All subsequent analysis of the Hi-GAL data was performed by me. This includes the by-eye examination of 3171 candidate IRDCs; the classification of each genuine IRDC based on the mid- and far-infrared data; the calculation of IRDC core lifetimes; and the revised calculation for the star formation rate occuring in IRDCs. I also ran all the modelling of the cores and completed the analysis of their physical properties (including the principal component analyses). A bibliography is appended.

Signed ..... Date .....

STATEMENT 2

I hereby give consent for my thesis, if accepted, to be available for photocopying and for inter-library loan, and for the title and summary to be made available to outside organisations.

Signed ..... Date .....

ACKNOWLEDGMENTS

First and foremost, I would like to express my gratitude to my supervisor, Prof. Derek Ward-Thompson, for his help, encouragement and advice throughout my PhD.

My thanks go to all members of the Star Formation Research Group but most especially to Dr. Jason Kirk, Dr. David Nutter, Dr. Dimitrios Stamatellos and Prof. Anthony Whitworth for their time and the answers to many questions over the last four years.

My gratitude also goes to my collaborators and co-authors for their suggestions and feedback which has improved my research.

Finally, I wish to thank my friends and family, in particular my mum and dad, for their continued love and support.

ABSTRACT

High mass stars affect their environments on a large scale. However, the processes behind the formation of high mass stars are still relatively poorly understood compared to their low mass counterparts. Infrared dark clouds (IRDCs) and their cold cores (gravitationally bound cores embedded within the IRDCs) are thought to be the earliest observable stage of high mass star formation. By observing these very young regions we gain insight into the formation of high mass stars.

IRDCs were initially found as regions of extended absorption in the mid-infrared (MIR). However, identifying IRDCs in the MIR alone can create problems because there is no way to distinguish between IRDCs and minima in the MIR background. In this thesis we use data taken by the Herschel Infrared Galactic Plane Survey to observe IRDCs and their cold cores at wavelengths where they are expected to be seen in emission, i.e. in the far-infrared (FIR).

We classify an IRDC as an object that shows absorption at 8 μm and emission at 250, 350 and 500 μm. It is found that only $\sim$40–60% of the regions showing absorption in the MIR are seen in emission in the FIR. Thus only $\sim$50$\pm$10% of the MIR-selected IRDCs are genuine. Cores are identified in the genuine IRDCs and separated into three stages based on whether or not they contain a MIR point source. Statistical lifetimes are calculated for each stage and the total lifetime of a cold core is estimated to be $\sim 1.3\times10^6$ years. The star formation rate occurring in IRDCs is calculated and found to be $\sim 0.4\,\mathrm{M}_\odot\,\mathrm{yr}^{-1}$. This is significantly lower than the Galactic rate of star formation ($\sim$1–2 $\mathrm{M}_\odot\,\mathrm{yr}^{-1}$) and leads to the conclusion that not all high mass stars are formed in IRDCs. Some must form via an alternative method.

Twenty of the youngest, most isolated cold cores are identified and modelled using the 3D radiative transfer Monte Carlo code, Phaethon. Their physical parameters are derived and the relationships between mass, density, size, temperature and the surrounding interstellar radiation field (ISRF) are deduced. The surface temperature is seen to depend heavily on the level of the local radiation field, while the temperature at the centre of a core is seen to depend on its mass and density. Using both central and surface temperatures, we fit the equation $G_{IS}e^{-AM/R^2} \propto T^{4+\beta}$, where G_{IS} is the local ISRF, M is the mass external to radius R, T is the temperature at radius R and A is a constant. We find a good fit to this equation in our data and that β, the dust emissivity index, is 1.8$\pm$0.2. No large cores were found in regions of high ISRF. We consider this to be possibly due to the outer layers of the cores being evaporated due to the high levels of radiation being absorbed. A principle component analysis is performed and it is found that the appearance of a core in the data depends upon the temperature gradient within the core and its density structure.

Contents

List of Figures

List of Tables

Chapter 1

An Introduction to High Mass Star Formation

In this thesis we present data from the *Herschel* Space Observatory, a far-infrared (FIR; ∼40–350 μm) and sub-millimetre (sub-mm; ∼300–1000 μm) observatory capable of performing photometry and spectroscopy between 55 and 671 μm (Pilbratt et al., 2010). Specifically, the data used in this thesis were taken as part of the *Herschel* Infrared Galactic Plane Survey (Hi-GAL), a *Herschel* open-time key project (Molinari et al., 2010a,b). The work shown here has focussed on the region $l = 300 - 330\,^{\circ}$, $|b| < 1^{\circ}$, which was the first region to be observed by Hi-GAL.

We have used the Hi-GAL data to study the earliest observable stages of high mass star formation: infrared dark clouds (IRDCs) and the cores embedded within them. IRDCs are the suspected birth-places of high mass stars. As they typically have temperatures around 15 K their SEDs peak at ∼200 μm, ideal for study with *Herschel*. We have studied the number statistics and lifetimes of IRDC cores as well as the physical properties of a subset of cores which appear starless. Through

this work it is hoped to gain insight into the earliest stages of high mass star formation.

1.1 Introduction

High mass stars are usually defined as those with a main sequence mass $\geq 8\,\mathrm{M}_{\odot}$. They play an important role in shaping the conditions of the interstellar medium (ISM) on a galactic scale. Their stellar winds and outflows are an important source of mixing and turbulence in the ISM. They output large amounts of ultra-violet (UV) radiation ($\sim 10 - 400\,\mathrm{nm}$) which is a primary source of heating for the ISM. Additionally, the most massive stars are the principal source of heavy elements (those with an atomic weight greater than that of iron, i.e. $\gtrsim 56$ atomic mass units) and trigger further star formation.

Despite their significance, the processes behind the formation of massive stars are still not well understood. There are several reasons for this. High mass stars evolve on a shorter timescale and have a shorter main sequence lifetime than low mass stars and so are relatively short-lived. For example, the main sequence lifetime of a star can be estimated using:

$$\frac{t_{MS}}{t_{\odot}} = \left(\frac{M}{M_{\odot}}\right)^{-2.5}, \tag{1.1}$$

where t_{MS} is the main sequence lifetime of a star with mass M, $M_{\odot}$ is the mass of our Sun and $t_{\odot}$ is the main sequence lifetime of our Sun, approximately 10^{10} years (e.g. Schroder & Connon Smith, 2008). Using Equation 1.1, an $8\,\mathrm{M}_{\odot}$ star will have a main sequence lifetime of a few 10^{7} years, significantly less than that of a $1\,\mathrm{M}_{\odot}$ star. Thus, compared to low mass stars, the different evolutionary stages

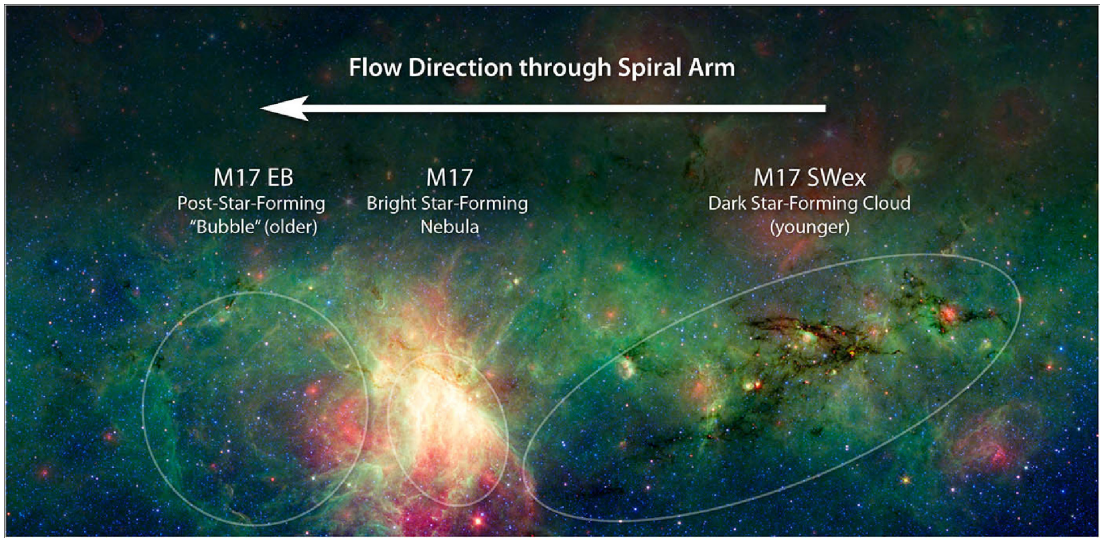

Figure 1.1: A 3-colour (3.6 μm is shown in blue, 8 μm is shown in green and 24 μm is shown in red) image showing all the stages of high mass star formation. On the far right (M17 SWex) IRDCs are visible against the mid-infrared background. In the middle (M17) is an infrared bright star forming region containing HMCs and HII regions. On the far left (M17 EB) are main sequence OB-type stars (Hadhazy, 2010). Courtesy: NASA/JPL-Caltech/M. Povich (Penn State Univ.)

of high mass stars are observable for a far shorter time-span and so are relatively rare. High mass star forming regions therefore generally exist at greater distances (typically $\geq$ 1kpc; e.g. the Cygnus-X region has a distance of $\sim$ 2.0 kpc, Reid et al. 2011) than low mass star forming regions (a few 100 pc; e.g. the Taurus star-forming region is $\sim$ 140 pc away, Bertout & Genova 2006) which makes them more difficult to observe. Finally, the earliest stages of high mass star formation take place deeply embedded within molecular clouds making them optically thick at optical wavelengths (390–750 nm) due to high dust extinction levels.

High mass stars are thought to evolve through four basic observational stages: IRDCs; hot molecular cores (HMCs); hyper-compact and ultra-compact HII (HCHII and UCHII, respectively) regions; and, finally, compact and classical HII regions. IRDCs are cold condensations of gas which are the densest parts of molecular clouds and often contain cold cores. The youngest cold cores are theorised to be

the high mass equivalent of prestellar cores in that they are gravitationally bound but do not yet show any evidence of internal heating (Ward-Thompson et al., 1994; Carey et al., 2000; Redman et al., 2003; Garay et al., 2004).

As the core continues to evolve a protostar (a hydrostatically supported mass of gas which contains no nucleosythesis and grows via accretion) forms in its centre. Infalling material impacts on the surface of the protostar and, as the material's kinetic energy is converted to heat, its temperature begins to increase. At this point the inner regions of the core may still be optically thin and the heat from the protostar can be radiated away. The core and the protostar therefore remain in thermal equilibrium. As the density of the inner regions of the core increase they become optically thick. When this occurs the infrared radiation from the central protostar can no longer be radiated away and the temperature of the protostar increases beyond that of the surrounding core. The increased temperature of the protostar causes ices condensed on dust grains to begin to evaporate and an HMC forms.

HMCs consist of a central protostar surrounded by a cloud of dense molecular gas and dust. Eventually the protostar heats to the point where it begins ionising the surrounding gas and an HII region forms. Initially an HCHII region and then, as the radius of the ionised region increases, an UCHII region. As the ionised region continues to expand, a compact HII region is formed until, eventually, a classical HII region forms. At this point the HII region begins to disrupt the parent molecular cloud. As the gas and dust surrounding the central stars disperse they become visible at optical wavelengths and the formation of the high mass star is complete. All four stages of high mas star formation are visible in Figure 1.1.

However, this evolutionary sequence is still fairly crude. Stars do not move

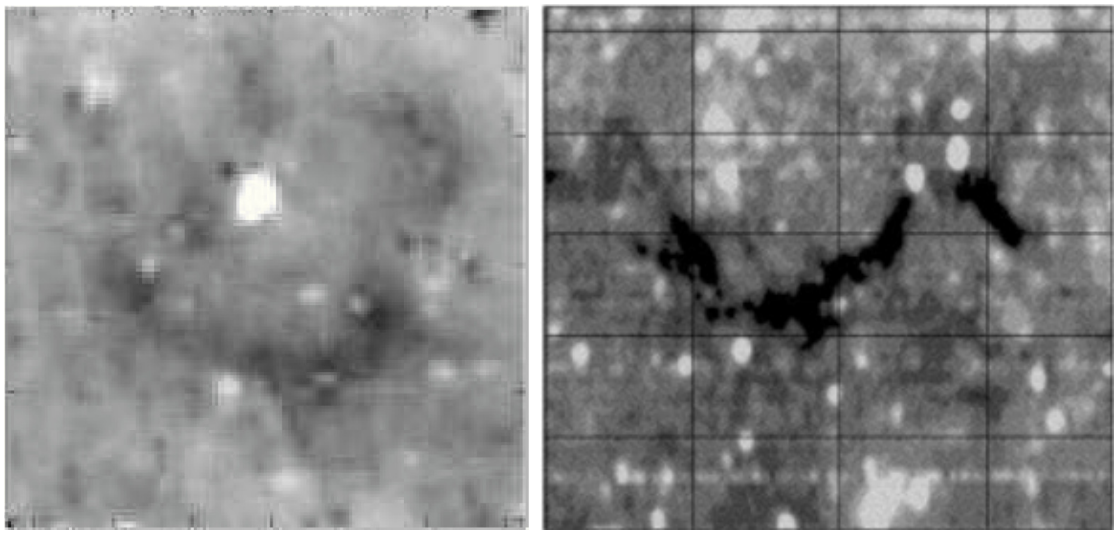

Figure 1.2: The original *ISO* (left; Perault et al. 1996) and MSX (right; Carey et al. 1998) images of IRDCs. The two images show regions of absorption at 15 μm and 8 μm, respectively.

neatly from one stage to the next and often more than one stage can be observed simultaneously (e.g. Rathborne et al. 2011).

1.2 Infrared Dark Clouds (IRDCs)

IRDCs were initially discovered by *MSX* (Midcourse Space Experiment; Carey et al., 1998; Egan et al., 1998) and *ISO* (Infrared Space Observatory; Perault et al., 1996), the latter as part of the ISOGAL survey (Omont et al., 2003). Both found extended dark regions against the mid-infrared (MIR; $\sim$5–40 μm) background (shown in Figure 1.2). These were predicted to be regions of absorption due to large quantities of cold dust. They were suggested as the precursors to high mass star formation (Perault et al., 1996).

1.2.1 Physical Properties

IRDCs exhibit very low temperatures, typically less than 25 K (e.g. Egan et al. 1998; Teyssier, Hennebelle, & Perault 2002). Many have been found to exhibit temperature gradients, with the temperature inside the cloud decreasing from surface to centre by up to 10 K (e.g. Peretto et al., 2010, see Figure 1.3). It is interesting to note, however, that this does not appear to be the case for all IRDCs. Some IRDCs have been shown to have relatively uniform temperatures, varying by only 2–4 K (Ragan, Bergin, & Wilner, 2011).

The IRDCs that do show a temperature gradient typically have hottest material at the surface of the cloud. This implies that the primary source of heating is external (Li, Goldsmith, & Menten, 2003). Heating in IRDCs is thought to be largely due to radiation falling on the surface of the core, and IRDCs are expected to have very little internal heating. This is verified by the lack of MIR emission, which suggests that there is no hydrogen burning and that heating via compression is minimal (Battersby et al., 2010).

IRDCs have high volume densities and high H_2 column densities. Peaks of $>10^5\,\mathrm{cm}^{-3}$ (e.g. Egan et al., 1998; Carey et al., 1998, 2000) and $>10^{22}\,\mathrm{cm}^{-2}$ (e.g. Peretto & Fuller, 2009; Vasyunina et al., 2009; Peretto et al., 2010), respectively, have been observed. An IRDC with a peak H_2 column density of $3\times10^{22}\,\mathrm{cm}^{-2}$ is shown in Figure 1.3. Ragan et al. (2011) showed that IRDCs have a roughly linear relationship between ammonia and molecular hydrogen column densities, with the former peaking at a few $10^{16}\,\mathrm{cm}^{-2}$.

They also tend to be very large. IRDCs have been observed with sizes up to a few parsecs (e.g. Rathborne, Jackson, & Simon 2006; Butler & Tan 2009). Butler

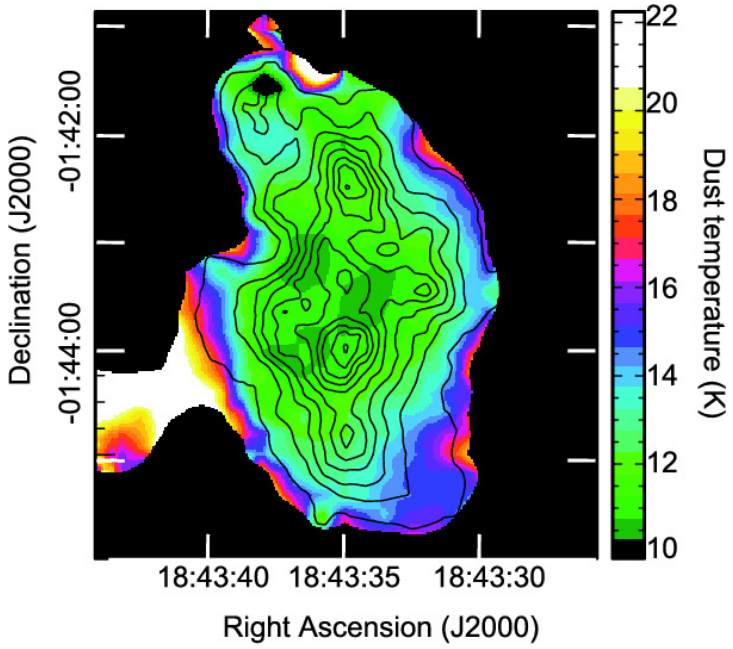

Figure 1.3: A temperature map of an IRDC, the coldest temperatures are seen in the centre of the IRDC and higher temperatures seen at the edge. The contours show the H_2 column density of the IRDC ranging from 1×10^{21} to $3.5 \times 10^{22}\,\mathrm{cm}^{-2}$ (Peretto et al., 2010).

& Tan (2009) find the size of 10 IRDCs from the Simon et al. (2006a) catalogue to have radii ranging from 0.8 to 17 pc with a median of 6.7 pc.

The masses of many IRDCs have been calculated. They typically range from a few hundred to tens of thousands of solar masses (e.g. Rathborne et al., 2006; Butler & Tan, 2009; Peretto & Fuller, 2009; Vasyunina et al., 2009). Rathborne et al. (2006) calculate the masses of 38 IRDCs. They find a median mass of 940 $\mathrm{M}_\odot$ and a mean mass of 3000 $\mathrm{M}_\odot$.

With sizes and masses greater than those of HMCs and with temperatures much lower, the physical properties of IRDCs led to the conclusion that they are the earliest observable phase of high mass star formation (e.g Perault et al., 1996; Rathborne et al., 2006).

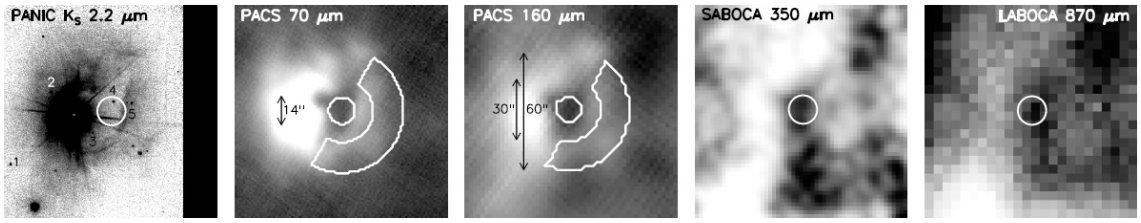

Figure 1.4: The region surrounding NGC1999, where a 'hole in the sky' has been identified by Stanke et al. (2010), shown as a white circle. The images shown here are at wavelengths of (left–right) 2.2, 70, 160, 350 and 870 μm. The dark patch is also seen at optical wavelengths. The white semi-circle highlights a shell of material surrounding the hole in the sky.

1.2.2 Observations of Infrared Dark Regions

Since their discovery, IRDCs have primarily been identified at MIR wavelengths as regions of absorption. There are currently two catalogues of known IRDCs: Simon et al. (2006a) and Peretto & Fuller (2009). Both catalogues list between 10,000 and 11,000 IRDCs searched for in the MIR. However, identifying IRDCs in the MIR alone can be problematic.

Firstly, there is no way of distinguishing between a dark region due to absorption (i.e. an IRDC) and a dark region due to a dip in the MIR background. We refer to the latter as a 'hole in sky' (see Figure 1.4; Stanke et al. 2010). Holes in the sky do not show emission at any wavelength. Unlike IRDCs, which have high densities and large masses, holes in the sky are areas with a dearth of material. Identifying IRDCs in the MIR alone can lead to holes in the sky being falsely labelled as IRDCs, thus over-estimating the numbers of IRDCs in the Galaxy.

Secondly, identifying IRDCs as regions of absorption against the MIR background introduces a significant selection bias. Only those IRDCs that exist in regions of high MIR background, i.e. in the Galactic Plane, will be found. Most notably, this means that all IRDCs on the far side of the Galaxy will most likely

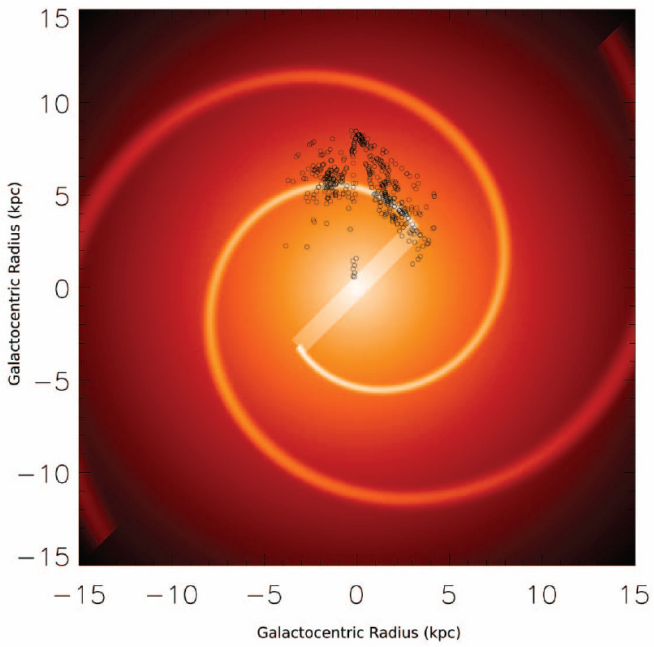

Figure 1.5: The location of first and fourth quadrant Galactic IRDCs overlaid onto an image of the Benjamin et al. (2006) spiral-arm model of the Milky Way (Jackson et al., 2008). The IRDCs can be seen to cluster around a spiral arm, where high levels of star formation take place.

be missed because, as viewed from Earth, they are behind the majority of the MIR-emission and so do not appear as regions of absorption.

However, IRDCs are seen in emission at FIR and sub-mm wavelengths (e.g. Peretto et al., 2010). Holes in the sky show no emission at any wavelength. By observing at FIR and sub-mm wavelengths, in addition to the MIR, some IRDCs can be differentiated from holes in the sky. Additionally, IRDCs not seen as regions of absorption in the MIR can still be seen in emission at the FIR and sub-mm. Battersby et al. (2011) recently used FIR data to identify five objects that are the first candidates for IRDCs located on the far side of the Galaxy.

1.2.3 Galactic Distribution

Using CO and CS velocities, kinematic distances have been calculated for several hundred IRDCs (Simon et al., 2006a; Jackson et al., 2008). The distribution of IRDCs in the first Galactic quadrant differs from those in the fourth quadrant. In the first quadrant IRDCs have a mean Galacto-centric distance (the distance from the Galactic centre) of $\sim$5 kpc (Jackson et al., 2008), whereas those in the fourth quadrant are typically found at $\sim$6 kpc (Peretto & Fuller, 2010).

Jackson et al. (2008) plotted the positions of IRDCs on several Galactic models and found that the distribution of IRDCs in our Galaxy best matches a Galactic model which contains two spiral arms (e.g. Drimmel 2000; Drimmel & Spergel 2001; Benjamin et al. 2006). When the IRDCs are superimposed on such a model, as shown in Figure 1.5, the IRDCs cluster around a spiral arm. Spiral arms typically have a high mass density and a high rate of star formation. The association of IRDCs with a spiral arm therefore lends weight to the theory that IRDCs are the birthplace of high mass stars (Jackson et al., 2008; Marshall, Joncas, & Jones, 2009).

1.2.4 The Role of IRDCs in Galactic Star Formation

Rathborne et al. (2006) calculated that the star formation rate within IRDCs is approximately $2\,\mathrm{M_{\odot}yr^{-1}}$. To do this they first calculated the total mass of IRDCs, $M_{IRDC,tot}$, in our Galaxy using:

$$M_{IRDC,tot} = N_{IRDC} \times M_{IRDC,ind} \times \frac{1}{f_{detect}}, \tag{1.2}$$

where N_{IRDC} is the total number of IRDCs in our Galaxy, $M_{IRDC,ind}$ is the mean mass of a single IRDC in our Galaxy and $1/f_{detect}$ is the fraction of IRDCs detected. They use the Simon et al. (2006a) catalogue and assume $N_{IRDC} \approx 10,000$ (approximately the number of IRDCs found by Simon et al. 2006a) and $M_{IRDC,ind} \approx 3000\,\mathrm{M}_{\odot}$ (the mean mass of the sample of IRDCs used by Rathborne et al. 2006). Due to the observational bias in selecting IRDCs from MIR data (i.e. only those that are against a high MIR background will be detected, while those far from the Galactic Plane and on the far side of the Galaxy are missed) they estimate $1/f_{detect}$ to be $\sim 1/3$. This gives the total mass of IRDCs in our Galaxy to be $\sim 10^8\,\mathrm{M}_{\odot}$.

They then calculate the rate of star formation occurring in IRDCs via:

$$\dot{M}_{SF,IRDCs} = \frac{\eta M_{IRDC,tot}}{\tau_{SF}} \tag{1.3}$$

where $\dot{M}_{SF,IRDCs}$ is the star formation rate in IRDCs, η is the star formation efficiency in IRDCs and τ_{SF} is the timescale for star formation in an IRDC. They estimate a star formation efficiency of 0.2 and a star formation timescale of 10^7 years, resulting in $\dot{M}_{SF,IRDCs} \approx 2\,\mathrm{M}_{\odot}\mathrm{yr}^{-1}$.

The total Galactic star formation rate is $\sim 1 - 2\,\mathrm{M}_{\odot}\mathrm{yr}^{-1}$ (Murray & Rahman, 2010; Robitaille & Whitney, 2010; Chomiuk & Povich, 2011), close to the estimated value formed within IRDCs. From this Rathborne et al. (2006) concluded that it is probable that IRDCs are the birthplaces of all high mass stars in the Galaxy.

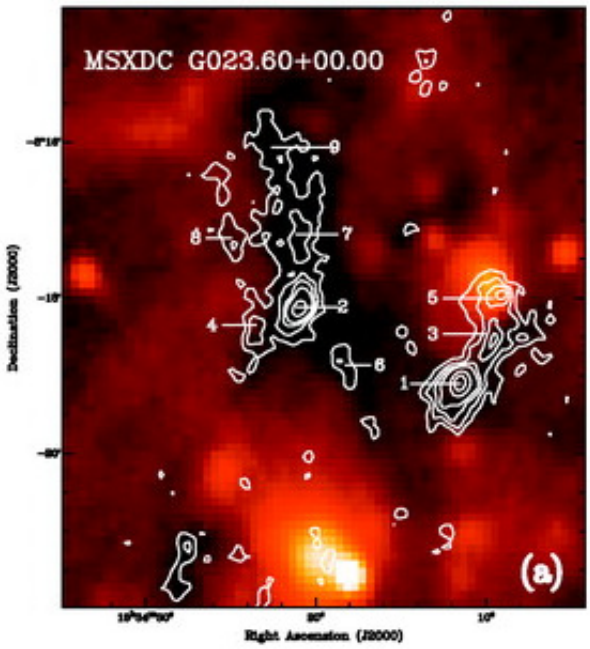

Figure 1.6: G023.60+00.00 - an IRDC as seen at 8 μm overlaid with contours from 1.2 mm. The 1.2 mm contours show evidence of up to nine cold cores within this IRDC, each is labelled with their Rathborne et al. (2006) designation.

1.3 Cold Cores Within IRDCs

Many IRDCs contain cold, compact condensations which we refer to as cold cores. An IRDC containing several cores can be seen in Figure 1.6. These objects have also been called 'clumps' (e.g. Battersby et al. 2010) and 'fragments' (e.g. Peretto & Fuller 2009). The youngest of these cold cores (which are called quiescent or starless) are gravitationally bound but not internally heated (Peretto & Fuller, 2010). Starless cold cores are therefore thought of as the high mass equivalent of low-mass prestellar cores (e.g. Ward-Thompson et al. 1994; Di Francesco et al. 2007; Ward-Thompson et al. 2007).

1.3.1 Physical Properties

The cores within IRDCs have been observed with diameters ranging from ∼0.1 to 2.0 pc (e.g. Rathborne et al., 2006; Butler & Tan, 2009). Butler & Tan (2009) calculated the radius of 43 cores and Rathborne et al. (2006) calculated the radius of 190. Both sets of cores were found to have a median radius of 0.55 pc.

Cores have been found with masses between ∼10 and a few 1000 $M_\odot$ (e.g. Garay et al., 2004; Ormel et al., 2005; Rathborne et al., 2005; Swift, 2009; Zhang et al., 2011). Rathborne et al. (2006) find 140 starless cold cores (i.e. cores with no MIR emission associated with them; see Section 1.3.2) and calculate their masses, assuming a temperature of 15 K throughout the cores. The masses range from 8 to 2115 $M_\odot$. They find the median mass of the starless cold cores to be 120 $M_\odot$. 67% of their starless cold cores are found to have masses between 30 and 300 $M_\odot$, with the majority below 200 $M_\odot$. They find an additional 50 cores that are associated with 8 μm emission, the median mass of all 190 cold cores is 140 $M_\odot$.

Peak densities within cold cores have been seen to range from 10^3 to 10^7 cm^{-3} (Garay et al., 2004; Ormel et al., 2005; Rathborne et al., 2005, 2006; Swift, 2009; Zhang et al., 2011). The density of cold cores are believed to decrease from centre to edge (e.g. Peretto et al., 2010), although the exact density profile is not yet well understood.

The physical parameters of cold cores are consistent with them being the precursors to HMCs, the next observable stage in high mass star formation (Rathborne et al., 2006). The properties of HMCs are discussed in Section 1.4. Cold cores are typically larger and colder than HMCs and a factor of ∼30 less dense. This is consistent with the theory that hot cores evolve from their cold counterparts.

1.3.2 The Evolution of Cold Cores

Chambers et al. (2009) use a selection of the Simon et al. (2006a) IRDCs to propose a hypothetical evolutionary sequence wherein cold cores evolve from a quiescent stage through an active phase and finally into a red core. Chambers et al. (2009) use a sample of 190 cold cores and find ∼54 % to be quiescent, ∼25 % to be active and ∼21 % to be red. Other studies have also used these, or similar, evolutionary stages when studying cold cores (e.g. Jiménez-Serra et al. 2010; Battersby et al. 2011; Devine et al. 2011).

Quiescent cold cores represent the earliest stage of a core. They contain no MIR activity nor any other evidence of internal heating. They are likely to be starless, meaning that they are not yet undergoing any form of active star formation. Examples of quiescent cold cores are shown in Figure 1.7.

As the core evolves it enters the active phase. An active core is defined as one that shows tracers indicating star formation. These tracers include: 24 μm emission, thought to be evidence of heated dust indicating an embedded protostar (e.g. Chambers et al., 2009); maser emission, H_20 and CH_3OH masers are associated with regions of high mass star formation (e.g. Walsh et al., 2001; Minier et al., 2003); and extended green objects (EGOs; Cyganowski et al. 2008), which are regions of enhanced 4.5 μm emission thought to be shocked H_2 gas and thus characteristic of an outflow (De Buizer & Vacca, 2010) — they are sometimes also called 'green fuzzies' (Chambers et al., 2009). Battersby et al. (2010) find that active cores show a mean temperature higher than that of quiescent cores, in agreement with what would be expected if quiescent cold cores evolved into the active stage. Examples of active cold cores are shown in Figure 1.7.

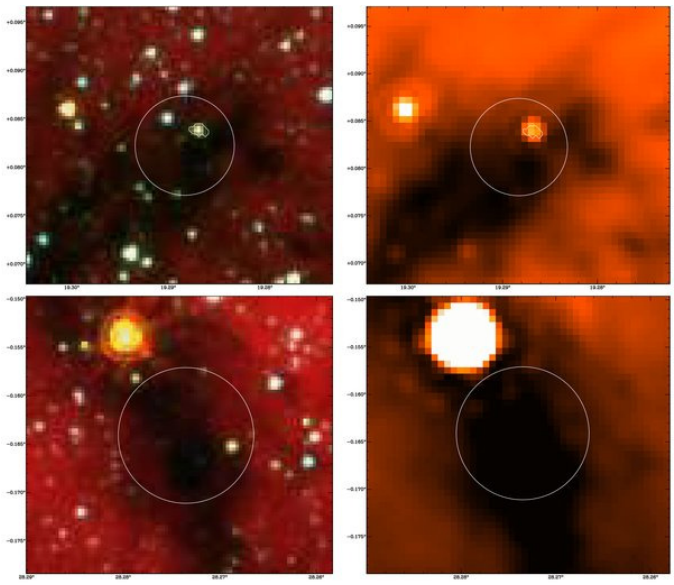

Figure 1.7: Upper: a 3-colour image (8.0 μm in red, 4.5 μm in green, 3.6 μm in blue; left) and a 24 μm image (right) of an active core (Chambers et al., 2009). Lower: a 3-colour image (8.0 μm in red, 4.5 μm in green, 3.6 μm in blue; left) and a 24 μm image (right) of a quiescent core (Chambers et al., 2009). The circles mark the position and angular size of the cores.

A cold core is said to be in the final red stage when it shows emission from polycyclic aromatic hydrocarbons (PAH) and is therefore bright at 8 μm. PAHs are molecules typically excited by a single high-energy photon. When the PAH molecules de-excite they emit many infrared photons. PAH emission is often seen in regions with a strong UV radiation field and so an abundance of high-energy photons. Hence, red cores may contain hyper-compact or ultra-compact HII regions, which are among the brightest UV objects in the Galaxy (e.g. Kurtz, Churchwell, & Wood, 1994). Chambers et al. (2009) specifically looked at PAH emission in the 8 μm band, which contains PAH features from 7.7 and 8.6 μm, to classify their cold cores as red.

1.3.3 The Lifetime of a Cold Core

There is some debate over the lifetime of the different stages of cores in IRDCs. Chambers et al. (2009) use 106 cold cores and equate the accretion timescale of high mass star formation to the lifetime of an active cold core. They make the assumption that no accretion is yet occurring in the quiescent phase and that by the red core stage, where the cold core likely contains an HII region, all accretion has halted. The accretion timescale is taken to be 2×10^5 years (Zinnecker & Yorke, 2007). The lifetime for the active phase is therefore also 2.0×10^5 years by this calculation. Chambers et al. (2009) then calculate the statistical lifetime for the quiescent phase to be 3.7×10^5 years.

Parsons, Thompson, & Chrysostomou (2009) observed a sample of 69 cold cores from Simon et al. (2006a), and found that $\sim$30 % are quiescent and $\sim$70 % have some form of embedded source — either active or red in the Chambers et al. (2009) nomenclature. They used a different estimated lifetime for the embedded YSO phase ($\sim10^4-10^5$ years) and found a timescale of about an order of magnitude less than Chambers et al. (2009) for the starless, quiescent phase ($\sim10^3-10^4$ years).

These lifetime estimates make the assumption that all starless cold cores will eventually form a single active cold core and that each active cold core will eventually form a single red core (Battersby et al., 2010). It is possible, for example, that one quiescent cold core will go on to form two or more active cold cores. As such, these lifetimes should be viewed as no more than order of magnitude estimates.

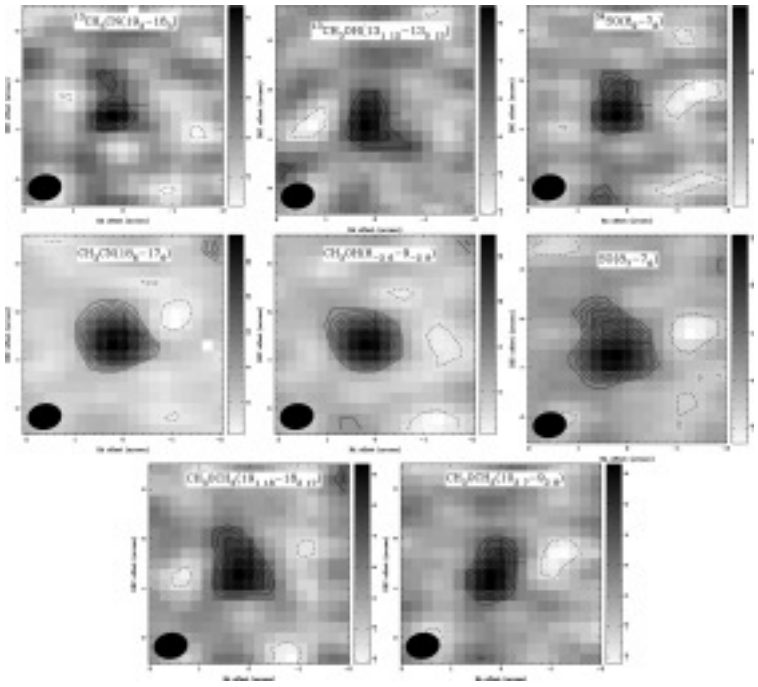

Figure 1.8: Integrated intensity images of G034.43+00.24, a hot molecular core, in a selection of different molecular lines (Rathborne et al., 2011). The cross marks the peak of emission in the continuum (approximately in the centre of each image).

1.4 Hot Molecular Cores

During the early cold phase, with temperatures <25 K, the heavier gas molecules (i.e. typically H_2 ad He remain in gaseous form) in cold cores condenses onto dust grains. On the surfaces of the grains, simple molecules interact and form complex molecules. As internal heating of the core begins, the temperature of the core increases to over 100 K (e.g. Cesaroni et al., 1994; Wright, Plambeck, & Wilner, 1996; Rolffs & Schilke, 2011). The ices on the dust grains begin to evaporate and eventually form a cloud of dense molecular gas surrounding the central protostar (Blake et al., 1987; Millar, Herbst, & Charnley, 1991). This is called a hot molecular core (HMC; see Figure 1.8).

HMCs are considered an early stage of high mass star formation, after the

cold IRDC phase but prior to the development of an HII region (e.g. Kurtz et al., 2000; Beuther et al., 2006). At this stage, the central protostar is internally heated but still actively accreting material and increasing in mass (e.g. Osorio, Lizano, & D'Alessio 1999; Furuya, Cesaroni, & Shinnaga 2011).

HMCs are typically smaller than IRDCs or cold cores, with sizes of $\lesssim$0.1 pc (e.g. Wright et al., 1996; Kurtz et al., 2000). However, many HMCs are surrounded by cooler, extended regions of molecular gas called 'molecular clumps'. Molecular clumps have been seen to extend to $\sim$1 pc in size (Cesaroni et al., 1991).

Masses of HMCs have been calculated to fall in the range of $\sim$10–10^3 $M_\odot$ (e.g. Cesaroni et al., 1994, 1997; Zhang & Ho, 1997). Smaller HMCs (those with masses of a few $\times 10\,M_\odot$) are thought to be formed by a single protostar, while those with higher masses are more likely to have a cluster of protostars powering them (Cesaroni, 2005).

They have high luminosities ($> 10^4 L_\odot$; e.g. Wyrowski et al., 1997; Cesaroni, Felli, & Walmsley, 1999) and high densities ($10^5 - 10^8\,cm^{-3}$, e.g. Cesaroni et al., 1999; Garay & Lizano, 1999; Rolffs & Schilke, 2011). Many are associated with water and methanol masers (e.g. Plume, Jaffe, & Evans, 1992; Hunter et al., 1999; De Buizer et al., 2002), which are themselves associated with the early stages of high mass star formation.

1.4.1 Heating Mechanisms

The temperature of HMCs (>100 K) is one of their defining attributes, but their heating mechanism is not yet well understood. A central heating source (e.g. a maser or accretion onto a central protostar; Walmsley, 1995) has been identified in

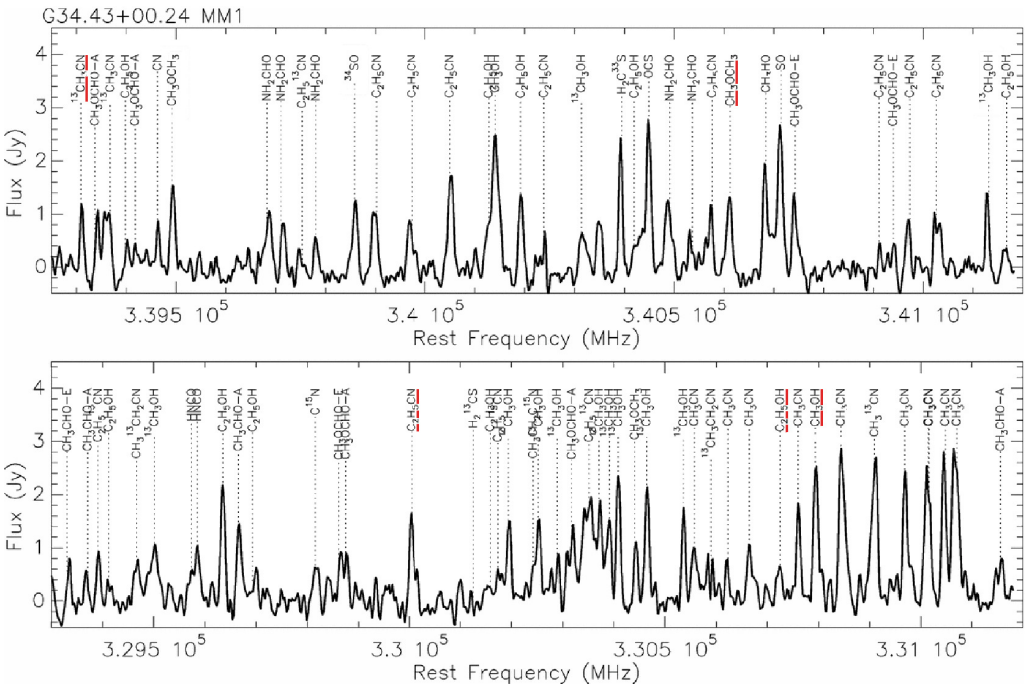

Figure 1.9: The spectrum towards G034.43+00.24 (Rathborne et al., 2011). Emission lines from many complex organic molecules can be seen, including: CH_3CN; CH_3OCH_3; CH_3OH; C_2H_5CN; and C_2H_5OH (examples of each line are underlined in red).

several HMCs using high resolution MIR continuum and molecular line observations (e.g. de Vicente et al., 2002; De Buizer et al., 2003). This has been reinforced by modelling which shows that internal heating sources better recreate the physical conditions seen in HMCs than those which model an external heating source (e.g. Kaufman, Hollenbach, & Tielens, 1998).

However, recent observations have found HMCs which do not appear to have any source of internal heating. These are generally found in close proximity to UCHII regions. It has thus been suggested that at least some HMCs may be heated by these nearby UCHII regions or, equally, by nearby main-sequence stars (e.g. Gomez, Garay, & Lizano, 1995; Favre et al., 2011).

1.4.2 The Molecular Line Spectrum

The gas around HMCs contains many different, exotic molecules. HMCs are characterised by a rich molecular line spectrum, typically containing numerous emission lines from these molecules (see Figure 1.9; e.g. Kurtz et al. 2000; Rathborne et al. 2011).

They contain high abundances of fully hydrogenated molecules (those with the maximum number of hydrogen atoms) such as H_2O (e.g. Marseille et al., 2010a; Melnick et al., 2010) and NH_3 (e.g. Osorio et al., 2004; de la Fuente et al., 2010).

Many complex organic molecules are also seen in HMCs. These include alcohols, nitriles, ethers and esters. Alcohols are compounds with an hydroxyl functional group, -OH, bound to a carbon atom for example: CH_3OH and C_2H_5OH, (e.g. Sutton et al., 1995; Wang et al., 2009; Rathborne et al., 2011). Nitriles are compounds with the cyano functional group, -CN, for example: CH_3CN and C_2H_5CN, (e.g. Cesaroni et al., 2011; Furuya et al., 2011; Nummelin et al., 2000; Wang et al., 2009). Ethers are those compounds which contain the ether functional group, an oxygen atom bonded to two carbon-hydrogen chains or rings, for example: CH_3OCH_3, (e.g. Sutton et al., 1995; Nummelin et al., 2000). Finally, esters are compounds formed by reacting an oxoacid, acids which contain oxygen, with another hydroxyl compound, i.e. one that contains the -OH group, for example, methyl formate, $C_2H_4O_2$ (e.g. Wang et al., 2009; Favre et al., 2011). Emission lines from these molecules are found in Figure 1.9, which shows the spectrum of a HMC.

Table 1.1: Parameters for classifying HII regions. (Hyper-Compact: Kurtz, 2002, Kurtz 2005; Ultra-Compact: Wood & Churchwell 1989; Compact & Classical: Kurtz 2005)

Class	Diameter (pc)	Density (cm^{-3})	Emission Measure (pc cm^{-6})
Hyper-compact	<0.01	$\geq 10^6$	$\geq 10^8$
Ultra-compact	<0.1	$\geq 10^4$	$\geq 10^7$
Compact	$\leq$0.5	$\geq 5x10^3$	$\geq 10^7$
Classical	$\sim$10	$\sim$100	$\sim 10^2$

1.5 HII Regions

Eventually, as its flux increases, the central protostar will begin to ionise the material surrounding it and an HII region is formed. This is the final stage in the formation of a high mass star. There are four types of HII region: hyper-compact HII (HCHII) regions, ultra-compact HII (UCHII) regions, compact regions and classical regions. The classification of an HII region depends on its size, density, and emission measure. The parameters for each type of HII region are given in Table 1.1.

Generally, HII regions are thought to begin as HCHII regions. As they evolve they grow in size and decrease in density until they become classical HII regions. However, this is a relatively simplistic view as the evolution of a protostar depends greatly on the nearby environmental conditions (e.g. the surrounding pressure) and the number density of protostars in the region. A large cluster, for instance, may not pass through the smallest stages and may simply create a compact or classical HII region without ever having been an HCHII or UCHII region. Here, we consider the general case where an HII region will begin as an HCHII region and evolve through all three subsequent stages.

1.5.1 Hyper-Compact HII Regions

HCHII regions are currently thought to be the first observable stage of an HII region (Gaume et al., 1995). They have the smallest sizes and the highest densities, see Table 1.1. They are thought to be formed from a single star (or possibly a binary system) as opposed to the cluster of stars at the heart of UCHII and compact HII regions.

HCHII regions were only discovered recently (Gaume et al., 1995) when compared to their larger counter-parts which were first observed much earlier (e.g. Churchwell, Felli, & Mezger, 1969). Early surveys searching for small HII regions were conducted at centimetre wavelengths, primarily at 6–20 cm (e.g. Wood & Churchwell, 1989; Garay et al., 1993). This is the optimal wavelength for objects with densities $\sim 10^4\,\mathrm{cm}^{-3}$ and so is ideal for searching for UCHII regions. However, HCHII regions have much higher densities ($\geq 10^6\,\mathrm{cm}^{-3}$) and so remain optically thick to shorter wavelengths, see Figure 1.10. This can be shown by considering thermal bremsstrahlung radiation, the dominant contributor to the spectrum of an HII region at radio wavelengths ($\lambda > 1\,\mathrm{mm}$, Mezger & Henderson, 1967).

Thermal bremsstrahlung radiation is produced by the deceleration of one charged particle when deflected by a second charged particle. In HII regions these particles are typically electrons and positively-charged ions. The expression for calculating the optical depth of thermal bremsstrahlung emission is:

$$\tau_\nu \approx 0.082 T_e^{-1.35} \nu^{-2.1} \int_0^D n_e^2 ds \tag{1.4}$$

(Altenhoff et al., 1960; Oster, 1961), where T_e is the electron temperature, typically $\sim 10,000\,\mathrm{K}$ in HII regions (Garnett & Kennicutt, 2004), τ_ν is the optical depth at

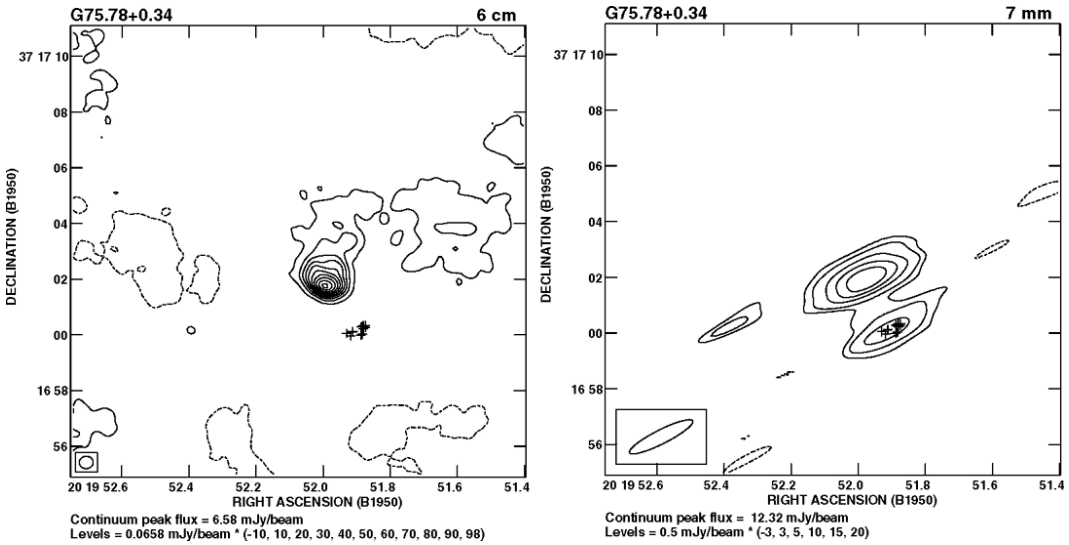

Figure 1.10: Left: A 6 cm continuum image of G075.78+0.34 (Wood & Churchwell, 1989). An UCHII region is visible at a right ascension (B1950) of 20h19m52.0s and declination (B1950) of 13°17'02". Crosses mark the positions of known water masers but no continuum emission is visible at this position. Right: A 7 mm continuum image of the same area (Carral et al., 1997). Here, continuum emission from a HCHII region coincident with the water masers is visible in addition to emission from the UCHII region (Kurtz, 2005).

frequency ν (in GHz), D is the diameter of the HII region and n_e is the electron density (in cm^{-3}).

The turnover frequency, $\tau_\nu = 1$, divides the optically thick part of the spectrum ($\tau_\nu > 1$) from the optically thin ($\tau_\nu < 1$). If $\tau_\nu = 1$, then Equation 1.4 becomes:

$$\nu = \left[0.082 T_e^{-1.35} \int_0^D n_e^2 ds\right]^{0.476} . \tag{1.5}$$

UCHII regions have diameters of $\sim$0.1 pc and electron densities of $\sim 10^4\,\mathrm{cm}^{-3}$ (Wood & Churchwell, 1989). Substituting in the typical values for an UCHII region gives a turnover frequency of $\sim$2 GHz (a wavelength of $\sim$20 cm). UCHII regions are therefore optically thin at frequencies greater than $\sim$2 GHz and wavelengths shorter than $\sim$20 cm and so are visible in surveys conducted between 6 and 20 cm.

HCHII regions are smaller ($\sim$0.01 pc) and have higher densities ($\sim 10^6\,\mathrm{cm}^{-3}$). Substituting these values into Equation 1.5 results in a turnover frequency of $\sim$50 GHz (a wavelength of $\sim$0.6 cm). HCHII regions are therefore optically thin only at frequencies greater than $\sim$50 GHz and wavelengths shorter than $\sim$0.6 cm. HCHII regions are optically thick at the wavelengths where early UCHII region surveys were conducted and so remained undetected for longer (Kurtz, 2005).

1.5.1.1 Radio Recombination Lines

Radio recombination lines are emission lines at radio wavelengths. They result from the transition of an electron between energy levels, generally in an atom with a principle quantum number greater than fifty (where the principle quantum number, n, is concerned with the energy of an electron; the higher the value of n, the greater the electron's energy). HCHII regions often have especially broad (40–250 kms^{-1}; e.g. Gaume et al., 1995; Sewilo et al., 2004; Kurtz, 2005) radio recombination lines, see Figure 1.11.

Line broadening in the more evolved, larger HII regions is primarily due to thermal and turbulent broadening. Thermal broadening is caused by the distribution of velocities in the atoms or molecules of the gas. The higher the temperature the greater the distribution of velocities and so the wider the spectral line. Turbulent line broadening is caused by the unresolved spatial motion of the ionised gas increasing the distribution of velocities. However, thermal and turbulent broadening effects typically only cause line widths of 25–30 kms^{-1}(Sewilo et al., 2004). The radio recombination lines in HCHII regions show widths in excess of 40 kms^{-1}, beyond what would be expected from these effects.

The line broadening in HCHII regions is therefore theorised to have an addi-

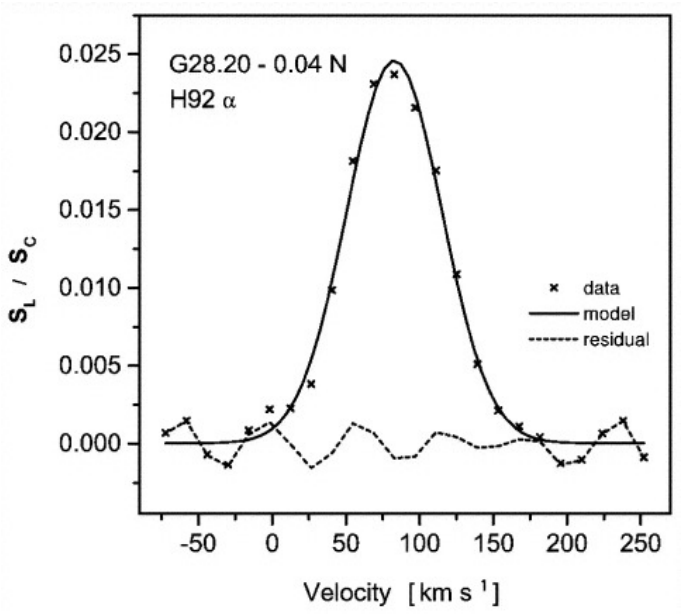

Figure 1.11: The H92α radio recombination line (ν_0 = 8309.38 MHz) from G028.20-0.04N, a HCHII region (Sewilo et al., 2004). The line width (FWHM) is greater than 40 kms^{-1} ($\sim$ 74 kms^{-1}), in excess of the expected thermal plus turbulent widths, and so indicating electron impact broadening is playing a role.

tional cause: electron impact (pressure) broadening. The radiative process of an electron transition occurs in a finite amount of time. In a high density gas the interval between atomic collisions is much smaller than the time taken to emit a photon (the radiating time). A collision can cause the atom to emit a photon prematurely. The decreased radiating time leads to an increased uncertainty in the energy of the emitted photon and thus broadens the emission line. The densities in HCHII regions are high enough for electron impact broadening to come into effect while the lower densities in the ultra-compact and larger HII regions mean that electron impact broadening does not play a significant role. However, the exact contribution of each of the line broadening mechanisms in HII regions is not yet known.

1.5.1.2 Theoretical Models

Traditionally, the evolution of HII regions was thought to be pressure-driven. The central star begins ionising the surrounding material. It expands until an equilibrium point is reached inside the HII region. At this point the ionisation rate (the rate of ionisation of hydrogen by photons emitted from the central star) is equal to the recombination rate (the rate at which free electrons recombine with HII ions). The ionisation rate is given by:

$$N_I = S_* \tag{1.6}$$

where S_* is the rate at which ionising photons are emitted by the central star. The recombination rate is given by:

$$N_R = n_e n_p \int^V \alpha(T_e) dV, \tag{1.7}$$

where n_e is the electron density, n_p is the proton density, V is the volume of the HII region and $\alpha(T_e)$ is the recombination coefficient of hydrogen and is typically $4 \times 10^{-13}\,\mathrm{cm^3 s^{-1}}$.

The temperature in the HII region is $\sim$100$\times$ greater than that of the neutral material surrounding it and so the ionised material in the HII region is subject to a higher pressure. The higher pressure causes the HII region to expand. This reduces the density of the HII region and thus the recombination rate and allows an increased number of ionising photons to reach the HII region boundary. These escape and ionise the previously neutral material, increasing the radius of the HII region, until a new equilibrium is reached. The process then repeats.

However, this theory estimates the lifetime of the HCHII and UCHII phase to be $\sim 10^4$ years. Number statistics of UCHII regions implies that they actually have

a lifetime of a few 10^5 years (Kaper et al., 2011). Pressure-driven expansion can not account for this long lifetime. It also ignores gravitational effects prevalent at smaller radii and which have a large effect in the smaller HCHII and UCHII regions (Keto, 2002, 2003). Pressure-driven expansion likely applies to larger, more evolved HII regions (compact and classical regions, see Section 1.5.3) but not HCHII and UCHII regions.

There are currently several theoretical models to describe HCHII regions. These include photoevaporated disks (e.g. Hollenbach et al., 1994; Lugo, Lizano, & Garay, 2004), ionised accretion disks (e.g. Keto, 2002, 2003) and outflow confined HII regions (Tan & McKee, 2003). All these models predict a longer lifetime than that given by thermal expansion.

The theory of photoevaporated disks was originally developed for UCHII regions (Hollenbach et al., 1994) but occurs on scales that are relevant for HCHII regions. In this model, HCHII regions are formed by the photoevaporation of neutral accretion disks which orbit the central star. This occurs as the disk is heated and ionised by Lyman continuum photons emitted from the star (i.e. photons with $\lambda < 9.12\,\mathrm{nm}$ that are capable of ionising hydrogen). In the case of a photoevaporated disk the ionised gas expands away from the star but is constantly replaced by the gas photoevaporated from the disk. Two scenarios exist within this model: the weak wind case and the strong wind case (see Figure 1.12).

In the weak wind case there is an ionised HII atmosphere of isothermal plasma out to r_g, the gravitational radius (i.e. inside r_g material is gravitationally bound). A weak stellar wind is defined as one where the ram pressure of the wind is less than the thermal pressure at the base of the HII atmosphere. The stellar wind therefore has no significant effect within r_g. Beyond r_g, a disk-wind is produced

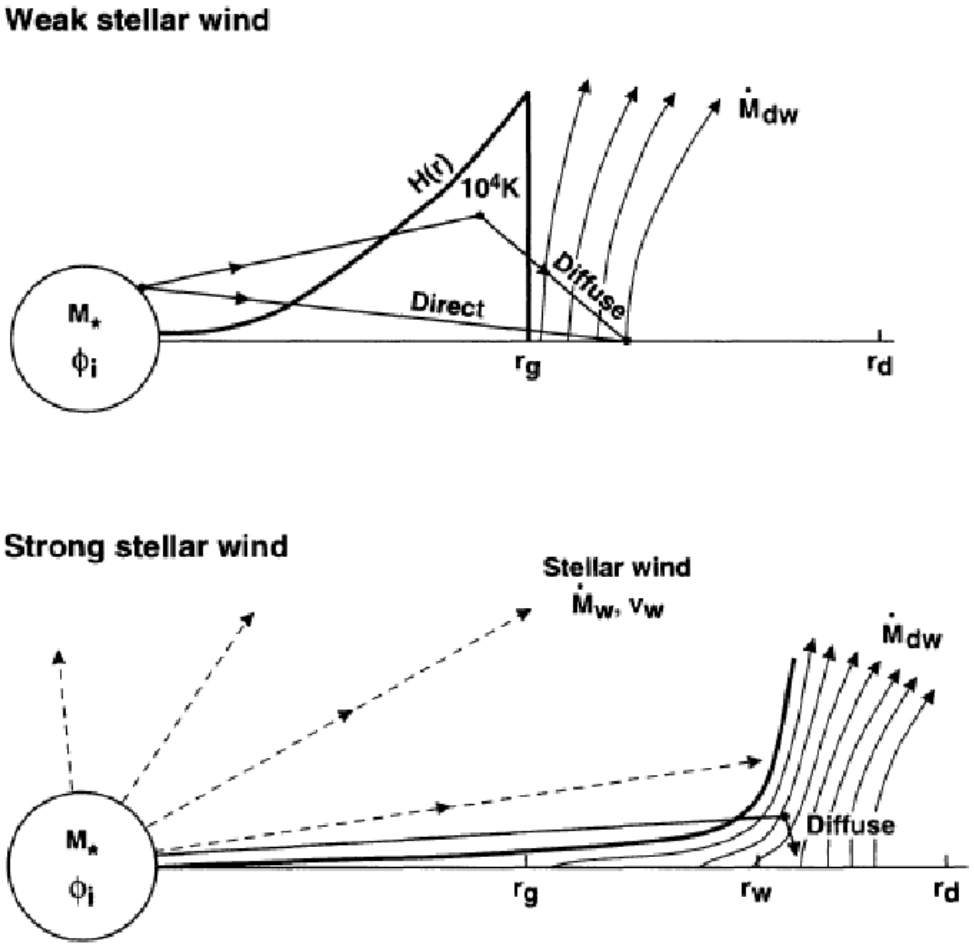

Figure 1.12: Diagrams showing two cases for the photoevaporating disk model (Hollenbach et al., 1994). Upper: the case for a weak stellar wind. Lower: the case for a strong stellar wind. M_* is the stellar mass; ϕ_i is the Lyman continuum photon luminosity; r_d is the disk radius; r_g the gravitational radius, for $r<r_g$ material is gravitationally bound to the star, r_w is where the stellar wind pressure equals the thermal pressure in the disk. $\dot{M}_{DE}$ is the mass loss rate from the disk and $\dot{M}_w$ the mass loss rate from the stellar wind. $H(r)$ is the scale height of the ionised atmosphere in the weak wind scenario. 'Direct' and 'diffuse' refer to the types of photon ionising the disk at different radii. Direct photons are from the central star, while diffuse photons are from the recombination of an electron to the ground state of a hydrogen or helium ion.

from the ionisation of the disk by Lyman continuum photons. This disk-wind gives a mass loss rate of $\dot{M}_{DE}$ from the outer disk as the material is photoevaporated and drifts away (Hollenbach et al., 1994).

In the strong wind scenario, the stellar wind is strong enough to blow away the HII atmosphere. Photons penetrate out to larger radii and the photoevaporation rates are greater than in the weak wind case (Hollenbach et al., 1994).

The theory of ionised accretion disks was also originally developed for UCHII regions but, again, works on smaller scales. Here, the HII region is formed inside the accretion flow from an accretion disk onto the central star. In its earliest stages, the HII region is gravitationally bound to the central star. The HII region can not expand as the thermal pressure is not great enough to overcome the gravitational force. Thermal expansion will only occur when the outer boundary of the HII region is at a radius where the sound speed of the ionised gas is greater than the escape velocity of the star's gravity. Within the HII region the ionisation rate is equal to the recombination rate. By equating Equations 1.6 and 1.7 and assuming $n_p = n_e$, the radius of the HII region, R_s, should therefore be given by:

$$R_s = \left(\frac{3}{4\pi} \frac{S_*}{n_e^2 \alpha(T_e)^2} \right)^{\frac{1}{3}} \tag{1.8}$$

(Strömgren, 1939). This is called the Strömgen radius and is proportional to S_*, the ionising flux of the central star. As the central star accretes more mass, its ionising flux will increase and therefore so too will the radius of the HII region. Eventually the HII region expands enough to overcome the star's gravitational attraction and it begins to expand due to thermal pressure (Keto, 2002, 2003).

With the outflow confined model an accretion disk is still assumed but the

accretion rates are much higher than when considering the ionised accretion disk model. In this case, the accretion rates are high enough to form massive bipolar outflows. The high density of the outflow gas confines the HII region to hyper-compact sizes until the accretion rates decrease and the outflows disperse (Tan & McKee, 2003).

1.5.2 Ultra-Compact HII Regions

Eventually, as HCHII regions expand, they will become UCHII regions. UCHII regions have larger diameters and are less dense than the hyper-compact phase, see Table 1.1. Any accretion disk will likely have been photoevaporated by this time and so accretion onto the central star will have stopped. The central star will therefore have achieved its main-sequence mass. It is possible that UCHII regions, unlike HCHII regions, are formed from a cluster of stars rather than a single star.

1.5.2.1 Morphologies

UCHII regions exhibit only a small number of different morphologies. These can be important as an indication of the conditions of the surrounding medium shortly after a star has formed. The morphology of a region depends on its age, the density of the surrounding material, the dynamics of the ionised and molecular gas and the motion of the UCHII region relative to the parent molecular cloud (Churchwell, 2002).

Wood & Churchwell (1989) developed a classification scheme for UCHII regions, based on their appearance at radio wavelengths. There are currently six defined morphologies: (1) spherical, regions that can easily be modelled with a

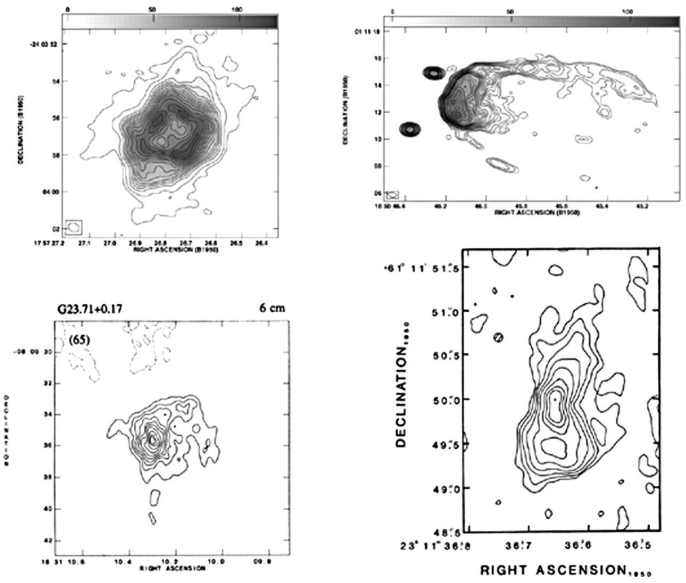

Figure 1.13: Upper row (left–right): G005.89–0.39, a UCHII region with a shell-like morphology, and G034.26+0.15, an UCHII region with a cometary morphology (Churchwell, 2002). Lower row (left–right): G023.71+0.17, a UCHII region with a core-halo morphology (Wood & Churchwell, 1989) and NGC7538 IRS1 with a bipolar morphology (Campbell, 1984).

Gaussian (many of the spherical sources are likely to show structure when viewed with a higher resolution); (2) cometary, regions with a parabolic ionisation front and that are shaped like a comet; (3) irregular or multiply peaked, regions where several sources are seen, these sources are usually associated with extended low surface-brightness emission; (4) core-halo, regions with a single peak surrounded by an extended low surface-brightness halo; (5) shell or shell-like, the region appears as a ring of emission in an optically thin regime and as a uniform disk in the optically thick; and (6) bipolar (added by Churchwell 2002), these UCHII regions have an hourglass shape when projected on the sky. More recent surveys (e.g. de Pree et al., 2005) have removed the core-halo classification and focused on the shape of the central object (the core) and the halo separately. Some examples of the different UCHII morphologies are shown in Figure 1.13. The percentages of each type found in three major surveys are shown in Table 1.2.

Table 1.2: Distribution of morphologies of UCHII regions (given as percentages, the remainder from each survey were unresolved). WC89: Wood & Churchwell (1989), K94: Kurtz et al. (1994), DP05; de Pree et al. (2005). de Pree et al. (2005) do not make use of the core-halo morphology, instead viewing the morphology central 'core' object separately from the extended 'halo'. They also use the bipolar classification which was not used in either Wood & Churchwell (1989) or Kurtz et al. (1994).

Class	WC89	K94	DP05
Spherical	24	36	21
Cometary	20	16	14
Irregular	17	19	11
Core-Halo	16	19	–
Shell/Shell-like	4	1	28
Bipolar	–	–	8

1.5.2.2 Theoretical Models

There are six major theories for describing UCHII regions: photoevaporating disks (Hollenbach et al., 1994); champagne flows (Tenorio-Tagle, 1979; Bodenheimer, Tenorio-Tagle, & Yorke, 1979); inflow models (e.g. Zheng et al., 1985; Ho & Haschick, 1986); pressure-confined nebulae (de Pree, Rodriguez, & Goss, 1995; de Pree, Goss, & Gaume, 1998); mass loaded stellar winds (Dyson, Williams, & Redman, 1995; Lizano et al., 1996; Redman, Williams, & Dyson, 1996; Williams, Dyson, & Redman, 1996); and stellar wind supported bow shocks (Wood & Churchwell, 1989). These models primarily seek to explain the morphologies, as described in Section 1.5.2.1, and the long lifetime of UCHII regions (see Section 1.5.1.2). However, most are only able to describe either a single morphology or the lifetime of UCHII regions.

The photoevaporating disk model is also used for HCHII regions (see Section 1.5.1.2). This model can explain the long life of UCHII regions as the ionised gas expanding away from the central star(s) is replaced by photoevaporated material from the disk. It does not address the morphologies of the regions.

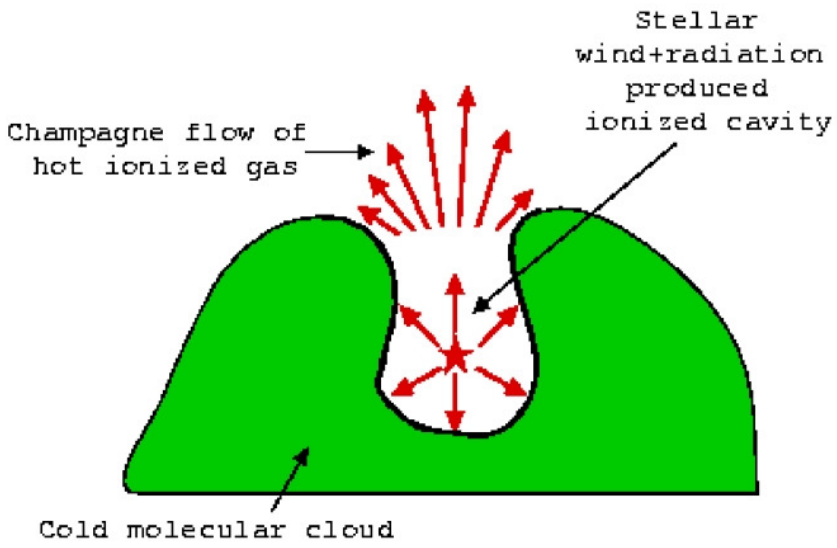

Figure 1.14: Diagram illustrating the creation of a cometary UCHII via a champagne flow (Churchwell, 1999).

Champagne flows are generally applicable when there is a density gradient from one side of the UCHII region to the other (e.g. when the UCHII region is at the edge of the parent molecular cloud, see Figure 1.14). The ionised gas is confined on one side but able to flow freely in the other direction (e.g. away from the molecular cloud), see Figure 1.14. This model can explain the cometary morphology but does not account for the long life of small HII regions (e.g. Forster et al., 1990; Hoare et al., 2007).

Infall models theorise that the lifetime of UCHII regions can be lengthened by infalling molecular gas (i.e. accretion onto the central star) halting the expansion of the ionised region. If the ISM surrounding an UCHII region has a high enough density ($\sim 10^7\,\mathrm{cm}^{-3}$), this can place enough thermal pressure on the UCHII region to confine the HII region for periods of up to 10^5 years (de Pree et al., 1995, 1998). Xie et al. (1996) suggest that, rather than thermal pressure which necessitates high emission measures, turbulent pressure can confine the HII region for a similar

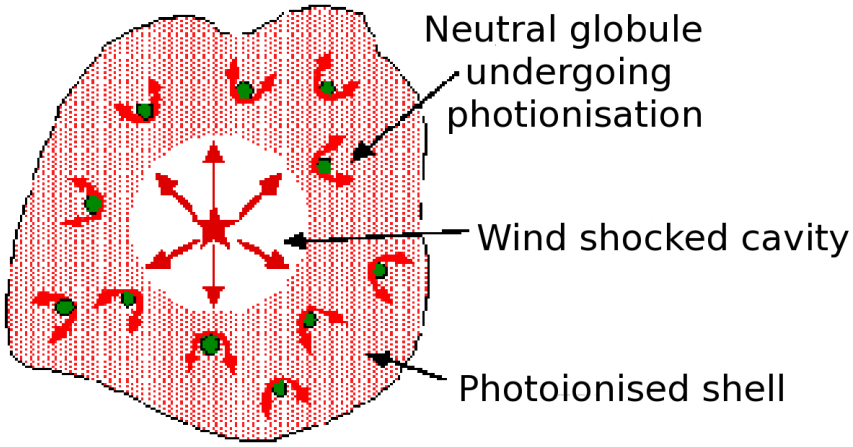

Figure 1.15: Diagram illustrating the theory of mass loaded stellar winds (Churchwell, 1999).

period of time and with emission measures of a level typical for an UCHII region, see Table 1.1. This model can explain long lifetimes but does not address the morphology of UCHII regions (Churchwell, 2002).

The theory of mass loaded stellar winds supposes that the UCHII region exists in a medium that contains many dense, neutral condensations, see Figure 1.15. The radiation from the star photoionises the envelopes of the condensations providing a continuous release of ionised gas into the HII region. This traps the ionisation front of the HII region, restricting its growth and thus extending the lifetime of the UCHII phase. Again, this explains the lifetime of UCHII regions but does not address their morphologies. This model also predicts many double-peaked line profiles which have not been seen in observations (Hoare et al., 2007).

Bow shock models are unlike the other five theories in that they explain both the lifetime of UCHII regions and cometary, core-halo and shell morphologies (e.g. van Buren et al., 1990; Mac Low et al., 1991; Arthur & Hoare, 2006). This theory

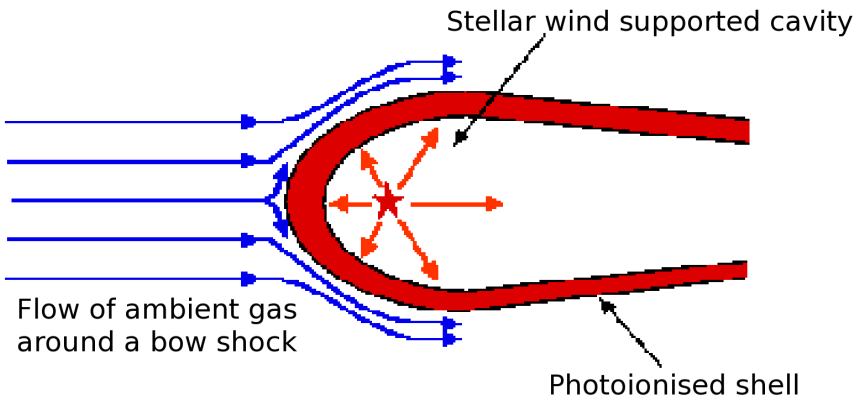

Figure 1.16: Diagram illustrating the confinement of an UCHII by a bow shock (Churchwell, 1999).

requires that the HII region has a small velocity relative to the parent molecular cloud. As the UCHII region moves through the cloud a bow shock is formed in the direction of motion. The stellar wind from the central star provides a countering force to the shock and a low density, hot shell is formed in the UCHII region, see Figure 1.16. The HII region will remain in this state until it leaves the parent molecular cloud. Viewed head-on the UCHII would appear to have a core-halo morphology and viewed side-on would appear to be cometary. Shell morphologies can be explained by a very small initial velocity (Churchwell, 1999).

Churchwell (1999) theorises that the different theories may be correct at different evolutionary stages in the lifetime of an UCHII region or be dependent upon the conditions in the UCHII region and its parent molecular cloud.

1.5.2.3 Density-Size Relation

Within the HII region we assume the ionisation rate is equal to the recombination rate. The radius of the HII region should therefore be the Strömgren radius, R_s, given by Equation 1.8. The diameter of the HII region, $D = 2 \times R_s$, should then

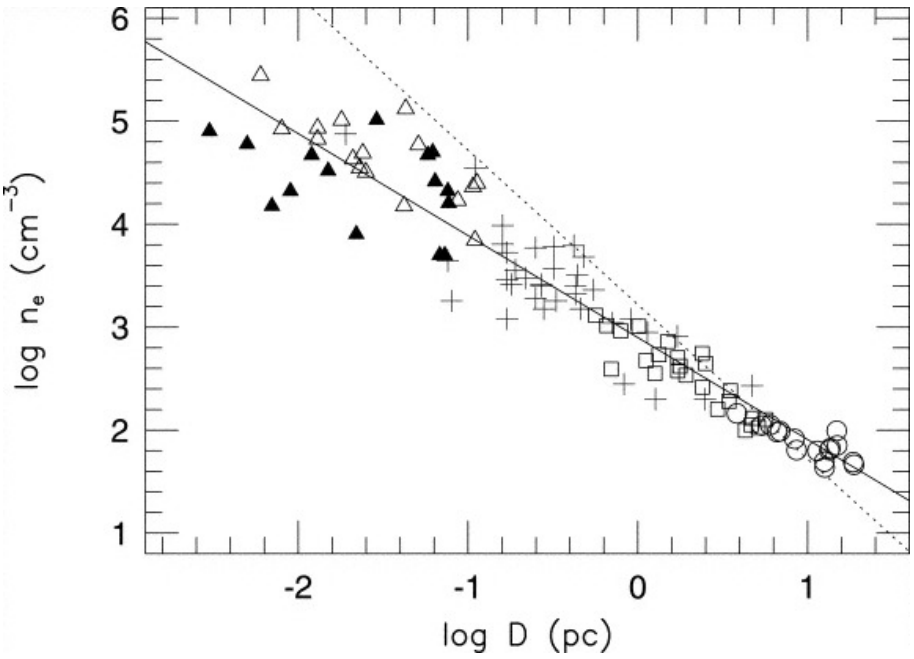

Figure 1.17: A log-log plot of the electron density of UCHII regions against their diameters (Kim & Koo, 2001). The solid line shows the least squares fit with the relation $n_e \propto D^{-0.99\pm0.03}$. The dashed line shows the relation $n_e \propto D^{-3/2}$, expected for a spherical, uniform density nebula.

be proportional to $n_e^{-2/3}$ and $n_e \propto D^{-3/2}$. However, Kim & Koo (2001) found that, for UCHII regions, $n_e \propto D^{-1}$ (shown in Figure 1.17).

Garay & Lizano (1999) suggested that this could be due to UCHII regions being formed by lower luminosity stars than larger HII regions. UCHII regions would therefore have a smaller size due to a the central star emitting fewer ionising photons. However, if the central star has a low UV luminosity then the high IR luminosities observed from UCHII regions can not be explained (Kurtz et al., 1994).

Alternatively, Kim & Koo (2001) theorised that the shallow relation was due to variation in ambient density, with smaller regions located in denser areas of the parent molecular cloud. The size-density relation seen in HII regions is then explained by the density-size relation of molecular clouds: $n_{H_2} \propto D^{-1.1}$ (Larson,

1981).

Another possible solution was offered by Dopita et al. (2006), who showed that the density-diameter relation can be explained if dust grains exist within the HII region. The dust grains absorb some of the ionising photons within the UCHII region and so decrease the diameter of the ionised region.

1.5.3 Compact and Classical HII Regions

An HII region will continue to expand until it leaves the ultra-compact phase and moves first into the compact and then into the classical stage. These regions are larger and less dense than either hyper- or ultra-compact HII regions. The approximate size and density parameters for compact and classical HII regions are shown in Table 1.1.

1.5.3.1 Compact HII Regions

Compact regions are thought to be the intermediate stage of an HII region. More evolved than HCHII and UCHII regions but still younger (and smaller) than classical regions.

Compact HII regions are similar to UCHII regions, see Figure 1.18. They show similar morphologies (Garay et al., 1993) which can be modelled using similar theories (for example, Arthur & Hoare, 2006, use bow-shock and champagne flow models, see Section 1.5.2.2, to describe cometary compact HII regions). They are also still mostly contained within their parent molecular cloud, the exception being 'blister' regions close to the edge of the molecular cloud that have begun to expand

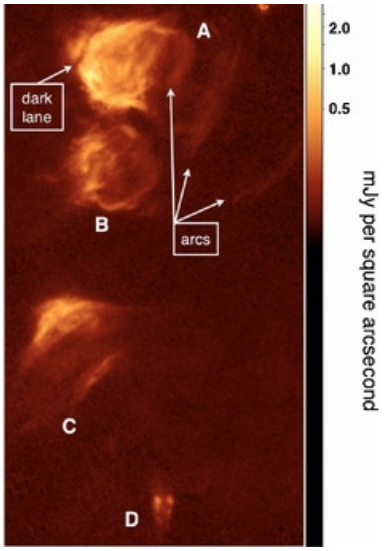

Figure 1.18: Paschen α (a recombination transition of hydrogen from n=4 to n=3) image of four HII regions. Three (A, B and C) have been classified as compact and one (D) as ultra-compact. The text in the image refers to interesting features of region A, including a dark lane and a series of filaments extending from the HII region (Mills et al., 2011).

beyond the molecular cloud via a champagne flow (see Section 1.5.2.2). Compact regions are also still optically thick at optical wavelengths but optically thin in the radio and the infrared.

However, unlike UCHII regions, in compact HII regions the ionised gas is no longer gravitationally bound to the central star and can expand freely. Compact HII regions are therefore expected to expand via pressure driven expansion, as described in Section 1.5.1.2.

1.5.3.2 Classical HII Regions

The final observed stage in the formation of a high mass star is a classical HII region. These are the largest HII regions seen in our Galaxy and are believed to be the most evolved. At this point the central stars are hydrogen-burning and

classical regions are often being ionised by numerous O and B type stars.

The expansion of a classical HII region means that it will eventually reach a point where it will begin to disrupt the parent molecular cloud (e.g. Matzner, 2002; Krumholz, Matzner, & McKee, 2006). This causes the dust and gas obscuring the stellar population to disperse and the central stars finally become visible at optical wavelengths.

1.6 Competing Concepts of High Mass Star Formation

There are several competing theories of high mass star formation including: monolithic collapse, where high mass stars form through the gravitational collapse of molecular cores; triggered star formation, where an event such as a nearby supernova (Desai et al., 2010), or an expanding HII region (Dale, Bonnell, & Whitworth, 2007; Bisbas et al., 2011) compresses a molecular cloud and initiates its gravitational collapse; competitive accretion, where the final mass of the star depends on the amount of material accreted during its formation; and stellar collisions and mergers, where low mass stars collide to form a single high mass star.

It is likely all four theories occur to varying degrees, dependent on the environment of the molecular cloud. Monolithic collapse, for instance, is more probable in cases where the parent molecular cloud is initially magnetically subcritical (when the gravitational potential energy is not strong enough to overcome the magnetic field) until ambipolar diffusion creates a supercritical core. Competitive accretion is more likely to occur in regions where the protostars are highly clustered, and

triggered star formation will only occur after there has been some form of triggering event. Monolithic collapse and competitive accretion assume that the initial protostar gains mass through disk accretion. Stellar mergers, on the other hand, assume that high mass stars are formed from collisions of low mass stars. This is only probable in extreme environments where the star number density is very high and stellar collisions are unavoidable.

1.6.1 Monolithic Collapse

This theory was originally developed by McKee & Tan (2003) and proposes that high mass stars form from the gravitational collapse of turbulent molecular cores. Each core has a mass of a few tens to several hundreds of solar masses and is formed by the fragmentation of molecular cloud clumps. These molecular clumps are much larger than the cores, with masses of hundreds or thousands of solar masses. The core accretes material via an accretion disk but only accretes material that is already gravitationally bound to it, typically that which was in the original molecular clump. In this case, only the highest mass cores will form high mass stars. Eventually the cores undergo gravitational collapse and the largest form a single high mass star or high mass binary system. Simulations by Yorke (2002) have shown that this method can create stars with masses up to $\sim 43\,\mathrm{M}_{\odot}$ when the initial mass of the core is $120\,\mathrm{M}_{\odot}$, and that larger initial masses could lead to higher mass stars.

A major problem with this theory is that of fragmentation. If the molecular cores fragment they would be expected to form a cluster of low mass stars rather than one or two high mass stars. Turbulence is assumed in the cores in order to slow down the gravitational collapse and increase the lifetime of the core. However,

turbulent cores are expected to undergo fragmentation (Krumholz, Matzner, & McKee, 2006). This has been much debated (e.g. Dobbs, Bonnell, & Clark, 2005; Krumholz, Klein, & McKee, 2007) and it has been suggested that strong magnetic fields (making the cores subcritical) could help to stabilise the cores and prevent fragmentation.

One advantage of monolithic collapse is the theoretical initial mass function (IMF) that it produces. Observations of star-forming regions have shown that the stellar IMF is similar to the core mass function (CMF), and which can be interpreted as one-to-one correlation between the two (e.g. Testi & Sargent, 1998; Alves, Lombardi, & Lada, 2007). For this to occur the core must not fragment or gain mass through its formation process (i.e. from the point where a core forms through to the core joining the main sequence). As monolithic collapse requires that cores do not fragment and all accretion is of material already gravitationally bound to the core, this is in agreement. However, it has also been shown that the opposite scenario, where all cores fragment before eventually forming multiple systems, can also explain the similarity between the CMF and IMF (Goodwin et al., 2008).

1.6.2 Triggered Star Formation

One of the more popular theories of triggered star formation is the 'collect-and-collapse' scenario, originally presented by Elmegreen & Lada (1977) and since expanded (e.g. Whitworth et al., 1994; Elmegreen, 1998; Dale et al., 2007). This theory requires some form of triggering event (e.g. an expanding HII region) to create an ionising shock front. Collect-and-collapse states that, as the shock wave travels through the ISM, molecular gas and dust are collected at the edge of the

shock front. The pressure from the shock front compresses the molecular gas and decreases its temperature. This stimulates gravitational instabilities and fragmentation in the gas and high mass protostars begin to form.

The ionisation shock can be induced through several methods, for instance: galactic interactions, both merging galaxies and galactic 'flybys' have been shown to induce starburst activity and increase the star formation rate in the affected galaxies by an order of magnitude for several million years (e.g. Mihos, Richstone, & Bothun, 1992); the movement of gas through the arms of spiral galaxies can induce large-scale galactic shock waves (e.g. Roberts, 1969); collisions of molecular clouds can cause smaller scale shocks (e.g. Scoville & Hersh, 1979; Whitworth et al., 1994; McLeod, Palouš, & Whitworth, 2011); and, as noted above, shocks can be caused by feedback from O/B-type stars themselves — expanding HII regions, stellar winds and supernovae have all been shown to induce further high mass star formation (e.g. Dale et al., 2007; Desai et al., 2010; Bisbas et al., 2011). The latter triggering mechanism is particularly interesting as it implies that high mass star formation is, at least in part, self-propagating.

Many regions of high mass star formation have been observed that are believed to have been brought about by such an event. The high mass star forming regions RCW120 and N49 are thought to have been triggered by the expansion of an HII region (Deharveng et al., 2009; Zavagno et al., 2010). Star-forming regions around the edge of the Carina nebula are believed to have been caused by stellar winds and UV radiation from the high mass stars at the nebula's centre (Smith & Brooks, 2007). Similarly, the Orion Nebula Cluster is another likely example of triggered star formation, probably due to energy output from the Orion OB1ab association subgroups (Blaauw, 1991).

1.6.3 Competitive Accretion

The third major theory of high mass star formation is that of competitive accretion (Bonnell et al., 1997, 2001). In this case all stars start out as low-mass protostars. The final mass of the star is directly related to how much mass it accretes during the formation process. High mass stars are formed from the protostars that accrete the greatest amount of material. The major difference between competitive accretion and monolithic collapse is that the material accreted in competitive accretion is not necessarily gravitationally bound to the core. In competitive accretion the accreted material can theoretically originate anywhere in the parent molecular cloud. The accretion rate of individual cores depends, among other factors, on their size, mass, velocity and position within the molecular cloud. Each protostar accretes from within its own reservoir or accretion domain. The amount of material entering each individual accretion domain will depend on the location within the cloud, the relative velocity of the material and star and the size of the domain (which will depend on the radius and mass of the central core). As the domains of different cores begin to overlap, the cores begin to compete for material. This occurs in large clusters and results in many cores accreting material. Matter is eventually gathered from larger distances as the accretion domains increase in size along with the cores. The matter is funneled towards the accreting cores, allowing them to continue growing into high mass stars.

This mechanism has several advantages. First, due to the mass of the final star being dependent on the accretion rate onto a point mass, it is able to predict a power-law IMF at high mass. This is in agreement with observations of the IMF in stellar clusters (Bonnell et al., 2001). Competitive accretion also explains why massive stars are found at the centre of clusters. Gas flows inwards to the centre

of the cluster. This increases the amount of material available for the cores at the centre to accrete. The final mass of the core is largely dependent on the mass available for accretion, so cores at the centre of clouds will have large final masses. Cores at the edge of the cluster will have less material available and so have smaller final masses.

However, this theory has drawn criticism for using un-physical starting parameters in simulations. For example, André et al. (2007) found that competitive accretion was unlikely to be the dominant mechanism in the Ophiuchus protocluster as the velocity dispersion between the pre-stellar condensations is too low to allow for any interaction before the cores evolve into pre-main sequence objects. Additionally, models have typically assumed gravitationally bound cores while, realistically, these cores are more likely to be turbulence-dominated (Krumholz, McKee, & Klein, 2007).

1.6.4 Stellar Collisions and Mergers

This theory supposes that a high mass star is formed by the collision and merger of two or more lower mass stars (Bonnell, Bate, & Zinnecker, 1998). It was originally suggested as a way to circumvent the radiation problem with stars of mass $> 10\,M_{\odot}$. The radiation output by such stars was thought to create outward pressures high enough to halt accretion and so limit the growth of the protostar. However, more recent models have shown that this is not necessarily the case. Outflows create a cavity in the polar direction but allow for high mass stars to form via disk accretion (as in the two alternate theories described in Sections 1.6.1 and 1.6.3; Yorke 2002; McKee & Tan 2003).

Stellar mergers are likely to be the rarest method through which high mass stars form, if they occur at all. They are only likely to happen in densely packed clusters, where high mass stars are in very close proximity and collisions are inevitable (e.g. Baumgardt & Klessen, 2011). However, it has been theorised that competitive accretion can increase the density of stars at the centre of clusters to the point where stellar collisions and mergers may occur. Stellar collisions which do not result in mergers may also be the starting point of rapidly rotating high mass stars.

1.7 Summary

The evolution of high mass stars is still poorly understood when compared to their lower mass counterparts. In this chapter we have outlined the basic evolutionary path for high mass stars and the physical parameters and conditions present at each stage.

High mass stars begin as cold condensations of gas and dust, which we term infrared dark clouds. They are the densest parts of molecular clouds and have masses of a few hundred solar masses and sizes up to a few parsecs. They show no evidence of internal heating and are likely to be entirely heated by external radiation sources. Observations have shown that IRDCs have low temperatures, $<$25 K, and the temperature within a single IRDC has been shown to vary by up to 10 K, decreasing from surface to centre.

Some IRDCs contain cold cores. Cold cores have radii ranging from $\sim$0.05 up to $\sim$1.0 pc and masses from $\sim$10 to a few thousand $M_{\odot}$. They are typically the densest parts of IRDCs. An evolutionary sequence has been suggested for cold

cores within IRDCs: initially the cores are starless, meaning they do not contain evidence of active star formation and so have no internal heating; as the cold core evolves star formation begins and we see star formation tracers (e.g. 24 μm point sources), this is the active phase; finally an HII region develops and we see PAH emission in the form of an 8 μm source, this is now a red core. Starless cold cores are thought to be the high mass equivalent of low mass prestellar cores in that they have no internal heating but are gravitationally bound.

As internal heating switches on, ices that had condensed on dust grains during the cold phase are evaporated. These include many complex organic molecules and a cloud of dense molecular gas forms around the protostar. This is called a hot molecular core. HMCs are characterised by their high temperatures, >100 K, and their complex molecular spectrum.

Eventually the star begins to ionise its surrounding material and an HII region develops. There are four main stages of evolution for HII regions. The youngest, and smallest, is the hyper-compact phase. HCHII regions have diameters <0.01 pc and densities $\geq 10^6$ cm^{-3}. Unlike their larger counterparts they are optically thick at centimetre wavelengths and their high densities result in especially broad radio recombination lines.

The second stage of evolution for an HII region is the ultra-compact phase, with diameters <0.1 pc and densities $10^4 - 10^6$ cm^{-3}. Lower emission measures mean that UCHII regions are visible at $\sim$6 cm and lower densities result in narrower radio recombination lines than in HCHII regions. Number statistics of UCHII regions give an estimated lifetime of $\sim 10^5$ years, longer than would be expected for a nebula evolving via pressure-driven expansion. This has resulted in many theories aimed at explaining the long lifetime (and the observed morphologies) of

UCHII regions but, as yet, there is no consensus.

As the HII region continues to expand it evolves through the compact phase (diameter up to 0.5 pc and density $5 \times 10^3 - 10^4\,\mathrm{cm}^{-3}$). Typically by the compact phase the region has reached a size where it is no longer gravitationally bound to the central star. The HII region continues to expand and reaches the final, classical phase (diameter $\sim$10 pc and density $\sim 100\,\mathrm{cm}^{-3}$). Eventually, as the classical HII region continues to grow, it begins to disrupt the parent molecular cloud. As this occurs, the gas and dust that were obscuring the stellar population are dispersed and the stellar population becomes visible at optical wavelengths.

There are several major theories to explain how high mass stars evolve, such as monolithic collapse, triggered star formation, competitive accretion and stellar collisions and mergers. All are thought to occur, to differing degrees, dependent on the initial conditions in the star-forming region. It is these initial conditions that this thesis aims to study observationally.

1.8 Thesis Outline

The work presented in this thesis is primarily concerned with the very early stages of high mass star formation: IRDCs and their cores. In this chapter the cores within IRDCs have been referred to as 'cold cores' in order to distinguish them from hot molecular cores. However, in subsequent chapters they will simply be called cores.

In Chapter 2 the *Herschel* Space Observatory is described. *Herschel* observations were used for the majority of the work described in this thesis. The science

goals of the mission are discussed and the three instruments on-board are described, including their basic function and in-flight performances. The *Herschel* Infrared Galactic Plane Survey is also summarised. This is where the data in this thesis are obtained.

Chapter 3 focuses on the 3D Monte Carlo, radiative transfer code, PHAETHON. The basic function of the code is explained, as are the various input variables. PHAETHON is then tested to determine its usefulness for modelling cold cores within IRDCs. Six cold cores are modelled using both PHAETHON and single-temperature fitting. PHAETHON is found to accurately reproduce the observations of the six cores and to produce a more realistic temperature profile than the single-temperature fitting.

In Chapter 4, FIR observations are used to identify the IRDCs, originally found in the MIR as regions of absorption, that show emission at 250 μm and beyond. Cold cores within these IRDCs are also then found and placed into an evolutionary category.

The starless cold cores found in Chapter 4 are then further examined in Chapter 5. The most isolated, starless cores are found and twenty are modelled using PHAETHON. The parameters for the model for each cold core are outlined (including their masses, temperatures, densities and the ambient radiation field) and, finally, a comparison is made between each observed cold core and its modelled counterpart.

Chapter 6 is a discussion of the implications of the findings from Chapters 4 and 5. The lifetime of a cold core is calculated and, using number statistics, a timescale for each stage is estimated. The implications of a reduced number of

Galactic IRDCs are considered. Finally, the relationships between the physical parameters of the modelled cores are examined and their implications considered.

Chapter 7 is the final conclusion of the thesis. All the major results from the main body of the work are summarised and possibilities for future work are outlined.

Chapter 2

The Herschel Space Observatory

2.1 Introduction

Herschel is a European Space Agency (ESA) FIR and sub-mm space observatory. It builds on previous infrared missions (e.g. IRAS, Beichmann et al. 1988; ISO, Kessler, Metcalfe, & Salama 1992; Spitzer Space Telescope, Werner et al. 2004; AKARI, Murakami et al. 2007) to extend coverage further into the lesser explored wavelengths between the mid-infrared (MIR) and radio regions.

Infrared radiation is electromagnetic (EM) radiation with a wavelength between $\sim$0.7 and $\sim$350 μm. It is typically divided into three sub-categories: the near-infrared (NIR), $\sim$0.7–5 μm; the MIR, $\sim$5–40 μm; and the FIR, $\sim$40–350 μm. The existence of infrared radiation was first proven by Sir William Herschel in 1800 (Herschel, 1800a). He directed sunlight through a prism to create a spectrum and measured the temperature change due to the light of wavelength longer than visible light. He noted that the temperature increased with decreasing wavelength.

However, the greatest temperature change was measured in the area just beyond the red band, the infrared. Further experimentation proved that infrared radiation behaves in the same manner as optical radiation in that it can be refracted, reflected, absorbed and transmitted (Herschel, 1800b). This was the first time that it was demonstrated that the EM spectrum extended beyond the optical.

The *Herschel* Space Observatory was first proposed in November 1982 as the Far-Infrared Sub-millimetre space Telescope (FIRST). A feasibility study was conducted in 1983 and the mission was included in the ESA 'Horizon 2000' plan (Longdon, 1984). FIRST was approved in 1993 by an ESA Science Programme Committee (SPC) as the fourth 'cornerstone' mission. FIRST was eventually renamed *Herschel* in December 2000.

Herschel was successfully launched in May 2009, and carries three instruments: the Spectral and Photometric Imaging Receiver (SPIRE, Griffin et al. 2010); the Photodetector Array Camera and Spectrometer (PACS; Poglitsch et al. 2010); and the Heterodyne Instrument for the Far Infrared (HIFI; de Graauw et al. 2010). Together, SPIRE, PACS and HIFI are capable of performing photometry and spectroscopy between 55 and 671 μm (Pilbratt et al., 2010).

From launch, *Herschel* took approximately six months to reach its final destination and is currently orbiting the second Lagrange (L2) point, 1.5×10^6 km from the Earth (Pilbratt et al., 2010). There are five Lagrangian points in any two-body system. These points are shown in Figure 2.1. At each of these points the centripetal force due to orbital motion balances the gravitational force of the two bodies. An object placed at a Lagrangian point will maintain its position relative to the two other bodies in the system. It was decided that *Herschel* should perform observations at the L2 point in the Earth-Sun system. The L2 point is far enough

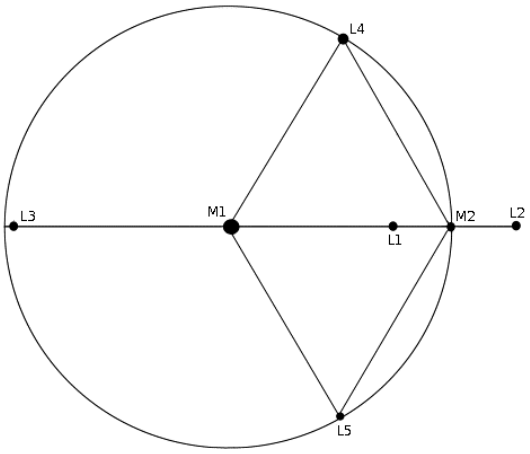

Figure 2.1: The five Lagrange points, L1–L5, in a two-body system, M1 and M2 (Maccone, 2002).

from the Moon and Earth that their FIR signature is minimised and therefore so too is their contribution to noise in the data. Additionally, the astronomical field of view is maximised as the Earth and Sun remain in the same direction at all times.

Herschel's available observing time is dictated by the lifetime of the cryostat. *Herschel*'s cryostat was initially filled with liquid helium. As the helium evaporates and leaves the cryostat it cools the instruments down to their operating temperatures. Once the helium supply runs out, the instruments will begin to warm up. It is not currently known how the helium will behave at very low levels and whether science observation will still be possible at this point. It is hoped that *Herschel* will perform observations for a minimum of three years, through to the end of 2012.

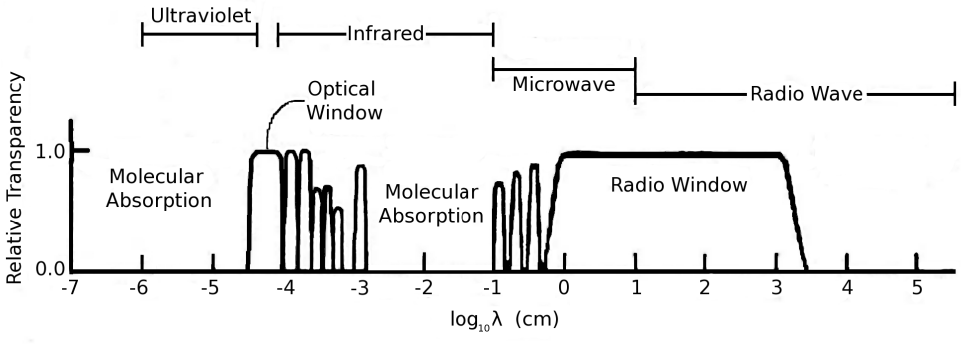

Figure 2.2: Relative atmospheric transparency at different wavelengths (Carroll & Ostlie, 1996).

2.2 Science Goals

Herschel was designed to observe the relatively poorly studied FIR and sub-mm wavelengths. The Earth's atmosphere causes problems for ground-based infrared telescopes. The atmosphere emits strongly at the infrared (peaking at $\sim$10 μm) and molecules, such as water vapour and carbon dioxide, absorb much of the longer-wavelength extra-terrestrial infrared radiation. Only a few small windows exist where infrared radiation can be observed from the Earth's surface (1–4 μm, 4.6–5.0 μm, 7.5–14 μm, 17–40 μm and in the sub-mm: 350 and 450 μm; see Figure 2.2). The relative transparency of Earth's atmosphere at different wavelengths is shown in Figure 2.2. To observe the entirety of the infrared spectrum, particularly the FIR and sub-mm, telescopes must be placed outside of the Earth's atmosphere.

A blackbody is an idealised object that absorbs all EM radiation incident upon it and re-radiates it in a blackbody spectrum. According to Wien's Law, the peak wavelength, λ_{max}, of this spectrum depends on the temperature, T, of the blackbody:

$$\lambda_{max} = \frac{b}{T}, \tag{2.1}$$

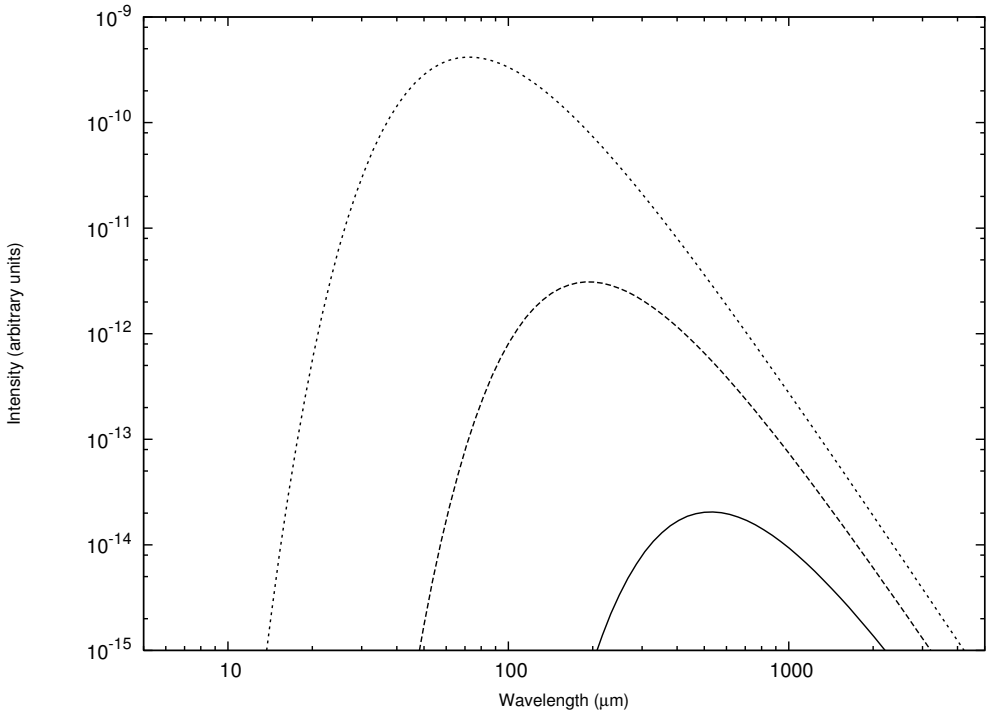

Figure 2.3: The spectrum of three blackbodies at different temperatures. The solid line shows the emission of a blackbody at 5 K, the dashed line at 15 K and the dotted line at 40 K. All three peaks are within *Herschel*'s observing range.

where $b = 2.90 \times 10^{-3}$ m K is Wien's constant. *Herschel* can observe continuum radiation from 70–550 μm. Using Equation 2.1, the peak of emission from blackbodies with temperatures from ∼5–40 K lie in *Herschel*'s range. Examples of the emission from three blackbodies with temperatures in this range are shown in Figure 2.3. Such objects include the youngest stages of star formation (e.g. pre-stellar cores and IRDCs), comets, asteroids and planetary atmospheres.

Optical and UV radiation is absorbed by interstellar dust grains. Thus, any object containing a large amount of dust is obscured at these shorter wavelengths. This includes regions of star formation, star-forming galaxies or active galactic nuclei. The radiation absorbed is re-radiated in the infrared. This makes *Herschel* ideal for studies of these dusty regions.

Additionally, the peak of emission from high-redshift (z=1–4) galaxies is redshifted into *Herschel*'s observing range due to cosmological expansion. These galaxies have a non-redshifted peak between 50 and 100 μm. Using the Doppler formula:

$$\lambda_r = \lambda_e(1 + z), \tag{2.2}$$

where λ_e is the emitted wavelength, λ_r is the received wavelength and z is the redshift of the galaxy, it can be calculated that the observed emission peak of these galaxies lies between 100 μm and 500 μm. Observations of these galaxies can aid our understanding of the formation and evolution both of galaxies and of the early universe.

Herschel is also capable of performing spectroscopy between 55 and 671 μm. Emission line spectra occur when atoms or molecules in hot gases move from an excited state to a lower energy level. The emission lines visible in any given region depend on its chemical composition and the states that are excited. *Herschel* can observe many emission lines, including those from isotopes and isotopologues of H_2O, CO, O, C, N and CS. These molecules exist in both galactic and extra-galactic star-forming regions as well as in cold objects within our own solar system.

Herschel's specific goals focus on the formation of galaxies, on the formation and evolution of stars and stellar systems, the effect stellar evolution has on galaxy evolution and the interaction of stellar systems with the interstellar medium (ISM).

2.3 Spacecraft

Herschel has a modular design and consists of the Payload Module (PLM) and the Service Module (SVM).

The PLM houses *Herschel*'s telescope (see Section 2.3.1) and the cryostat vacuum vessel. The cryostat contains the optical bench and the superfluid helium tank. The optical bench is where the Focal Plane Units (FPUs; which contain the detector arrays) of the three instruments are located. The optical bench is supported on top of the helium tank (Pilbratt et al., 2010). The superfluid helium is at a temperature of 1.6 K and is continually evaporating. The evaporated helium gas cools the detector arrays down to ∼1.7 K and other parts of the instruments down to 4 or 10 K, depending on their operating specifications.

The SVM is located next to the PLM and contains all the warm payload electronics, i.e. the parts of the instruments that do not require the cooling of the cryostat. It also houses the equipment necessary for handling the satellite's power, orbit and attitude control, on-board data-handling, communications and safety monitoring (Pilbratt et al., 2010). The SVM also contains the sun-shield and a thermal shield that isolates the SVM from the PLM and helps to minimise the heat load on the PLM.

2.3.1 The Telescope

The *Herschel* telescope (Pilbratt et al., 2010) is a classical Cassegrain design. Cassegrain telescopes have a parabolic primary mirror and a hyperbolic secondary. The secondary mirror reflects light through a hole in the primary mirror to the in-

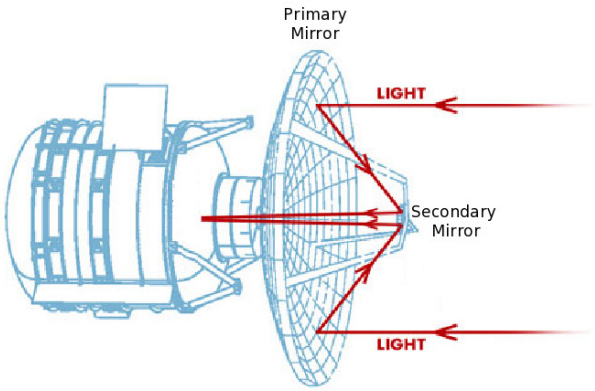

Figure 2.4: Cartoon showing light entering the *Herschel* telescope (Silberg, 2011). Courtesy NASA/JPL-Caltech.

strument FPUs. The basic design of the *Herschel* telescope is shown in Figure 2.4. *Herschel*'s telescope has a 3.5 m diameter primary mirror and a 30.8 cm diameter secondary (Pilbratt et al., 2010). It has a total wavefront error of less than 6 μm. The wavefront error, ω, is a measurement of how much the wavefront deforms from an idealised sphere and is calculated via:

$$\omega = \sqrt{\overline{W^2} - \overline{W}^2} \tag{2.3}$$

(Shannon & Wyant, 1992), where W is the wavefront deviation from an idealised sphere, $\overline{W^2}$ is the average of the squared wavefront deviation and $\overline{W}^2$ is the square of the average wavefront deviation.

The telescope is made almost entirely (90% by mass) from silicon carbide (SiC). SiC has a low thermal expansion coefficient, ensuring the telescope will keep its shape despite any temperature changes, and a high thermal conductivity, allowing the telescope to cool quickly (Pilbratt et al., 2010). SiC is also lighter than metal or glass, allowing the weight of the telescope to be kept to a minimum. The primary mirror was formed from twelve segments which were brazed together

to form a single mirror with a thickness of 3 mm. The secondary mirror was small enough to be constructed from a single segment (Pilbratt et al., 2010).

The telescope cools radiatively and is protected by a sunshield, allowing the telescope to remain at an operational temperature of approximately 85 K.

2.3.2 Instruments

Herschel carries three science instruments, each of which was provided by international PI-led consortia. The three instruments are: the Spectral and Photometric Imaging Receiver (SPIRE, Griffin et al. 2010) led by M. J. Griffin, University of Cardiff; the Photodetector Array Camera and Spectrometer (PACS, Poglitsch et al. 2010) led by A. Poglitsch, MPE and the Heterodyne Instrument for the Far-Infrared (HIFI, de Graauw et al. 2010) led by Th. de Graauw, SRON. SPIRE and PACS are primarily photometers, although both contain low resolution spectrometers. HIFI is a dedicated high resolution spectrometer.

2.4 The Spectral and Photometric Imaging Receiver (SPIRE)

SPIRE consists of a photometer and an imaging Fourier-transform spectrometer (FTS; Dohlen et al. 2000; Swinyard et al. 2003). The photometer performs broadband photometry $\left(\frac{\lambda}{\Delta\lambda} \approx 3\right)$ in three wavebands centred on 250, 350 and 500 μm. The FTS uses two overlapping bands (short: 194–324 μm and long: 316–671 μm) to cover the whole of the range of 194-671 μm (Griffin et al., 2010).

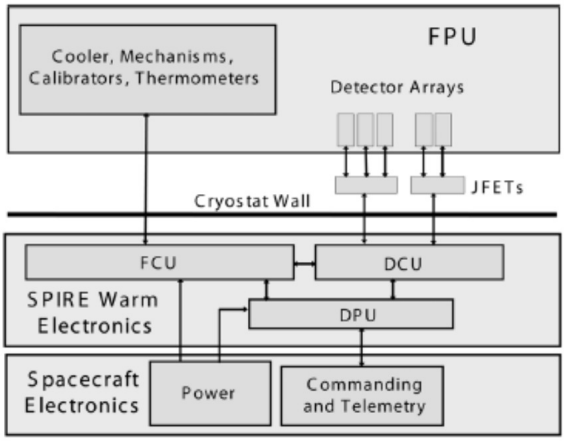

Figure 2.5: SPIRE instrument design, separated into three sections. The Focal Plane Unit (FPU) containing the cold electronics and detector arrays. The SPIRE Warm Electronics containing the Detector Control Unit (DCU), FPU Control Unit (FCU) and the Digital Processing Unit (DPU) (Griffin et al., 2010).

Both the photometer and spectrometer use bolometer arrays cooled to 0.3 K. A bolometer is a thermal infrared detector. It measures the energy of incident EM radiation through an electrical-resistance thermometer (Richards, 1994). SPIRE has five arrays in total, three in the photometer and two in the spectrometer.

2.4.1 Instrument Design

SPIRE is separated into three parts: the spacecraft electronics, the warm electronics and the FPU. The basic design of SPIRE is shown in Figure 2.5 (Griffin et al., 2010).

The SPIRE warm electronics and spacecraft electronics contain the equipment necessary to control and run the instrument. The FPU contains the optics, all five detector arrays and the ^{3}He sorption cooler to provide the necessary operating temperature, 0.3 K, for the bolometers.

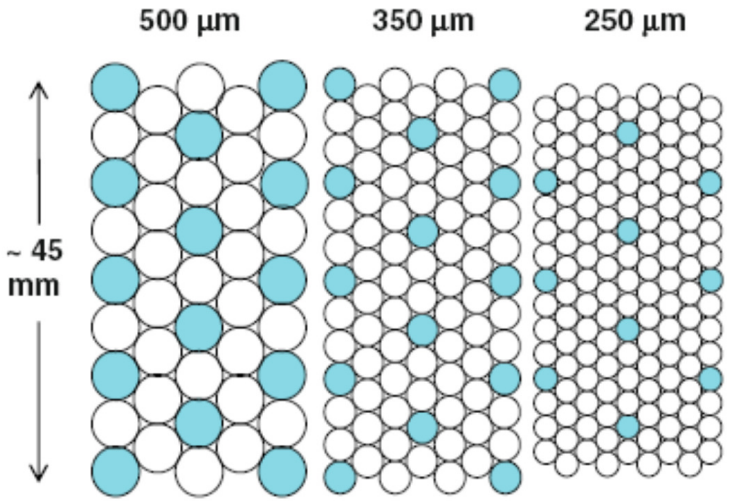

Figure 2.6: Layout of the SPIRE detector arrays. Overlapping bolometers are shaded in blue (Griffin et al., 2010).

Both SPIRE and PACS use the same design of ^{3}He sorption cooler (Duband et al., 2008). This cooler provides the necessary operating temperature for the detector arrays (0.3 K), not possible with the cryostat alone. Sorption refers, collectively, to the processes of adsorption and desorption. Adsorption is where a liquid or gas adheres to a solid surface (an adsorbent). Desorption is the reverse process. The level of adsorption is inversely proportional to temperature. The SPIRE cooler is separated into two sections: the pump, containing the adsorbent (activated charcoal, chosen for its large surface area) and the evaporator. The evaporator initially contains liquid ^{3}He and is connected to the bolometer arrays. The temperature of the adsorbent is raised and the ^{3}He evaporates and adsorbs to the activated charcoal. As the helium evaporates it lowers the temperature of the evaporator and thus the bolometers to which it is connected. The temperature of the adsorbent is then lowered and the ^{3}He desorbs and re-condenses in the evaporator. The process is repeated approximately every 48 hours to keep the bolometers cool.

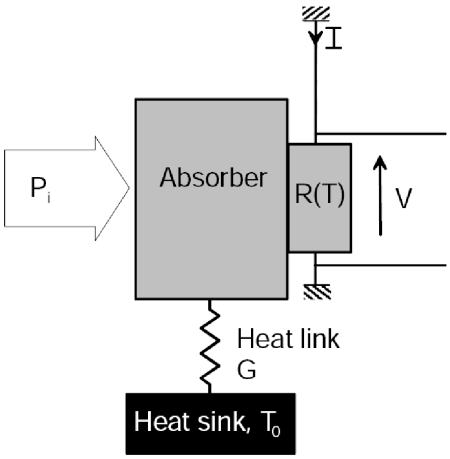

Figure 2.7: The basic schematic of a bolometer. P_i is the incident power. *V*, *I* and *R(T)* are the voltage, current and temperature-dependent resistance across the thermometer (Gunther et al., 2009).

2.4.2 Detector Arrays

SPIRE's five detector arrays all use hexagonally close-packed feedhorn-coupled bolometers (Turner et al., 2001; Chattopadhyay et al., 2003; Rownd et al., 2003). Feedhorn-coupled bolometers have a conical feedhorn above the detector. The photometer arrays contain 139, 88 and 43 detectors for 250, 350 and 500 μm, respectively. The layout of the photometer arrays are shown in Figure 2.6 (Griffin et al., 2010). The two spectrometer arrays contain 37 and 19 detectors for the short and long wavebands respectively.

Bolometers work by measuring the temperature change caused by incident EM radiation. They consist of an absorber, an electrical resistance thermometer with a current running through it and a heat sink kept at temperature T_0 which is connected to the absorber. A basic schematic of a bolometer is shown in Figure 2.7. The radiation impacts on the absorber and its temperature increases from T_0 to T. Assuming $R(T) \propto T$, the temperature change causes the thermometer's internal resistance, $R(T)$, to alter. According to Ohm's Law the output voltage,

V, is equal to the product of the current, I, and the resistance, $R(T)$:

$$V = IR(T). \tag{2.4}$$

If I remains constant, then V changes proportional to $R(T)$. Thus, the output voltage will be proportional to the amount of radiation incident on the absorber. The temperature of the absorber decreases back to T_0 because of its connection to the heat sink and the process repeats.

SPIRE uses feedhorn-coupled detectors. The input beam enters the feedhorn and propagates to the detector surface. The aperture of the feedhorn is much larger than the size of the detector. Using feedhorns therefore means the number of detectors required to fill an array is reduced compared to a naked array architecture. SPIRE's feedhorns have an aperture of $2F\lambda$, where F is the focal ratio of the beam and λ is the wavelength of light being observed (Griffin et al., 2010). $2F\lambda$ feedhorns provide the maximum efficiency for detection of a point source as the majority of the power from the source is concentrated on a single detector.

Unless the feedhorns are $< 0.5F\lambda$ a feedhorn array will not fully sample the image. To guarantee Nyquist sampling (ensuring that the signal recieved can be accurately reconstructed), with feedhorns of $2F\lambda$, a minimum of sixteen pointings are required, therefore either jiggling (moving the array pointing) or scanning of the telescope are required, see Section 2.4.5.

2.4.3 The SPIRE Photometer

The 1.7 K box, see Figure 2.8, contains the detector arrays and two dichroic beam splitters. The beam splitters separate the input beam into distinct beams of dif-

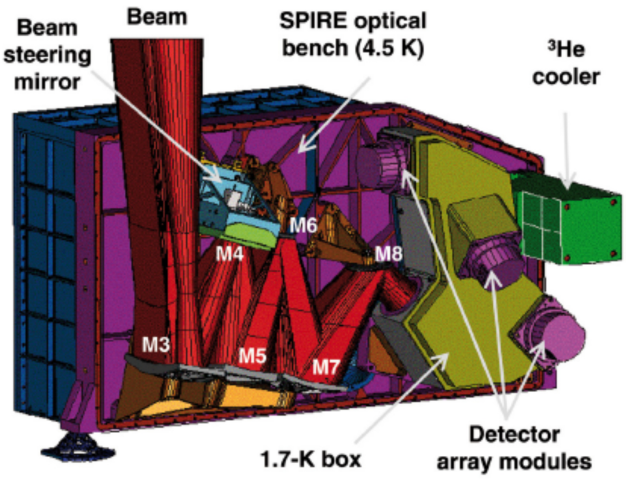

Figure 2.8: Cutout of the SPIRE FPU showing the layout of the photometer (Griffin et al., 2010). Mirrors M1 and M2 are the primary and secondary telescope mirrors and not shown on this diagram.

ferent wavelengths. Here, the input beam is split into 250, 350 and 500 μm and directed onto the respective bolometer arrays. This allows the three bands to observe the same field of view simultaneously, maximising science output.

Figure 2.8 shows the layout of the photometer inside the FPU (Griffin et al., 2010). The majority of the photometer optics are cooled to 4.5 K, with the exception of the 1.7 K box. The design is all-reflective, minimising the number of moving parts and thus the chance of malfunction. The input beam is reflected through the mirrors until its enters the 1.7 K box and is directed onto the detector arrays (Griffin et al., 2010).

2.4.4 The SPIRE Spectrometer

The SPIRE spectrometer is a Fourier-Transform spectrometer (FTS). The input beam is split into two using a beam splitter. The two beams then travel different

path lengths before being recombined. The path difference between the two beams is altered using a moving mirror. An interferogram (a record of the interference pattern of the recombined beams) is created showing the signal as a function of path difference. The Fourier transform of this interferogram is the spectrum of the observed object (Herschel Observer's Manual, 2011).

The spectrometer is located on the opposite side of the optics bench to the photometer. It uses the same initial input optics but the spectrometer beam is split off close to the M6 mirror, see Figure 2.8, (Herschel Observer's Manual, 2011).

The spectrometer's array modules are similar to those used in the photometer with an identical interface to the 1.7 K box. The spectrometer feedhorns are sized to give $2F\lambda$ apertures at 225 μm in the short band and at 389 μm in the long band (Griffin et al., 2010).

2.4.5 Observing Modes

The SPIRE photometer has three observing modes: large area maps, small area maps and point source photometry. All three observe simultaneously at 250, 350 and 500 μm.

Large area mapping is used primarily for observations of large regions of the sky or individual sources greater than 5″. The telescope is scanned along lines at an angle of +42.4° with respect to the telescope's Z-axis. Each scan line is separated by 348″ from the next to provide overlap and good coverage at all three wavebands – see Figure 2.9. The scans are then repeated at an angle of −42.4° (i.e. cross-scanning) to improve coverage of the scanned region. The scans can be performed at speeds of 30″/sec and 60″/sec.

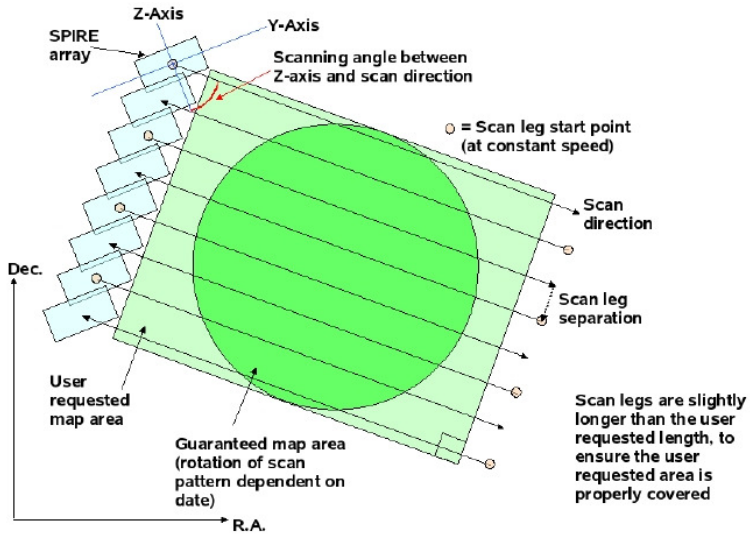

Figure 2.9: Large map build up, showing the scan angle and scan legs (typical separation of 348″). The user requested area is shown in light green, with the guaranteed area in dark green (SPIRE Observer's Manual, 2011).

Small area mapping is used to observe regions of sky <4′ in diameter. This is a 1×1 scan map, similar to large area scan mapping. The speed of the scan is fixed to 30″/sec and the map is made of a two short cross-scans at angles of $\pm 42.4°$.

Point source photometry is recommended for observing bright (∼0.2–4 Jy), isolated point sources. A seven-point map is created by observing a central position and then six points arranged in a symmetrical hexagon around the central point at 6″ distance before returning to repeat the observation at the central point. Sixteen chop cycles are performed at each position and nodding is performed every 64 s. With chop-nod observing the telescope moves rapidly between an on-source position and a sky position (i.e. chopping). The telescope is then moved to a second position (i.e. nodding) and the process is repeated to remove asymmetry, generally with a sky position on the opposite side of the source. This is shown in Figure 2.10. The SPIRE photometer can also observe in the SPIRE-PACS Parallel

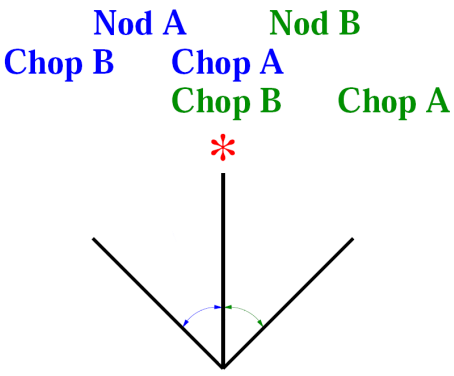

Figure 2.10: An illustration of the telescope positions during chop-nod observations. Nod A, Chop A and Nod B, Chop B are both on-source. The red star represents the target source (Volk, 2007).

mode (see Section 2.6).

The SPIRE spectrometer can observe small sources with a single pointing or larger areas ($>2'$) using raster pointing. Single pointing takes the spectra of an area covered by the instrument field of view. For larger regions, raster mapping is required. With raster mapping the telescope is pointed at various positions to create a hexagonally-packed map. Both methods are able to be observed with high, medium or low resolution. These resolutions correspond to resolutions of 0.04, 0.24 and 0.83 cm^{-1} respectively (SPIRE Observer's Manual, 2011).

2.4.6 In-Flight Performance

The SPIRE instrument is currently fully functional, with in-flight tests showing all systems and detectors meeting their key requirements and in-line with on-ground measurements (Griffin et al., 2010).

Tests have shown that only six of the photometer bolometers (four in the 250 μm detector and one each in the 350 and 500 μm detectors) and two of the spec-

trometer bolometers (both in the 194–324 μm band) are non-operational (Griffin et al., 2010).

The beam profiles of the photometer and spectrometer have both been measured using scan and spectral maps, respectively, of Neptune. Neptune was chosen as it appears as a bright point-source in all bands. The photometer beams can be described using 2-D Gaussians with full-width half-maxima (FWHM) of 18.1, 25.2 and 36.6″ at 250, 350 and 500 μm. The short band of the spectrometer has a beam with a FWHM between 17 and 21″ depending on the specific wavelength used. The long band has a FWHM between 37 and 42″ (Griffin et al., 2010).

The sensitivity of the photometer was estimated by performing scan maps of dark regions of extragalactic sky. Instrument noise is defined as the standard deviation of flux density off-source in a map. The instrument noise levels for SPIRE scan-mapping at 30″/sec are 9.0, 7.5 and 10.8 mJy/$N_{rep}^{\frac{1}{2}}$ at 250, 350 and 500 μm where N_{rep} is the number of map repeats. The instrument noise increases by a factor of $\sqrt{2}$ when increasing the scan speed to 60″/s. These agree with pre-launch estimates, except for 350 μm which is improved by a factor of 1.7. The line sensitivity of the spectrometer is 1.5×10^{-17} Wm^{-2} at the short band and 2.0×10^{-17} Wm^{-2} for the long band (Griffin et al., 2010).

The $1/f$ noise (the dominant form of noise at low frequencies with a power spectral density inversely proportional to the frequency) of the SPIRE photometer has a knee frequency of 1–3 mHz, corresponding to a spatial scale of several degrees at the nominal scanning speed (Griffin et al., 2010). The knee frequency is the frequency at which the $1/f$ noise becomes approximately equal to other sources of noise (i.e. the frequency when the 1/f noise is no longer dominant). The effect of $1/f$ noise on SPIRE observations is therefore minimal.

2.5 The Photodetector Array Camera and Spectrometer (PACS)

PACS, like SPIRE, also consists of two sub-instruments: a photometer and an integral-field spectrometer. The photometer performs dual band observations in wavebands centred on 160 μm (red filter) and either 70 or 100 μm (blue or green filters, respectively; Poglitsch et al. 2010). It has a field of view of $1.75' \times 3.5'$ with a relative bandwidth of $\frac{\lambda}{\Delta\lambda} > 2$ (Poglitsch et al., 2010).

The spectrometer covers the wavelength range 51–220 μm. It has two channels, red and blue (102-220 μm and 51–105 μm, respectively), that operate simultaneously over a field of view of $47'' \times 47''$.

2.5.1 Instrument Design

PACS is divided into three sections: the front optics, the spectrometer and the photometer. This can be seen in Figure 2.11.

The front optics are common to both instrument channels. They contain the internal calibration sources and the instrument chopper. The calibration sources are FIR, greybody sources placed near to the entrance of the instrument (Poglitsch et al., 2010). Observing the internal calibrators helps to map the dark current (the residual current in the detectors when the instrument is not observing) and the changes in detector sensitivity over time. The chopper is used during chop-nod observations, see Section 2.5.4. Once through the front optics the input beam is split between the spectroscopy and photometer channels, see Figure 2.11.

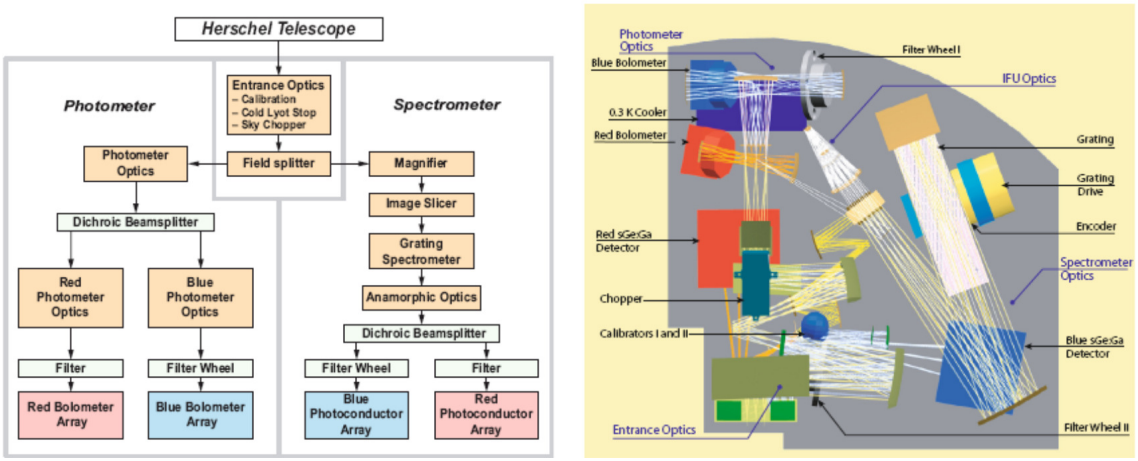

Figure 2.11: Left: PACS focal plane unit block diagram, showing the optical paths through the instrument, filters are coloured in green and imaging optics in orange, active components are named in bold Poglitsch et al. (2010). Right: Focal Plane Unit layout. Shows the entrance optics common to the spectrometer and photometer (lower left), the photometer optics (top left) and spectrometer optics (right).

2.5.2 The PACS Photometer

The photometer beam is split into the long-wave (red) and short-wave (blue or green) channels using a dichroic splitter (Ade et al., 2006). Both channels observe the same field of view simultaneously. The short-wave band is selected by a filter wheel, shown as Filter Wheel I in Figure 2.11, the blue and green wavelengths are thus mutually exclusive.

2.5.2.1 The Bolometer Arrays

As with SPIRE, the PACS photometer uses bolometer detector arrays. Unlike SPIRE, PACS uses filled array bolometers (Agnese et al., 1999, 2003; Simoens et al., 2004). This type of bolometer doesn't have any coupled-feedhorns, instead it is a 'naked-array' of square pixels covering the entire surface of the array. Using filled-array bolometers does however mean that PACS is more vulnerable to stray

light and electromagnetic interference and requires around 16× more detectors to fill a given area (Griffin, 1999; Griffin, Bock, & Gear, 2002).

The PACS photometer has two bolometer arrays, one for the red waveband and one for the blue/green waveband. Both are made of sub-arrays tiled together. Each sub-array consists of 16×16 pixels. The red array is formed from 2 sub-arrays and the blue/green array from 4×2 sub-arrays (Poglitsch et al., 2010). The greater number of detectors results in more data being collected, when compared to SPIRE. Thus, data compression is required for PACS observations. The arrays have an operating temperature of 0.3 K. This is provided by a ^{3}He sorption cooler, identical to that used in SPIRE (Duband et al., 2008).

2.5.3 The PACS Spectrometer

The spectrometer beam is passed through a Littrow-mounted grating. In Littrow gratings the entrance and exit paths coincide (i.e. the light is reflected back towards the source). The grating splits the light into first, second and third diffraction orders. Similar to the photometer, the diffracted light is split between the red and blue wavebands using a dichroic splitter (Poglitsch et al., 2010).

The first order diffracted light covers 102-210 μm and goes to the red detector, while the second and third order light cover 71-105 μm and 51-73 μm, respectively, and go to the blue detector. As with the photometer, a filter wheel before the short-wavelength detector selects either the second or third grating order.

2.5.3.1 The Photoconductor Arrays

The PACS spectrometer uses Gallium doped Germanium (Ge:Ga) photoconductor arrays with 25×16 pixels (Kraft et al., 2000, 2001; Poglitsch et al., 2003). The electrical conductivity of the photoconductor detectors increases in response to increased amounts of electromagnetic radiation.

Ge:Ga photoconductors are responsive to wavelengths out to $\sim$120 μm in unstressed conditions. To extend the photoconductive response to higher wavelengths the detectors must be placed under stress. The stress placed on the red detector array is $\sim$10$\times$ greater than placed on the blue array and allows the detectors to observe wavelengths beyond 200 μm.

2.5.4 Observing Modes

The PACS photometer has two observing modes: point source photometry mode and scan mapping. Both options observe simultaneously at 160 μm and either 70 or 100 μm (PACS Observer's Manual, 2011).

The point-source photometer mode uses a chop-nod technique. With PACS, this mode is intended for use when observing objects less than $50'' \times 50''$ in size. Twenty-five chopper cycles are performed in each nod position and each nod position is observed three times.

The PACS scan mapping mode is very similar to the large area mapping mode used with SPIRE; the telescope scans across the sky at a constant speed in parallel lines. With PACS, however, the angles of the cross scans and separation between scan lines are selectable by the observer. Scanning speeds of $20''$/sec and 'fast'

60″/sec are available. PACS scan mapping is primarily used when observing large areas of sky but can also be used for smaller areas as well as point sources (PACS Observer's Manual, 2011). The PACS photometer can also observe in the SPIRE-PACS Parallel mode (see Section 2.6).

The PACS Spectrometer has two observing modes: line spectroscopy and range spectroscopy. If a region larger than the instrument field of view (47″×47″) is required then raster mapping is used. Line spectroscopy is used when observing a small number of narrow spectral lines within a wavelength range of $\sim$1 μm. Range spectroscopy allows a much broader wavelength range. Both methods are limited in that the second and third order wavebands are mutually exclusive (Poglitsch et al., 2010).

2.5.5 In-flight Performance

All the mechanical and thermal systems on-board PACS are currently working within required specifications. The detector arrays are cooled down to their operating temperatures and the hold time of the sorption cooler is substantially better than the predicted two days.

Tests of the PACS photometer were performed using the asteroid Vesta and best fit point spread functions (PSFs; a measure of how an image of a point source is spread due to the optics of the telescope) were found. When scanning at 10″/sec, fitting 2-D Gaussians to the PSF in each band gives FWHMs of 5.26×5.61″ for the blue band, 6.57×6.81″ in the green band and 10.46×12.06″ in the red band. These worsen as the scanning speed increases and with the use of parallel mode. Using observations of Neptune, the PACS spectrometer was found to have a PSF

of $9.4 \times 9.4''$ (PACS Observer's Manual, 2011).

The 5σ point-source sensitivities for the photometer bands in scan map mode (where σ is the instrument noise as defined previously) are 3.7, 5.0 and 9.5 mJy/30h for the 70, 100 and 160 μm respectively. The spectrometer shows a first order $5\sigma/1$ hour line sensitivity of approximately 2×10^{-18} Wm^{-2}. The second and third order sensitivity decreases by a factor of 2.5.

2.6 The SPIRE-PACS Parallel Mode

The SPIRE-PACS Parallel mode observes with the photometers of SPIRE and PACS simultaneously. Observations are taken in five wavebands: 160, 250, 350 and 500 μm and either 70 or 100 μm.

The SPIRE-PACS Parallel Mode is designed for use with large area surveys where both SPIRE and PACS data are desirable. For shallow Galactic surveys, Parallel Mode gives a gain in efficiency and scientific data because the same amount of integration time can yield nearly double the data. Parallel Mode places less than twice the load on *Herschel*'s cooling system than when using a single instrument, thus increasing the amount of science achievable in the time available.

Deep extra-galactic and Galactic surveys can benefit from Parallel Mode but, as the PACS data suffer some degradation due to increased data compression, the benefits are not as great as with shallow surveys (SPIRE PACS Parallel Mode Observer's Manual, 2010).

Parallel mode observations are performed via scan mapping. Parallel mode was designed for large area observations, for which scan mapping is the sensible option.

It is also the only observing mode in which SPIRE and PACS are compatible. The map is created in the same way as SPIRE large area mapping and PACS scan-mapping, with the telescope observing along parallel lines at a constant speed. Two scanning speeds are available in this mode, 20″/sec or 60″/sec (SPIRE PACS Parallel Mode Observer's Manual, 2010).

SPIRE observations in parallel mode show little to no degradation, particularly when scanning at 20″/sec. However, to ensure that the data rate for the five bands remains within allowed limits additional data compression is applied to the PACS data. This results in an elongated PSF with respect to PACS-only observations. Parallel mode is therefore used when SPIRE data are crucial and PACS data are advantageous. In cases where the reverse is true, the observations are run on the instruments separately (SPIRE PACS Parallel Mode Observer's Manual, 2010).

2.7 The Heterodyne Instrument for the Far-Infrared (HIFI)

The third instrument on-board *Herschel* is the Heterodyne Instrument for the Far-Infrared (HIFI; de Graauw et al. 2010). HIFI is a dedicated spectrometer and performs spectroscopy in seven bands between 480 and 1250 GHz. Five, approximately equally spaced, bands (bands 1–5) cover 480-1250 GHz (240–625 μm) and an additional two bands (bands 6 and 7) cover 1410–1910 GHz (213–157 μm; de Graauw et al. 2010).

2.7.1 Instrument Design

HIFI has four spectrometers on-board; two in the Wide-band Spectrometer (WBS; Schieder et al. 2002) and two in the High Resolution Spectrometers (HRS; Belgacem et al. 2003).

Sky signals in the sub-mm and FIR are very weak. No amplifiers exist for use in these frequency ranges, making it difficult to detect spectral lines. HIFI therefore uses frequency mixers, where the sky signal is mixed with another signal (the Local Oscillator; LO). This shifts the signal frequency into a range where suitable amplifiers are available. HIFI uses semiconductor-insulator-semiconductor (SIS; Jackson et al. 2005; Delorme et al. 2005; Jackson et al. 2006) mixers at the five lower bands and hot electron bolometer (HEB; Cherednichenko et al. 2002; Cherednichenko, Drakinsky, & Berg 2005) mixers at the two highest bands. The output frequency of the mixers is called the Intermediate Frequency (IF; HIFI Observer's Manual 2011). The data obtained from HIFI is dual sideband data.

HIFI consists of five sub-instruments: the focal plane unit, which contains the frequency mixers and IF amplifiers; the LO subsystem, which generates the LO signal; the WBS; the HRS; and the instrument control unit, which controls the communication to and operation of HIFI.

2.7.2 Observing Modes

HIFI has three observing modes: single-point observations, mapping observations and spectral scan observations. The single point mode is used for point sources. Mapping observations are used to map emission over a large region of sky. Both

single point and mapping observations use only a single frequency band. Spectral scan observations are used to cover a range of frequency bands.

Within each of the three modes are options for how the observation will be carried out: point switch (not available for spectral maps), dual beam switch, frequency switch and load chop. In point switch observing the beam is moved between the source position and a sky position, this gives very accurate flux measurements and is intended for use in confused regions. Dual beam switch is similar to point switch but uses an internal chopper to switch between on and off source positions and is used in unconfused regions. Frequency switching is used when there is no off-source position that is free from emission (HIFI Observer's Manual, 2011). Finally, load chop mode uses internal calibrators to correct for changes in the instrument behaviour.

2.7.3 In-flight Performance

The WBS has a bandwidth of 4 GHz for all seven bands. A spectral scan of the Orion hot core showed the WBS to have a spectral resolution of 1.1 MHz in dual beam switch mode. The High Resolution Auto-correlation Spectrometer has a range of resolutions (0.125–1.00 MHz) depending on the band and method of observation (de Graauw et al., 2010).

2.8 The *Herschel* Infrared Galactic Plane Survey (Hi-GAL)

Herschel will not perform an all-sky survey for much of its wavelength range, instead *Herschel* will perform a number of large spatial and spectral surveys. These surveys are called key projects and were selected for observation early in the mission (in order that any interesting results could be followed up using *Herschel* itself). *Herschel*'s observing time is split into open and guaranteed time. Open time is available for anyone in the community to apply for while guaranteed time is owned by and available only to various PI consortia. The *Herschel* Infrared Galactic Plane Survey (Hi-GAL) is one of *Herschel*'s open-time key projects (Molinari et al., 2010a,b).

Hi-GAL aims to perform a survey of the Galactic Plane using the PACS and SPIRE instruments. The two are used in parallel mode to map the Milky Way Galaxy simultaneously at five wavelengths (70, 160, 250, 350 and 500 μm), with resolutions up to $5''$ at 70 μm. This is done using a series of overlapping $2^\circ \times 2^\circ$ tiles to survey the area $|b| \leq 1^\circ$, $-180^\circ \leq l \leq +180^\circ$ (Molinari et al., 2010b).

Previous large-scale surveys have observed the Galactic Plane in the MIR (e.g. ISOGAL, Omont et al. 2003; MSX, Price et al. 2001; GLIMPSE, Benjamin et al. 2003; MIPSGAL, Carey et al. 2009) and sub-mm (e.g. ATLASGAL, Schuller et al. 2009) with resolutions below 30" – see Figure 2.12. Hi-GAL will fill the gap that currently exists for a high resolution, Galactic Plane survey in the FIR.

Hi-GAL's primary science goal is to address the lack of a galaxy-scale predictive model for massive star formation. Within this, there are many questions that

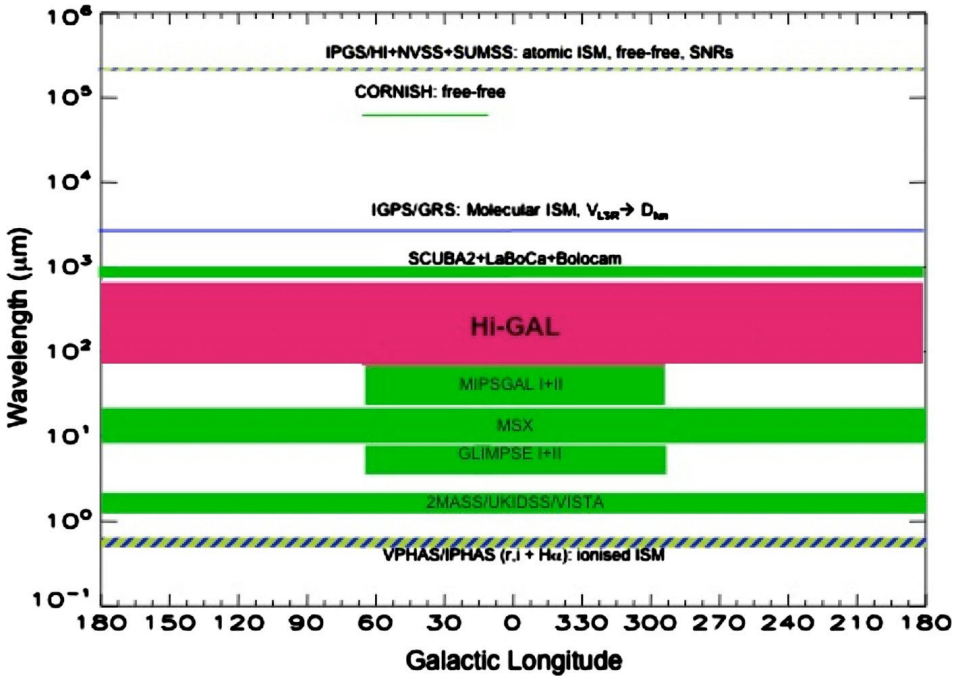

Figure 2.12: A wavelength-longitude plot for current and planned photometric (green) and spectroscopic (blue) Galactic plane surveys. Hi-GAL, shown in pink, will cover the FIR and sub-mm at resolutions up to 5″ (Molinari et al., 2010a).

Hi-GAL seeks to address: how molecular clouds form and evolve, the origin of the stellar initial mass function, how massive stars and clusters form, how the star formation rate and efficiency vary with galacto-centric distance and environmental factors, the temperature and structure of the ISM in our galaxy and how the local properties of the ISM relate to global scaling laws in other galaxies (Molinari et al., 2010a).

PACS data reduction was performed using the *Herschel* Interactive Pipeline Environment (HIPE; Ott 2010), albeit with some departures from the standard processing (Poglitsch et al., 2010). Most notably, the standard deglitching (deglitching is the identification and removal of bolometer outliers) and crosstalk correction (a type of noise where the signal in one bolometer contaminates the signal in its neighbours) were not used due to poor results in the HI-GAL science demonstration

fields. Custom procedures were also developed for drift removal (the elimination of changes in the detector's responsivity over time) to deal with the bright and irregular background.

SPIRE data processing also made use of HIPE. The SPIRE data required less deviation from the standard processing methods (Griffin et al., 2010), with both standard deglitching and drift removal producing acceptable results. In both cases, the ROMAGAL algorithm (Traficante et al., 2011), a map-making programme based upon the generalised least-squares method (Lupton, 1993), was used to produce the final maps.

2.9 Summary

Herschel is a far-infrared and sub-millimeter observatory which can observe between wavelengths of 55 and 671 μm. As such it is primarily concerned with the formation of stars and galaxies and studying the ISM.

Herschel was launched in May 2009 and is currently orbiting the Sun at the second Lagrange point, 1.5×10^6 km from the Earth. It is expected to function for a minimum of three years, though the actual lifetime is currently unknown.

Herschel carries three instruments: SPIRE, PACS and HIFI. SPIRE and PACS are both primarily photometers, although both also contain low resolution spectrometers. PACS carries out broadband photometry in bands centred on 70, 100 and 160 μm and spectroscopy between 51–220 μm, while SPIRE performs photometry at 250, 350 and 500 μm and spectroscopy between 194–671 μm. HIFI is a dedicated high-resolution spectrometer and performs spectral line observations in

seven bands between 157 and 625 μm. For large scale surveys *Herschel* also allows for the SPIRE and PACS photometers to be used simultaneously in parallel mode.

Hi-GAL will perform a survey of the Galactic Plane using SPIRE and PACS in parallel mode. The survey will cover the area between $-180° \leq l \leq +180°$, $|b| \leq 1°$ at five wavelengths (70, 160, 250, 350 and 500 μm). Hi-GAL will fill the need for a high resolution, Galactic plane survey in the FIR. The *Herschel* data used in the work presented here were taken as part of the Hi-GAL survey.

Chapter 3

Radiative Transfer Modelling with Phaethon

3.1 Introduction

Phaethon is a 3D Monte Carlo radiative transfer code (Lefevre, Bergeat, & Daniel, 1982; Lefevre, Daniel, & Bergeat, 1983; Wolf, Henning, & Stecklum, 1999; Lucy, 1999; Bjorkman & Wood, 2001; Misselt et al., 2001; Ercolano et al., 2003; Niccolini, Woitke, & Lopez, 2003; Stamatellos & Whitworth, 2003; Stamatellos et al., 2004; Stamatellos & Whitworth, 2005; Stamatellos et al., 2010). Monte Carlo simulations rely on repeated random sampling to compute results and radiative transfer codes look at how EM radiation propagates through a system.

Phaethon follows luminosity packets (L-packets) as they travel through and interact with a prescribed medium. Similar methods have been used previously to study various different astrophysical systems including planetary atmospheres (e.g.

Crespin et al. 2006; Gratiy 2009; Beaulieu et al. 2011), protostellar envelopes (e.g. Jørgensen et al. 2006; Marseille et al. 2010b), circumstellar disks (e.g Glauser et al. 2008; Woitke et al. 2010; Hughes et al. 2010), supernovae (e.g. Kasen et al. 2008; Dessart & Hillier 2011), planetary disks (e.g. Tatulli et al. 2011), disks around black holes (e.g. Baes & Piasecki 2007) and prestellar cores (e.g. Stamatellos & Whitworth 2003; Stamatellos et al. 2004).

Here, PHAETHON is used to model the cores embedded within IRDCs. Six examples are given, using data from the Hi-GAL science demonstration phase. The models shown here illustrate what PHAETHON can do and why it is preferable to more basic single-temperature fitting.

3.2 Phaethon

PHAETHON was developed by Stamatellos & Whitworth (2003, 2005). A computational domain is created to represent the phenomena being studied (in this case, cores within IRDCs). The system is divided into hundreds of cells. Within each cell the temperature and density are approximately constant. A large number of monochromatic L-packets are used to represent the ambient radiation field in the system. These L-packets are injected into the system where they interact (are scattered or absorbed and re-emitted) stochastically. The L-packets are followed until they leave the computational domain. At this point, their frequency, position and direction are recorded.

3.2.1 Monte Carlo Theory

PHAETHON uses the Monte Carlo fundamental principle. This states that a quantity, $\zeta \in [\zeta_1, \zeta_2]$, can be sampled from a probability distribution, p_ζ, if ζ is chosen so that

$$\frac{\int_{\zeta_1}^{\zeta} p_{\zeta'} d\zeta'}{\int_{\zeta_1}^{\zeta_2} p_{\zeta'} d\zeta'} = \mathcal{R}_\zeta. \tag{3.1}$$

$\mathcal{R}_\zeta$ is a uniformly distributed random number, between 0 and 1:

$$\mathcal{R}_\zeta \in [0, 1]\,. \tag{3.2}$$

3.2.2 L-packet Properties

Each L-packet is given a luminosity equal to

$$\delta L = \frac{L}{N} \tag{3.3}$$

where δL is the luminosity of an individual L-packet, L is the total luminosity of the system (discussed in Section 3.2.4.2) and N is the total number of L-packets emitted in time Δt (Stamatellos, 2003). The energy contained in each L-packet is therefore:

$$\delta E = \frac{L \Delta t}{N}. \tag{3.4}$$

The L-packets are each given an individual frequency, direction and optical depth. Each parameter for each L-packet is decided using the Monte Carlo fundamental principle (Equation 3.1). The L-packets are then injected into the computational domain.

3.2.2.1 Frequency

The probability distribution of the L-packet frequency, $p_\nu d\nu$, is given by the specific intensity of the luminosity source(s) of the system, $I_\nu(T)$. Equation 3.1 then becomes:

$$\frac{\int_0^{\nu_0} I_\nu(T)d\nu}{\int_0^{\infty} I_\nu(T)d\nu} = \mathcal{R}_\nu \tag{3.5}$$

where $\mathcal{R}_\nu$ is defined as in Equation 3.2 (Stamatellos & Whitworth, 2003).

The cores studied here have only a single source of radiation — the interstellar radiation field (ISRF). The form chosen for the ISRF is discussed in Section 3.2.4.2.

3.2.2.2 Injection Point and Direction

When modelling the cores within IRDCs, all radiation is assumed to come from the ambient radiation field. No internal heat sources are modelled, nor any nearby point sources within the system being simulated.

L-packets representing the ambient radiation field are injected from the edge of the computational domain. The injection point and direction of each L-packet are chosen to best represent an isotropic radiation field.

The injection point is described using spherical co-ordinates (r, θ, ϕ). The radial distance, r, is typically the boundary of the object being modelled. θ and ϕ are the polar and azimuthal angles, respectively. They are defined using the probability distributions:

$$p_\theta d\theta = \frac{\sin\theta d\theta}{2} \quad 0 \leq \theta \leq \pi \tag{3.6}$$

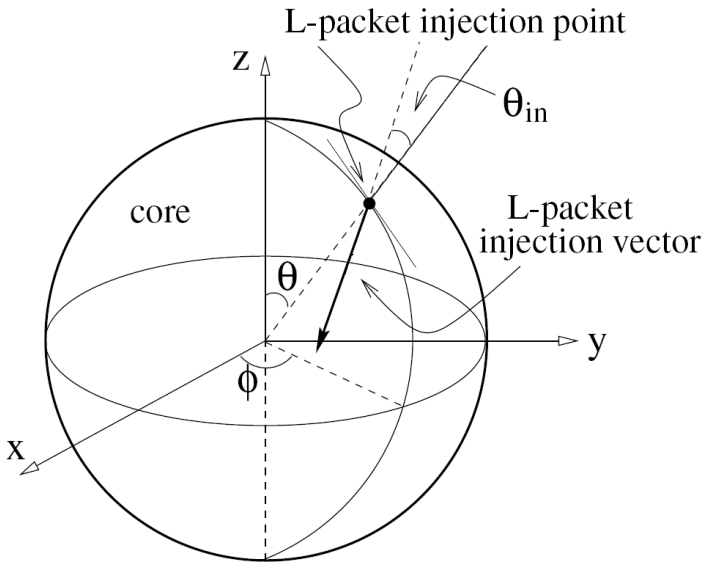

Figure 3.1: A diagram to show the where the injection point angles, θ and ϕ, and injection vector angles, θ_{in} and ϕ_{in}, are measured. ϕ_{in} is defined similarly to ϕ (Stamatellos et al., 2004).

$$p_\phi d\phi = \frac{d\phi}{2\pi} \quad 0 \leq \phi < 2\pi \tag{3.7}$$

(Stamatellos, 2003). Equations 3.6 and 3.7 are substituted into Equation 3.1 resulting in

$$\theta = \arccos\left(1 - 2\mathcal{R}_\theta\right) \tag{3.8}$$

$$\phi = 2\pi\mathcal{R}_\phi \tag{3.9}$$

(Stamatellos et al., 2004). $\mathcal{R}_\theta$ and $\mathcal{R}_\phi$ are random numbers defined by Equation 3.2.

The direction of each L-packet is defined upon injection using ϕ_{in} and θ_{in}. θ_{in} is the direction between the normal vector to the tangent plane at the point of entry and the L-packet injection vector. This is shown in Figure 3.1. ϕ_{in} is the polar angle defined on the tangent plane. ϕ_{in} is found using the same probability

distribution as ϕ (Equation 3.7). The probability distribution for θ_{in}, however, changes from Equation 3.6 to:

$$p_{\theta_{in}} d\theta_{in} = 2\cos(\theta_{in})\sin(\theta_{in})\, d\theta_{in} \quad \frac{\pi}{2} \leq \theta_{in} \leq \pi \tag{3.10}$$

(Stamatellos, 2003) resulting in

$$\theta_{in} = \arccos\left(\mathcal{R}_{\theta_{in}}^{\frac{1}{2}}\right), \tag{3.11}$$

where $\mathcal{R}_{\theta_{in}}$ is, again, a random number defined by Equation 3.2.

3.2.2.3 Optical Depth

The third, and final, L-packet component defined upon injection is the optical depth. Similar to frequency and direction, optical depth is chosen via Equation 3.1 using a probability distribution (Stamatellos, 2003):

$$p_\tau d\tau = e^{-\tau} d\tau \quad 0 \leq \tau \leq \infty. \tag{3.12}$$

When substituted into Equation 3.1 this results in

$$\tau_\nu = -\ln \mathcal{R}_\tau \tag{3.13}$$

where $\mathcal{R}_\tau$ is defined as in Equation 3.2 (Stamatellos & Whitworth, 2003).

3.2.3 L-Packet Interactions

Once inside the domain the L-packets interact stochastically with the system. The computational domain is separated into hundreds of cells, within each cell the temperature and density are uniform (Stamatellos & Whitworth, 2003).

The L-packets propagate through the system until they reach an interaction point. How far an L-packet can travel before reaching an interaction point depends on the L-packet's optical depth. The propagation distance, ΔS, is defined via

$$\Delta S = \int_0^{\tau_{total}} \frac{d\tau}{\kappa_\lambda \rho} \tag{3.14}$$

where $\kappa_\lambda \rho$ is the opacity (a measure of the impenetrability of the material to EM radiation) and τ_{total} is the total optical depth of the L-packet. As the opacity is not generally constant across the entire propagation distance Equation 3.14 must be approximated with a sum:

$$\Delta S \approx \sum_i \frac{\delta\tau_i}{\kappa_\lambda \rho_i} = \sum_i \delta S_i. \tag{3.15}$$

ΔS is split into a number of element steps and δS_i is the elemental propagation distance (i.e. the distance travelled in an element step). The elemental propogation distance should be small enough that the density (ρ_i) is constant throughout each element step. $\delta\tau_i$ is the elemental optical depth:

$$\delta\tau_i = \kappa_\lambda \rho_i \delta S_i. \tag{3.16}$$

$\delta\tau_i$ should not be larger than τ_i, the remaining optical depth after i steps, where

$$\tau_i = \tau_{total} - \sum_{j=0}^{i} \delta\tau_j. \tag{3.17}$$

δS_i is chosen to be the minimum distance that satisfies these conditions.

The L-packet is propagated by this method until $\tau_i \leq 0$. If, at this point,the L-packet is still within the system then it has reached an interaction point. It is either then scattered or absorbed. A random number is generated, $\mathcal{R}_\gamma \in [0, 1]$. If $\mathcal{R}_\gamma$ is greater than the albedo of the system then the L-packet is absorbed. If $\mathcal{R}_\gamma$ is less than the albedo then the L-packet is scattered.

3.2.3.1 Absorption and Re-Emission

If the L-packet is absorbed it is immediately re-emitted with a new frequency and the temperature of the cell that absorbed the L-packet will rise. The cell's new temperature is calculated so as to conserve energy of the system. The new frequency of the L-packet is chosen so that the emissivity of all the L-packets re-emitted by that cell correspond to the latest cell emissivity.

The new temperature of the cell is calculated assuming conservation of energy, i.e. that the energy absorbed, E^{abs}, is equal to the energy emitted E^{em}:

$$E_i^{abs} = E_i^{em}. \tag{3.18}$$

The total energy absorbed by the cell is the total energy of all the L-packets absorbed by that cell:

$$E_i^{abs} = N_i \left(\frac{L\Delta t}{N} \right) \tag{3.19}$$

where N_i is the number of L-packets absorbed (Baes et al., 2005). The energy emitted by the cell is

$$E_i^{em} = 4\pi\Delta t \int_0^\infty \int_{cell} j_\nu d\nu dV_i \tag{3.20}$$

$$= 4\pi\Delta t \int_0^\infty \kappa_\nu B_\nu(T_i) d\nu \int_{cell} \rho dV_i \tag{3.21}$$

$$= 4\pi m_i \Delta t \int_0^\infty \kappa_\nu B_\nu(T_i) d\nu \tag{3.22}$$

where V_i is the cell's volume, $B_\nu(T)$ is the Planck function and m_i is the cell's mass. j_ν is the cell's thermal emissivity:

$$j_\nu = \kappa_\nu \rho B_\nu(T) \tag{3.23}$$

(Stamatellos, 2003; Baes et al., 2005) .

The Planck mean opacity, κ_p, is an average of the local opacity weighted by the Planck function at the local temperature (i.e. the temperature along the element step). It is defined as:

$$\kappa_p(T_i) = \frac{\int_0^\infty \kappa_\nu B_\nu(T_i) d\nu}{B} \tag{3.24}$$

where B is the Planck function integrated with respect to frequency and equals $\sigma T_i^4/\pi$. T_i is the temperature of the cell after absorbing the i^{th} L-packet. Substituting the Planck mean opacity into Equation 3.22 and using with Equation 3.19 gives:

$$\sigma T_i^4 = \frac{N_i L}{4N\kappa_p(T_i) m_i} \tag{3.25}$$

(Bjorkman & Wood, 2001). As κ_p is a function of T_i the temperature must be found through interpolation. This equation must be solved each time an L-packet is absorbed by a cell.

The L-packet is re-radiated with a new frequency. Prior to absorbing the current, i^{th}, L-packet, the cell had absorbed and re-emitted $(i-1)$ other L-packets. These carried away an energy corresponding to the cell's emissivity at its previous temperature, T_{i-1}. With the absorption of the i^{th} L-packet the cell's temperature has increased to T_i and so its emissivity has also altered. The energy re-radiated by the i^{th} L-packet should correspond to the difference in the dust emissivities at T_i and T_{i-1}, thus ensuring that the total spectrum of the cell's emitted L-packets agrees with its current emissivity (Stamatellos, 2003; Baes et al., 2005). Assuming a small temperature change, the probability distribution of the new frequency is therefore:

$$p_{BW}(\nu)d\nu = \frac{\kappa_\nu B'_\nu(T)d\nu}{\int_0^\infty \kappa_\nu B'_\nu(T)d\nu} \tag{3.26}$$

(Stamatellos, 2003; Bjorkman & Wood, 2001), where B'_ν is the derivative of the Planck function with respect to temperature. This equation is substituted into Equation 3.1 to find the re-emitted L-packet's frequency.

The re-emitted L-packet is assigned a new optical depth and direction. The L-packet then propagates as before until it either leaves the computational domain or it reaches another interaction point.

3.2.3.2 Scattering

The second type of possible interaction is scattering. If the L-packet is scattered then the cell temperature and the L-packet's frequency remain the same but the direction of the L-packet is changed.

If the scattering is isotropic then the new direction is chosen using two new random numbers and solving Equations 3.6 and 3.7 again. Due to the shape of the

dust grains, the scattering in these cores is anisotropic with some directions being favoured over others. In the case of anisotropic scattering, PHAETHON takes:

$$p(\theta_{scat})d\theta = \frac{(1-g^2)\,sin(\theta_{scat})}{2\left[(1+g)-2gcos(\theta_{scat})\right]^{\frac{3}{2}}}d\theta \tag{3.27}$$

(Henyey & Greenstein, 1941), where θ_{scat} is the change in angle from the direction before scattering to the direction after scattering and g is the mean scattering cosine:

$$g = \int_0^{\pi} cos(\theta_{scat})p(\theta_{scat})d\theta_{scat} \tag{3.28}$$

(Henyey & Greenstein, 1941). For $g > 0$ a forward direction is favoured, for $g < 0$ a backwards direction is favoured. Equation 3.27 is substituted into Equation 3.1 and the new direction of the L-packet is found by solving:

$$cos(\theta_{scat}) = \frac{1}{2g}\left[1+g^2-\left(\frac{1-g^2}{1+g^2-2gR_{\theta_{scat}}}\right)^2\right], \tag{3.29}$$

(Stamatellos, 2003). θ_{scat} must then be converted into a direction in the initial core co-ordinate system.

An L-packet continues to propagate and interact with the medium until it leaves the system. When the L-packet leaves the domain its frequency, position and direction are recorded. SEDs can then be constructed at different viewing angles by placing the L-packets into frequency and direction-of-observation bins.

3.2.4 Phaethon Input Variables

The medium through which the L-packets propagate is defined by the user. The input variables of the code are the strength of the ambient radiation field, the

density profile, the size and geometry of the core and the dust properties of the system.

3.2.4.1 Geometry

PHAETHON has two options for the geometry of the modelled cores: spherical or flattened.

Spherical geometry uses a Plummer-like density profile (Plummer, 1915):

$$\rho(r) = \rho_0 \frac{1}{1 + \left(\frac{r}{R_0}\right)^2}, \tag{3.30}$$

where r is the radial distance, ρ_0 is the density at the centre of the core and R_0 is the flattening radius (i.e the radial distance for which the density is approximately constant; Stamatellos et al. 2004; Stamatellos et al. 2010). This geometry is consistent with low-mass prestellar cores in nearby cloud forming regions (Whitworth & Ward-Thompson, 2001).

For elongated objects, a flattened geometry is more appropriate. For a flattened geometry, the density profile is given by:

$$\rho\left(r, \theta\right) = \rho_0 \frac{1 + A\left(\frac{r}{R_0}\right)^2 \left[\sin(\theta)\right]^p}{\left[1 + \left(\frac{r}{R_0}\right)^2\right]^2}, \tag{3.31}$$

(Stamatellos et al., 2004; Stamatellos et al., 2010), where θ is the polar angle, A is the asymmetry factor and p is the power to which $sin\left(\theta\right)$ is raised.

The asymmetry factor controls the equatorial to polar optical depth ratio,

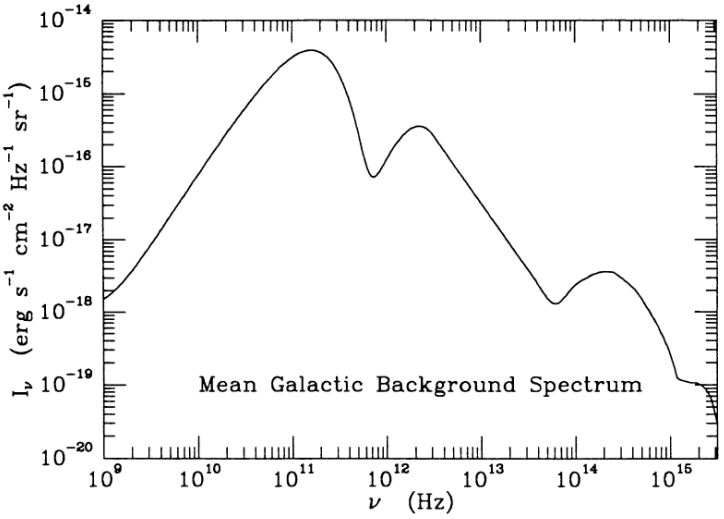

Figure 3.2: The unmodified Black (1994) radiation field.

i.e. the maximum optical depth from centre to surface (which occurs at $\theta = 90°$) divided by the minimum optical depth from centre to surface ($\theta = 0°$ or $180°$). p determines how quickly the optical depth changes with increasing θ.

As most of the cores within IRDCs appear to be at least slightly elliptical (although it should be noted that the direction at which we view the cores is not known), the flattened geometry is likely to be more realistic than the spherical profile (Stamatellos et al., 2010). In both geometries the radius/semi-major axis and the central density of the core can be chosen by the user.

3.2.4.2 Ambient Radiation Field

We assume that the object being modelled has no internal heat source and is heated solely by ambient radiation falling on the surface of the core. This radiation field is taken to be a modified version of the Black (1994) radiation field (Andre et al., 2002) — see Figure 3.2.

The Black (1994) field is an approximation of the mean Galactic background spectrum in the solar neighbourhood. It covers the wavelength range 0.3 to 3×10^{-7} m. The spectrum consists of radiation from giant stars and dwarfs with a peak at 1 μm (3×10^{14} Hz), thermal emission from dust grains peaking at 100 μm (3×10^{12} Hz), mid-infrared radiation from non-thermally heated dust grains emitting from 5–100 μm and cosmic microwave background radiation peaking at 1.5 mm (2×10^{11} Hz).

The Black (1994) field gives a good approximation of the background radiation field in the solar neighbourhood but not always for cores embedded in surrounding clouds. PHAETHON therefore uses a modified version of the Black (1994) field. This modified field is attenuated at short wavelengths ($< 30 - 40\,\mu$m), where a surrounding cloud would absorb radiation, and enhanced at wavelengths $> 50\,\mu$m, where a cloud would emit. The modified field better duplicates the ISRF in areas where IRDC cores are thought to exist, deeply buried within molecular clouds (Stamatellos & Whitworth, 2003).

The radiation field in the Galactic Plane is typically higher than that in the solar neighbourhood. PHAETHON allows for multiples of the Black (1994) radiation field to be used to better simulate the ambient background in these regions. This scales the Black (1994) radiation field wholesale, retaining the ratio between the three major sources of radiation. It is possible that this is therefore not a completely accurate picture of the external radiation field in the Galactic Plane. For example, a core in the Galactic Plane is likely to be closer to regions of high mass star formation than a core in the solar neighbourhood. This could increase the relative amount of radiation from thermally heated dust grains compared to radiation from the cosmic microwave background which is likely to remain constant throughout the Galaxy. We model cores over wavelengths from 8 to 500 μm,

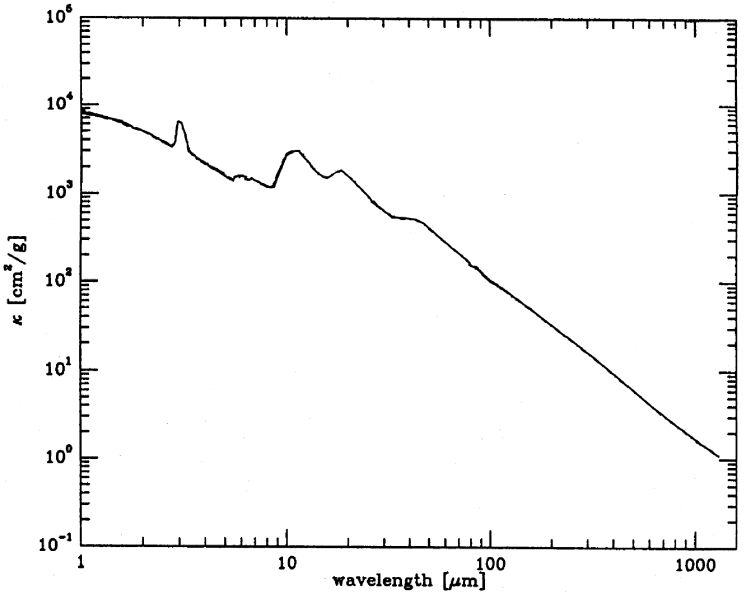

Figure 3.3: The Ossenkopf & Henning (1994) opacity for a coagulated Mathis et al. (1977) grain mixture with accreted ice mantles.

outside of this range we can not comment on the accuracy of the the external radiation field.

3.2.4.3 Dust Properties

Dust grains in dense clouds are expected to coagulate and form ice mantles. PHAETHON therefore uses Ossenkopf & Henning (1994) opacities for a standard Mathis et al. (1977) grain mixture of 53% silicate and 47% graphite with grains that have coagulated and accreted thin ice mantles over 10^5 years at densities of $10^6\,\mathrm{cm}^{-3}$. The Ossenkopf & Henning (1994) opacities are shown in Figure 3.3. A gas-to-dust mass ratio of 100 is assumed.

3.3 Modelling IRDCs with Phaethon

Three IRDCS, containing a total of six cores, were found within the data from the Hi-GAL Science Demonstration Phase (SDP). They were each modelled in two different ways: first, using a greybody single-temperature fit, and second, using PHAETHON.

3.3.1 Identifying IRDCs

Two regions of the Hi-GAL survey were completed during SDP time. They are both four degrees square and center around l=30^o, b=0^o and l=59^o, b=0^o. Here, we focus on the region centred on l=30^o, b=0^o.

Identifying IRDCS using MIR observations alone can cause problems. IRDCs appear as dark regions against the bright MIR background. However, there is no way in the MIR of distinguishing between an area of low emission caused by absorption by an IRDC and an area of low emission caused by a local dip in the MIR background, sometimes referred to as a 'hole in the sky' (Stanke et al., 2010). One way of identifying genuinely dense, cold regions is to look for emission in the FIR and sub-mm, where cold dust should emit strongly. We label such regions as '*Herschel*-bright' (referring only to the longer wavelength *Herschel* data).

The Simon et al. (2006a, hereafter S06) and Peretto & Fuller (2009, hereafter PF09) catalogues both identified IRDCs via regions of absorption in the MIR. Each of the sources in the l=30^o region was studied at 6 wavebands: *Spitzer* GLIMPSE 8 μm (Benjamin et al., 2003; Werner et al., 2004); and the five Hi-GAL wavelengths (70, 160, 250, 350 and 500 μm). If the source showed extinction at

Table 3.1: The physical properties of the six cores. R_0 is the flattening radius within the core, $n_0(H_2)$ is the central density of each core, $ISRF_{Habing}$ is the ISRF of the core at FUV given in multiples of the Habing flux — i.e. 1.6×10^{-3} erg s^{-1} cm^{-2} (Habing, 1968), $\tau_{\theta=90^o}/\tau_{\theta=0^o}$ is the ratio of optical depths at $\theta = 90^o$ and at $\theta=0^o$ and $F_{500\,\mu m}$ is the flux density of each core at 500 μm. The model temperature is the range of temperatures in the core calculated from the model, and the SED temperature was calculated from single-temperature greybody fitting. The model mass was calculated using κ=0.05 cm^{2}g^{-1} at 500 μm (Ossenkopf & Henning, 1994). The two SED masses were calculated using the method of Hildebrand (1983), the SED temperature and the flux density at 500 μm (see Section 3.4.1). The difference in ISRFs, $\ln\left(\frac{I_1}{I_2}\right)$, was calculated from the model (see Section 3.4.3). L_{max} is the maximum luminosity of a star that could be embedded in each core (see Section 3.4.4).

	G030.50+00.95		G031.03+00.26		G031.03+00.76	
	Core A	Core B	Core A	Core B	Core A	Core B
R.A. (2000)	18:43:34.7	18:43:34.9	18:47:01.5	18:47:04.2	18:45:10.2	18:45:17.3
Dec. (2000)	−01:42:29	−01:44:36	−01:34:36	−01:33:39	−01:20:00	−01:19:12
Name in PF09	SDC30.442+0.958		SDC31.039+0.241		Not included	
Distance (pc)	3400	3400	4900	4900	3400	3400
Semi-major Axis (pc)	0.6	0.7	0.45	0.55	0.4	1.0
R_0 (pc)	0.06	0.07	0.04	0.05	0.04	0.1
Aspect ratio	1.93	3.16	2.46	2.22	1.70	1.65
Position Angle	50	85	125	340	335	85
$n_0(H_2)$ (cm^{-3})	1.4×10^5	4.5×10^4	3.8×10^5	4.2×10^5	6.0×10^5	2.5×10^4
$ISRF_{Habing}$	8.5	18	18	81	17	4.8
$\tau_{\theta=90^o}/\tau_{\theta=0^o}$	1.93	3.16	2.46	2.22	1.59	1.65
$F_{500\,\mu m}$ (Jy)	5.0±0.5	9.0±0.9	3.3±0.3	10±1	4.5±0.5	4.4±0.4
Model Temperature (K)	9–19	11–22	9–22	11–28	8–22	10–18
SED Temperature (K)	14±1	16±2	14±1	17±2	14±1	14±1
Model mass (M$_\odot$)	120	140	170	290	110	90
SED mass – κ=0.05 cm^2 g^{-1} (M$_\odot$)	130	170	170	310	110	100
SED mass – κ=0.03 cm^2 g^{-1} (M$_\odot$)	210	280	280	510	180	160
$\ln\left(\frac{I_1}{I_2}\right)$	0.75	–	1.50	–	1.25	–
L_{max} ($L_\odot$)	<6	<3	<200	<1000	<40	<9

Table 3.2: The observed, integrated flux densities of the six cores.

Wavelength	Flux Density (Jy)					
	G030.50+00.95		G031.03+00.26		G031.03+00.76	
	Core A	Core B	Core A	Core B	Core A	Core B
70 μm	<0.03	<3.6	<0.5	<10.1	<1.0	<1.3
160 μm	13.4	41.9	10.9	60.3	13.7	15.4
250 μm	18.0	31.4	11.7	47.5	13.4	13.3
350 μm	9.6	16.0	6.8	23.0	8.8	8.8
500 μm	5.0	9.0	3.2	9.7	4.5	4.4

8 μm but emission at 250, 350 and 500 μm it was identified as *Herschel*-bright and thus a genuine IRDC.

At 70 μm a cloud may be expected to be seen in absorption, but less strongly than at 8 μm. Furthermore, the noise in the 70 μm data sometimes tended to make it unclear whether the core was in emission or absorption at 70 μm. Likewise, a source's appearance at 160 μm depends heavily on the temperature of the cloud. These wavelengths were therefore largely ignored when classifying an IRDC and were only used if the longer wavelengths left some ambiguity about an object's status.

Our aim was to model those IRDCs without embedded protostars. We focus on three objects, G030.50+00.95, G031.03+00.26 and G031.03+00.76, which meet the criteria for IRDCs. All three contain two cores each, designated 'Core A' and 'Core B' in order of Right Ascension within each cloud. Positions and physical properties of all six cores can be found in Table 3.1, and images are displayed in Figures 3.5–3.7.

3.3.1.1 G030.50+00.95

In G30.50+00.95, Core B is the more extended and brighter of the two cores and located to the south of Core A (see Figure 3.5). In the 250 μm and 350 μm wavebands, it is possible to see that Core B can be separated into two cores. However, as the individual peaks cannot be seen at either 160 μm or 500 μm, the two are grouped together and modelled as a single core. A distance of 3.4 kpc for the entire cloud is assumed (Simon et al., 2006b). No previously calculated masses are available for these cores. Results calculated from our data are presented in Table 3.1.

3.3.1.2 G031.03+00.26

S06 find three cores in G031.03+00.26. However, only two can be seen as significant emission sources in the FIR and so here the third is ignored. Core B is the more extended and brighter of the two and is located to the north of Core A (see Figure 3.6). Emission from Core B can be clearly seen at wavelengths as short as 160 μm, whereas emission from Core A is not seen shortward of 250 μm.

We take a distance of 4.9 kpc for both cores (Teyssier et al., 2002) although we note that there are two emission line components along the line of sight, with the second emission line giving a distance of 6.6 kpc. Therefore there is some uncertainty in this distance.

Parsons et al. (2009) use 850 μm data and find masses of 420 and 560 $M_{\odot}$, respectively, for these cores. However, these authors used a different size of aperture. We make a direct comparison with these results in Section 3.4.1. Results calculated from our data are presented in Table 3.1.

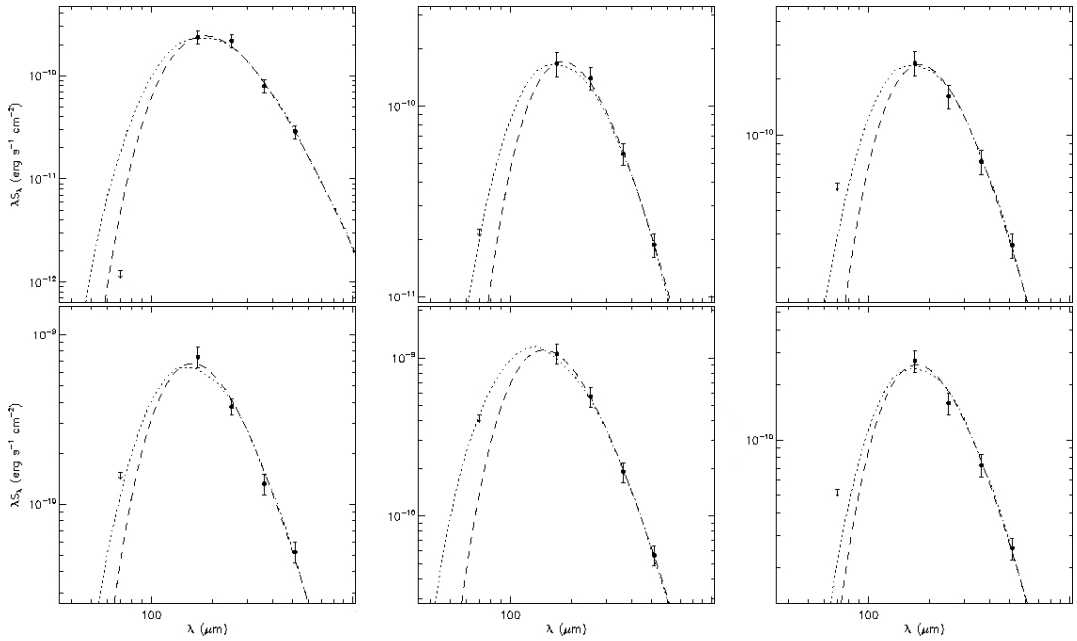

Figure 3.4: SEDs of all six cores. Upper row (left–right): G030.50+00.95, G031.03+00.26 and G031.03+00.76 Core A. Lower row (left–right): G030.50+00.95, G031.03+00.26 and G031.03+00.76 Core B. The dotted line shows the SED calculated from PHAETHON, using β=1.85. The dashed line shows the single-temperature greybody, with temperatures as noted in Table 3.1, also using β=1.85.

3.3.1.3 G031.03+00.76

In G031.03+00.76, Core B is located to the north of Core A (Figure 3.7) and, although it is the more extended of the two, it is actually fainter than Core A. Neither core can be seen in emission at wavelengths shorter than 160 μm. A distance of 3.4 kpc is assumed (Simon et al., 2006b). No previously calculated masses are available for these cores.

A third core in this cloud, located to the south of Core A, is not modelled here due to a bright 8μm source at the same position, implying the core may have an internal heating source. A possible fourth core exists to the north of Core B, we ignore this as S06 state that it belongs to a different IRDC with no known distance. Results calculated from our data are presented in Table 3.1.

3.3.2 Single Temperature Fitting of SEDs

The flux density, integrated over twice the FWHM of each core at 250 μm using an elliptical aperture, was measured at 70, 160, 250, 350 and 500 μm (see Table 3.2). From these flux densities an SED (spectral energy distribution) was plotted. These flux densities have been background subtracted, where the background was defined using an off-cloud, elliptical aperture. For example, with G031.03+00.76 the area to the right of Core B was used. The background subtraction removed up to 50% of the original flux, the exception being at 70 μm where over 90% of the original flux was removed.

A single-temperature greybody (modelling thermal emission from cold dust) was fitted (using MPFit; Markwardt, 2008) to each core, shown as a dashed line in Figure 3.4. This has the form

$$F_\nu = B_\nu(T)\,\Omega\,\left[\frac{2m_H}{X}N(H_2)\kappa_\nu\right], \tag{3.32}$$

where: F_ν is the flux density at frequency ν; $B_\nu(T)$ is the blackbody function at temperature T; Ω is the solid angle subtended at the observer by the source; $2m_H$ is the mass of a hydrogen molecule; X is the mass fraction of hydrogen and κ_ν is the dust mass opacity (e.g. Kirk et al. 2010; Ward-Thompson et al. 2010). κ_ν is given by

$$\kappa_\nu = 0.1\,\mathrm{cm^2 g^{-1}} \times \left(\frac{\nu}{1000\mathrm{GHz}}\right)^\beta, \tag{3.33}$$

where β, the dust emissivity index, was set to 1.85 (Ossenkopf & Henning, 1994). The reasons this value was chosen for β are discussed in Section 3.2.4.3.

The model was fitted between 160 μm and 500 μm. The flux density at 70 μm was used as an upper limit, because the cores are not visible at this wavelength. The

temperature was allowed to vary over a range 3–40 K. The best fit temperatures for the cores are given in Table 3.1.

3.3.3 Radiative Transfer Modelling of the Cores

The six cores were modelled in PHAETHON. They each showed some measure of eccentricity in the observations and so were modelled with a flattened geometry (see Section 3.2.4.1).

The FWHM of the major axis of each observed core was measured at 250 μm and used as the semi-major axis of the model core. The observations were not deconvolved from the instrument beam before the FWHM of the cores were found, the effect this had on the measurements of core radius is discussed in Chapter 5. The FWHM of the cores have an error of $\pm 15\,\%$, due primarily to the uncertainties in the background levels. The flattening radius, R_0, was set at one tenth of the FWHM.

The central density, $n_0(H_2)$, and interstellar radiation field (ISRF) incident on the core were varied until the output model's SED matched the observed data. The model SED is shown as a dotted line in Figure 3.4. The final values for $n_0(H_2)$ and the incident ISRF are noted in Table 3.1. The final values for $n_0(H_2)$ and the incident ISRF have an uncertainty of $\pm 15\,\%$. This is based on a by-eye estimation of how much they can be varied until the model SED no longer fits the observed SED.

The central density of the core primarily affected the SED at the longest wavelengths. The ISRF, conversely, had most effect on the shortest wavelengths in the SED. It was found that the level of the ISRF had no effect on the SED at

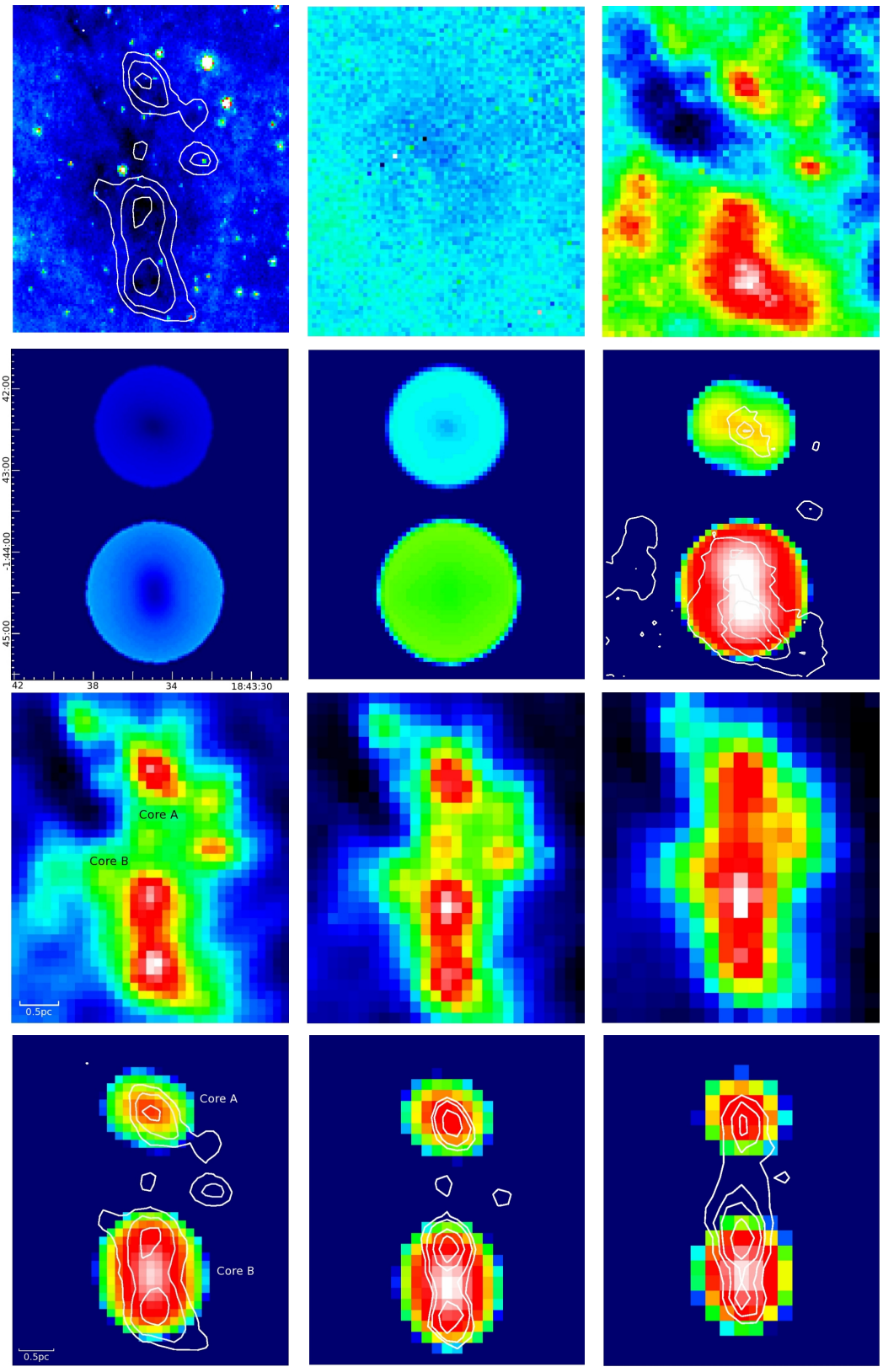

Figure 3.5: Upper row: Observations of G030.50+00.95 taken at (left–right) *Spitzer* 8 μm (with 250 μm contours), PACS 70 & 160 μm and SPIRE 250, 350 and 500 μm. Lower row: Model output for G030.50+00.95 at (left–right) 8 and 70 μm (example background only — showing core in absorption in middle) and 160, 250, 350 and 500 μm (in emission). Overlaid contours correspond to the observed data.

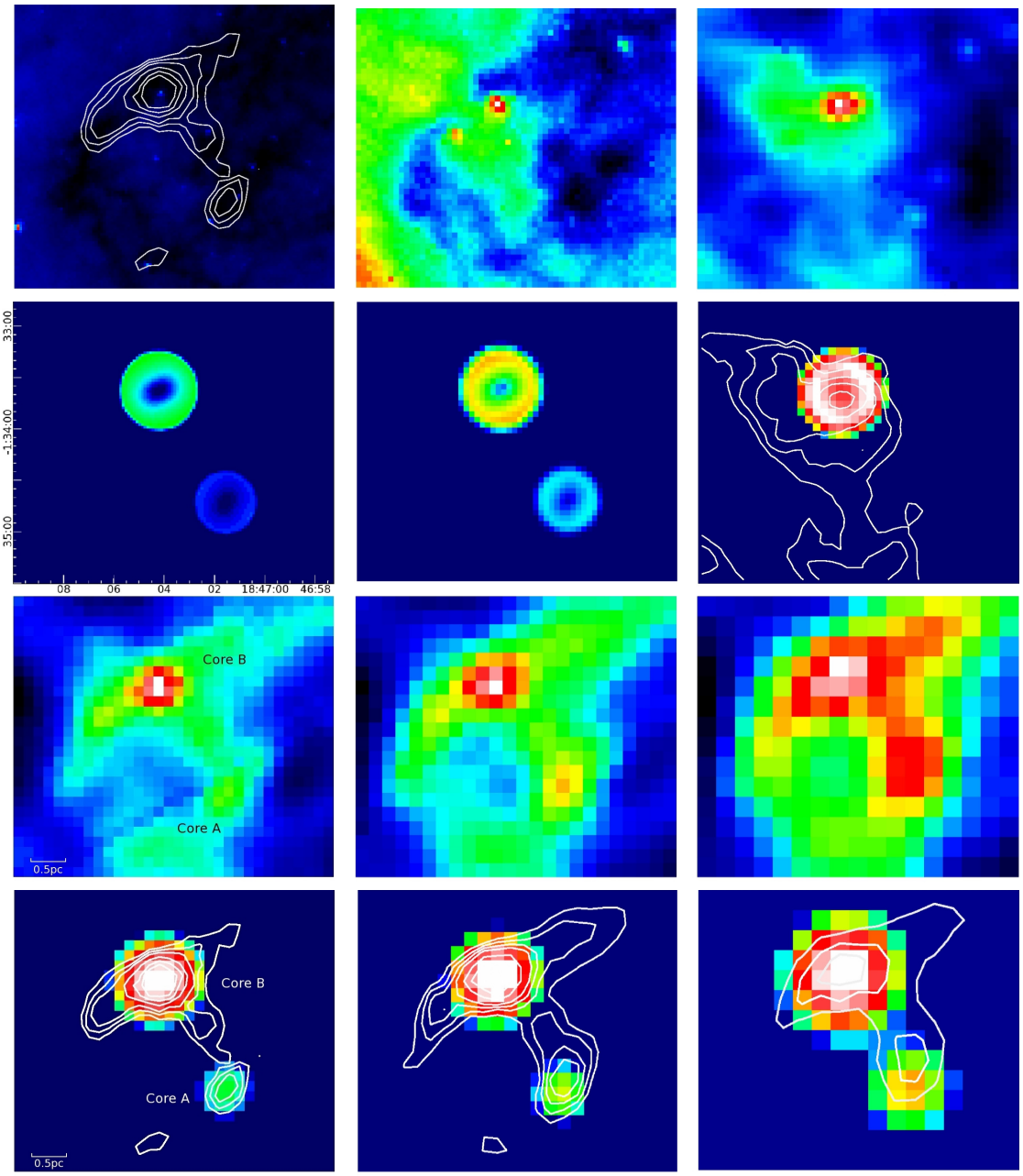

Figure 3.6: Upper row: Observations of G031.03+00.26 taken at (left–right) *Spitzer* 8 μm (with 250 μm contours), PACS 70 & 160 μm and SPIRE 250, 350 and 500 μm. Lower row: Model output for G031.03+00.26 at (left–right) 8 and 70 μm (example background only — showing core in absorption in middle) and 160, 250, 350 and 500 μm (in emission). Overlaid contours correspond to the observed data.

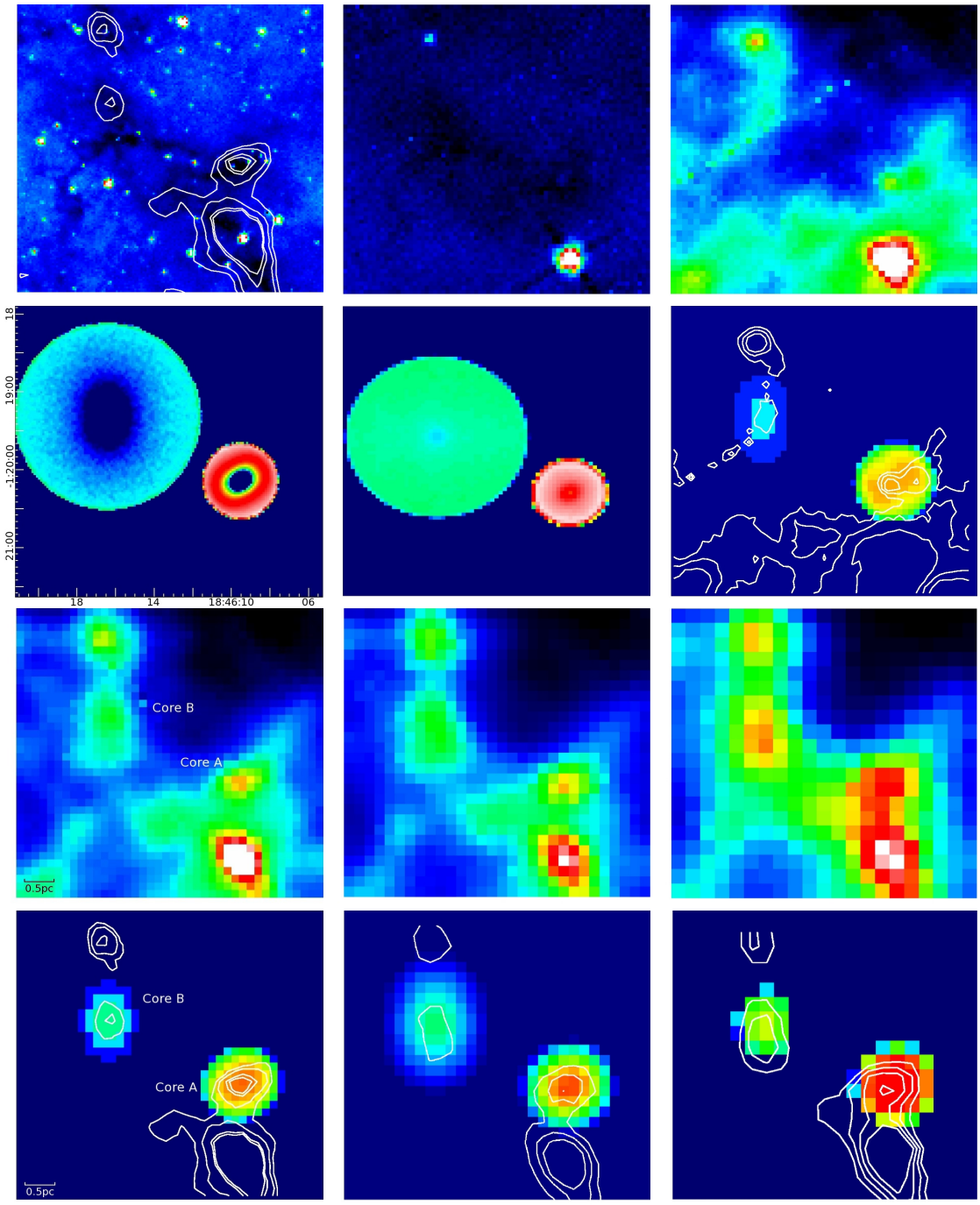

Figure 3.7: Upper row: Observations of G031.03+00.76 taken at (left–right) *Spitzer* 8 μm (with 250 μm contours), PACS 70 & 160 μm and SPIRE 250, 350 and 500 μm. Lower row: Model output for G031.03+00.76 at (left–right) 8 and 70 μm (example background only — showing core in absorption in middle) and 160, 250, 350 and 500 μm (in emission). Overlaid contours correspond to the observed data.

500 μm and that the model flux at this wavelength was dependent solely on the central density. This ensures the uniqueness of the fit and means that the central density could be found to a high degree of accuracy. Similarly, the flux at 160 μm was dependent on the level of ISRF but not central density, allowing the central density to be fit accurately and uniquely.

It should be noted that the internal structures of cores within infrared dark clouds have not yet been observed in detail. Hence our assumption of an elliptical geometry may be an over-simplification. If there is structure on smaller scales than we can resolve this might affect our results. For example, small scale fragmentation might allow the ISRF to penetrate further into the cores, meaning that our calculated values of central density are probably upper limits.

Figures 3.5–3.7 show the output of the model at wavelengths corresponding to the wavelengths of the observed data. The modelled images have pixels of 0.02×0.02 pc in size, which corresponds to 8″ pixels for G031.03+00.26 and 14″ pixels for G030.50+00.95 and G031.03+00.76. The images show an area 2.56×2.56 pc in total.

To allow for better comparison between the observed and modelled images, all the images have been convolved with the telescope beam at their respective wavelengths: 2″ at 8 μm; 5.2″ at 70 μm; 11.5″ at 160 μm; 18″ at 250 μm; 25″ at 350 μm; and 36″ at 500 μm (Werner et al., 2004; Griffin et al., 2010).

For wavelengths where no emission is visible in the model (i.e. 8 and 70 μm), an image showing background radiation is shown. As no attempt was made to correctly model the surrounding area, these images are not an accurate representation of the parent cloud but do show the cores in absorption as seen in the observations.

With the possible exception of G31.03+00.26 Core B (which may have evidence of an 8 μm point source), the 8 μm images show no emission in either the model or the observed data, as IRDCs do not emit significantly in the MIR due to their low temperatures. The modelled images show emission starting at 250 μm for G031.03+00.26 Core A and 160 μm for the remaining five cores (albeit only faintly for the cores in G031.03+00.76) and absorption at shorter wavelengths. The modelled emission fits well with the observations, at all wavelengths.

3.4 Discussion

3.4.1 Masses

The masses of the cores were calculated in two ways: (i) using the radiative transfer models; and (ii) using the observed flux densities at 500 μm and the temperature from the greybody fitting of the SED. We call the former the model mass and the latter the SED mass. The SED masses had uncertainties of $\pm 20\,\%$, based on the uncertainties on the flux densities (although it should be noted that errors in the opacity and helio-distance would increase this figure). The model masses have errors of $\pm 15\,\%$, based on how much the mass can be changed until the 500 μm flux is no longer in agreement with the observed SED.

The SED mass was found using the equation

$$M = \frac{F_\nu D^2}{B_\nu(T)\kappa_\nu}, \tag{3.34}$$

(Hildebrand, 1983), where D is the source distance. Two different values of opacity at 500 μm were used when calculating the SED mass: κ=0.03 cm^2 g^{-1} (Preibisch

et al., 1993; Henning, Michel, & Stognienko, 1995) and κ=0.05 $cm^2\,g^{-1}$ (Ossenkopf & Henning, 1994). The former is the value used to calculate the masses of low-mass prestellar cores (e.g. Kirk, Ward-Thompson, & Andre 2005). The model masses were found using the Ossenkopf & Henning (1994) opacities (see Section 3.2.4.2).

As would be expected, the model masses match well with the SED masses calculated using κ=0.05 $cm^2\,g^{-1}$, but not with those calculated using κ=0.03 $cm^2\,g^{-1}$ (the same opacity as was used in the model). Both sets of SED masses and the model masses are shown in Table 3.1.

The masses calculated here are in agreement with those found in previous studies of IRDCs (e.g. Williams, Ward Thompson, & Whitworth 2001; Simon et al. 2006b; Rathborne et al. 2006). In particular, Rathborne et al. (2006) calculated masses of cores and found them to vary from 10 to 2100$M_\odot$. All of our cores fit within this range.

850 μm masses for both cores in G031.03+00.26 were calculated by Parsons et al. (2009). Core A was found to have a mass of 460 $M_\odot$ and Core B of 520 $M_\odot$. When using the same core boundaries as in Parsons et al. (2009) and κ=0.05 $cm^2\,g^{-1}$, we find 500 μm masses of 470 $M_\odot$ and 540 $M_\odot$, similar to the 850 μm masses. This gives us additional confidence in our models.

3.4.2 Temperatures

The energy deposited in the gas due to cosmic ray ionisation heating is much lower than the energy absorbed by the dust due to external heating from the ISRF (Evans et al., 2001). Thus, we can safely assume that the dust temperature is not affected by the energy exchange between gas and dust. The lack of MIR point

sources also implies that heating via compression is minimal (Battersby et al., 2010). These cores (again with the possible exception of G031.03+00.26 Core B) therefore have no significant internal heating sources and are heated mainly by the external radiation field.

The temperature profiles of the modelled cores are shown in Figure 3.8. They show a low temperature throughout the centres of the cores, rising to the outer edges. A higher temperature at the edges than the centre is expected due to the lack of any internal heating source (Ward-Thompson & Andr'e, 1999). Some stepping can be seen in the graphs, this is due to the temperature lookup table having a spacing of 0.2 K.

This gradient is consistent with previous studies of IRDCs (e.g. Peretto et al. 2010) and is similar to what is seen in low-mass prestellar cores (e.g. Nutter et al. 2008). However, these IRDCs have higher outer temperatures than low-mass prestellar cores, which can be explained by a higher ISRF around these IRDCs relative to nearby regions of star formation.

As all six cores have a flattened geometry, the temperature-radius profile varies with the direction inside the core. The two extreme cases, $\theta = 0^o$ and $\theta = 90^o$, are shown in the temperature-radius profiles. $\theta = 90^o$ is along the midplane of the structure, while $\theta = 0^o$ corresponds to the short axis of a flattened core, perpendicular to the midplane.

The average temperature from the model of each core agrees with the result from the single-temperature greybody fit. However, the temperature-radius profile shows this fit to be an over-simplification, with temperatures within each core varying by $\sim$10 K and being dependent upon angular direction in the core. PHAETHON

gives a far more accurate representation of the temperatures inside the cores than the single-temperature fitting.

3.4.3 The Interstellar Radiation Field

Five of the six cores required a higher ISRF than the solar neighbourhood value in order to correctly match the observed flux densities at the shorter wavelengths (i.e. 160 and 250 μm). As an example we show the cores' ISRF at far-ultraviolet (FUV) in Table 3.1. This is merely to indicate how the ISRF varies from core to core. For comparison, the solar neighbourhood ISRF at FUV is 7.6×10^{-3} erg s^{-1} cm^{-2} (Black, 1994) or 4.6 times the Habing flux (1.6×10^{-3} erg s^{-1} cm^{-2}, Habing 1968). The IRDCs typically have an ISRF around four times greater, consistent with them being in the stronger interstellar radiation field of the inner Galactic Plane.

Differences between the ISRF required for cores within the same field can be explained by one core being more deeply buried within the parent cloud and thus having less external radiation heating it. The difference between the ISRFs of the cores are listed in Table 3.1 as $\ln\left(\frac{I_1}{I_2}\right)$, where I_1 corresponds to the core that is modelled using a higher ISRF and I_2 to the core modelled with the lower ISRF (within the same field). This ratio can be thought as a measure of how much more deeply a core is embedded when compared with the other core in the same field.

Core B in G031.03+00.26 appears to reside in an unusually intense radiation field. The ISRF surrounding G031.03+00.26 Core B is 17 times that of the solar neighbourhood and far higher than any of the other cores, possibly pointing to an abnormally high ISRF in this field. Core A in the same cloud has an ISRF value comparable to the other cores, which implies that it is either more deeply

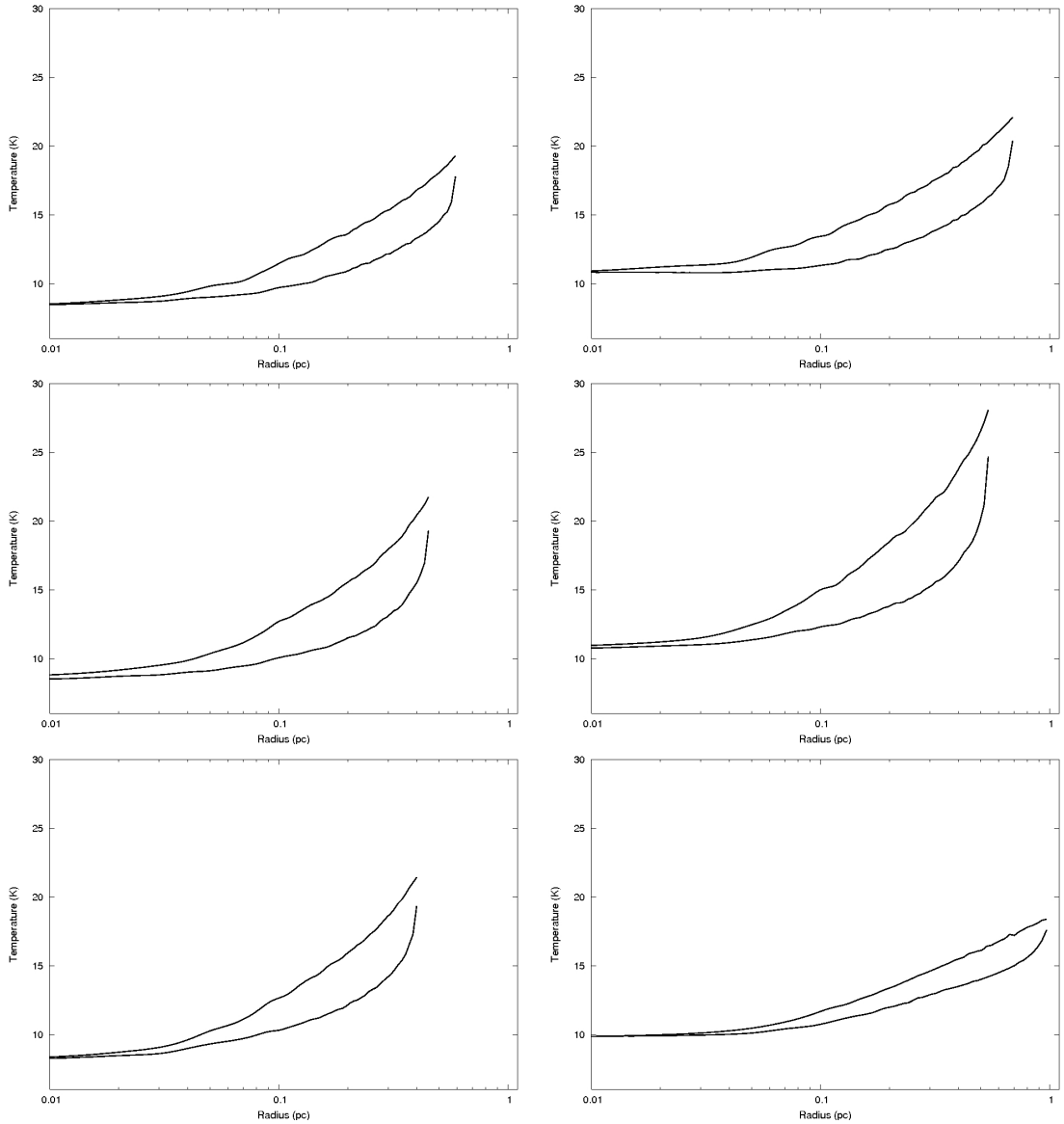

Figure 3.8: Dust temperature profiles of the cores at two different directions of the cloud, as calculated from the radiative transfer model. The lower line corresponds to the midplane of the flattened structure ($\theta = 90\,^o$), whereas the upper line corresponds to the direction perpendicular to the midplane ($\theta = 0\,^o$). Upper row: G030.50+00.95 Cores A and B; Middle row: G31.03+00.26 Cores A and B; Lower row: G31.03+00.76 Cores A and B

buried within the IRDC than Core B or there is a highly asymmetrical external radiation field incident on this cloud. Alternatively, differences in emission from the cores could be the result of different physical properties (e.g. dust grain size) between different cores in the same IRDC. Core B may not, in fact, be completely externally heated. This one is unusual in our sample, in that it may have an embedded protostar. There is some evidence for an 8 μm source associated with this core.

3.4.4 Internal Heating Sources

In order to determine whether any massive star formation is likely to be taking place in these cores we found the maximum luminosity of an 8 μm source within the core.

To find the column density, $N(H_2)$, of the cores we integrated the density profile

$$N(H_2) = \int_0^R \rho(r,\theta)dr \tag{3.35}$$

where ρ is the density profile and R is the semi-major axis/radius (depending on its geometry) of the core. We use a flattened geometry for all six cores, which means the modelled cores have the density profile described in Equation 3.31. We make the assumption that $sin(\theta) = 1$ and Equation 3.35 becomes

$$N(H_2) = \rho_0 \int_0^R \frac{1 + A\left(\frac{r}{R_0}\right)^2}{\left[1 + \left(\frac{r}{R_0}\right)^2\right]^2} dr \tag{3.36}$$

$$= \frac{\rho_0 R_0^2}{2}\left[\frac{(A+1)}{R_0}\arctan\left(\frac{R}{R_0}\right) - \frac{(A-1)R}{R_0^2 + R^2}\right], \tag{3.37}$$

where A, ρ_0, R_0 and R, the semi-major axis of the core, are inputs of the PHAETHON code. Further details of this integration can be found in Appendix A. Substituting the values used for our six cores (see Table 3.1) into Equation 3.37 gave the column density for each core.

The visual extinctions of the cores were then calculated via

$$A_v = \frac{N(H_2)}{2.21 \times 10^{21}} \tag{3.38}$$

where A_v is the visual extinction (Güver & Özel, 2009). The K-band extinction, A_K, is one tenth of the visual extinction. From A_K, the 8 μm extinction (A_8) can be calculated using:

$$\log\left(\frac{A_\lambda}{A_K}\right) = 0.61 - 2.22\log(\lambda) + 1.21\left[\log(\lambda)\right]^2 \tag{3.39}$$

where λ is the wavelength in μm and A_λ is the extinction at that wavelength (Indebetouw et al., 2005). When $\lambda = 8\,\mu$m this simplifies to

$$A_8 = 0.39 A_K. \tag{3.40}$$

A_8 is the number of magnitudes theoretically obscured by the parent IRDC at 8 μm:

$$A_8 = M_1 - M_2 = 2.5\,\log\left(\frac{F_2}{F_1}\right) \tag{3.41}$$

which, when re-arranged, gives

$$F_2 = F_1 10^{\left(\frac{A_8}{2.5}\right)} \tag{3.42}$$

where M_1 and F_1 are the absolute magnitude and flux of the core as seen by the

telescope (i.e. with the core obscured by the parent cloud) and M_2 and F_2 are the absolute magnitude and flux of the core as seen at the source (i.e. with no obscuration).

F_1 is calculated from the 8 μm flux density, F_8, via

$$F_1 = 10^{-26} \int_{\nu_2}^{\nu_1} F_8 \, d\nu \tag{3.43}$$

where F_8 is the measured peak flux density (in Jy) at 8 μm and $\nu_1 - \nu_2$ is the *Spitzer* 8μm bandwidth. The flux at the source (F_2) is then calculated using Equation 3.42 and converted to a luminosity, L, using

$$L = 4\pi D^2 F_2. \tag{3.44}$$

where D is the distance to the core. This gives the maximum luminosity of an 8 μm source embedded within the core.

These luminosities are listed in Table 3.1. We note that G31.03+00.76 Core A has some 8 μm sources around its edge, but they do not appear to be centred on the core.

Our upper limits for G030.50+00.95 Cores A and B and G031.03+00.76 Core B are fairly low. We can thus rule out any significant massive star formation having occurred in their centres, making it possible that these cores are the high-mass equivalents of low-mass prestellar cores. For both cores in G031.03+00.26 and in G031.03+00.76 Core A, the upper limits are too high to reach this conclusion.

In the case of G031.03+00.26 Core B a very faint source can be seen at 8 μm from which F_8 was measured. These calculations make the assumption that this

source is deeply embedded within the cloud. Should the source instead be in the foreground or towards the nearer edge of the IRDC then the maximum embedded luminosity would be very much lower.

3.5 Summary

PHAETHON is a 3D Monte Carlo radiative transfer code. Within PHAETHON, L-packets are followed as they travel through and interact with a prescribed medium. Six cores within three IRDCs (G030.50+00.95, G031.03+00.26 and G031.03+00.76) have been modelled. The radiative transfer models reproduce the observed SEDs and the FIR images of these cores and it has thus been proven that PHAETHON is a suitable method for studying these objects.

The PHAETHON code calculated masses for the cores ranging from 90 to 290 $M_\odot$. The masses calculated from the SED temperature ranged from 100 $M_\odot$ to 310 $M_\odot$ (with $\kappa_{500\mu m}$=0.05 $cm^2\,g^{-1}$). These are in agreement with previous mass estimates found for clouds. It should be noted that objects of this size and mass are not likely to create a single star, but rather a cluster of stars.

The greybody fitted SED temperatures varied from 14 to 17 K. The average temperatures calculated from the model agreed with these values. However, the model showed that the single-temperature fits were an over-simplification of the temperatures inside the cores, as temperature-radius profiles showed variations in temperature of ∼10 to 17 K within a single core. The model calculated temperatures of 8 to 11 K at the centre of each core and 18 to 28 K at the surface. These results imply that PHAETHON is more accurate than single-temperature fitting when finding the physical parameters of IRDCs and their cores.

Significant temperature gradients were also seen by Peretto et al. (2010), where temperature maps of 22 IRDCs were created and non-uniform temperatures ranging from 10 to 22 K were found. Stamatellos et al. (2010) used PHAETHON to model an IRDC core and found temperatures from 10 to 21 K, consistent with our results.

The maximum luminosity of a star embedded within each core was found. The upper luminosity limits for three of the cores (G30.50+00.95 Cores A and B and G31.03+00.76 Core B) are low, ruling out the possibility of any significant high mass star formation having yet occurred and making it likely that these cores are the high-mass equivalent of prestellar cores.

In most cases, the amount of radiation incident on the cores was found to be higher than that in the local neighbourhood, as expected for objects within active star-forming regions in the Galactic Plane. Differences in the amount of radiation falling on cores in the same cloud were attributed to one core being more deeply buried within the IRDC than the other. This method can now be used on all cores within IRDCs found in the Hi-GAL survey.

Chapter 4

IRDCs and their Cores in the Region l=300-330°

4.1 Introduction

Traditionally IRDCs are identified by their appearance in the MIR where they are seen in absorption (see Section 1.2). However, observing IRDCs in the MIR alone can be problematic as there is no way to distinguish between a genuine IRDC and a dip in the MIR background. Longer wavelength observations, especially in the FIR and sub-mm, where IRDCs are seen in emission are required to accurately separate the genuine IRDCs from the holes in the sky.

Here, Hi-GAL data are used to observe the candidate IRDCs of PF09 at FIR wavelengths. Those that show emission in the longest *Herschel* wavelengths are found and labelled *Herschel*-bright. These are the objects thought to be genuine IRDCs.

Each *Herschel*-bright IRDC is then searched for evidence of one or more cores at 250 μm. Each cold core is then sorted into one of three evolutionary phases (see Section 1.3.2): starless, containing no MIR point sources and equivalent to the quiescent phase of Chambers et al. (2009); 24 μm point source only, where the cold core contains one or more 24 μm point sources but no 8 μm point source, this stage is equivalent to the active phase of Chambers et al. (2009); and the 8 μm point source phase, by which point the cold core shows evidence of an 8 μm point source. This is equivalent to the red core phase in Chambers et al. (2009).

4.2 Identifying *Herschel*-bright IRDCs

The PF09 catalogue used *Spitzer* GLIMPSE (Werner et al., 2004; Benjamin et al., 2003) 8 μm data to find 11,303 candidate IRDCs in the regions $10^\circ < l < 65^\circ$ and $295^\circ < l < 350^\circ$ with $|b| < 1^\circ$. They identified the candidate IRDCs as connected structures with an apparent mean 8 μm opacity greater than 0.35 and an apparent peak opacity above 0.7. This corresponds to molecular hydrogen column density (N_{H_2}) detection thresholds of a mean of $\sim 10^{22}$, and a peak of $\sim 2 \times 10^{22}$ cm^{-2}. Each candidate IRDC had to be at least $4''$ in diameter. We refer to the PF09 candidate IRDCs as '*Spitzer*-dark' regions, meaning that they are apparently seen in absorption at 8 μm.

We focused on the region from $l = 300^\circ$ to $l = 330^\circ$ with $|b| < 1^\circ$. This region was chosen as it was the first large continuous area to be covered in the Hi-GAL survey. It had also been observed in both the GLIMPSE and MIPSGAL (Carey et al., 2009) surveys and was included in the PF09 survey. The region was therefore used to search for IRDCs and their cold cores. The PF09 catalogue contained 3171

Spitzer-dark candidate IRDCs in this region.

Each of the 3171 *Spitzer*-dark objects within our search area was studied using *Spitzer* data at 8 μm, and *Herschel* data at 70, 160, 250, 350 and 500 μm. They were viewed in a similar fashion to Figures 4.1 and 4.2. The 24 μm data was not used at this point due to its similarity to the 8 μm data in terms of extended regions of absorption.

The criteria for classifying an object as *Herschel*-bright was the same as in Chapter 3. Any object seen in absorption at 8 μm and seen simultaneously in emission at 250, 350 and 500 μm was classed as both *Spitzer*-dark and *Herschel*-bright. *Spitzer*-dark and *Herschel*-bright objects are thought to be genuine IRDCs. Figure 4.1 shows an example of a *Spitzer*-dark and *Herschel*-bright source. The centre of the IRDC, according to PF09, is marked with a cross. Absorption at 8 μm can be seen at this point and also extending out towards the right and upper left of the image. At 250 μm the same area seen in absorption at 8 μm is now seen in emission. The emission extends from the centre following the same path as the absorption in 8 μm. This emission is also seen at 350 and 500 μm. This object is believed to be a genuine IRDC.

If an object was seen in absorption throughout all six wavelengths it was classed as *Spitzer*-dark and *Herschel*-dark. *Spitzer*-dark and *Herschel*-dark objects are suspected of being caused by a local dip in the MIR and FIR background. They are not thought to be genuine IRDCs and are sometimes referred to as a 'hole in the sky' (Stanke et al., 2010). Holes in the sky show little or no emission throughout the entire EM spectrum (see Section 1.2.2). Figure 4.2 shows an example of a region that is classed as *Spitzer*-dark and *Herschel*-dark. As with Figure 4.1, the centre of the region is marked with a cross. At 8 μm apparent absorption is seen

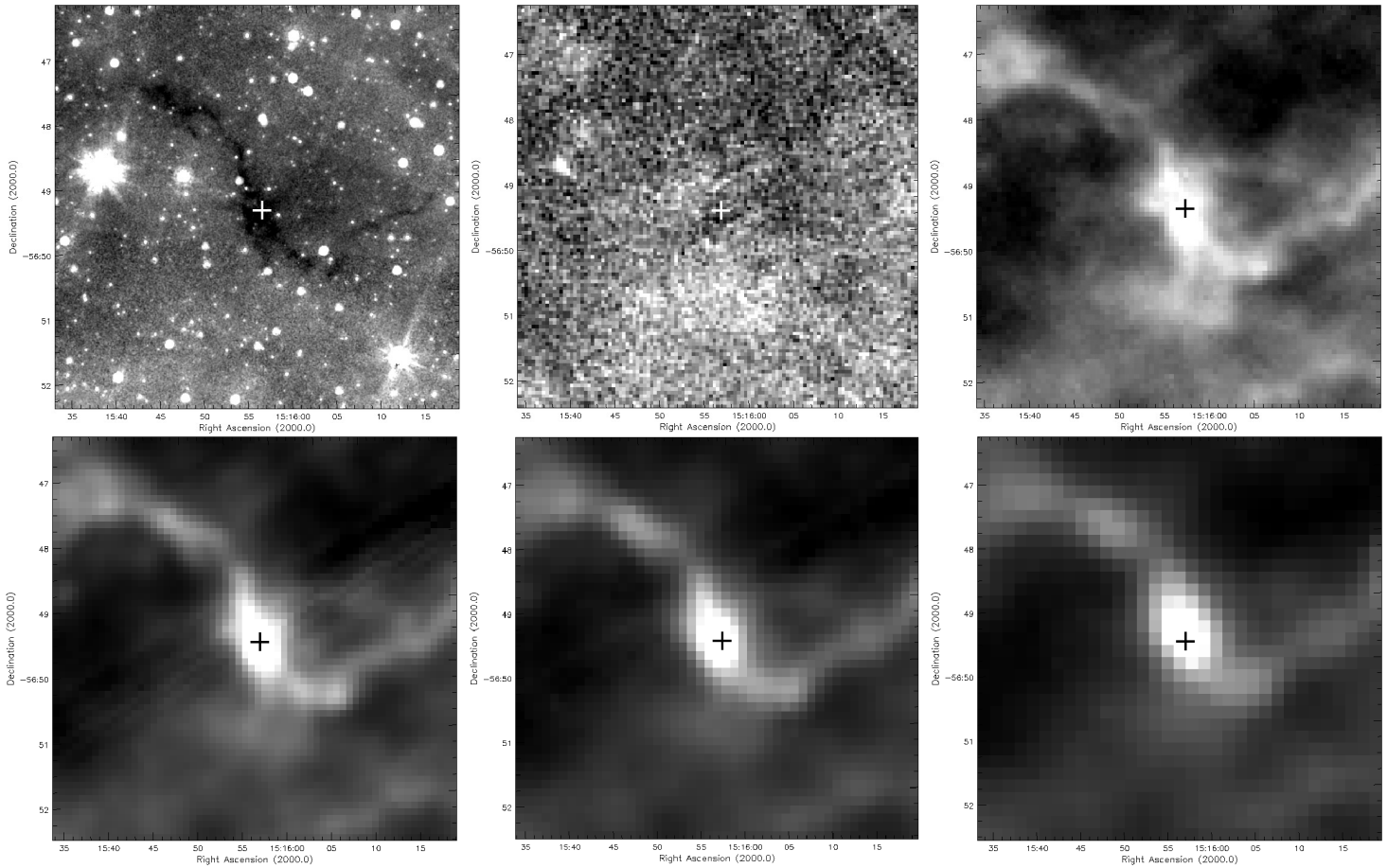

Figure 4.1: G321.753+0.669. Upper (left–right): 8 μm, 70 μm, 160 μm. Lower (left–right): 250 μm, 350 μm, 500 μm. The position of the candidate IRDC is shown with a cross. This is an example of a *Spitzer*-dark and *Herschel*-bright cloud. Note how the same structure that is seen in absorption (black) at 8 μm is seen in emission (white) in all three of the longer *Herschel* wavelengths. This is believed to be a genuine IRDC.

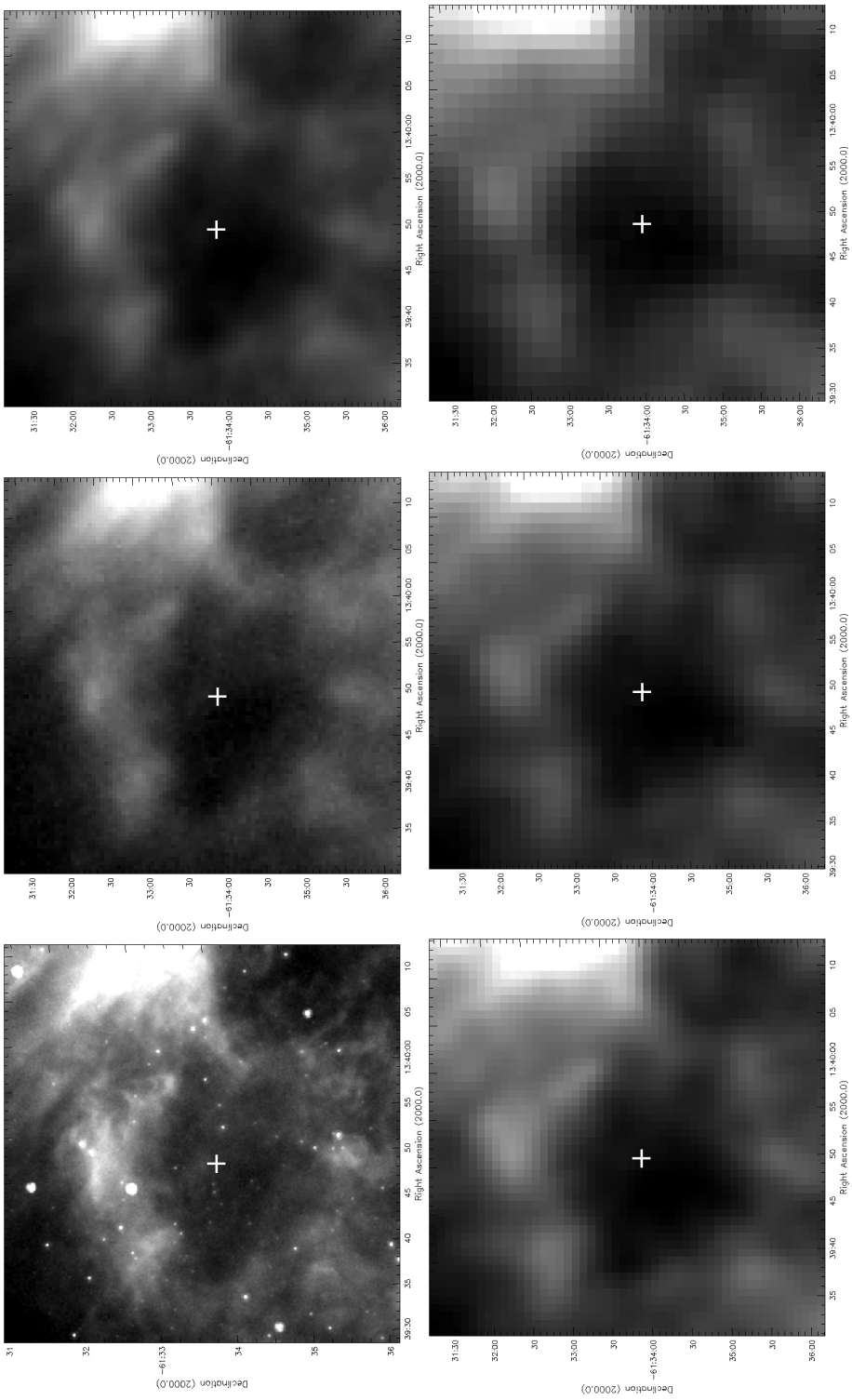

Figure 4.2: G308.656+0.760. Upper (left–right): 8 μm, 70 μm, 160 μm. Lower (left–right): 250 μm, 350 μm, 500 μm. The position of the candidate IRDC is shown with a cross. This is an example of a candidate IRDC that is *Spitzer*-dark but is not *Herschel*-bright. The same structure that appears dark (black) at 8 μm is also dark (black) in the longest *Herschel* wavelengths. We refer to such a candidate as a 'hole in the sky' (Stanke et al., 2010). This is not believed to be a genuine IRDC.

as the region shows a decreased amount of emission compared to its surroundings. However, unlike the IRDC shown in Figure 4.1, the same region still shows a lower emission than its surroundings at 250, 350 and 500 μm. This region is therefore not thought to be an IRDC but rather a hole in the sky.

In total, of the original 3171 objects in the PF09 catalogue in our search area, we found 1966 to be *Herschel*-dark and only 1205 ($\sim$38 %) to be genuine IRDCs under our simultaneous *Spitzer*-dark and *Herschel*-bright definition. The objects thought to be genuine IRDCs are listed in Table 4.1.

This method of identifying IRDCS relies upon human interpretation of the data. To estimate the error-bars introduced by this method a second person observed all the candidates in a circular region with a radius of 0.5 °. They classified each candidate as *Herschel*-bright or *Herschel*-dark as before. Of the 107 candidate IRDCs in this region, only three were classified differently by the second person. We therefore estimate that the inherent human error is approximately $\pm$3 %.

4.3 List of IRDCs and their Cores

Table 4.1 shows the 1,205 genuine IRDCs and their cores referred to throughout this Chapter. Column 1 states the IRDC name as it appears in PF09. If >1 cold core is evident in a single IRDC they are listed as A, B, C etc. Columns 2 and 3 are the position of the IRDC according to PF09. Columns 4 and 5 give details on whether the object contains a MIR source. If no cold core is visible in the IRDC then these columns are left blank. Column 6 gives additional information about the cloud, including whether it contains a visible cold core and whether any cores are isolated at 160 and 500 μm (see Chapter 5).

Table 4.1: List of genuine IRDCs.

IRDC Name	Right Ascension 2000.0 (°)	Declination 2000.0 (°)	8 μm source?	24 μm source?	Additional comments
300.345−0.357	187.13	−63.11	Yes		
300.356−0.358	187.16	−63.12	Yes		
300.596+0.098	187.77	−62.68	Yes		
300.743+0.036	188.08	−62.75	Yes		
300.746+0.550	188.16	−62.24	Yes		
301.131−0.274	188.88	−63.09	Yes		
301.206−0.193	189.06	−63.01	No	No	Confused at 500 μm
301.283−0.242	189.22	−63.07	Yes		
301.423−0.116	189.54	−62.95	Yes		
301.504−0.464	189.68	−63.30	Yes		
301.512−0.350	189.71	−63.19	No	No	Confused at 500 μm
301.519−0.467	189.71	−63.30	Yes		
301.550−0.121	189.82	−62.96	Yes		
301.558−0.380	189.81	−63.22	Yes		
301.595−0.107	189.92	−62.95	Yes		
301.605−0.118	189.94	−62.96	Yes		
301.659−0.367	190.04	−63.21	Yes		
301.659+0.245	190.09	−62.60	No	No	Confused at 500 μm
301.671−0.201	190.08	−63.05	Yes		
301.689−0.414	190.10	−63.26	Yes		
301.785+0.145	190.36	−62.70	Yes		
301.861+0.694	190.57	−62.16	No	Yes	
301.876+0.589	190.59	−62.26	Yes		
302.097+0.233	191.04	−62.63	Yes		
302.172+0.258	191.21	−62.60	Yes		
302.458−0.783	191.79	−63.65	Yes		
302.543+0.000	192.01	−62.87	Yes		

continued on next page

IRDC Name	Right Ascension 2000.0 (°)	Declination 2000.0 (°)	8 μm source?	24 μm source?	Additional comments
302.593+0.122	192.12	−62.75	Yes		
302.688+0.084	192.33	−62.79	Yes		
302.764−0.082	192.49	−62.95	No	No	Confused at 500 μm
302.813−0.034	192.60	−62.91	Yes		
302.844+0.235	192.67	−62.64	Yes		
302.847−0.049	192.67	−62.92	No	No	Confused at 500 μm
302.883−0.431	192.75	−63.30	Yes		
302.939−0.445	192.88	−63.32	Yes		
303.043−0.449	193.11	−63.32	No	Yes	
303.044−0.434	193.11	−63.31	Yes		
303.049+0.113	193.12	−62.76	Yes		
303.059−0.450	193.14	−63.32	Yes		
303.359+0.418	193.78	−62.45	Yes		
304.013+0.485	195.19	−62.37	No	No	Confused at 500 μm
304.115+0.279	195.43	−62.57	Yes		
304.132−0.384	195.53	−63.23	Yes		
304.526−0.037	196.36	−62.87	Yes		
304.584+0.333	196.44	−62.49	No	Yes	
304.601+0.353	196.47	−62.47	No	No	Confused at 500 μm
304.723+0.266	196.75	−62.55	Yes		
304.795+0.202	196.91	−62.61	No	Yes	
304.812+0.222	196.95	−62.59	Yes		
304.816+0.431	196.93	−62.38	Yes		
304.823+0.324	196.96	−62.49	Yes		
304.831+0.336	196.97	−62.47	Yes		
304.836+0.578	196.95	−62.23	No	Yes	
304.856+0.270	197.04	−62.54	Yes		
305.022+0.325	197.39	−62.47			No distinct core
305.045+0.446	197.42	−62.35	Yes		
305.049+0.561	197.41	−62.24	Yes		

continued on next page

IRDC Name	Right Ascension 2000.0 (°)	Declination 2000.0 (°)	8 μm source?	24 μm source?	Additional comments
305.059−0.170	197.54	−62.96	Yes		
305.079+0.660	197.46	−62.13	Yes		
305.083+0.258	197.53	−62.54	No	Yes	
305.085−0.166	197.60	−62.96			No distinct core
305.086+0.548	197.49	−62.25	Yes		
305.103+0.582	197.52	−62.21	Yes		
305.131−0.027	197.68	−62.82	No	Yes	
305.134+0.067	197.67	−62.72	Yes		
305.162+0.224	197.70	−62.56	No	Yes	
305.162+0.554	197.65	−62.23	Yes		
305.183+0.464	197.71	−62.32	No	No	Confused at 500 μm
305.183+0.475	197.71	−62.31	Yes		
305.200+0.001	197.82	−62.78	Yes		
305.209+0.205	197.81	−62.58	Yes		
305.228+0.270	197.84	−62.51	Yes		
305.307−0.259	198.10	−63.03			No distinct core
305.339−0.254	198.17	−63.03	No	No	Confused at 500 μm
305.376+0.461	198.13	−62.31	Yes		
305.412+0.355	198.22	−62.41	Yes		
305.425+0.436	198.24	−62.33	No	Yes	
305.433−0.262	198.38	−63.03	No	Yes	
305.440+0.109	198.33	−62.66	Yes		
305.498+0.180	198.44	−62.58	Yes		
305.504+0.168	198.46	−62.59	Yes		
305.523+0.402	198.45	−62.36	Yes		
305.540+0.434	198.48	−62.32	Yes		
305.547−0.054	198.59	−62.81	Yes		
305.575−0.342	198.71	−63.09	Yes		
305.590+0.333	198.61	−62.42	Yes		
305.595+0.392	198.61	−62.36	Yes		

continued on next page

IRDC Name	Right Ascension 2000.0 (°)	Declination 2000.0 (°)	8 μm source?	24 μm source?	Additional comments
305.595+0.421	198.60	−62.33	Yes		
305.633−0.043	198.78	−62.79	Yes		
305.651−0.008	198.81	−62.75	No	Yes	
305.688−0.025	198.89	−62.77	Yes		
305.689+0.423	198.80	−62.32			No distinct core
305.696−0.147	198.94	−62.89	Yes		
305.706+0.026	198.92	−62.71	Yes		
305.741+0.163	198.97	−62.57	Yes		
305.798−0.097A	199.15	−62.83	No	No	
305.798−0.097B	199.15	−62.83	Yes		
305.801+0.120	199.11	−62.61	No	Yes	
305.818−0.073	199.18	−62.80	No	Yes	
305.866−0.148	199.31	−62.87	Yes		
305.898−0.029A	199.35	−62.75	Yes		
305.898−0.029B	199.35	−62.75	Yes		
305.898−0.029C	199.35	−62.75	Yes		
305.923−0.097	199.42	−62.82	No	Yes	
305.924+0.034	199.39	−62.69	Yes		
305.928−0.185	199.45	−62.90	Yes		
305.984−0.078	199.55	−62.79	Yes		
306.037−0.120	199.67	−62.83	Yes		
306.090−0.095	199.78	−62.80	No	Yes	
306.188−0.246	200.03	−62.94	Yes		
306.190−0.214	200.03	−62.90	Yes		
306.230−0.007	200.07	−62.69	Yes		
306.230−0.565	200.20	−63.25	Yes		
306.237−0.559	200.22	−63.24	Yes		
306.309−0.036	200.24	−62.71	Yes		
306.324−0.053	200.28	−62.73	Yes		
306.451+0.049	200.53	−62.61	Yes		

continued on next page

IRDC Name	Right Ascension 2000.0 (°)	Declination 2000.0 (°)	8 μm source?	24 μm source?	Additional comments
306.495+0.070	200.62	−62.59	Yes		
306.531+0.022	200.71	−62.63	Yes		
306.614−0.161	200.94	−62.80	Yes		
306.627−0.168	200.97	−62.81			No distinct core
306.664−0.209	201.06	−62.84	Yes		
306.780−0.406	201.37	−63.02	Yes		
306.841−0.070	201.40	−62.68	Yes		
307.150−0.776	202.29	−63.34	Yes		
307.495+0.660	202.57	−61.87	No	No	
307.567−0.689	203.18	−63.19	Yes		
307.751−0.838	203.64	−63.31	Yes		
307.873+0.079	203.57	−62.38	Yes		
308.123−0.332	204.25	−62.74	Yes		
308.138−0.454	204.33	−62.86	Yes		
308.307−0.027	204.53	−62.41	Yes		
308.323+0.078	204.52	−62.30	Yes		
308.338+0.082	204.55	−62.30	Yes		
308.378+0.190	204.60	−62.18	Yes		
308.386+0.211	204.60	−62.16	Yes		
308.397−0.175	204.78	−62.54	Yes		
308.458+0.025	204.83	−62.33	Yes		
308.512+0.025	204.94	−62.32	No	No	Confused at 500 μm
308.588+0.763	204.81	−61.58	Yes		
308.641−0.097	205.27	−62.42	No	Yes	
308.650−0.437	205.43	−62.75	No	Yes	
308.662−0.065	205.30	−62.38	No	Yes	
308.781+0.091	205.49	−62.21	Yes		
308.792−0.434	205.73	−62.72	Yes		
308.891−0.135	205.81	−62.41			No distinct core
308.943+0.068	205.83	−62.20	Yes		

continued on next page

IRDC Name	Right Ascension 2000.0 (°)	Declination 2000.0 (°)	8 μm source?	24 μm source?	Additional comments
308.949−0.457	206.08	−62.71	Yes		
308.968−0.115	205.97	−62.37	Yes		
308.969+0.203	205.83	−62.06	Yes		
308.972−0.196	206.01	−62.45	Yes		
308.972−0.244	206.03	−62.50			No distinct core
308.985−0.459	206.15	−62.70	Yes		
308.993−0.180	206.05	−62.43	No	No	Confused at 500 μm
308.997−0.261	206.09	−62.51	No	Yes	
309.003−0.187	206.07	−62.44	Yes		
309.004−0.089	206.03	−62.34	Yes		
309.013−0.732	206.34	−62.97	Yes		
309.014−0.415	206.20	−62.66	Yes		
309.019−0.270	206.14	−62.51	Yes		
309.028−0.412	206.22	−62.65	Yes		
309.045−0.044	206.10	−62.29	Yes		
309.045−0.178	206.16	−62.42	Yes		
309.046−0.139	206.14	−62.38			No distinct core
309.058−0.027	206.12	−62.27	No	Yes	
309.068−0.244	206.23	−62.48	Yes		
309.079−0.208	206.24	−62.44	No	No	
309.085−0.146	206.23	−62.38	Yes		
309.101−0.074	206.23	−62.30	Yes		
309.111−0.298	206.35	−62.52	No	No	
309.117−0.484	206.45	−62.70	Yes		
309.124−0.993	206.70	−63.20	Yes		
309.124+0.112	206.20	−62.12	No	Yes	
309.129−0.144	206.32	−62.37	Yes		
309.131−0.191	206.34	−62.41	Yes		
309.136−0.165	206.34	−62.39	Yes		
309.146−0.491	206.51	−62.70	Yes		

continued on next page

IRDC Name	Right Ascension 2000.0 (°)	Declination 2000.0 (°)	8 μm source?	24 μm source?	Additional comments
309.154−0.550	206.56	−62.76	Yes		
309.154+0.122	206.25	−62.10	No	Yes	
309.157−0.345	206.47	−62.56	Yes		
309.160−0.223	206.42	−62.44	Yes		
309.171−0.147	206.41	−62.36	Yes		
309.178−0.552	206.61	−62.76	Yes		
309.219−0.654	206.74	−62.85			No distinct core
309.222−0.545	206.70	−62.74	Yes		
309.238−0.228	206.59	−62.43	Yes		
309.242−0.214	206.59	−62.41	Yes		
309.242+0.951	206.08	−61.27	No	No	Confused at 500 μm
309.254−0.620	206.80	−62.81			No distinct core
309.267−0.557	206.80	−62.74	No	Yes	
309.292−0.197	206.69	−62.38	Yes		
309.304−0.578	206.89	−62.75	No	Yes	
309.306−0.615	206.91	−62.79	Yes		
309.308−0.213	206.73	−62.40	Yes		
309.311−0.513	206.87	−62.69	Yes		
309.334−0.643	206.98	−62.81	Yes		
309.346−0.706	207.04	−62.87			No distinct core
309.362−0.628	207.04	−62.79	Yes		
309.374−0.093	206.81	−62.27	Yes		
309.374−0.622	207.06	−62.78	Yes		
309.392−0.410	207.00	−62.57	Yes		
309.401+0.465	206.61	−61.71	Yes		
309.409−0.574	207.11	−62.73	No	Yes	
309.418+0.973	206.43	−61.21			No distinct core
309.420−0.641	207.17	−62.79			No distinct core
309.434−0.661	207.21	−62.81			No distinct core
309.440−0.566	207.17	−62.71	Yes		

continued on next page

IRDC Name	Right Ascension 2000.0 (°)	Declination 2000.0 (°)	8 μm source?	24 μm source?	Additional comments
309.444−0.741	207.27	−62.88	Yes		
309.452−0.345	207.09	−62.49	Yes		
309.488−0.679	207.33	−62.81	Yes		
309.509−0.650	207.36	−62.78	Yes		
309.651+0.080	207.31	−62.04	Yes		
309.666−0.749	207.74	−62.84	No	No	Confused at 500 μm
309.671−0.829	207.80	−62.92	Yes		
309.759−0.438	207.79	−62.52	Yes		
309.759−0.471	207.80	−62.55	Yes		
309.781+0.381	207.44	−61.71	Yes		
309.894+0.647	207.54	−61.43	Yes		
309.903+0.230	207.76	−61.83	Yes		
309.915+0.323	207.74	−61.74	Yes		
309.916+0.493	207.66	−61.57	Yes		
309.950+0.391	207.78	−61.66	Yes		
309.967+0.595	207.71	−61.46	Yes		
309.975+0.301	207.87	−61.75	Yes		
309.990+0.435	207.84	−61.61	Yes		
309.994−0.230	208.18	−62.26	No	Yes	
310.013+0.485	207.86	−61.56	Yes		
310.024+0.302	207.97	−61.73			No distinct core
310.037−0.587	208.45	−62.60	Yes		
310.064−0.235	208.32	−62.25	No	Yes	
310.069+0.393	208.02	−61.63	Yes		
310.080+0.296	208.09	−61.73	Yes		
310.087+0.712	207.90	−61.32	Yes		
310.089+0.303	208.11	−61.72	Yes		
310.090−0.283	208.40	−62.29	Yes		
310.091−0.268	208.40	−62.27	Yes		
310.103+0.714	207.93	−61.31			No distinct core

continued on next page

IRDC Name	Right Ascension 2000.0 (°)	Declination 2000.0 (°)	8 μm source?	24 μm source?	Additional comments
310.132+0.379	208.16	−61.63	Yes		
310.136+0.399	208.15	−61.61			No distinct core
310.148+0.368	208.19	−61.64	Yes		
310.159+0.703	208.05	−61.31	Yes		
310.166+0.697	208.07	−61.32	Yes		
310.173+0.519	208.17	−61.49			No distinct core
310.173+0.719	208.07	−61.29	Yes		
310.183+0.469	208.22	−61.53	Yes		
310.193+0.414	208.26	−61.59	Yes		
310.198+0.320	208.32	−61.68	Yes		
310.199+0.430	208.27	−61.57	Yes		
310.209+0.042	208.48	−61.94	No	Yes	
310.221−0.586	208.83	−62.55	No	No	Confused at 500 μm
310.222+0.076	208.49	−61.91	No	Yes	
310.228+0.234	208.42	−61.75	Yes		
310.229+0.275	208.41	−61.71	No	No	Confused at 500 μm
310.231+0.381	208.36	−61.61	Yes		
310.243+0.403	208.37	−61.58			No distinct core
310.246+0.493	208.33	−61.50			No distinct core
310.248+0.473	208.35	−61.51	Yes		
310.297+0.705	208.33	−61.28	No	No	
310.319−0.546	209.02	−62.49	No	No	Confused at 500 μm
310.327−0.279	208.89	−62.23	Yes		
310.350−0.506	209.06	−62.44	Yes		
310.355−0.548	209.10	−62.48			No distinct core
310.362−0.563	209.12	−62.49			No distinct core
310.364−0.578	209.13	−62.51	Yes		
310.398−0.289	209.05	−62.22	No	Yes	
310.417+0.108	208.88	−61.83			No distinct core
310.474−0.460	209.30	−62.37	Yes		

continued on next page

IRDC Name	Right Ascension 2000.0 (°)	Declination 2000.0 (°)	8 μm source?	24 μm source?	Additional comments
310.482−0.095	209.12	−62.01	No	Yes	
310.495−0.515	209.37	−62.41	Yes		
310.523−0.036	209.17	−61.94	Yes		
310.526−0.066	209.19	−61.97	Yes		
310.542−0.480	209.45	−62.37	No	Yes	
310.581−0.070	209.31	−61.96	No	Yes	
310.598+0.725	208.93	−61.19	Yes		
310.600+0.688	208.95	−61.22	Yes		
310.601−0.599	209.64	−62.47			No distinct core
310.604+0.591	209.01	−61.31			No distinct core
310.613−0.613	209.67	−62.48	Yes		
310.613+0.765	208.94	−61.14			No distinct core
310.619−0.083	209.40	−61.96	Yes		
310.681+0.484	209.22	−61.40	Yes		
310.686+0.466	209.24	−61.42	Yes		
310.696+0.017	209.50	−61.85	Yes		
310.717−0.547	209.85	−62.39	Yes		
310.822+0.770	209.35	−61.09	Yes		
310.868+0.472	209.60	−61.36	Yes		
310.948+0.723	209.63	−61.10	Yes		
310.952−0.691	210.43	−62.46	Yes		
310.974+1.010	209.53	−60.82			No distinct core
310.982−0.243	210.23	−62.02	No	Yes	
311.000+0.738	209.73	−61.07	Yes		
311.016+0.434	209.92	−61.36	Yes		
311.020−0.326	210.35	−62.09	Yes		
311.021+0.467	209.91	−61.33	No	Yes	
311.024+0.895	209.69	−60.91	Yes		
311.033−0.291	210.36	−62.06	No	Yes	
311.042+0.689	209.84	−61.11	Yes		

continued on next page

IRDC Name	Right Ascension 2000.0 (°)	Declination 2000.0 (°)	8 μm source?	24 μm source?	Additional comments
311.046+0.420	209.99	−61.37	Yes		
311.051+0.392	210.02	−61.39	No	Yes	
311.051+0.792	209.80	−61.01			No distinct core
311.055+0.859	209.77	−60.94	Yes		
311.061+0.425	210.02	−61.36			No distinct core
311.065+0.696	209.88	−61.10	No	Yes	
311.065+0.816	209.81	−60.98	Yes		
311.086+0.370	210.10	−61.40	No	Yes	
311.088+0.403	210.08	−61.37	No	Yes	
311.094+0.733	209.92	−61.05	No	Yes	
311.107+0.411	210.12	−61.36	Yes		
311.131+0.790	209.96	−60.99	Yes		
311.167+1.000	209.92	−60.78	Yes		
311.178+0.155	210.40	−61.59	No	Yes	
311.181+0.785	210.06	−60.98	Yes		
311.191−0.586	210.86	−62.30	Yes		
311.202+0.722	210.14	−61.03	Yes		
311.209−0.605	210.91	−62.31	Yes		
311.246+0.023	210.62	−61.70	Yes		
311.285−0.113	210.78	−61.82			No distinct core
311.335−0.349	211.01	−62.03	Yes		
311.352+0.356	210.64	−61.35	Yes		
311.432−0.473	211.29	−62.12	Yes		
311.570−0.208	211.41	−61.83	No	Yes	
311.641−0.609	211.80	−62.19			No distinct core
311.670−0.687	211.91	−62.26	Yes		
311.670+0.278	211.32	−61.33	Yes		
311.721−0.335	211.79	−61.91			No distinct core
311.747−0.691	212.07	−62.24	No	Yes	
311.756−0.673	212.08	−62.22	No	No	Confused at 500 μm

continued on next page

IRDC Name	Right Ascension 2000.0 (°)	Declination 2000.0 (°)	8 μm source?	24 μm source?	Additional comments
311.801+0.029	211.73	−61.53			No distinct core
311.823−0.805	212.30	−62.33	No	No	Confused at 500 μm
311.825−0.738	212.26	−62.26	No	Yes	
311.832−0.761	212.29	−62.28	Yes		
311.835−0.699	212.25	−62.22			No distinct core
311.848−0.382	212.08	−61.92	Yes		
311.856+0.244	211.72	−61.31	Yes		
311.857−0.841	212.39	−62.35	No	No	Confused at 500 μm
311.875+0.026	211.88	−61.52	Yes		
311.893+0.375	211.71	−61.18			No distinct core
311.903−0.866	212.50	−62.36	Yes		
311.903+0.234	211.81	−61.31	Yes		
311.937+0.353	211.81	−61.19			No distinct core
311.943+0.137	211.95	−61.39	Yes		
311.992−0.544	212.48	−62.03	Yes		
311.995−0.168	212.24	−61.67	Yes		
312.012−0.590	212.55	−62.07	Yes		
312.022−0.219	212.33	−61.71	No	Yes	
312.028−0.553	212.56	−62.03	Yes		
312.034−0.739	212.69	−62.20			No distinct core
312.045−0.467	212.53	−61.94	Yes		
312.046−0.576	212.61	−62.04			No distinct core
312.050−0.564	212.61	−62.03			No distinct core
312.063−0.529	212.61	−61.99	Yes		
312.068−0.529	212.62	−61.99	Yes		
312.070−0.468	212.59	−61.93			No distinct core
312.088−0.525	212.66	−61.98	No	No	Confused at 500 μm
312.089−0.619	212.72	−62.07	No	Yes	
312.103−0.523	212.69	−61.97			No distinct core
312.116−0.625	212.78	−62.07	No	No	Confused at 500 μm

continued on next page

IRDC Name	Right Ascension 2000.0 (°)	Declination 2000.0 (°)	8 μm source?	24 μm source?	Additional comments
312.122−0.040	212.42	−61.51	Yes		
312.126−0.765	212.89	−62.20	Yes		
312.165−0.205	212.61	−61.65	Yes		
312.168−0.077	212.54	−61.53	Yes		
312.174−0.032	212.52	−61.48	Yes		
312.197−0.156	212.64	−61.60	Yes		
312.214+0.740	212.12	−60.73	Yes		
312.216−0.857	213.14	−62.26			No distinct core
312.232−0.103	212.68	−61.54	Yes		
312.235−0.788	213.13	−62.19	Yes		
312.248+0.040	212.62	−61.39	Yes		
312.266+0.759	212.21	−60.70	Yes		
312.267+0.049	212.65	−61.38	Yes		
312.276−0.802	213.22	−62.19			No distinct core
312.295+0.089	212.68	−61.33	Yes		
312.295+0.737	212.28	−60.71	No	No	Confused at 500 μm
312.332−0.086	212.87	−61.49	Yes		
312.356−0.029	212.88	−61.43	Yes		
312.358−0.285	213.05	−61.67	Yes		
312.376−0.123	212.98	−61.51			No distinct core
312.377−0.301	213.10	−61.68	No	Yes	
312.380−0.309	213.11	−61.69	Yes		
312.385−0.104	212.99	−61.49			No distinct core
312.393−0.333	213.15	−61.71	Yes		
312.396−0.487	213.26	−61.85	Yes		
312.397+0.934	212.36	−60.50	No	No	Confused at 500 μm
312.476−0.053	213.14	−61.41	Yes		
312.505−0.361	213.39	−61.70	Yes		
312.508+0.008	213.16	−61.34			No distinct core
312.513−0.017	213.19	−61.37	Yes		

continued on next page

IRDC Name	Right Ascension 2000.0 (°)	Declination 2000.0 (°)	8 μm source?	24 μm source?	Additional comments
313.560+0.149	215.12	−60.87	No	Yes	
313.613−0.188	215.46	−61.17	Yes		
313.627−0.212	215.51	−61.19	No	Yes	
313.629−0.073	215.41	−61.06	Yes		
313.630+0.267	215.18	−60.74			No distinct core
313.637−0.359	215.63	−61.32	No	No	Confused at 500 μm
313.637−0.803	215.96	−61.74	Yes		
313.693−0.155	215.60	−61.11			No distinct core
313.701−0.531	215.88	−61.46	No	Yes	
313.726−0.310	215.77	−61.25	No	Yes	
313.738−0.108	215.65	−61.05	Yes		
313.744+0.391	215.31	−60.58	Yes		
313.753−0.085	215.66	−61.03			No distinct core
313.759−0.127	215.71	−61.06	Yes		
313.760+0.366	215.36	−60.60	No	No	Confused at 500 μm
313.765−0.496	215.98	−61.41	Yes		
313.765+0.230	215.46	−60.73	No	No	Confused at 500 μm
313.768+0.211	215.48	−60.74	No	Yes	
313.773+0.254	215.46	−60.70	Yes		
313.778−0.185	215.78	−61.11	Yes		
313.778−0.327	215.89	−61.24	Yes		
313.782+0.208	215.51	−60.74			No distinct core
313.783−0.170	215.78	−61.10			No distinct core
313.790−0.194	215.81	−61.12	Yes		
313.798+0.049	215.66	−60.88	Yes		
313.800+0.202	215.55	−60.74	Yes		
313.806−0.247	215.88	−61.16	Yes		
313.809−0.278	215.91	−61.19	Yes		
313.815+0.359	215.47	−60.59	No	No	Confused at 500 μm
313.817−0.271	215.92	−61.18			No distinct core

continued on next page

IRDC Name	Right Ascension 2000.0 (°)	Declination 2000.0 (°)	8 μm source?	24 μm source?	Additional comments
313.826−0.293	215.95	−61.20	Yes		
313.828+0.684	215.27	−60.28	Yes		
313.845+0.188	215.65	−60.74	Yes		
313.852−0.226	215.96	−61.12	No	Yes	
313.872+0.052	215.79	−60.86	No	No	Confused at 160 μm
313.887+0.151	215.75	−60.76	Yes		
313.935−0.033	215.98	−60.91	No	Yes	
313.938+0.064	215.91	−60.82	Yes		
313.946−0.016	215.99	−60.89	No	Yes	
313.986+0.037	216.03	−60.83	Yes		
313.994−0.234	216.24	−61.08	Yes		
314.083−0.461	216.58	−61.26	Yes		
314.087−0.113	216.33	−60.94	Yes		
314.087+0.372	215.98	−60.48			No distinct core
314.128−0.068	216.38	−60.88	Yes		
314.146−0.085	216.42	−60.89	Yes		
314.175−0.073	216.47	−60.87	Yes		
314.214−0.309	216.72	−61.07	Yes		
314.271+0.925	215.94	−59.90	No	No	Confused at 500 μm
314.282+0.055	216.58	−60.71	No	Yes	
314.296+0.035	216.62	−60.72	Yes		
314.315−0.047	216.72	−60.79	No	No	Confused at 500 μm
314.324−0.393	216.99	−61.11			No distinct core
314.325−0.177	216.83	−60.91	Yes		
314.327−0.044	216.74	−60.79	No	Yes	
314.327+0.028	216.69	−60.72			No distinct core
314.340+0.021	216.71	−60.72			No distinct core
314.350−0.025	216.77	−60.76	Yes		
314.372+0.933	216.12	−59.85	No	No	Confused at 500 μm
314.373+0.096	216.72	−60.64	Yes		

continued on next page

IRDC Name	Right Ascension 2000.0 (°)	Declination 2000.0 (°)	8 μm source?	24 μm source?	Additional comments
314.382−0.084	216.87	−60.80	Yes		
314.383+0.942	216.14	−59.84	No	No	Confused at 500 μm
314.392+0.069	216.78	−60.66			No distinct core
314.393+0.112	216.75	−60.61	Yes		
314.397−0.023	216.86	−60.74	No	Yes	
314.400−0.039	216.88	−60.75	Yes		
314.400−0.071	216.90	−60.78	Yes		
314.402+0.049	216.81	−60.67	No	Yes	
314.406−0.016	216.87	−60.73	Yes		
314.412+0.138	216.77	−60.58	Yes		
314.430+0.008	216.90	−60.70	No	Yes	
314.432+0.153	216.79	−60.56	Yes		
314.436−0.013	216.92	−60.72	No	No	Confused at 500 μm
314.461−0.030	216.98	−60.72	Yes		
314.563+0.185	217.02	−60.49	Yes		
314.582+0.703	216.68	−60.00	No	No	Confused at 500 μm
314.592−0.294	217.43	−60.92	No	No	Confused at 500 μm
314.597−0.316	217.46	−60.94	No	No	Confused at 500 μm
314.603−0.011	217.24	−60.65	Yes		
314.612−0.326	217.49	−60.94	Yes		
314.629+0.068	217.23	−60.57	No	No	Confused at 500 μm
314.631−0.327	217.53	−60.94	Yes		
314.634+0.150	217.18	−60.49	Yes		
314.639−0.308	217.53	−60.92			No distinct core
314.644+0.085	217.24	−60.55	Yes		
314.649−0.292	217.54	−60.90	Yes		
314.663+0.221	217.18	−60.42	Yes		
314.673−0.292	217.59	−60.89	Yes		
314.697−0.308	217.64	−60.90	Yes		
314.701+0.183	217.28	−60.44	No	No	

continued on next page

IRDC Name	Right Ascension 2000.0 (°)	Declination 2000.0 (°)	8 μm source?	24 μm source?	Additional comments
314.710+0.201	217.28	−60.42			No distinct core
314.713−0.313	217.68	−60.89	Yes		
314.720+0.243	217.27	−60.37			No distinct core
314.723−0.292	217.68	−60.87	Yes		
314.730−0.064	217.52	−60.66	Yes		
314.737−0.277	217.70	−60.85	No	No	Confused at 500 μm
314.738−0.322	217.73	−60.89	Yes		
314.742−0.186	217.64	−60.76			No distinct core
314.746−0.171	217.63	−60.75	Yes		
314.755−0.373	217.81	−60.93			No distinct core
314.756−0.382	217.81	−60.94			No distinct core
314.758−0.350	217.79	−60.91			No distinct core
314.760−0.368	217.81	−60.93			No distinct core
314.760+0.216	217.37	−60.38	Yes		
314.763−0.028	217.56	−60.61	No	No	Confused at 500 μm
314.768−0.333	217.80	−60.89	No	No	Confused at 160 μm
314.770+0.212	217.39	−60.38	No	No	Confused at 500 μm
314.777−0.055	217.60	−60.63			No distinct core
314.784−0.358	217.85	−60.91	Yes		
314.800−0.080	217.66	−60.65	Yes		
314.801+0.088	217.54	−60.49			No distinct core
314.806−0.172	217.75	−60.73	No	Yes	
314.808−0.643	218.12	−61.16	Yes		
314.828−0.188	217.80	−60.73			No distinct core
314.848−0.388	217.99	−60.91	Yes		
314.869+0.093	217.66	−60.46	No	No	Confused at 500 μm
314.878−0.143	217.86	−60.67	Yes		
314.889−0.149	217.89	−60.68			No distinct core
314.901−0.298	218.02	−60.81	Yes		
314.911−0.292	218.04	−60.80			No distinct core

continued on next page

IRDC Name	Right Ascension 2000.0 (°)	Declination 2000.0 (°)	8 μm source?	24 μm source?	Additional comments
314.916−0.622	218.31	−61.10	Yes		
314.935+0.542	217.45	−60.02	No	No	Confused at 500 μm
314.942−0.508	218.27	−60.99	Yes		
314.942−0.605	218.34	−61.08	No	No	Confused at 500 μm
314.954+0.539	217.49	−60.01	Yes		
314.963−0.187	218.06	−60.68			No distinct core
314.970−0.214	218.09	−60.71			No distinct core
314.970−0.324	218.18	−60.81			No distinct core
314.978+0.038	217.91	−60.47	No	Yes	
314.988−0.232	218.14	−60.72	Yes		
315.005−0.076	218.05	−60.56	No	Yes	
315.010−0.139	218.11	−60.62	Yes		
315.015+0.046	217.97	−60.45	No	Yes	
315.016−0.158	218.13	−60.64	Yes		
315.017+0.028	217.99	−60.46			No distinct core
315.036+0.200	217.9	−60.30	Yes		
315.039−0.173	218.19	−60.64			No distinct core
315.049+0.181	217.93	−60.31	Yes		
315.150−0.319	218.51	−60.73	No	No	Confused at 500 μm
315.151−0.328	218.52	−60.74	Yes		
315.214−0.291	218.61	−60.68	Yes		
315.518−0.920	219.70	−61.14	Yes		
315.686−0.598	219.75	−60.78	Yes		
315.696−0.555	219.73	−60.74	No	No	Confused at 500 μm
315.933−0.659	220.26	−60.73	No	No	Confused at 500 μm
315.967−0.606	220.28	−60.67			No distinct core
315.971−0.599	220.28	−60.66			No distinct core
315.997−0.590	220.32	−60.65	Yes		
316.003−0.769	220.48	−60.81			No distinct core
316.013−0.673	220.42	−60.71			No distinct core

continued on next page

IRDC Name	Right Ascension 2000.0 (°)	Declination 2000.0 (°)	8 μm source?	24 μm source?	Additional comments
316.040−0.618	220.42	−60.65	No	No	Confused at 500 μm
316.293−0.364	220.68	−60.32	Yes		
316.306−0.330	220.67	−60.28	No	No	Confused at 500 μm
316.313−0.350	220.70	−60.30			No distinct core
316.320−0.391	220.75	−60.33	Yes		
316.347−0.545	220.93	−60.46	Yes		
316.389−0.470	220.94	−60.37	Yes		
316.402−0.463	220.96	−60.36	Yes		
316.402−0.675	221.14	−60.55	No	No	Confused at 500 μm
316.416−0.455	220.98	−60.35	Yes		
316.424−0.478	221.01	−60.37	No	Yes	
316.424−0.633	221.15	−60.51	No	No	Confused at 500 μm
316.429−0.492	221.04	−60.38			No distinct core
316.468−0.730	221.31	−60.58			No distinct core
316.471−0.271	220.92	−60.16	Yes		
316.473−0.517	221.14	−60.38			No distinct core
316.482−0.230	220.91	−60.12	No	Yes	
316.483+0.273	220.50	−59.66	No	No	Confused at 500 μm
316.506+0.274	220.54	−59.65	No	No	Confused at 500 μm
316.513−0.223	220.96	−60.10	Yes		
316.526−0.252	221.01	−60.12	Yes		
316.536+0.059	220.77	−59.83	Yes		
316.553+0.045	220.81	−59.84	Yes		
316.575+0.067	220.83	−59.81	No	Yes	
316.579−0.217	221.08	−60.06	Yes		
316.591+0.068	220.86	−59.80			No distinct core
316.634−0.432	221.36	−60.24	Yes		
316.640−0.408	221.35	−60.21	Yes		
316.647−0.367	221.33	−60.17			No distinct core
316.656−0.268	221.26	−60.08	No	Yes	

continued on next page

IRDC Name	Right Ascension 2000.0 (°)	Declination 2000.0 (°)	8 μm source?	24 μm source?	Additional comments
316.724+0.130	221.05	−59.69	No	Yes	
316.804+0.144	221.18	−59.64			Stripy at 250 μm
316.828+0.100	221.26	−59.67	Yes		
316.902+0.174	221.33	−59.57	No	Yes	
316.903+0.459	221.09	−59.31	No	Yes	
316.920+0.228	221.32	−59.52			No distinct core
316.944−0.014	221.56	−59.73	Yes		
316.950+0.131	221.45	−59.59			No distinct core
317.048+0.432	221.37	−59.28			No distinct core
317.074−0.087	221.86	−59.74			Stripy at 250 μm
317.397+0.198	222.19	−59.34	No	Yes	
317.400−0.161	222.50	−59.66	Yes		
317.430−0.371	222.74	−59.84	No	Yes	
317.445−0.059	222.49	−59.55	No	Yes	
317.452−0.026	222.48	−59.52	No	Yes	
317.461−0.948	223.31	−60.34	No	No	Confused at 500 μm
317.470−0.211	222.67	−59.67	Yes		
317.480−0.684	223.11	−60.09			No distinct core
317.562+0.099	222.56	−59.35	No	Yes	
317.564−0.094	222.74	−59.53	Yes		
317.574−0.824	223.41	−60.18			No distinct core
317.580−0.098	222.77	−59.52	Yes		
317.591−0.835	223.44	−60.18			No distinct core
317.596−0.837	223.46	−60.18			No distinct core
317.614+0.072	222.68	−59.36	No	No	Confused at 500 μm
317.628−0.820	223.50	−60.15			No distinct core
317.649+0.012	222.79	−59.39	No	Yes	
317.657+0.105	222.73	−59.31			No distinct core
317.742+0.120	222.86	−59.26	No	No	Confused at 500 μm
317.783−0.078	223.11	−59.42	Yes		

continued on next page

IRDC Name	Right Ascension 2000.0 (°)	Declination 2000.0 (°)	8 μm source?	24 μm source?	Additional comments
317.849+0.485	222.73	−58.88	Yes		
317.866−0.306	223.46	−59.58	Yes		
317.870−0.149	223.32	−59.44	Yes		
317.876−0.175	223.36	−59.46	No	No	Confused at 500 μm
317.910−0.007	223.27	−59.30	No	No	Confused at 500 μm
317.942+0.013	223.31	−59.26	No	No	Confused at 500 μm
318.014+0.052	223.40	−59.19	Yes		
318.015+0.064	223.39	−59.18	Yes		
318.039+0.158	223.35	−59.09			No distinct core
318.058+0.134	223.40	−59.10			No distinct core
318.063+0.174	223.37	−59.06	No	Yes	
318.080+0.114	223.46	−59.11			No distinct core
318.086+0.097	223.48	−59.12			No distinct core
318.103+0.107	223.50	−59.10	No	Yes	
318.133−0.664	224.25	−59.78	Yes		
318.157−0.335	223.99	−59.47	No	Yes	
318.187−0.358	224.07	−59.48	Yes		
318.199+0.076	223.70	−59.09			No distinct core
318.227+0.031	223.79	−59.12			No distinct core
318.228−0.739	224.49	−59.80	No	Yes	
318.306−0.131	224.07	−59.23	Yes		
318.306−0.732	224.62	−59.76	No	Yes	
318.343+0.309	223.74	−58.82	No	No	Confused at 500 μm
318.390−0.152	224.23	−59.21	Yes		
318.404+0.394	223.77	−58.71	Yes		
318.419−0.085	224.22	−59.13	Yes		
318.499−0.278	224.54	−59.27	Yes		
318.550−0.274	224.62	−59.24			No distinct core
318.553−0.165	224.53	−59.14	No	Yes	
318.563−0.174	224.55	−59.14			No distinct core

continued on next page

IRDC Name	Right Ascension 2000.0 (°)	Declination 2000.0 (°)	8 μm source?	24 μm source?	Additional comments
318.566−0.184	224.57	−59.15	No	No	Confused at 500 μm
318.573−0.173	224.57	−59.14			No distinct core
318.573+0.642	223.84	−58.41	No	No	
318.585−0.206	224.62	−59.16	Yes		
318.614+0.301	224.21	−58.70	No	No	Confused at 500 μm
318.617−0.342	224.80	−59.27	Yes		
318.655+0.666	223.96	−58.36	No	No	Confused at 500 μm
318.677+0.652	224.01	−58.36	No	No	Confused at 500 μm
318.688−0.783	225.33	−59.62			No distinct core
318.689−0.128	224.73	−59.04	Yes		
318.703+0.673	224.03	−58.33	Yes		
318.727−0.687	225.31	−59.52	Yes		
318.738−0.098	224.78	−58.99			No distinct core
318.755−0.011	224.73	−58.91	No	No	Confused at 500 μm
318.757−0.002	224.73	−58.90	Yes		
318.763−0.448	225.15	−59.29	No	Yes	
318.778−0.175	224.92	−59.04	Yes		
318.785−0.397	225.14	−59.24	Yes		
318.802+0.416	224.43	−58.51	No	No	
318.875−0.272	225.18	−59.08	No	Yes	
318.895−0.244	225.19	−59.05	No	No	Confused at 500 μm
318.907−0.239	225.20	−59.04	No	Yes	
318.916−0.284	225.26	−59.07	No	No	
318.932−0.266	225.27	−59.05	Yes		
318.937−0.043	225.07	−58.85			Stripy at 250 μm
318.997−0.224	225.34	−58.98	No	No	Confused at 500 μm
319.000+0.164	224.99	−58.64	Yes		
319.094−0.491	225.76	−59.17	No	No	Confused at 160 μm
319.263+0.851	224.81	−57.91			No distinct core
319.334+0.828	224.95	−57.90	Yes		

continued on next page

IRDC Name	Right Ascension 2000.0 (°)	Declination 2000.0 (°)	8 μm source?	24 μm source?	Additional comments
319.374+0.897	224.96	−57.82	No	Yes	
319.402+0.863	225.03	−57.83	No	No	Confused at 500 μm
319.420+0.824	225.10	−57.86	No	No	Confused at 500 μm
319.460+0.835	225.15	−57.83	Yes		
319.644+0.812	225.48	−57.76	Yes		
319.728−0.873	227.20	−59.19			No distinct core
319.740−0.874	227.22	−59.18	Yes		
319.821−0.388	226.89	−58.72	Yes		
319.828+0.670	225.91	−57.80	Yes		
319.904−0.256	226.90	−58.57	Yes		
319.988+0.101	226.70	−58.21	Yes		
319.998+0.706	226.15	−57.68			No distinct core
320.014+0.724	226.16	−57.66			No distinct core
320.022+0.709	226.19	−57.67	No	No	Confused at 500 μm
320.052+0.700	226.25	−57.66	No	No	Confused at 500 μm
320.074+0.683	226.30	−57.67	No	Yes	
320.146+0.077	226.98	−58.16	Yes		
320.234+0.331	226.89	−57.89	No	No	Confused at 500 μm
320.235+0.346	226.87	−57.88	No	Yes	
320.271+0.249	227.02	−57.95			No distinct core
320.271+0.293	226.98	−57.91	Yes		
320.284+0.270	227.03	−57.92			No distinct core
320.287−0.538	227.81	−58.62	Yes		
320.302+0.217	227.10	−57.96			No distinct core
320.304+0.398	226.94	−57.80			No distinct core
320.317−0.443	227.76	−58.52	Yes		
320.321+0.213	227.14	−57.95			No distinct core
320.328−0.430	227.77	−58.50	Yes		
320.328+0.585	226.80	−57.63	Yes		
320.338+0.907	226.52	−57.34	No	No	Confused at 500 μm

continued on next page

IRDC Name	Right Ascension 2000.0 (°)	Declination 2000.0 (°)	8 μm source?	24 μm source?	Additional comments
320.387+0.141	227.31	−57.98	No	Yes	
320.389+0.123	227.33	−58.00	Yes		
320.469−0.204	227.78	−58.24	Yes		
320.551−0.206	227.92	−58.20	No	No	Confused at 500 μm
320.565+0.429	227.33	−57.64	Yes		
320.574−0.187	227.93	−58.17	No	No	Confused at 500 μm
320.590+0.497	227.31	−57.57	No	No	Confused at 500 μm
320.605+0.458	227.37	−57.60	No	No	Confused at 500 μm
320.629−0.521	228.35	−58.43	Yes		
320.639+0.331	227.54	−57.69	Yes		
320.773−0.448	228.51	−58.29	No	No	Confused at 500 μm
320.786+0.697	227.43	−57.30	No	No	Confused at 160 μm
320.864−0.362	228.58	−58.17	No	Yes	
320.879−0.397	228.64	−58.19	Yes		
320.884−0.575	228.82	−58.34			No distinct core
320.993−0.196	228.62	−57.96	Yes		
321.011−0.477	228.93	−58.19	No	Yes	
321.213−0.593	229.37	−58.18			No distinct core
321.313+0.348	228.60	−57.33	No	No	Confused at 500 μm
321.322−0.372	229.32	−57.94	No	No	Confused at 500 μm
321.332+0.881	228.13	−56.86	Yes		
321.336−0.373	229.35	−57.93	No	No	Confused at 500 μm
321.336−0.393	229.37	−57.95	No	No	Confused at 500 μm
321.341−0.381	229.36	−57.94	No	No	Confused at 500 μm
321.356+0.142	228.87	−57.48			No distinct core
321.397+0.934	228.18	−56.78	No	No	Confused at 500 μm
321.409+0.515	228.60	−57.14	Yes		
321.429+0.107	229.02	−57.47			No distinct core
321.468+0.774	228.44	−56.88	Yes		
321.472+0.574	228.64	−57.05	No	No	Confused at 500 μm

continued on next page

IRDC Name	Right Ascension 2000.0 (°)	Declination 2000.0 (°)	8 μm source?	24 μm source?	Additional comments
321.557+0.029	229.30	−57.47	No	No	Confused at 500 μm
321.560+0.116	229.22	−57.40	No	No	Confused at 500 μm
321.617+0.055	229.37	−57.42	Yes		
321.619+0.103	229.33	−57.38	Yes		
321.642+0.078	229.39	−57.39	Yes		
321.659+0.049	229.44	−57.40			No distinct core
321.670−0.016	229.52	−57.45	No	No	Confused at 500 μm
321.672+0.092	229.42	−57.36	Yes		
321.678+0.965	228.59	−56.61	No	No	
321.680+0.082	229.44	−57.36			No distinct core
321.688−0.015	229.55	−57.44			No distinct core
321.697+0.048	229.50	−57.38			No distinct core
321.721−0.010	229.60	−57.42	Yes		
321.725+0.830	228.79	−56.70			No distinct core
321.729−0.007	229.61	−57.41			No distinct core
321.736+0.804	228.83	−56.72	No	No	Confused at 500 μm
321.740+0.830	228.81	−56.70	No	No	Confused at 500 μm
321.746−0.629	230.26	−57.93	No	No	Confused at 500 μm
321.753+0.669A	228.99	−56.83	Yes		
321.753+0.669B	228.99	−56.83	No	No	
321.758+0.033	229.61	−57.36	Yes		
321.766+0.777	228.90	−56.73	No	No	Confused at 500 μm
321.818−0.605	230.35	−57.87	Yes		
321.892−0.059	229.92	−57.37			No distinct core
321.898−0.012	229.88	−57.33	No	No	Confused at 500 μm
321.899−0.234	230.10	−57.51	Yes		
321.950−0.064	230.01	−57.34	Yes		
321.950−0.092	230.04	−57.37			No distinct core
322.012−0.112	230.16	−57.35			No distinct core
322.023+0.851	229.23	−56.53			No distinct core

continued on next page

IRDC Name	Right Ascension 2000.0 (°)	Declination 2000.0 (°)	8 μm source?	24 μm source?	Additional comments
322.027−0.256	230.32	−57.46	Yes		
322.063−0.077	230.20	−57.29	Yes		
322.084−0.061	230.22	−57.27	Yes		
322.334+0.561A	229.99	−56.61	Yes		
322.334+0.561B	229.99	−56.61	No	No	
322.413−0.565	231.24	−57.51			No distinct core
322.518+0.404	230.42	−56.64	Yes		
322.626+0.652	230.34	−56.37	Yes		
322.632+0.029	230.97	−56.89	No	No	Confused at 500 μm
322.659+0.053	230.99	−56.86	No	No	Confused at 500 μm
322.666−0.588	231.65	−57.39	No	No	
322.680+0.032	231.04	−56.86	No	No	Confused at 500 μm
322.686+0.208	230.87	−56.71	No	No	Confused at 500 μm
322.795−0.569	231.83	−57.30	Yes		
322.813+0.801	230.48	−56.15	Yes		
322.822−0.780	232.09	−57.46	No	No	Confused at 500 μm
322.895+0.277	231.12	−56.54	Yes		
322.901+0.236	231.17	−56.57			No distinct core
322.905+0.223	231.19	−56.58	No	No	Confused at 500 μm
322.914+0.321	231.11	−56.49	No	No	
322.984+0.211	231.32	−56.55	Yes		
323.116−0.652	232.41	−57.19	No	No	Confused at 500 μm
323.122+0.050	231.69	−56.60	Yes		
323.142+0.173	231.60	−56.49	No	No	Confused at 500 μm
323.204+0.063	231.80	−56.55			No distinct core
323.212+0.315	231.56	−56.34	No	No	Confused at 500 μm
323.230−0.398	232.32	−56.92			No distinct core
323.238−0.406	232.34	−56.92			No distinct core
323.261−0.011	231.97	−56.58	Yes		
323.312−0.392	232.44	−56.86	Yes		

continued on next page

IRDC Name	Right Ascension 2000.0 (°)	Declination 2000.0 (°)	8 μm source?	24 μm source?	Additional comments
323.325−0.375	232.44	−56.84	Yes		
323.338−0.053	232.12	−56.57	No	No	Confused at 500 μm
323.424−0.441	232.65	−56.84	Yes		
323.479+0.099	232.18	−56.36	Yes		
323.483+0.502	231.78	−56.03	No	No	Confused at 500 μm
323.507−0.466	232.80	−56.81	Yes		
323.546+0.065	232.31	−56.35	Yes		
323.547−0.411	232.81	−56.75	Yes		
323.573+0.256	232.16	−56.18	No	No	Confused at 500 μm
323.621+0.275	232.21	−56.14	No	No	Confused at 500 μm
323.824+0.208	232.58	−56.08	Yes		
323.839+0.487	232.32	−55.84			No distinct core
323.845+0.052	232.77	−56.20	Yes		
323.870−0.250	233.12	−56.43			Stripy at 250 μm
323.893−0.516	233.43	−56.63	Yes		
323.931−0.287	233.25	−56.42	Yes		
323.934+0.410	232.54	−55.85			No distinct core
323.987+0.423	232.60	−55.81	Yes		
324.005+0.633	232.42	−55.63	No	No	Confused at 500 μm
324.048−0.425	233.57	−56.47	No	No	Confused at 500 μm
324.056+0.561	232.56	−55.66	No	No	Confused at 500 μm
324.067−0.428	233.60	−56.46	No	Yes	
324.079+0.447	232.71	−55.74	Yes		
324.100−0.576	233.80	−56.56	Yes		
324.103+0.167	233.03	−55.95	Yes		
324.110−0.425	233.66	−56.43	No	No	Confused at 500 μm
324.243+0.095	233.31	−55.93	Yes		
324.320+0.526	232.98	−55.53	Yes		
324.330+0.514	233.01	−55.54	Yes		
324.338+0.511	233.02	−55.54			No distinct core

continued on next page

IRDC Name	Right Ascension 2000.0 (°)	Declination 2000.0 (°)	8 μm source?	24 μm source?	Additional comments
324.466−0.462	234.22	−56.25			No distinct core
325.027+0.306	234.22	−55.30	Yes		
325.129−0.038	234.72	−55.52	Yes		
325.312−0.261	235.22	−55.59			No distinct core
325.434+0.468	234.63	−54.93	No	No	Confused at 500 μm
325.529+0.209	235.03	−55.08	No	No	Confused at 500 μm
325.635+0.459	234.92	−54.82			No distinct core
325.660+0.326	235.09	−54.91	No	No	Confused at 500 μm
325.742+0.530	234.99	−54.70	Yes		
325.794−0.228	235.86	−55.27	Yes		
325.813+0.469	235.15	−54.71	No	Yes	
325.838−0.225	235.92	−55.24	Yes		
325.873+0.245	235.47	−54.85			No distinct core
325.884+0.229	235.50	−54.85	Yes		
325.885−0.153	235.91	−55.16	No	No	Confused at 500 μm
325.908−0.005	235.78	−55.03	Yes		
325.913−0.084	235.87	−55.09	No	No	Confused at 500 μm
325.940+0.068	235.75	−54.95	No	No	Confused at 500 μm
325.958+0.075	235.77	−54.93	No	Yes	
326.057−0.314	236.32	−55.18	No	Yes	
326.154−0.511	236.67	−55.28	No	Yes	
326.310+0.428	235.88	−54.44	Yes		
326.311+0.542	235.76	−54.35	No	Yes	
326.322+0.458	235.87	−54.41	No	No	Confused at 500 μm
326.334+0.439	235.90	−54.42	No	No	Confused at 500 μm
326.337+0.461	235.88	−54.40	No	No	Confused at 500 μm
326.352+0.458	235.91	−54.39			No distinct core
326.356+0.444	235.93	−54.40	Yes		
326.369−0.200	236.63	−54.90	Yes		
326.376+0.488	235.91	−54.35	No	Yes	

continued on next page

IRDC Name	Right Ascension 2000.0 (°)	Declination 2000.0 (°)	8 μm source?	24 μm source?	Additional comments
326.382+0.366	236.04	−54.44	Yes		
326.384−0.197	236.64	−54.89	Yes		
326.394+0.847	235.56	−54.05	No	Yes	
326.400+0.715	235.70	−54.16	Yes		
326.409+0.594	235.84	−54.25	No	No	Confused at 500 μm
326.413+0.394	236.06	−54.40	Yes		
326.416+0.042	236.43	−54.68	Yes		
326.424+0.499	235.96	−54.31	No	No	Confused at 500 μm
326.434−0.149	236.66	−54.82	Yes		
326.453+0.757	235.73	−54.09	Yes		
326.458−0.092	236.63	−54.76			No distinct core
326.466−0.507	237.09	−55.08	No	Yes	
326.478−0.132	236.70	−54.78	Yes		
326.485−0.172	236.75	−54.81	Yes		
326.490+0.629	235.92	−54.17	Yes		
326.491−0.158	236.75	−54.79	No	Yes	
326.495+0.581	235.97	−54.20	No	No	
326.496+0.355	236.21	−54.38	Yes		
326.501−0.489	237.12	−55.04	Yes		
326.503−0.127	236.73	−54.76			No distinct core
326.509−0.125	236.74	−54.75			No distinct core
326.521+0.582	236.01	−54.19	Yes		
326.526+0.529	236.07	−54.23	Yes		
326.529−0.787	237.48	−55.26	Yes		
326.532−0.751	237.45	−55.23	Yes		
326.537+0.931	235.67	−53.90	No	No	Confused at 500 μm
326.539+0.942	235.66	−53.89	No	No	Confused at 500 μm
326.546+0.938	235.67	−53.89			No distinct core
326.549−0.228	236.90	−54.81	Yes		
326.557+0.314	236.34	−54.38	Yes		

continued on next page

IRDC Name	Right Ascension 2000.0 (°)	Declination 2000.0 (°)	8 μm source?	24 μm source?	Additional comments
326.560+0.924	235.71	−53.89	No	No	Confused at 500 μm
326.560+0.947	235.68	−53.87			No distinct core
326.575+0.952	235.70	−53.86	No	No	Confused at 500 μm
326.579+0.945	235.71	−53.86			No distinct core
326.590+0.941	235.73	−53.86			No distinct core
326.596+0.957	235.72	−53.84	No	No	Confused at 500 μm
326.598+0.835	235.85	−53.94			No distinct core
326.598+0.939	235.74	−53.86	Yes		
326.611+0.811	235.89	−53.95	Yes		
326.618−0.209	236.98	−54.75	Yes		
326.620−0.143	236.91	−54.70	No	No	
326.622+0.372	236.36	−54.29	Yes		
326.622+0.919	235.80	−53.86			No distinct core
326.632+0.951	235.77	−53.83	No	No	
326.634+0.978	235.75	−53.80			No distinct core
326.635−0.507	237.32	−54.98			No distinct core
326.635+0.421	236.33	−54.25			No distinct core
326.637+0.700	236.04	−54.02	Yes		
326.641+0.941	235.80	−53.83	Yes		
326.642+0.966	235.77	−53.81			No distinct core
326.643+0.917	235.83	−53.85	No	No	Confused at 500 μm
326.648−0.129	236.93	−54.67	Yes		
326.664+0.342	236.45	−54.29	Yes		
326.666+0.711	236.07	−54.00	Yes		
326.667+0.878	235.90	−53.86	Yes		
326.668+0.035	236.78	−54.53	Yes		
326.673+0.068	236.75	−54.50	Yes		
326.673+0.300	236.51	−54.32	Yes		
326.677+0.892	235.90	−53.85	Yes		
326.686−0.321	237.19	−54.80			No distinct core

continued on next page

IRDC Name	Right Ascension 2000.0 (°)	Declination 2000.0 (°)	8 μm source?	24 μm source?	Additional comments
326.699+0.869	235.95	−53.85	No	No	Confused at 500 μm
326.701−0.194	237.07	−54.69			No distinct core
326.704+0.741	236.09	−53.95	No	Yes	
326.706+0.347	236.50	−54.26			No distinct core
326.706+0.875	235.95	−53.84			No distinct core
326.718−0.127	237.02	−54.63	Yes		
326.720+0.032	236.86	−54.50	Yes		
326.724+0.337	236.54	−54.26	Yes		
326.735−0.093	237.01	−54.59	Yes		
326.745−0.147	237.08	−54.63	Yes		
326.750+0.133	236.79	−54.40			No distinct core
326.758+0.213	236.72	−54.33	Yes		
326.759−0.100	237.05	−54.58	Yes		
326.760−0.169	237.13	−54.63	Yes		
326.763+0.864	236.04	−53.82	Yes		
326.783−0.707	237.74	−55.04	Yes		
326.786−0.757	237.80	−55.08	No	Yes	
326.787−0.357	237.37	−54.76	Yes		
326.787−0.399	237.41	−54.80	Yes		
326.795−0.045	237.04	−54.51			No distinct core
326.811+0.511	236.47	−54.07	Yes		
326.811+0.656	236.32	−53.95	No	No	
326.812+0.425	236.56	−54.13	Yes		
326.815−0.772	237.86	−55.07	Yes		
326.824+0.466	236.54	−54.09	Yes		
326.826−0.315	237.37	−54.71	Yes		
326.826−0.753	237.85	−55.05			No distinct core
326.826+0.510	236.49	−54.06			No distinct core
326.828+0.072	236.96	−54.40	No	Yes	
326.831+0.549	236.46	−54.02			Stripy at 250 μm

continued on next page

IRDC Name	Right Ascension 2000.0 (°)	Declination 2000.0 (°)	8 μm source?	24 μm source?	Additional comments
326.834+0.582	236.43	−54.00			Stripy at 250 μm
326.835−0.069	237.12	−54.51	Yes		
326.836+0.068	236.97	−54.40			No distinct core
326.850+0.641	236.39	−53.94	Yes		
326.851+0.521	236.52	−54.03	No	No	Confused at 500 μm
326.857−0.311	237.41	−54.68	Yes		
326.857+0.496	236.55	−54.05	Yes		
326.870+0.071	237.02	−54.38	Yes		
326.872+0.410	236.66	−54.11	No	No	Confused at 500 μm
326.875+0.704	236.36	−53.87	No	No	Confused at 500 μm
326.876+0.639	236.43	−53.93			No distinct core
326.877−0.214	237.33	−54.60	Yes		
326.884+0.448	236.64	−54.07	Yes		
326.885+0.142	236.96	−54.31			No distinct core
326.886+0.307	236.79	−54.18	Yes		
326.889+0.294	236.81	−54.19	No	Yes	
326.890−0.350	237.50	−54.69	Yes		
326.898+0.155	236.96	−54.29	Yes		
326.900+0.568	236.53	−53.97			Stripy at 250 μm
326.902+0.839	236.25	−53.75	No	No	Confused at 160 μm
326.908+0.457	236.66	−54.05	Yes		
326.910+0.561	236.55	−53.97			Stripy at 250 μm
326.911+0.442	236.68	−54.06	No	No	Confused at 500 μm
326.917−0.038	237.20	−54.43	No	Yes	
326.923+0.452	236.68	−54.04	No	No	Confused at 500 μm
326.924+0.716	236.41	−53.84	Yes		
326.926+0.736	236.39	−53.82	No	No	Confused at 500 μm
326.928+0.427	236.72	−54.06			No distinct core
326.929+0.538	236.60	−53.97	Yes		
326.938+0.561	236.59	−53.95			Stripy at 250 μm

continued on next page

IRDC Name	Right Ascension 2000.0 (°)	Declination 2000.0 (°)	8 μm source?	24 μm source?	Additional comments
326.944+0.350	236.82	−54.11			No distinct core
326.950−0.164	237.38	−54.51	Yes		
326.951+0.325	236.86	−54.13			No distinct core
326.952−0.003	237.21	−54.38	Yes		
326.956−0.007	237.22	−54.38	Yes		
326.956+0.497	236.68	−53.99	Yes		
326.956+0.517	236.66	−53.97	Yes		
326.959+0.463	236.72	−54.01	No	No	Confused at 500 μm
326.962+0.451	236.74	−54.02	Yes		
326.970−0.033	237.26	−54.40	Yes		
326.992+0.007	237.25	−54.35			No distinct core
326.995−0.183	237.46	−54.50	Yes		
327.002−0.174	237.46	−54.49	No	Yes	
327.004−0.079	237.36	−54.41	Yes		
327.010−0.032	237.32	−54.37	No	Yes	
327.019+0.008	237.29	−54.33	Yes		
327.021−0.162	237.47	−54.47	No	Yes	
327.023+0.477	236.79	−53.96	Yes		
327.025−0.045	237.35	−54.37	No	Yes	
327.027−0.296	237.62	−54.57	No	Yes	
327.034−0.110	237.43	−54.42	No	Yes	
327.043−0.290	237.64	−54.55	No	Yes	
327.044+0.019	237.31	−54.31	Yes		
327.049−0.302	237.66	−54.56	No	Yes	
327.069−0.288	237.67	−54.53	Yes		
327.074−0.012	237.38	−54.32	No	Yes	
327.076−0.104	237.48	−54.39	Yes		
327.086+0.007	237.38	−54.29	No	Yes	
327.090−0.250	237.66	−54.49	Yes		
327.093−0.350	237.77	−54.57	Yes		

continued on next page

IRDC Name	Right Ascension 2000.0 (°)	Declination 2000.0 (°)	8 μm source?	24 μm source?	Additional comments
327.098+0.234	237.15	−54.11	Yes		
327.112−0.291	237.73	−54.51	Yes		
327.123+0.723	236.67	−53.71	No	No	Confused at 500 μm
327.129−0.461	237.94	−54.63	No	Yes	
327.143−0.335	237.82	−54.52	Yes		
327.144−0.303	237.79	−54.50	Yes		
327.162−0.337	237.85	−54.51	Yes		
327.167−0.300	237.81	−54.48	Yes		
327.224+0.225	237.33	−54.04			No distinct core
327.237+0.231	237.34	−54.02	No	Yes	
327.238+0.241	237.33	−54.01			No distinct core
327.251−0.134	237.75	−54.30	Yes		
327.252−0.093	237.71	−54.27			No distinct core
327.277+0.224	237.40	−54.00	Yes		
327.391−0.387	238.21	−54.41	No	No	Confused at 500 μm
327.402−0.416	238.25	−54.42	No	Yes	
327.429−0.397	238.27	−54.39	Yes		
327.457−0.694	238.63	−54.60	Yes		
327.485+0.761	237.11	−53.45	Yes		
327.486−0.694	238.67	−54.58	Yes		
327.491−0.311	238.26	−54.29	Yes		
327.535−0.534	238.56	−54.43	No	Yes	
327.572+0.326	237.68	−53.74	Yes		
327.610+0.802	237.23	−53.34	Yes		
327.653−0.605	238.79	−54.41			No distinct core
327.659+0.609	237.50	−53.46			No distinct core
327.676−0.566	238.78	−54.36	Yes		
327.683−0.543	238.76	−54.34	Yes		
327.695−0.552	238.79	−54.34			No distinct core
327.723−0.535	238.81	−54.31	Yes		

continued on next page

IRDC Name	Right Ascension 2000.0 (°)	Declination 2000.0 (°)	8 μm source?	24 μm source?	Additional comments
327.725+0.894	237.28	−53.20	No	No	Confused at 500 μm
327.727−0.566	238.85	−54.33	Yes		
327.729−0.051	238.29	−53.93			No distinct core
327.746+0.925	237.28	−53.16	No	Yes	
327.753−0.090	238.37	−53.95	Yes		
327.763−0.513	238.84	−54.27			No distinct core
327.765−0.490	238.82	−54.25	No	Yes	
327.778−0.091	238.40	−53.93	Yes		
327.787−0.491	238.85	−54.24	Yes		
327.795−0.466	238.83	−54.21			No distinct core
327.804+0.064	238.26	−53.80	Yes		
327.808+0.495	237.81	−53.46	Yes		
327.811−0.288	238.66	−54.06	No	Yes	
327.815−0.560	238.96	−54.27	Yes		
327.815+0.488	237.83	−53.46	Yes		
327.816−0.451	238.84	−54.19	Yes		
327.848−0.479	238.91	−54.19			No distinct core
327.852+0.503	237.86	−53.43	Yes		
327.863+0.470	237.91	−53.44	Yes		
327.880−0.461	238.94	−54.15	Yes		
327.887−0.474	238.96	−54.16			No distinct core
327.893+0.435	237.99	−53.45	No	Yes	
327.914−0.611	239.14	−54.25	Yes		
327.917−0.397	238.91	−54.08			No distinct core
327.923+0.566	237.89	−53.33			No distinct core
327.924−0.536	239.07	−54.18			No distinct core
327.929+0.430	238.04	−53.43	No	Yes	
327.936+0.511	237.96	−53.37	No	No	Confused at 500 μm
327.937−0.538	239.09	−54.18			No distinct core
327.950−0.723	239.31	−54.31	Yes		

continued on next page

IRDC Name	Right Ascension 2000.0 (°)	Declination 2000.0 (°)	8 μm source?	24 μm source?	Additional comments
327.952+0.520	237.97	−53.35	Yes		
327.964+0.388	238.13	−53.44	Yes		
327.974+0.371	238.16	−53.45	Yes		
327.980−0.490	239.10	−54.11	Yes		
327.988−0.711	239.35	−54.27	No	Yes	
327.990+0.506	238.04	−53.34	Yes		
328.004−0.509	239.15	−54.11			No distinct core
328.007+0.416	238.15	−53.40	Yes		
328.022+0.382	238.21	−53.41			No distinct core
328.035+0.615	237.98	−53.22	Yes		
328.036+0.395	238.21	−53.39	Yes		
328.044−0.391	239.07	−53.99	No	Yes	
328.050−0.538	239.24	−54.10	Yes		
328.054−0.026	238.69	−53.71	Yes		
328.057−0.293	238.98	−53.91			No distinct core
328.061−0.278	238.97	−53.90			No distinct core
328.068−0.284	238.99	−53.90	No	Yes	
328.068+0.513	238.13	−53.28	Yes		
328.073−0.128	238.82	−53.77			No distinct core
328.077+0.528	238.13	−53.26			No distinct core
328.086−0.102	238.81	−53.75			No distinct core
328.088−0.321	239.05	−53.91	Yes		
328.094+0.567	238.11	−53.22			No distinct core
328.100−0.542	239.31	−54.07	No	Yes	
328.101+0.626	238.05	−53.17	Yes		
328.102+0.368	238.33	−53.37	Yes		
328.103−0.445	239.21	−54.00	Yes		
328.103+0.602	238.08	−53.19	No	Yes	
328.108−0.175	238.92	−53.79			No distinct core
328.108−0.383	239.15	−53.95	No	Yes	

continued on next page

IRDC Name	Right Ascension 2000.0 (°)	Declination 2000.0 (°)	8 μm source?	24 μm source?	Additional comments
328.119+0.358	238.36	−53.37	No	Yes	
328.163−0.282	239.11	−53.83	Yes		
328.167+0.021	238.78	−53.60			No distinct core
328.175+0.310	238.48	−53.37	Yes		
328.176−0.671	239.55	−54.12	Yes		
328.178+0.285	238.51	−53.39	No	Yes	
328.196−0.672	239.58	−54.11			Stripy at 250 μm
328.220−0.392	239.30	−53.88	Yes		
328.220+0.094	238.77	−53.51	Yes		
328.227−0.378	239.29	−53.87			No distinct core
328.232−0.367	239.29	−53.86	Yes		
328.251−0.301	239.24	−53.79			No distinct core
328.255−0.412	239.37	−53.87	Yes		
328.258−0.255	239.20	−53.75	Yes		
328.264−0.302	239.26	−53.78	Yes		
328.273−0.193	239.15	−53.70	Yes		
328.274+0.596	238.31	−53.09			No distinct core
328.282−0.046	239.01	−53.58	Yes		
328.303−0.106	239.10	−53.61	No	Yes	
328.303−0.302	239.31	−53.76	No	Yes	
328.3.4−0.012	239.00	−53.54	Yes		
328.309+0.237	238.74	−53.34			No distinct core
328.311−0.549	239.59	−53.94	Yes		
328.320−0.521	239.57	−53.92			No distinct core
328.348−0.246	239.31	−53.69	No	Yes	
328.386−0.308	239.43	−53.71	Yes		
328.397−0.336	239.47	−53.72	Yes		
328.400−0.495	239.65	−53.84			Stripy at 250 μm
328.406−0.085	239.21	−53.53	No	Yes	
328.409−0.109	239.24	−53.54	Yes		

continued on next page

IRDC Name	Right Ascension 2000.0 (°)	Declination 2000.0 (°)	8 μm source?	24 μm source?	Additional comments
328.424+0.070	239.06	−53.40	Yes		
328.432−0.522	239.72	−53.84	No	No	
328.433+0.594	238.51	−52.99	Yes		
328.514+0.276	238.96	−53.18			No distinct core
328.584+0.645	238.65	−52.85	No	No	Confused at 500 μm
328.624+0.274	239.10	−53.11	Yes		
328.641−0.303	239.75	−53.54			No distinct core
328.657−0.422	239.90	−53.62	Yes		
328.665+0.502	238.91	−52.91	Yes		
328.684+0.018	239.45	−53.27	Yes		
328.690−0.310	239.82	−53.51	Yes		
328.693+0.255	239.21	−53.08			No distinct core
328.741+0.614	238.89	−52.78	No	Yes	
328.755+0.606	238.91	−52.77	No	Yes	
328.762+0.354	239.19	−52.96	Yes		
328.765+0.716	238.81	−52.68	Yes		
328.768+0.664	238.87	−52.72	Yes		
328.771−0.570	240.21	−53.66			Stripy at 250 μm
328.816+0.745	238.84	−52.63			Stripy at 250 μm
328.822+0.468	239.15	−52.84			No distinct core
328.822+0.753	238.84	−52.62			Stripy at 250 μm
328.834+0.457	239.17	−52.84			No distinct core
328.854+0.752	238.88	−52.60			Stripy at 250 μm
328.859+0.277	239.40	−52.96	Yes		
328.865+0.752	238.90	−52.59			Stripy at 250 μm
328.869+0.257	239.43	−52.97	Yes		
328.899+0.750	238.94	−52.57	Yes		
328.904−0.101	239.86	−53.22			No distinct core
328.913−0.099	239.87	−53.21			No distinct core
328.923+0.284	239.47	−52.91	Yes		

continued on next page

IRDC Name	Right Ascension 2000.0 (°)	Declination 2000.0 (°)	8 μm source?	24 μm source?	Additional comments
328.947+0.369	239.41	−52.83	No	Yes	
328.951+0.816	238.94	−52.49	No	No	Confused at 500 μm
328.992+0.786	239.02	−52.48	No	No	Confused at 500 μm
329.021−0.166	240.08	−53.19			No distinct core
329.028−0.202	240.13	−53.21	Yes		
329.039−0.119	240.05	−53.14	Yes		
329.039−0.140	240.08	−53.16	No	Yes	
329.042−0.177	240.12	−53.18			No distinct core
329.042−0.281	240.23	−53.26	Yes		
329.058−0.289	240.26	−53.26	Yes		
329.067−0.112	240.08	−53.12			No distinct core
329.077+0.415	239.52	−52.71	No	Yes	
329.088−0.399	240.42	−53.32	Yes		
329.101−0.394	240.43	−53.31	Yes		
329.114−0.379	240.43	−53.29	No	No	Confused at 500 μm
329.169−0.745	240.91	−53.53	Yes		
329.178−0.602	240.76	−53.42	Yes		
329.179+0.446	239.62	−52.62	Yes		
329.201+0.559	239.53	−52.52	Yes		
329.208−0.742	240.95	−53.50			No distinct core
329.213−0.757	240.97	−53.51	Yes		
329.227+0.482	239.64	−52.56	Yes		
329.247−0.233	240.44	−53.09	No	Yes	
329.251−0.267	240.48	−53.12	No	No	Confused at 500 μm
329.265−0.339	240.58	−53.16			Stripy at 250 μm
329.276−0.258	240.50	−53.09	Yes		
329.278−0.341	240.60	−53.15			Stripy at 250 μm
329.313−0.302	240.60	−53.10	Yes		
329.374−0.284	240.65	−53.05	Yes		
329.389−0.659	241.09	−53.32	Yes		

continued on next page

IRDC Name	Right Ascension 2000.0 (°)	Declination 2000.0 (°)	8 μm source?	24 μm source?	Additional comments
329.403−0.736A	241.19	−53.37	Yes		
329.403−0.736B	241.19	−53.37	No	No	
329.413−0.226	240.64	−52.98	Yes		
329.424+0.475	239.89	−52.44	No	Yes	
329.437+0.853	239.51	−52.14	Yes		
329.441+0.518	239.87	−52.40	Yes		
329.444−0.765	241.27	−53.36	Yes		
329.463−0.770	241.30	−53.35	Yes		
329.463+0.517	239.90	−52.38	Yes		
329.489+0.404	240.05	−52.45	Yes		
329.494+0.106	240.38	−52.67	Yes		
329.557−0.362	240.97	−52.99	Yes		
329.568−0.354	240.97	−52.97	Yes		
329.568−0.392	241.01	−53.00	Yes		
329.589+0.045	240.56	−52.66	Yes		
329.621−0.407	241.10	−52.98			No distinct core
329.627+0.855	239.74	−52.02	No	No	Confused at 500 μm
329.633−0.387	241.09	−52.95	No	Yes	
329.638+0.836	239.78	−52.03	Yes		
329.642+0.908	239.70	−51.97	Yes		
329.648+0.857	239.76	−52.00	Yes		
329.648+0.957	239.66	−51.93	Yes		
329.652+0.073	240.61	−52.59	No	Yes	
329.655+0.852	239.78	−52.00			No distinct core
329.684+0.819	239.85	−52.01	Yes		
329.684+0.875	239.79	−51.97	No	No	Confused at 500 μm
329.691−0.353	241.12	−52.89			No distinct core
329.726+0.848	239.87	−51.96			No distinct core
329.745−0.038	240.85	−52.62	Yes		
329.748+0.855	239.89	−51.94	No	No	Confused at 500 μm

continued on next page

IRDC Name	Right Ascension 2000.0 (°)	Declination 2000.0 (°)	8 μm source?	24 μm source?	Additional comments
329.749+0.868	239.88	−51.93	No	Yes	
329.863+0.456	240.46	−52.17	Yes		
329.875+0.121	240.83	−52.41	Yes		
329.902+0.969	239.96	−51.75			No distinct core
329.904+0.417	240.55	−52.17	Yes		
329.938−0.113	241.16	−52.55	Yes		
329.989−0.396	241.54	−52.72	Yes		

4.4 The Sensitivity Limit of *Herschel*

1966 of the original 3171 *Spitzer*-dark candidate IRDCs were found to show no emission at 250, 350 or 500 μm. We assume this is because they are holes in the sky and there is no emission to detect. However, it is possible that some of these objects are genuine IRDCs but that *Herschel* does not detect the emission due to the sensitivity limits of the instruments.

To ascertain how many IRDCs may have been missed due to sensitivity limits we modelled several IRDCs and placed them in the Hi-GAL data in regions with differing backgrounds. The modelled IRDCs were observed in the same manner as the original candidates. The dimensions and flux levels of the smallest IRDC visible by *Herschel* were determined.

4.4.1 Creating the Model IRDCs

To model the IRDCs we used PHAETHON, as described in Chapter 3 (Stamatellos & Whitworth, 2003, 2005; Stamatellos et al., 2010). IRDCs were created with three different radii: 0.2, 0.4 and 0.7 pc. For each of the three radii two IRDCs were created: one with a peak column density of $2 \times 10^{22}\,\mathrm{cm}^{-2}$ (the detection threshold of PF09); and one with a peak column density of twice this value, $4 \times 10^{22}\,\mathrm{cm}^{-2}$. Using the mean parameters of the cores modelled in Chapter 5, we placed our model IRDCs at a distance of 3.1 kpc and used a surrounding ISRF of 3.2 times the Black (1994) radiation field. As most IRDCs do not appear spherical, they were modelled with a flattened geometry which has a density profile given by Equation 3.31. The asymmetry factor was set at 2.5 and corresponds to an aspect ratio of $\sim 1:3$. The radial density profile was taken to be a Plummer-like profile with R_0, the flattening radius, taken as one tenth of the maximum radius. The dust opacity at 500 μm was taken to be $0.03\,\mathrm{cm}^2\,\mathrm{g}^{-1}$ (Ossenkopf & Henning, 1994).

4.4.2 Placing IRDCs into Hi-GAL Observations

Each of the six IRDCs was convolved with the telescope beam at each wavelength and placed into the Hi-GAL data in four positions. The locations selected were typical areas within the Hi-GAL field. They did not contain any candidate IRDCs and were chosen to cover a range of different background levels. The background levels were measured using an elliptical aperture placed near each location but away from any point sources. The four locations were labelled Position A, Position B, Position C and Position D.

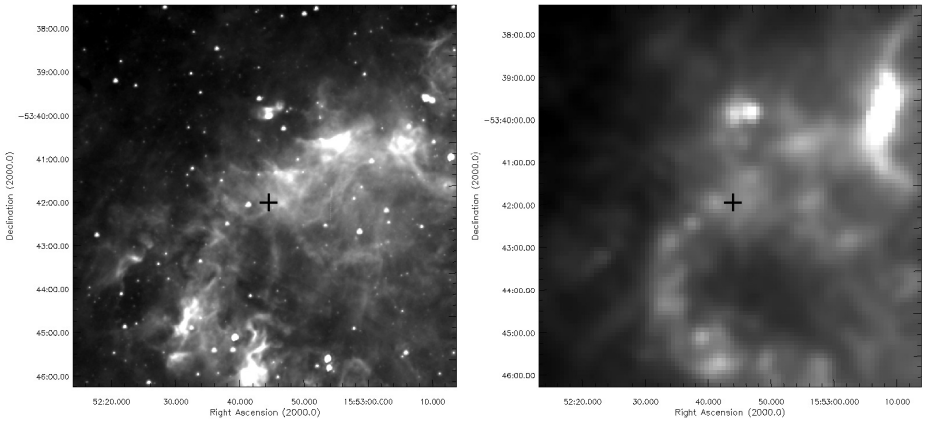

Figure 4.3: Position A, shown without the addition of any modelled IRDCs, at 8 μm (left) and 250 μm (right). A cross marks the point where the IRDCs are added.

4.4.2.1 Position A

Position A is located at $l = 327.829\,^{\circ}$, $b = +0.17\,^{\circ}$. The original 8 and 250 μm observations of the region are shown in Figure 4.3. A cross marks the exact location of Position A and shows where the modelled IRDCs were added to the data. Position A is a confused region near the centre of the Galactic Plane. We define a confused region as one with many nearby sources. All of the nearby sources seen in emission at 250 μm are also in emission at 8 μm and so none are thought to be IRDCs. Care was taken to select a point which did not lie on the peak of a source as this could result in confusion over whether the modelled IRDC was seen in emission or not. This area has the highest background level at 2600 MJy sr^{-1} at 250 μm

4.4.2.2 Position B

Position B is located at $l = 328.427\,^{\circ}$, $b = +0.04\,^{\circ}$. As with Position A this location is close to the centre of the Galactic Plane but, unlike Position A, Position B is

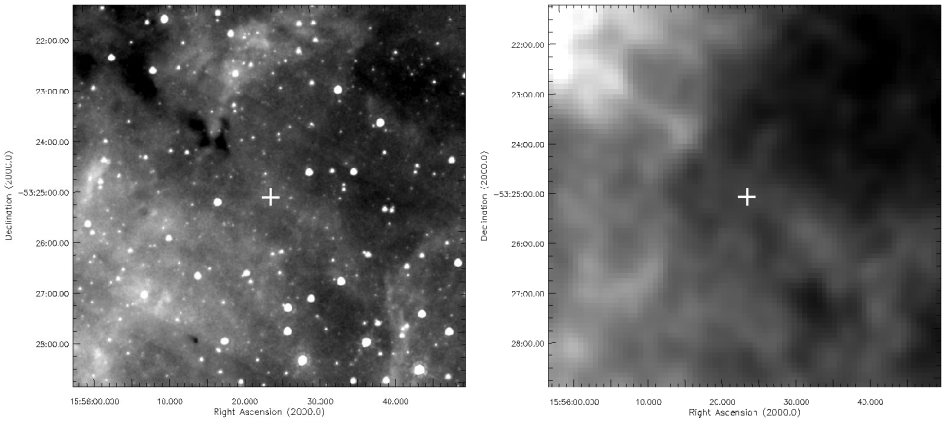

Figure 4.4: Position B, shown without the addition of any modelled IRDCs, at 8 μm (left) and 250 μm (right). A cross marks the point where the IRDCs are added.

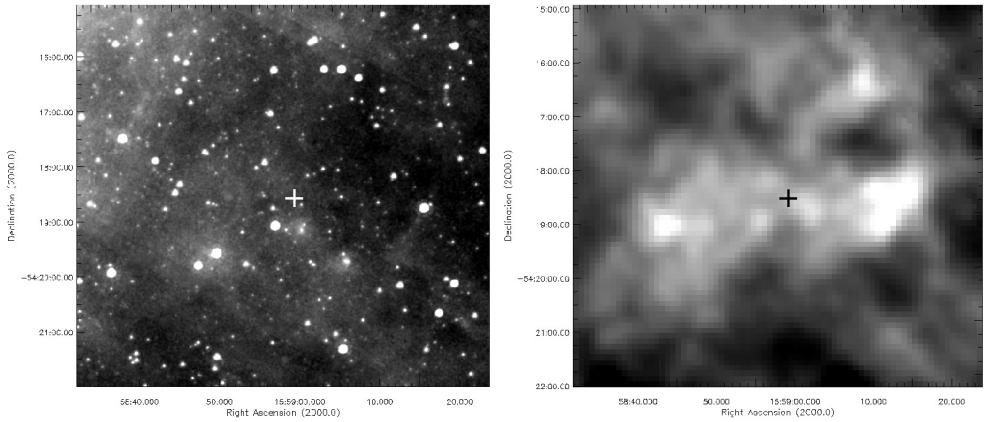

Figure 4.5: Position C, shown without the addition of any modelled IRDCs, at 8 μm (left) and 250 μm (right). A cross marks the point where the IRDCs are added.

an unconfused region. The unaltered observations of Position B can be seen in Figure 4.4. There is a high level of diffuse radiation, resulting in a background of 1300 MJy sr^{-1} at 250 μm, but no resolved sources in the immediate vicinity.

4.4.2.3 Position C

Position C can be seen in Figure 4.5, with a cross marking the location l = 328.141 °, b = −0.89 °. Unlike Positions A and B, Position C was chosen to be

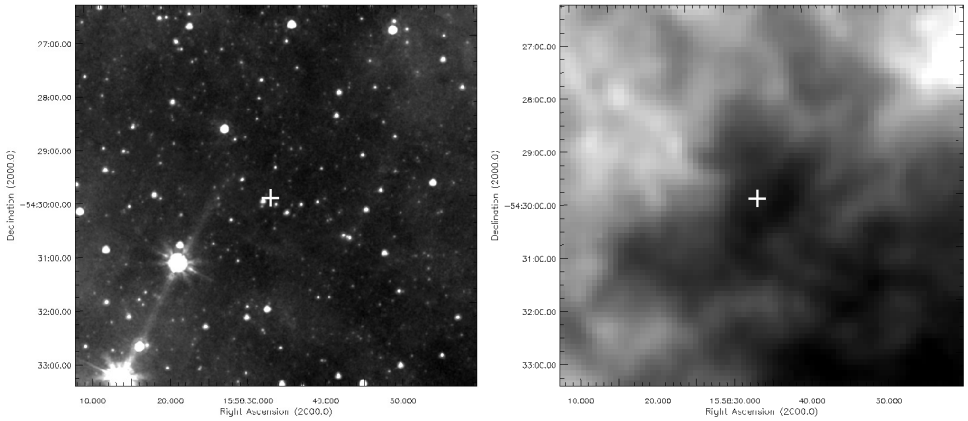

Figure 4.6: Position D, shown without the addition of any modelled IRDCs, at 8 μm (left) and 250 μm (right). A cross marks the point where the IRDCs are added.

towards the edge of the Hi-GAL data, as far from the Galactic Plane as possible. It therefore has a lower background than either A or B and was measured to be 450 MJy sr^{-1} at 250 μm. Position C is a confused area with many local point sources. As with Position A, none of these sources are thought to be IRDCs and Position C was chosen to be a point that did not coincide with the peak of any source.

4.4.2.4 Position D

The final location chosen to place our modelled IRDCs was $l = 327.973\,^{\circ}$, $b = -0.99\,^{\circ}$, Position D. Unaltered observations of Position D can be seen in Figure 4.6. This location was selected as it was far from the Galactic Plane, towards the edge of the Hi-GAL data and also because it showed a relatively unconfused region. Position D has the lowest background at 65MJy sr^{-1} at 250 μm.

4.4.3 Viewing the Model IRDCs

Synthetic observations were created of the six model IRDCs in each position at *Spitzer* 8 μm and *Herschel* 70, 160, 250, 350 and 500 μm. As with the original candidates, if the model IRDC was seen in emission at the three longest wavelengths it was then classed as *Spitzer*-dark and *Herschel*-bright and thus detectable by *Herschel*. If there was no clear emission at 250, 350 and 500 μm then it was classed as *Spitzer*-dark and *Herschel*-dark and so below the detection limit of *Herschel*. As PHAETHON only models the emission of the IRDC, the 8 and 70 μm maps with the added IRDCs appear no different from the original data and so the IRDCs are not necessarily *Spitzer*-dark.

The smallest modelled IRDC (0.2 pc, 2×10^{22} cm^{-2}) can clearly be seen in emission in Positions B, C and D but not in Position A. Figure 4.7 shows the IRDC at Position A. When compared with Figure 4.3, which shows the unaltered observations of Position A, all the original emission sources are still seen but there are no new sources. If the model IRDC was visible by *Herschel* we would expect a new source at the position marked by the cross. As no IRDC is visible we state that this IRDC is below the detection limits of *Herschel* at these background levels. Figures 4.8–4.10 show the model IRDC at Positions B, C and D respectively. In these images, when compared to the original observations shown in Figures 4.4–4.6, there is a new source at the point of the cross. This is our model IRDC. The model IRDC is therefore detectable by *Herschel* at these background levels. As this is the smallest and most diffuse cloud we model we assume all larger and denser IRDCs will also be visible in *Herschel* data at Positions B, C and D and in areas of their equivalent background levels.

A small amount of emission can be seen from the 0.2 pc IRDC with a peak

column density of $4\times10^{22}\,\mathrm{cm}^{-2}$ and the 0.4 pc, $2\times10^{22}\,\mathrm{cm}^{-2}$ IRDC (Figures 4.11 and 4.12, respectively) in Position A. However, it can not be stated with absolute certainty that these objects would have been classed as *Herschel*-bright. We conclude that these IRDCs are also below the sensitivity limit of *Herschel* at this background level.

The smallest IRDC that can clearly be seen in emission at Position A is 0.4 pc in radius with a peak column density of $4\times10^{22}\,\mathrm{cm}^{-2}$, shown in Figure 4.13. This IRDC is therefore above the sensitivity limit of *Herschel* at these background levels.

We therefore conclude that any IRDC whose major axis is $\leq 26''$ (corresponding to 0.4 pc at a distance of 3.1 kpc) with a peak column density less than $4\times10^{22}\,\mathrm{cm}^{-2}$ in an area where the background level is greater than $1300\,\mathrm{MJy\,sr}^{-1}$ at $250\,\mu$m is not likely to be found to be *Herschel*-bright, regardless of whether it is a genuine IRDC or not.

4.4.4 The Percentage of Undetectable IRDCs

We then attempted to estimate what percentage of the PF09 catalogue falls below our estimated sensitivity limits. We focused on a 2 degree-square region centred on $l = 327\,^\circ$, $b = 0\,^\circ$ containing 690 PF09 IRDC candidates. This area was chosen as it is typical of the $l = 300 - 330\,^\circ$ region and contains many *Spitzer*-dark objects.

The background levels of the *Spitzer*-dark sources ranged from approximately 390 to $2900\,\mathrm{MJy\,sr}^{-1}$ (equivalent to Positions C and A respectively), with an average of $1400\,\mathrm{MJy\,sr}^{-1}$ (equivalent to Position B). They were defined using an off-cloud, elliptical aperture close to the position of each candidate IRDC. The

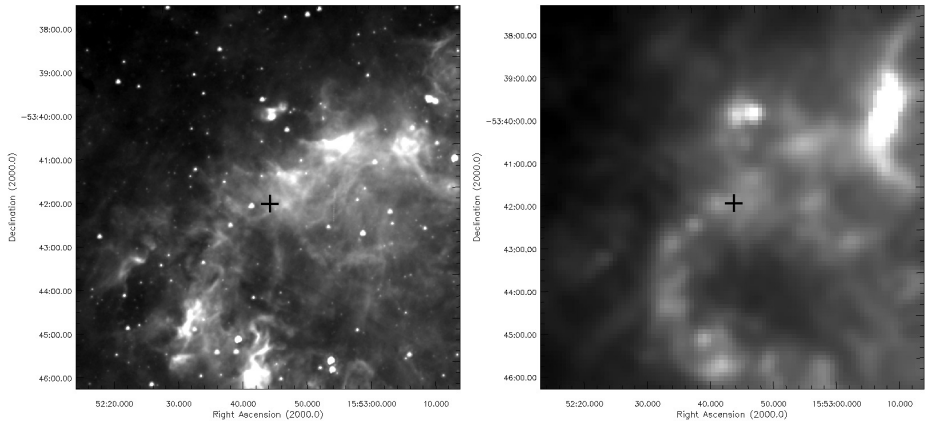

Figure 4.7: A core with radius 0.2 pc and a peak column density of $2\times10^{22}\,\mathrm{cm}^{-2}$ placed in Position A (marked with a cross), shown at 8 μm (left) and 250 μm (right).

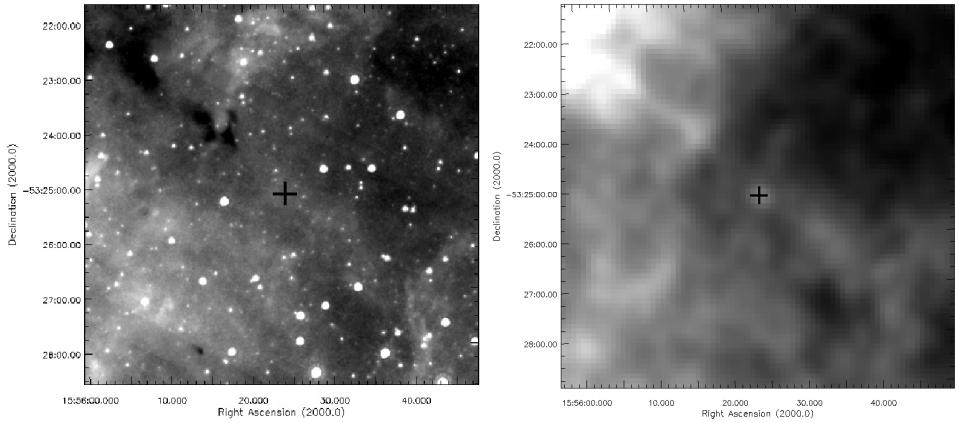

Figure 4.8: A core with radius 0.2 pc and a peak column density of $2\times10^{22}\,\mathrm{cm}^{-2}$ placed in Position B (marked with a cross), shown at 8 μm (left) and 250 μm (right).

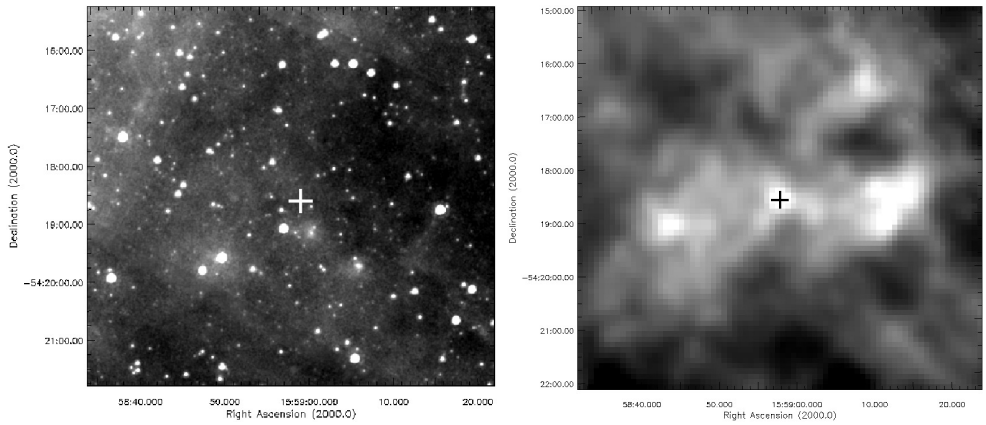

Figure 4.9: A core with radius 0.2 pc and a peak column density of $2\times10^{22}\,\mathrm{cm}^{-2}$ placed in Position C (marked with a cross), shown at 8 μm (left) and 250 μm (right).

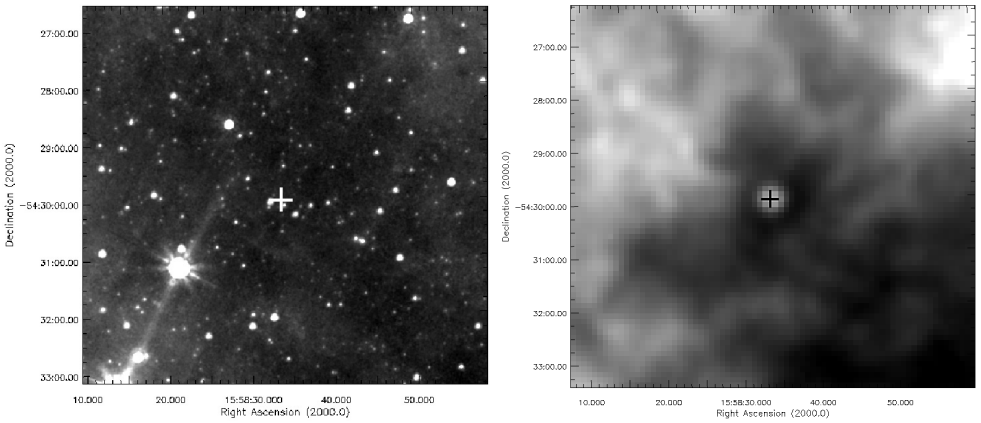

Figure 4.10: A core with radius 0.2 pc and a peak column density of $2\times10^{22}\,\mathrm{cm}^{-2}$ placed in Position D (marked with a cross), shown at 8 μm (left) and 250 μm (right).

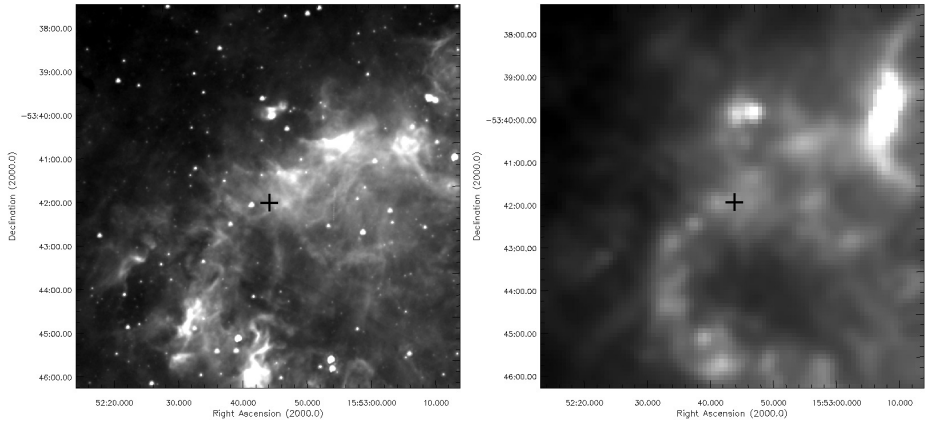

Figure 4.11: A core with radius 0.2 pc and a peak column density of $4\times10^{22}\,\mathrm{cm}^{-2}$ placed in Position A (marked with a cross), shown at 8 μm (left) and 250 μm (right).

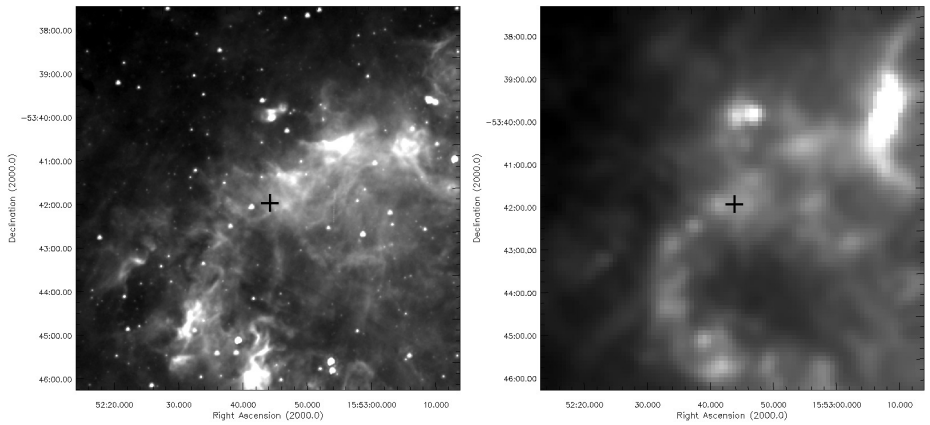

Figure 4.12: A core with radius 0.4 pc and a peak column density of $2\times10^{22}\,\mathrm{cm}^{-2}$ placed in Position A (marked with a cross), shown at 8 μm (left) and 250 μm (right).

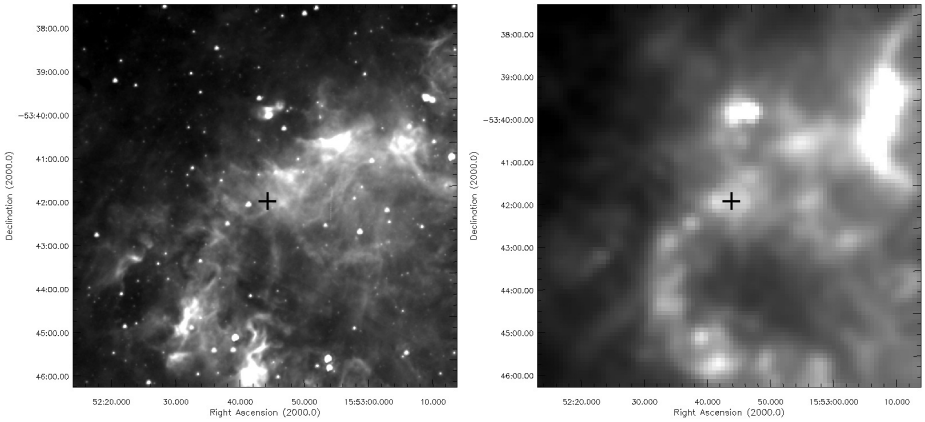

Figure 4.13: A core with radius 0.4 pc and a peak column density of $4{\times}10^{22}\,\mathrm{cm}^{-2}$ placed in Position A (marked with a cross), shown at 8 μm (left) and 250 μm (right).

column density of each was calculated using:

$$N_{H_2} = \tau_{8\,\mu m} \times 3\,[\pm 1] \times 10^{22}\,\mathrm{cm}^{-2}, \tag{4.1}$$

(PF09), where N_{H_2} is the peak column density of the IRDC and $\tau_{8\,\mu m}$ is the peak 8 μm opacity taken from PF09. The axis size of each source was taken to be the size of the semi-major axis listed in PF09.

The $2 \times 2\,^\circ$ region contains 690 IRDC candidates. The candidates that fell below our completeness criteria were isolated using the measured background levels, the column densities and the axis sizes. 141 of the 690 candidates are *Herschel*-dark with a radius less than $26''$, a peak column density lower than $4{\times}10^{22}\,\mathrm{cm}^{-2}$ and a background level above $1300\,\mathrm{MJy\,sr}^{-1}$. For these 141 objects we can not state their true status. Therefore, the unknown objects comprise 141/690, or approximately 20%, of the PF09 IRDC candidates in this $2 \times 2\,^\circ$ area.

We therefore surmise that, if this pattern is typical of the whole Galactic Plane, ∼38% of the PF09 candidate IRDCS are *Herschel*-bright, ∼42% are *Herschel*-dark and ∼20% are unlikely to be seen in emission by *Herschel* regardless of their

true status. To one significant figure we will take these ratios as 40:40:20 for the remainder of this thesis.

4.5 Reduced Numbers of Galactic IRDCs

We have found that only 40–60% of IRDCs identified in the MIR are genuine IRDCs. The rest are believed to be holes in the sky. This implies that all previous catalogues of IRDCs, which are based solely on MIR data, have over-estimated the total number of IRDCs in the Galaxy. In this region the number has been over-estimated by a factor of ∼1.7–2.6. Similar factors might be expected elsewhere. Jackson et al. (2008) carried out a 'reliability' test on the IRDC catalogue of Simon et al. (2006a), and found values ranging from ∼50 % to ∼100 % for the fraction of genuine IRDCs in the catalogue, depending on the contrast level in the MIR. In other words, they also found up to a factor of ∼2 over-estimate in the number of genuine IRDCs – in agreement with our results.

The discovery that only ∼40 % of candidate IRDCs, in a catalogue based on MIR data, turn out to be *Herschel*-bright (see upper part of Table 4.2) has ramifications for all such catalogues based on MIR data alone. The total number of candidate IRDCs in the PF09 catalogue is ∼11,000, with a similar number found by Simon et al. (2006a). If our observed ratio is consistent throughout these catalogues, then the total number of genuine IRDCs in each may be as low as ∼4000–6000 (c.f. Jackson et al. 2008). This has consequences for calculations of the total number of IRDCs in the Galaxy and is discussed in Chapter 6.

4.6 Cores within IRDCs

To find the embedded cores (which they termed fragments), PF09 used apparent opacity contours with a step of 0.35. The number of local peaks between each consecutive level was then the number of fragments extracted. We did not use the fragments identified by PF09 but rather identified cores by the emission at 250 μm.

Each *Herschel*-bright IRDC was examined at 250 μm for evidence that one or more cores had formed in the cloud. The 250 μm band was chosen as this had the best resolution of the three wavelengths where all the IRDCs were required to be seen in emission. The 160 μm waveband does have a higher resolution but, as emission at 160 μm was not a requirement for classification as *Herschel*-bright, it was not guaranteed that all *Herschel*-bright IRDCS would be in emission at this wavelength. Some IRDCs were seen to have relatively simple structures at 250 μm, while others were more complex.

A Gaussian profile was fitted to the intensity map of each core at 250 μm. The Gaussian fitted at 250 μm was used to determine the FWHM of each core. Some IRDCs could be fitted with more than one Gaussian, indicating the presence of more than one cold core. In total, we found cores in 966 *Herschel*-bright IRDCs.

There were 239 objects to which no Gaussian could be fitted. In the case of 221 IRDCs, cloud emission was seen in the FIR at 250 μm, but there was no discernible 250 μm peak. These IRDCs were deemed not to have any cores within them. Figure 4.14 shows an example of an IRDC that is thought to be genuine but which contains no cold core. The centre of the IRDC, according to PF09, is marked with a cross. Around this point diffuse emission can be seen at 250, 350 and 500 μm that follows the approximate path of the absorption at 8 μm. However,

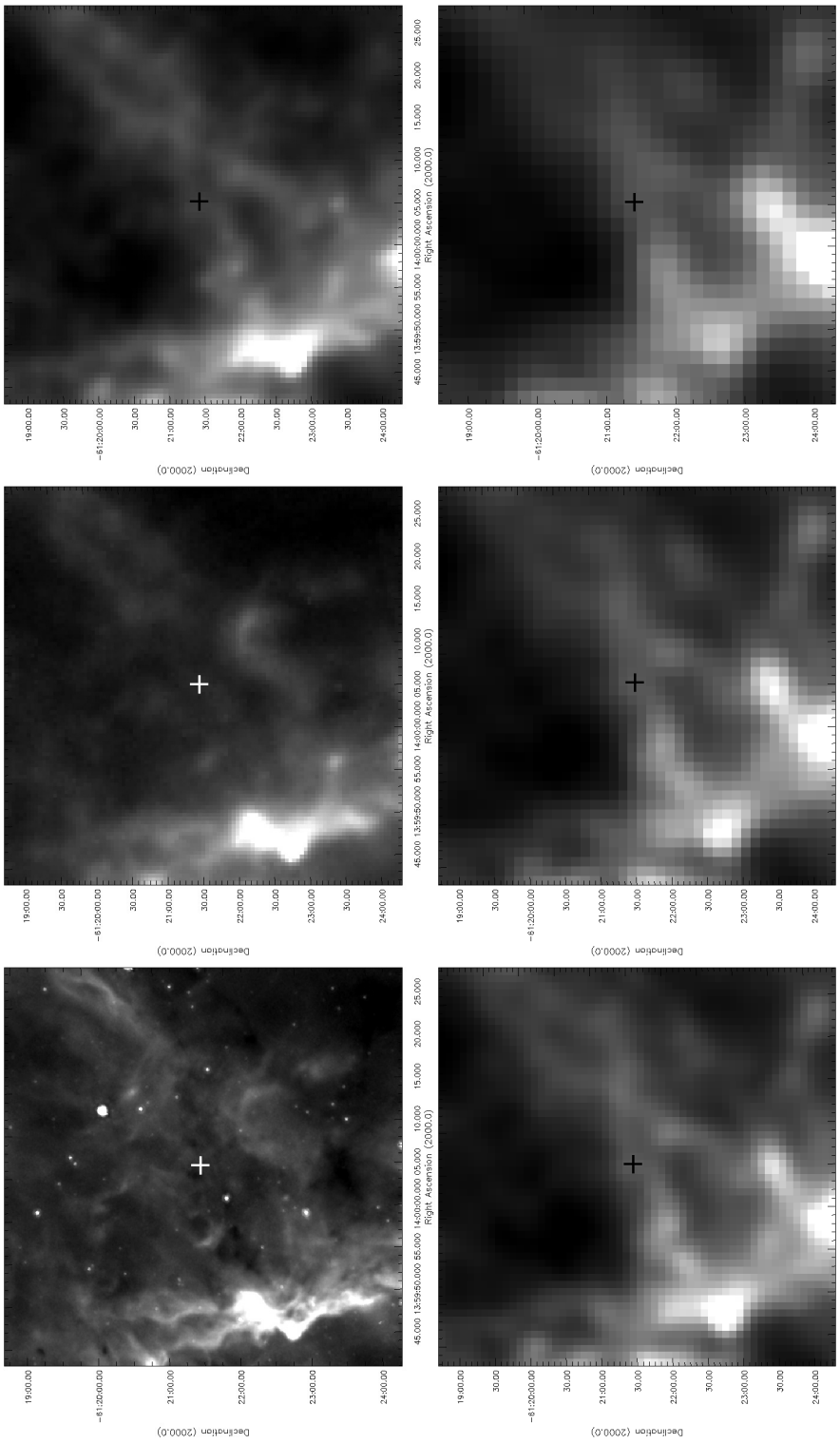

Figure 4.14: G311.061+0.425. Upper (left–right): 8 μm, 70 μm, 160 μm. Lower (left–right): 250 μm, 350 μm, 500 μm. The position of the IRDC is marked with a cross. This is an example of a genuine *Spitzer*-dark, *Herschel*-bright IRDC. However, it does not appear to contain any dense cores. Only diffuse and filamentary emission can be seen at 250 μm.

at no point in the 250 μm observation is there a definite peak in the flux to indicate a cold core. A further 18 IRDCs were found to be in regions of excessively 'stripy' data at 250 μm, resulting in no Gaussian being able to be fitted. In these cases it is possible that the IRDC does contain a cold core but poor data quality prohibits any conclusion.

The 239 IRDCs to which no Gaussian could be fitted were discarded from further analysis. This left us with a 'clean' sample of 966 IRDCs that contain one or more dense cores. A total of 972 cores were found in the 966 IRDCs.

4.7 Protostars within Cores

The 972 cores were studied closely in the 8 μm data for evidence of an 8 μm point source. The presence or lack of an 8 μm point source within a cold core is most likely to be indicative of the presence or absence of an embedded protostar. Hence, this is an indication of the evolutionary status of the core. More evolved cores, namely those already undergoing star formation, are more likely to have an 8 μm point source within them (see Sections 1.3.2 and 3.4.4).

Every cold core was searched for an embedded 8 μm point source. An embedded 8 μm point source was defined as a resolved, roughly circular source with an 8 μm peak flux greater than 3σ. This had to found found within the radius of the cold core. We define the radius as the distance from the centre of the cold core to its outer edge, equal to the FWHM of the cold core at 250 μm. The centre of the core in this case was defined as the peak of emission at 250 μm. It should be noted that, as no distance information is available for the majority of these cores, it is therefore possible that the 8 μm point sources noted here are, in some cases, not

Table 4.2: IRDC statistics. The upper part of the Table lists the percentage of candidates in the PF09 catalogue that were found to be true IRDCs (Herschel-bright). The lower part of the Table refers to the sample of 972 cold cores identified at 250 μm, and lists those with embedded 8 μm sources, those without 8 μm sources that contain 24 μm sources, and those with neither 8 μm nor 24 μm sources.

Source Type	Equivalent Class of Chambers et al. (2009)	Number	%
PF09 sample		3171	100
Herschel-bright		1205	38
Herschel-bright with $\geq$1 cold core		966	30
Number of cores		972	100
Cores with 8 μm source	Red Core	653	67
Cores with 24 μm source only	Active Core	149	15
Cores with no MIR source	Quiescent Core	170	18

associated with the cold core itself but are instead foreground stars contaminating the field of view (see also Lumsden et al. 2002).

653 out of 972 cores (67 %) were found to have at least one embedded 8 μm point source. An example of a cold core with an 8 μm point source is shown in Figure 4.15. In this case the parent IRDC can be seen in absorption at 8 μm. This same area is seen in emission at 250, 350 and 500 μm and so is classed as *Herschel*-bright. This IRDC appears to contain a single cold core. At the centre of the cold core is a bright 8 μm point source (circled in Figure 4.15). This cold core therefore shows evidence of 8 μm emission and likely contains a HCHII or UCHII region (see Section 1.3.2). This left 319 cores which did not contain an 8 μm point source.

The 319 cores without an 8 μm point source were searched for a 24 μm point source. A cold core with a 24 μm point source but no 8 μm point source is thought to be at an earlier evolutionary stage than a cold core that contains an 8 μm point source but still more evolved than a starless core (one which contains no MIR point

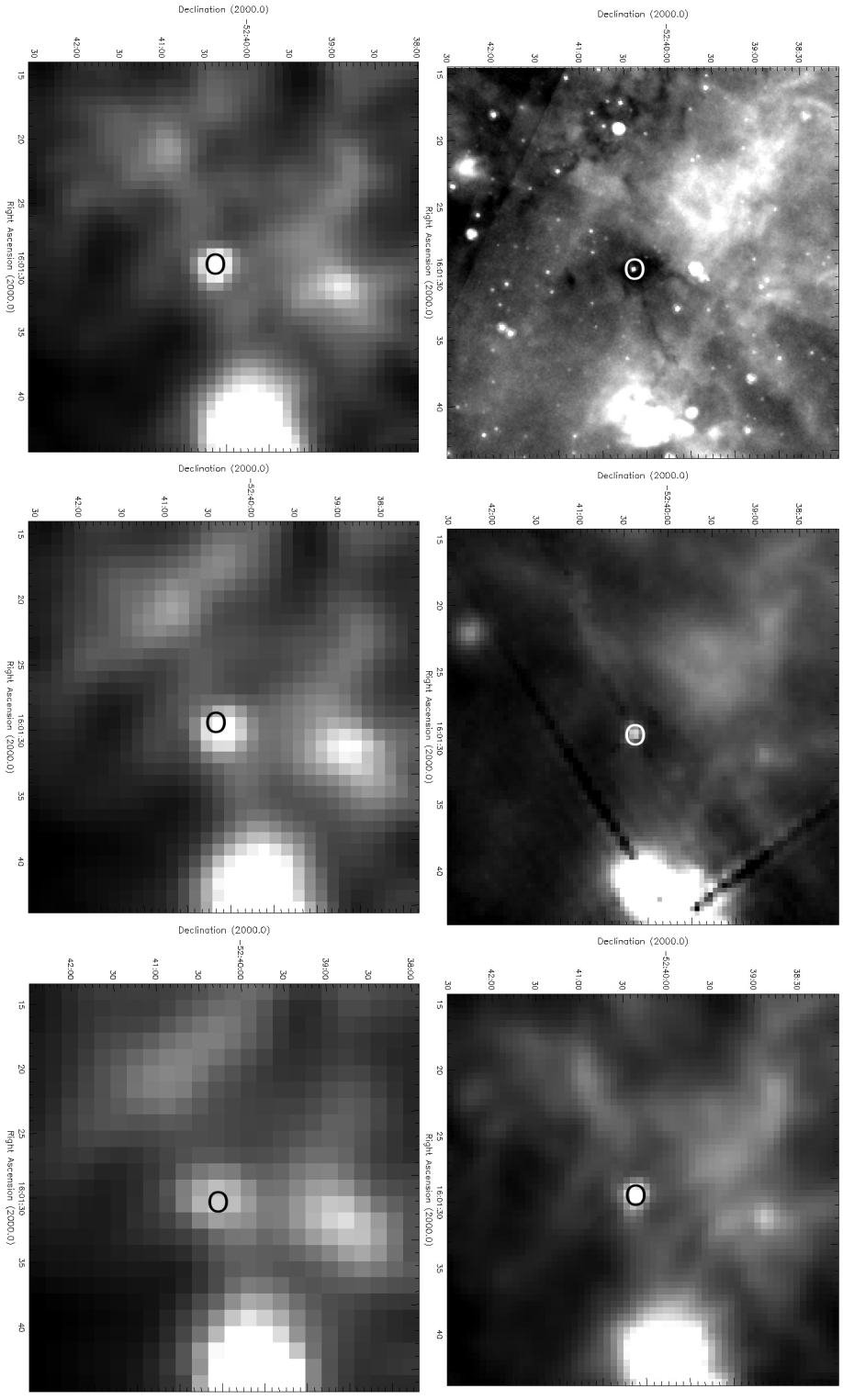

Figure 4.15: G329.494+0.106. Upper (left–right): 8 μm, 70 μm, 160 μm. Lower (left–right): 250 μm, 350 μm, 500 μm. This is an example of a genuine *Spitzer*-dark and *Herschel*-bright IRDC, which contains an 8-μm point source. The point source is circled in all six panels.

source). The search was carried out using the same criteria as when looking for an 8 μm point source (i.e. a $> 3\sigma$ peak within the FWHM as defined at 250 μm). Of the 319 cores with no 8 μm point source, 149 were found to have one or more 24 μm point sources. The remaining 170 cores were deemed to be starless. An example of a core with a 24 μm point source is shown in Figure 4.16. The parent IRDC can be seen in absorption at 8 μm and in emission at 250, 350 and 500 μm. A single cold core is evident at 250 μm. In this case the cross marks the position of the centre of the parent IRDC according to PF09. The centre of the cold core is slightly offset from this, lower and to the left in Figure 4.16. This cold core shows no evidence of an 8 μm point source but at 24 μm there is at least one and possibly two point sources which coincide with the cold core visible at 250 μm.

In summary, we found a total of 966 IRDCs that contained one or more discernible cores at 250 μm and a total of 972 cores. Of these, 653 of the cores have an 8 μm point source. Of the cores with no 8 μm point source, a further 149 have a 24 μm point source. We designate the remaining 170, which contain no evidence of a MIR point source, as starless cores. Starless cores could be the high-mass equivalents of low-mass prestellar cores in that they are gravitationally bound but have no internal heating. They are believed to be the youngest evolutionary stage observable in high mass star formation. The total numbers of cores in each category are summarised in Table 4.2.

4.8 Summary

PF09 created a catalogue of candidate IRDCs in the Galactic Plane based on their appearance at 8 μm. We refer to these objects as *Spitzer*-dark, meaning they are

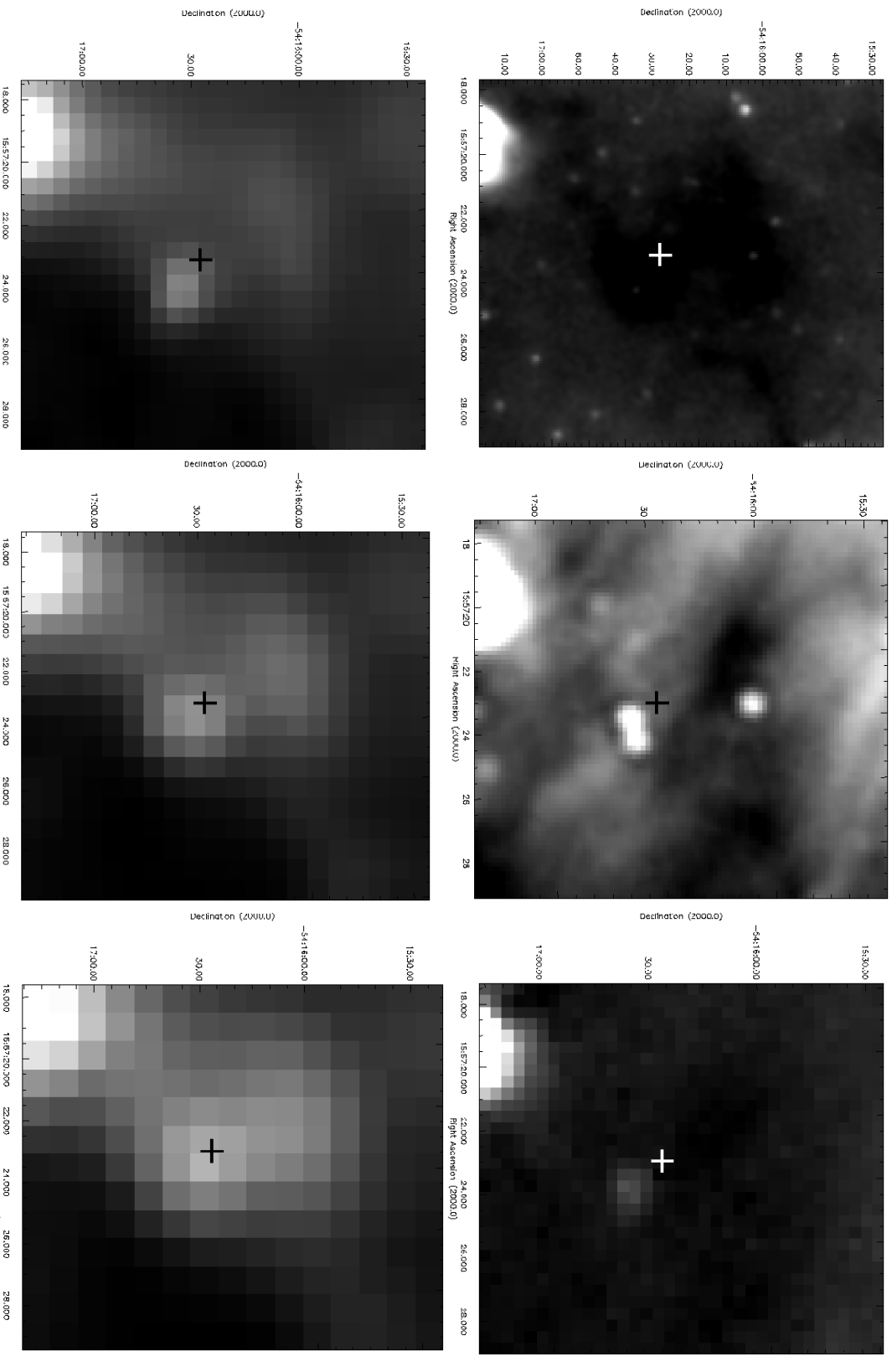

Figure 4.16: G327.988-0.711. Upper (left–right): 8 μm, 24 μm, 70 μm. Lower (left–right): 160 μm, 250 μm, 350 μm. This is an example of a genuine *Spitzer*-dark and *Herschel*-bright IRDC, which contains an 24 μm point source. The IRDC is marked with a cross in all six panels.

seen in absorption at 8 μm. However, when identifying IRDCs in the MIR alone it is impossible to distinguish between a genuine IRDC and a hole in the sky. To overcome this limitation a selection of the PF09 *Spitzer*-dark sources were viewed in the FIR, where they are expected to show emission. Any *Spitzer*-dark object that showed emission at 250, 350 and 500 μm was labelled *Herschel*-bright. Of the 3171 *Spitzer*-dark objects observed, only 1205 ($\sim$40%) were found to be *Herschel*-bright. These are the objects we believe are genuine IRDCs.

The sensitivity limits of *Herschel* were tested in regards to the detection of IRDCs. It was found that any IRDC whose major axis is $\leq 26''$ (corresponding to 0.4 pc at a distance of 3.1 kpc) with a peak column density less than 4×10^{22} cm^{-2} in an area where the background level is greater than 1300 MJy sr^{-1} at 250 μm is not likely to be found to be *Herschel*-bright, regardless of whether it is a genuine IRDC or not. Approximately 20% of the initial sample of *Spitzer*-dark objects met with these criteria. We therefore state that $\sim$40% of the *Spitzer*-dark sample are *Herschel*-bright and genuine IRDCs and $\sim$40% are *Herschel*-dark and possible candidate for holes in the sky. The remaining $\sim$20% are too small or too diffuse to appear in the *Herschel* observations and we are unable to make any conclusions about their status.

Therefore only 40–60% of the *Spitzer*-dark candidate IRDCs are believed to be genuine IRDCs. This suggests that IRDC searches based solely on MIR data may over-estimate the total number of IRDCs in the Galaxy by up to a factor of $\sim$2. The implications of this are discussed in Chapter 6.

Within the 1205 *Herschel*-bright IRDCs, 972 cores were found at 250 μm. 221 IRDCs were found to contain no discernible peak at 250 μm and so were deemed to contain no cores. The *Spitzer* data were examined to see whether the cores

contained either an 8 μm or a 24μm point source. 653 are seen to harbour one or more 8 μm point sources and a further 149 contained one or more 24 μm point sources. 170 were found to contain neither an 8 μm nor a 24 μm point source and were labelled as starless. This is thought to be an evolutionary sequence with cores evolving from a starless state, first developing a 24 μm point source and eventually an 8 μm source.

Chapter 5

Twenty Young, Isolated Cores

5.1 Introduction

In Chapter 4, data from Hi-GAL were used to study the candidate IRDCs from PF09 at FIR wavelengths. We identified 1205 IRDCs that were simultaneously *Spitzer*-dark and *Herschel*-bright. 966 of them contained identifiable cores, as defined by peaks in their emission at 250 μm. We classified the cores depending on the presence or absence of an embedded MIR source at 8 or 24 μm. We identified the youngest, least-evolved cores as those which contained no embedded MIR point sources, and labelled them starless. We found 170 IRDCs containing starless cores.

In this chapter we identify the most isolated of these 170 starless cores, based on their appearance at FIR wavelengths. We find 20 starless cores that satisfy our conditions for being the most isolated. We then model these 20 cores, using PHAETHON to determine their physical parameters (see Chapter 3).

5.2 Source Selection

In Chapter 4 we found 966 IRDCs which showed evidence for one or more cores at FIR wavelengths. Each core was placed into an evolutionary stage based on whether or not it showed any evidence of internal heating. The cores were assumed to begin life as starless, containing no 8 or 24 μm point sources, and then to develop first 24 μm and eventually 8 μm point sources. We found 170 starless cores, 149 with a 24 μm point source but no 8 μm point source and 653 which contained at least one 8 μm point source.

Phaethon can best model objects which have no significant internal heating and are therefore heated only by external radiation falling on their surfaces. Phaethon also assumes a relatively simple geometry – see Section 3.2.4.1. Isolated cores are more likely to have simple structures as they are least likely to be effected by nearby sources, and starless cores are those with no evidence of internal heating. Phaethon is therefore best suited to modelling the subset of cores that are both isolated and starless.

We took as our initial sample the 170 starless cores identified in Chapter 4 as having no 8 or 24 μm point source, and searched for those that were most isolated. For a core to be deemed isolated, it had to be unconfused by any neighbouring sources. We defined this by saying that there had to be a minimum depth of magnitude greater than 3σ between the peak of the core and the peak of any neighbouring object. This had to be true at all FIR wavelengths (160, 250, 350 and 500 μm). Of the 170 starless cores, only 20 were found to be truly isolated according to this definition. These isolated, starless cores are discussed in Section 5.3.

Table 5.1: The flux densities of each core at the five *Herschel* wavelengths. The values at 70 μm are an upper limit only.

Name of the	Flux Densities (Jy)				
Parent IRDC	70 μm	160 μm	250 μm	350 μm	500 μm
305.798−0.097	<2.4	76.5	79.9	42.4	17.8
307.495+0.660	<0.4	4.6	5.9	3.2	1.5
309.079−0.208	<1.7	11.9	17.1	8.9	3.7
309.111−0.298	<2.4	24.4	16.6	8.1	3.3
310.297+0.705	<0.8	12.4	14.3	6.9	2.8
314.701+0.183	<0.0	10.3	14.3	8.4	3.9
318.573+0.642	<0.9	9.6	10.6	6.4	2.8
318.802+0.416	<2.2	13.5	9.8	3.7	1.5
318.916−0.284	<0.3	11.2	12.9	7.3	3.3
321.678+0.965	<0.6	7.7	14.8	8.4	4.1
321.753+0.669	<0.4	10.6	9.8	4.6	1.6
322.334+0.561	<1.6	20.8	22.0	11.7	4.8
322.666−0.588	<0.6	7.1	9.9	5.3	2.3
322.914+0.321	<2.5	17.7	14.6	7.0	3.1
326.495+0.581	<1.7	51.1	42.8	20.7	7.9
326.620−0.143	<2.5	21.4	17.5	8.8	3.7
326.632+0.951	<0.7	9.8	11.8	3.5	2.6
326.811+0.656	<3.7	47.9	30.0	15.9	6.5
328.432−0.522	<0.1	17.3	17.8	7.2	2.8
329.403−0.736	<2.4	16.9	14.4	8.4	2.9

5.3 Observations of Isolated, Starless Cores

Observations of the 20 isolated, starless cores selected for modelling are shown in Figures 5.1–5.20. These show the cores at wavelengths of 8, 70, 160, 250, 350 and 500 μm. The 8 μm data were taken by *Spitzer* as part of the GLIMPSE survey. The 70–500 μm data were taken by *Herschel* as part of Hi-GAL. Each image is oriented so that north is upwards and east to the left. The flux densities of each core at all five Hi-GAL wavelengths are given in Table 5.1.

5.3.1 305.798−0.097

The observations for the core in 305.798−0.097 are shown in Figure 5.1. The core we focus on is found at the centre of the images. With a flux density of ∼80 Jy at 250 μm, it is the brightest core in 305.798−0.097 as well as the brightest core we model (see Table 5.1). Its semi-major axis lies east to west. The entire IRDC is seen in absorption at 8 μm. By 70 μm most of the core is still seen in absorption but to a lesser degree than at 8 μm. The core is seen in emission at 160, 250, 350 and 500 μm.

There are up to four other possible cores visible in the 160 μm data. All the other cores are significantly fainter and smaller than the core we model. The second brightest core in 305.798−0.097 has a flux density of ∼9 Jy and the second largest a FWHM of 15″. The core we model has a FWHM of ∼60″ at 250 μm. Two of the four cores lie to the south-west of the bright central core and two lie directly to the south. The two cores to the south-west are part of 305.798−0.097, but the two to the south are likely to be part of a different IRDC. None of these cores are isolated at wavelengths beyond 160 μm.

5.3.2 307.495+0.660

Images of 307.495+0.660 can be seen in Figure 5.2. The core studied here is the bright object in the centre of the images. The parent IRDC and its core are seen in absorption at 8 μm, but at 70 μm it is unclear whether they are in absorption or emission because of the noise in the background. By 160 μm both show clear emission, and this is visible at 250, 350 and 500 μm. In the 160 and 250 μm data there appears extended emission to the west of the core. As this emission appears

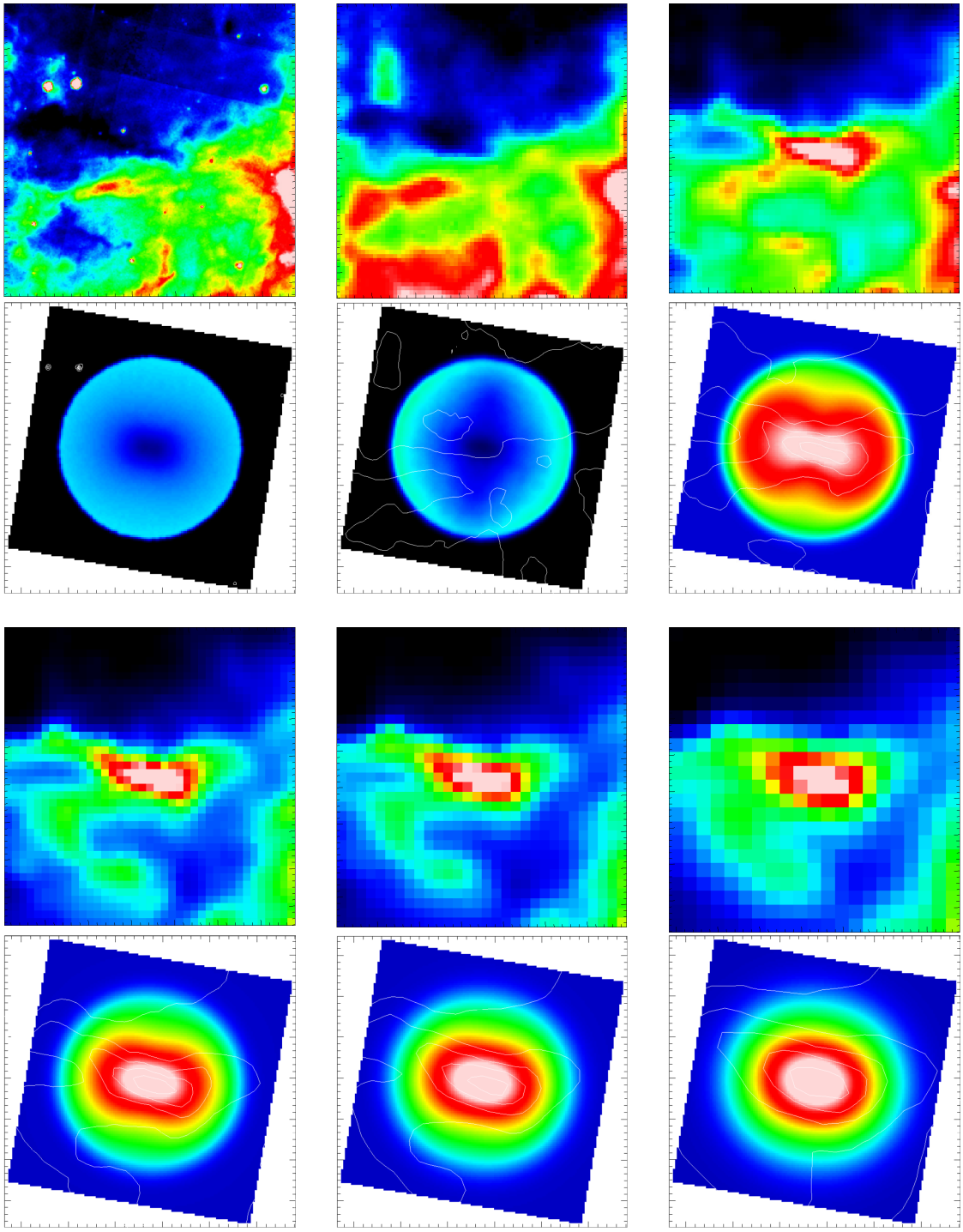

Figure 5.1: 305.798−0.097 - Upper row: Observational images of the infrared dark core at (left-right) *Spitzer* 8 μm, PACS 70 μm and PACS 160 μm. Second row: Modelled images at 8 μm, 70 μm and 160 μm. Third row: Observational at SPIRE 250, 350 and 500 μm. Lower row: Modelled images at 250, 350 and 500 μm. All images are $\sim$0.05$\times$0.05° in size, equivalent to 2.56$\times$2.56 pc.

to have disappeared in the 350 and 500 μm data it is unclear whether or not this is due to the parent IRDC. No other IRDCs are seen in these images.

5.3.3 309.079−0.208

Observations of 309.079−0.208 can be seen in Figure 5.3. The core is located at the centre of the images, with unrelated emission located to the east in all six wavelengths. The core and its parent IRDC are seen in absorption at 8 and 70 μm. The core is seen in emission between 160 and 500 μm. Emission from the parent IRDC can be seen surrounding the core and extending to the south at wavelengths of 250 μm and beyond, although this region still appears to be in absorption at shorter wavelengths. No other IRDCs are seen in these observations.

5.3.4 309.111−0.298

Observations of 309.111−0.298 and its single core can be seen in Figure 5.4. The core and parent IRDC are seen in absorption at 8 and 70 μm, and in emission at 160–500 μm. The absorption at 8 and 70 μm appears to extend to the south of the core but, as this region is not seen in emission at the four longer wavelengths, it is more likely to be a hole in the sky. At 160 μm and beyond, there appears to be extended emission, possibly connected to the core, in the north-easterly direction. However, as this area is also seen in emission at 70 μm and no clear absorption is seen at 8 μm, it is unlikely to be part of the parent IRDC. Similarly, a second source can be seen to the south-east of the core. This object is seen in emission at all six wavelengths, and so is also not considered to be part of the IRDC.

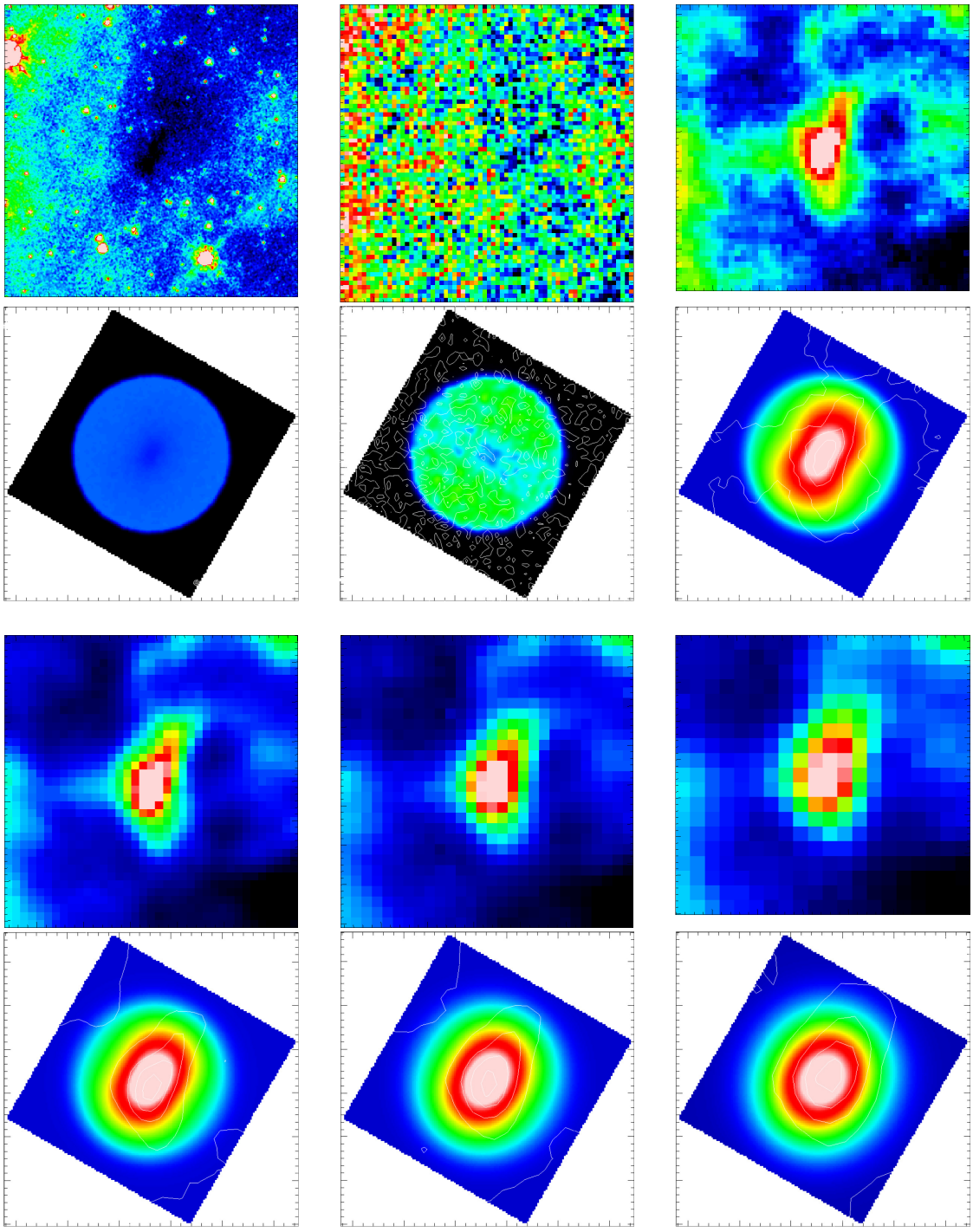

Figure 5.2: 307.495+0.660 - Upper row: Observational images of the infrared dark core at (left-right) *Spitzer* 8 μm, PACS 70 μm and PACS 160 μm. Second row: Modelled images at 8 μm, 70 μm and 160 μm. Third row: Observational at SPIRE 250, 350 and 500 μm. Lower row: Modelled images at 250, 350 and 500 μm. All images are $\sim$0.04$\times$0.04° in size, equivalent to 2.56$\times$2.56 pc.

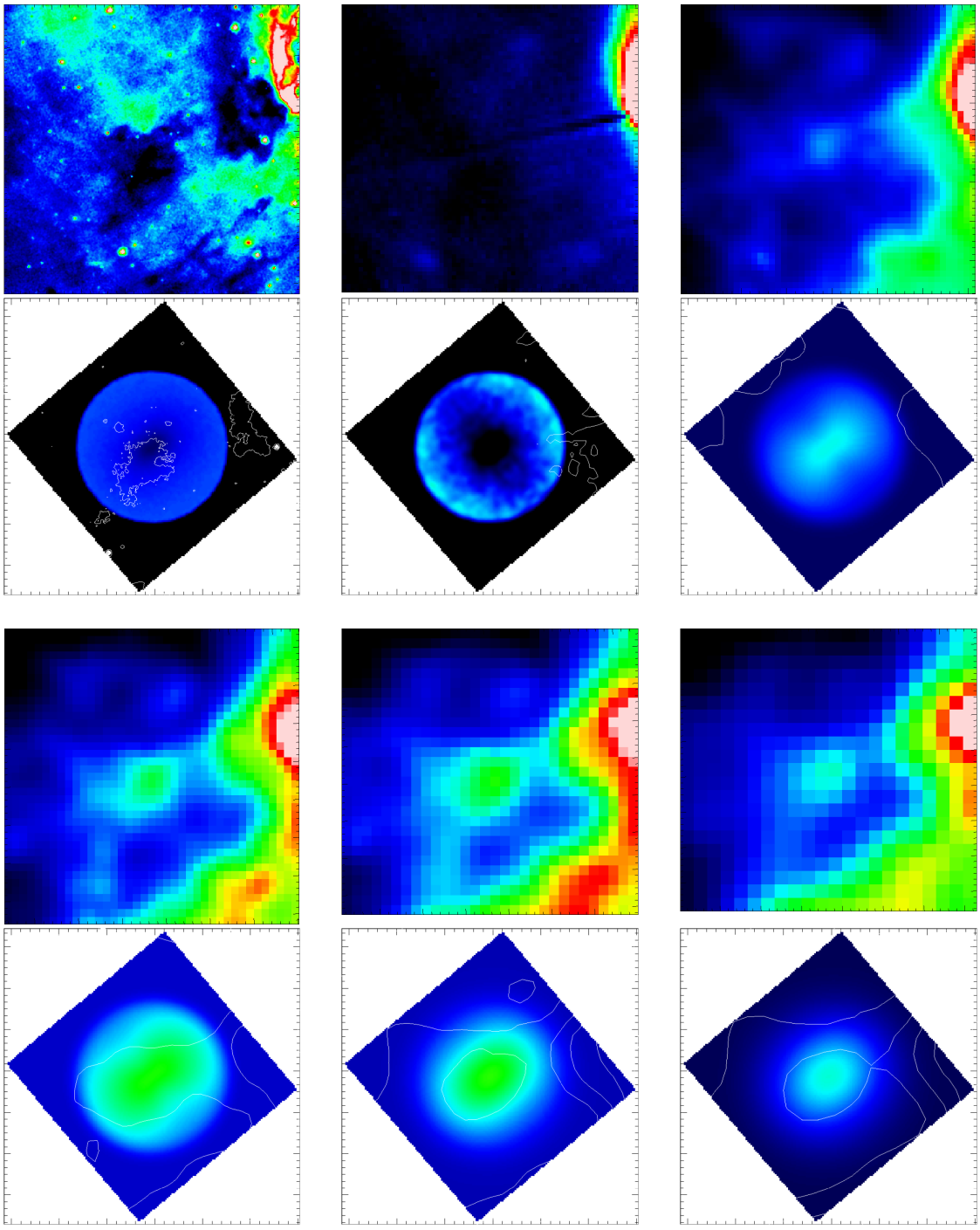

Figure 5.3: 309.079−0.208 - Upper row: Observational images of the infrared dark core at (left-right) *Spitzer* 8 μm, PACS 70 μm and PACS 160 μm. Second row: Modelled images at 8 μm, 70 μm and 160 μm. Third row: Observational at SPIRE 250, 350 and 500 μm. Lower row: Modelled images at 250, 350 and 500 μm. All images are $\sim$0.04$\times$0.04° in size, equivalent to 2.56$\times$2.56 pc.

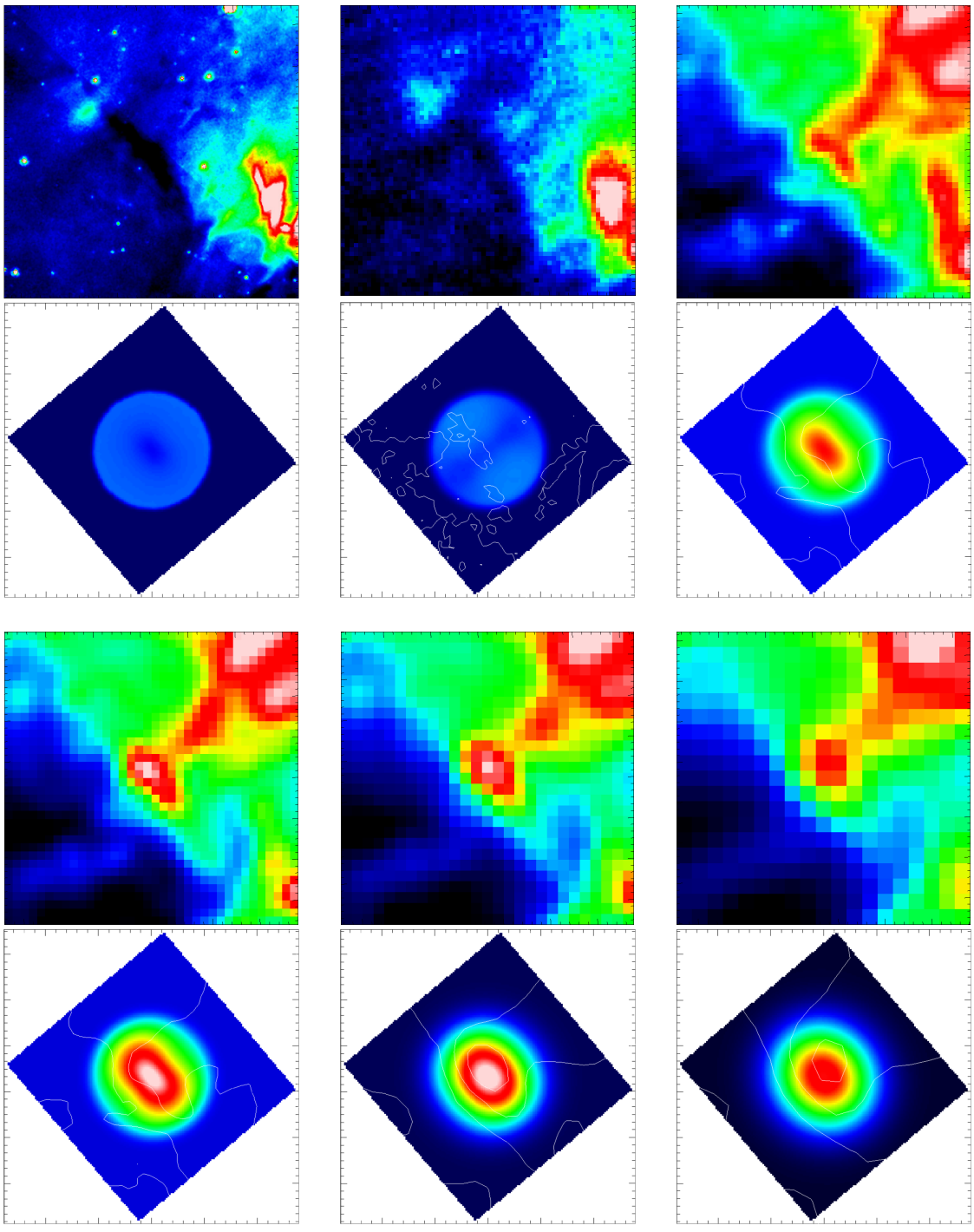

Figure 5.4: 309.111−0.298 - Upper row: Observational images of the infrared dark core at (left-right) *Spitzer* 8 μm, PACS 70 μm and PACS 160 μm. Second row: Modelled images at 8 μm, 70 μm and 160 μm. Third row: Observational at SPIRE 250, 350 and 500 μm. Lower row: Modelled images at 250, 350 and 500 μm. All images are $\sim$0.04×0.04° in size, equivalent to 2.56×2.56 pc.

5.3.5 310.297+0.705

Images of 310.297+0.705 can be seen in Figure 5.5. The starless core is located in the centre of the data tiles and can be seen most clearly at 250 μm. Emission from the parent IRDC extends to the east and the south of the core. The core and parent IRDC are seen in absorption in 8 μm and the core is seen in absorption at 70 μm. However, it is not clear whether the parent IRDC is in emission or absorption at 70 μm. By 160 μm both core and IRDC are clearly seen in emission. No other IRDCs appear in the immediate vicinity, nor do any other cores appear to be present in 310.297+0.705. This makes the starless core in 310.297+0.705 one of the most isolated that we modelled.

5.3.6 314.701+0.183

Observations of 314.701+0.183 can be seen in Figure 5.6. The core is located in the centre of the images, and is very clearly seen in absorption at 8 and 70 μm. There is some emission visible at 160 μm, however it is not until 250 μm that we see clear evidence of a core. Possible emission from the parent IRDC can be seen extending to the south. However, this region is not seen in absorption at 8 μm. This could be due to the parent IRDC being particularly diffuse, or the emission could be from a separate source.

A second *Spitzer*-dark and *Herschel*-bright region is visible in the top left corner of the observations, to the north-west of 314.701+0.183. According to PF09, this is a different IRDC, named 314.710+0.201, and so is unrelated to 314.701+0.183. 314.710+0.210 was not modelled because it does not appear to contain a distinct core at 250 μm.

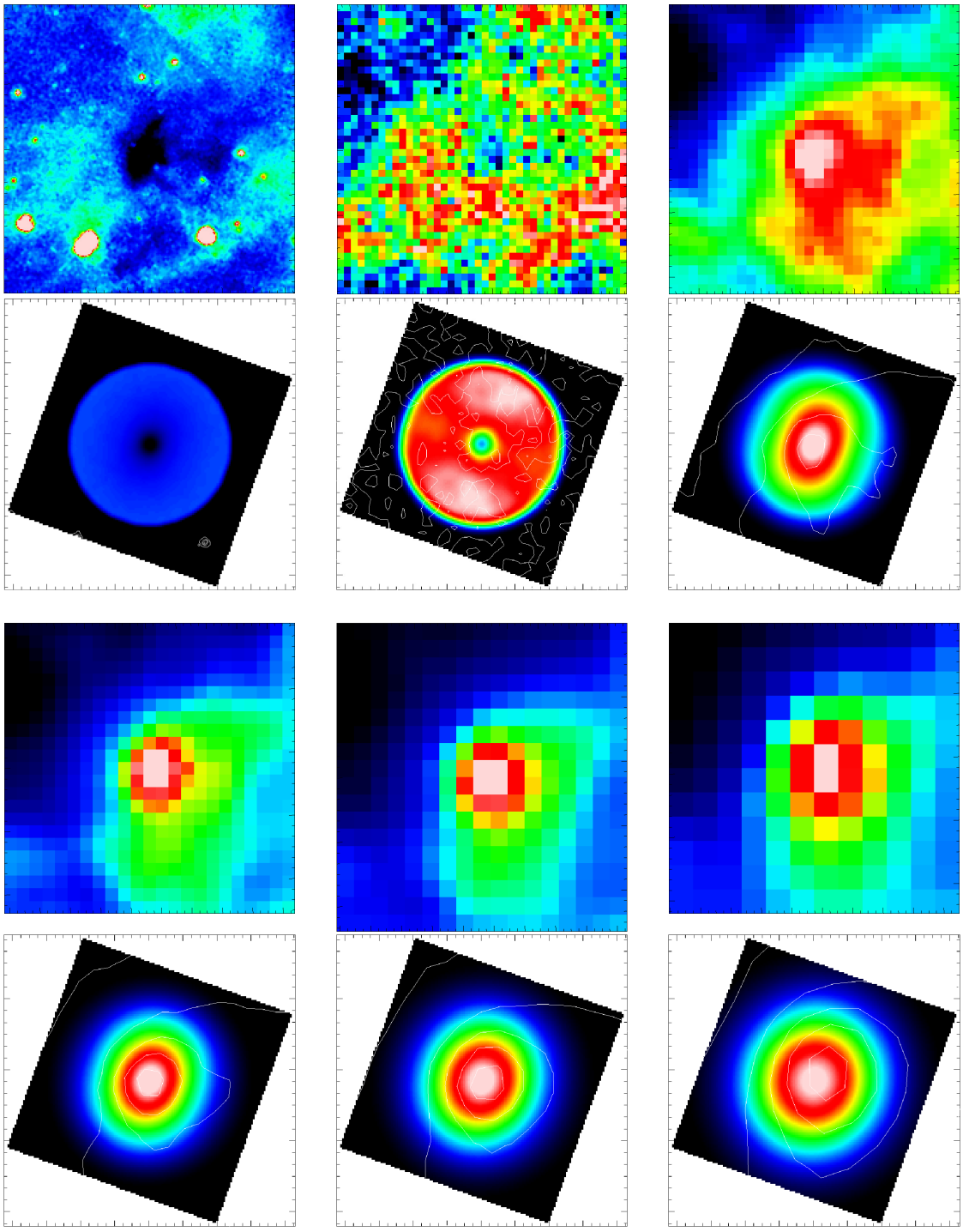

Figure 5.5: 310.297+0.705 - Upper row: Observational images of the infrared dark core at (left-right) *Spitzer* 8 μm, PACS 70 μm and PACS 160 μm. Second row: Modelled images at 8 μm, 70 μm and 160 μm. Third row: Observational at SPIRE 250, 350 and 500 μm. Lower row: Modelled images at 250, 350 and 500 μm. All images are $\sim$0.03$\times$0.03° in size, equivalent to 2.56$\times$2.56 pc.

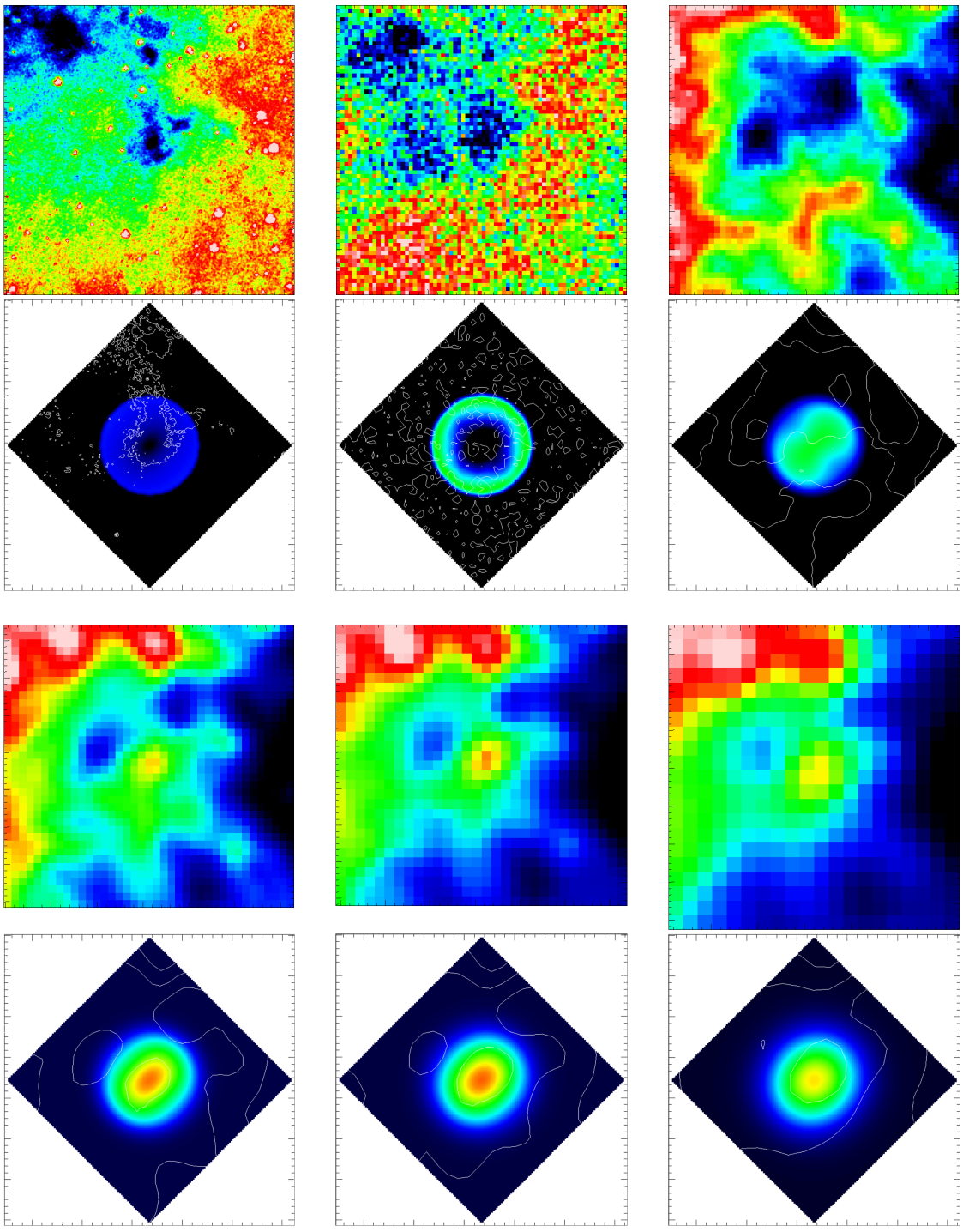

Figure 5.6: 314.701+0.183 - Upper row: Observational images of the infrared dark core at (left-right) *Spitzer* 8 μm, PACS 70 μm and PACS 160 μm. Second row: Modelled images at 8 μm, 70 μm and 160 μm. Third row: Observational at SPIRE 250, 350 and 500 μm. Lower row: Modelled images at 250, 350 and 500 μm. All images are $\sim$0.04$\times$0.04° in size, equivalent to 2.56$\times$2.56 pc.

5.3.7 318.573+0.642

The core in 318.573+0.642 can be seen in Figure 5.7. The isolated, starless core is seen in the centre of the images. The core within 318.573+0.642 is seen in absorption at 8 μm but, unlike many of our isolated, starless cores, it is seen in emission at wavelengths as short as 70 μm. Emission is then seen through the FIR wavelengths until 500 μm. Very little extended emission appears from the parent IRDC. That which there is extends southwards of the core and is best seen at 160 μm, before becoming increasingly faint at longer wavelengths.

A second *Spitzer*-dark and *Herschel*-bright region, containing a single core, is visible to the east of 318.573+0.642. This is part of a separate IRDC, 318.665+0.666. The core in 318.665+0.666 was not modelled because it is confused at 160 μm. However, it is not connected to 318.573+0.642 and so is not relevant to the modelling of this core.

5.3.8 318.802+0.416

The starless core in 318.802+0.416 can be seen at the centre of the images shown in Figure 5.8. However, this is one of the more confused regions as the majority of the sources emitting in the FIR are also visible in emission at 8 μm. We assume they are not connected to 318.802+0.416. This means that the emission from the parent IRDC is difficult to isolate. The core is seen in absorption at 8 μm and emission from 160 μm to 500 μm. However, the data at 70 μm shows a large amount of noise. It is unclear whether the core is in absorption or emission at this wavelength.

The region to the north-east is seen in absorption at 8 μm. As it shows no

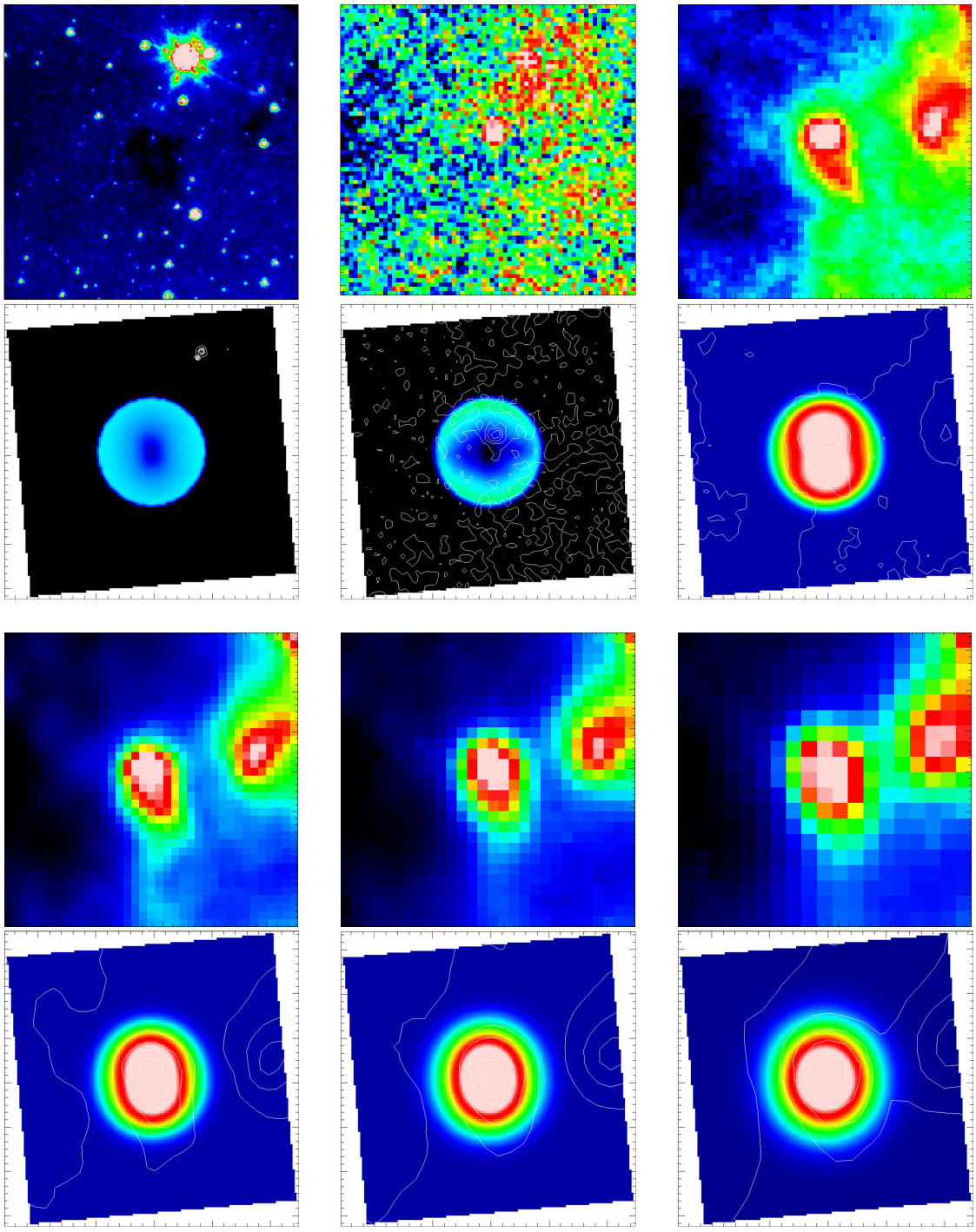

Figure 5.7: 318.573+0.642 - Upper row: Observational images of the infrared dark core at (left-right) *Spitzer* 8 μm, PACS 70 μm and PACS 160 μm. Second row: Modelled images at 8 μm, 70 μm and 160 μm. Third row: Observational at SPIRE 250, 350 and 500 μm. Lower row: Modelled images at 250, 350 and 500 μm. All images are $\sim$0.05$\times$0.05° in size, equivalent to 2.56$\times$2.56 pc.

emission in any FIR waveband we label it *Spitzer*-dark and also *Herschel*-dark. It is likely to be a hole in the sky.

5.3.9 318.916−0.284

Three cores can be seen in the observations of 318.916−0.284, shown in Figure 5.9. One is seen in the centre of the images – this is the starless core which we modelled. According to PF09, the other cores belong to different IRDCs. One can be found at the top of the images and is part of 318.932−0.266. The second core can be found towards the south-west of the core in 318.916−0.284, in the bottom left corner of the observations. This core belongs to the IRDC called 318.875−0.272. The former is not isolated at longer wavelengths, while the latter contains 8 μm point sources within its FWHM. Therefore neither was chosen to be modelled.

Our focus is the core in 318.916−0.284. It is seen in absorption at 8 and 70 μm, while the parent IRDC is only seen in absorption at 8 μm. Both begin to show faint emission at 160 μm and continue in emission throughout the FIR wavelengths. Emission from the parent IRDC extends to the south and south-west of the core.

5.3.10 321.678+0.965

The observations of 321.678+0.965 are shown in Figure 5.10. The data at 70 and 160 μm are particularly stripy in this region. However, as these wavelengths were not vital to the classification of the IRDC or its core, 321.678+0.965 was included regardless. It should be noted that this does increase the uncertainty on the flux density measurements for these wavelengths.

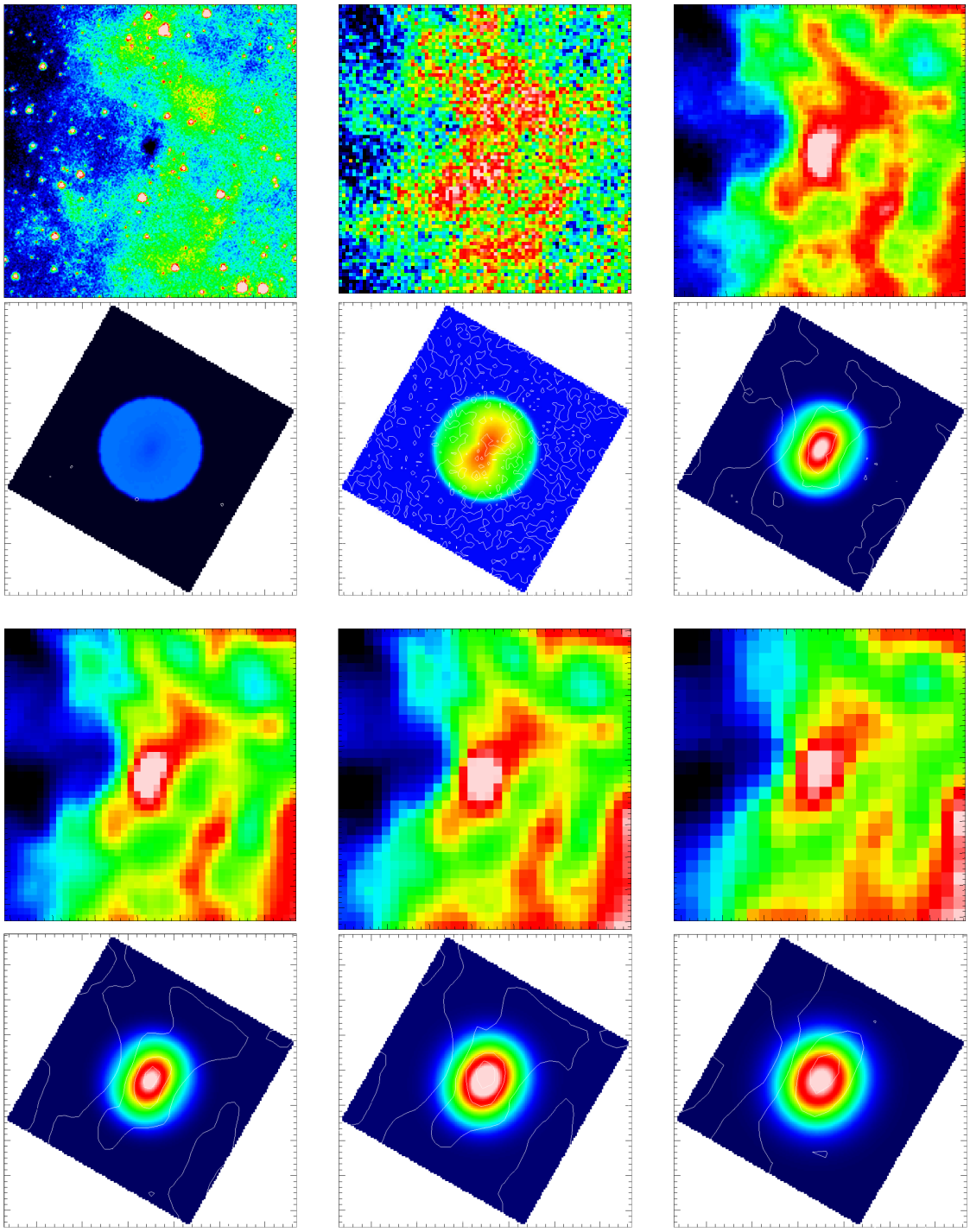

Figure 5.8: 318.802+0.416 - Upper row: Observational images of the infrared dark core at (left-right) *Spitzer* 8 μm, PACS 70 μm and PACS 160 μm. Second row: Modelled images at 8 μm, 70 μm and 160 μm. Third row: Observational at SPIRE 250, 350 and 500 μm. Lower row: Modelled images at 250, 350 and 500 μm. All images are $\sim$0.05$\times$0.05° in size, equivalent to 2.56$\times$2.56 pc.

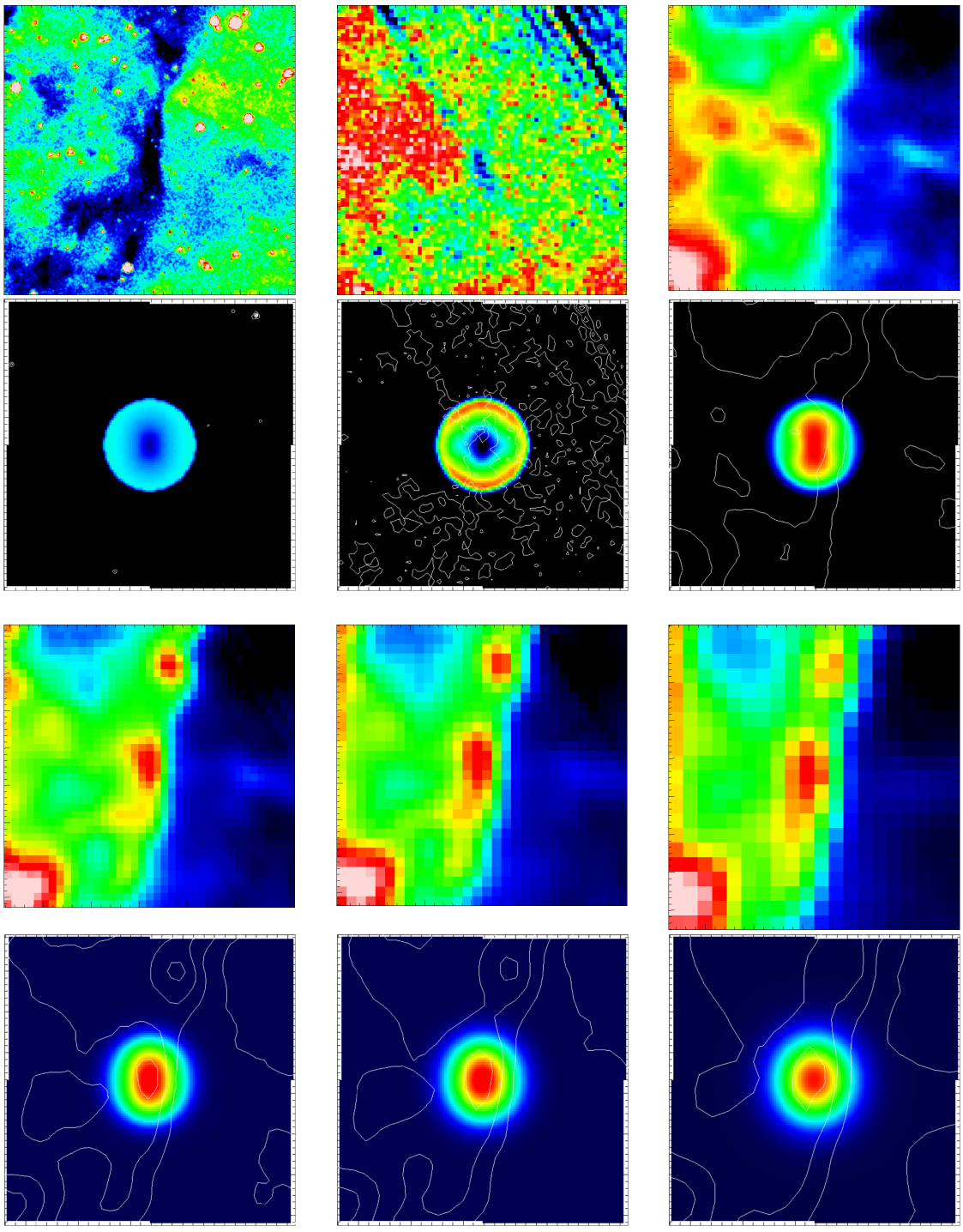

Figure 5.9: 318.916−0.284 - Upper row: Observational images of the infrared dark core at (left-right) *Spitzer* 8 μm, PACS 70 μm and PACS 160 μm. Second row: Modelled images at 8 μm, 70 μm and 160 μm. Third row: Observational at SPIRE 250, 350 and 500 μm. Lower row: Modelled images at 250, 350 and 500 μm. All images are $\sim$0.06$\times$0.06° in size, equivalent to 2.56$\times$2.56 pc.

The core selected for modelling is shown in the centre of these images. It is seen in absorption at 8 μm and in emission at 160, 250, 350 and 500 μm. An additional core is seen in 321.678+0.965, to the west of the bright central core. However this was seen to contain 8 μm point sources and so did not meet our starless criteria required for modelling.

Two other *Spitzer*-dark and *Herschel*-bright regions are also visible in the images. One in the top left corner, to the north-west of 321.678+0.965, and one directly to the east. Both appear to contain a single core. As neither of these regions were listed in PF09 and it is unclear whether or not they are connected to 321.678+0.965 they were not included in our list of *Spitzer*-dark and *Herschel*-bright regions. All other sources in the images show emission at 8 μm and are not considered IRDCs.

5.3.11 321.753+0.669

321.753+0.669 contains several cores as seen in Figure 5.11. We focus solely on the brightest core at the centre of the images. This core has a peak flux density of $\sim$0.4Jy compared with a peak of $\sim$0.2 Jy in the surrounding cores. The two other cores exist to the north-west of the central core, although neither of these cores is isolated at 160 μm and so they were not included in the modelling. Extended emission from the parent IRDC also continues to the east. No other IRDCs are seen in these images.

The cores and parent IRDC are seen in absorption in 8 μm and in emission by 160 μm. The noise in the 70 μm data make it difficult to ascertain whether 321.753+0.669 is in emission at this wavelength, although extended structure away

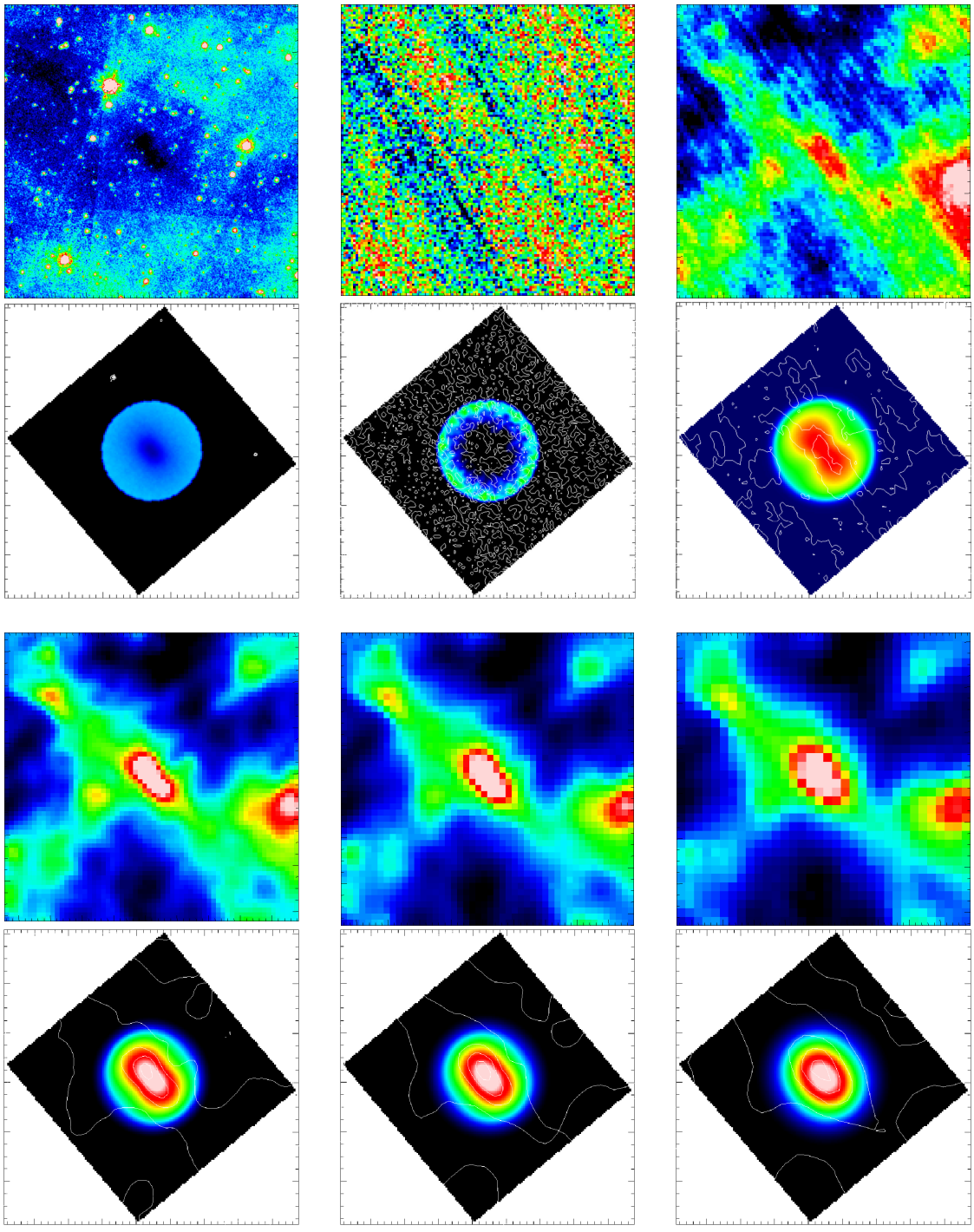

Figure 5.10: 321.678+0.965 - Upper row: Observational images of the infrared dark core at (left-right) *Spitzer* 8 μm, PACS 70 μm and PACS 160 μm. Second row: Modelled images at 8 μm, 70 μm and 160 μm. Third row: Observational at SPIRE 250, 350 and 500 μm. Lower row: Modelled images at 250, 350 and 500 μm. All images are $\sim$0.07$\times$0.07° in size, equivalent to 2.56$\times$2.56 pc.

from the central core in the north-west direction does appear to show in absorption.

5.3.12 322.334+0.561

Observations of 322.334+0.561 are shown in Figure 5.12. The isolated, starless core is located in the centre of the images. It is seen in absorption at 8 μm and in emission at 160 μm and longwards. Although no absorption is seen in the 70 μm data, no emission beyond that of the background material is seen either. The 8 μm data show several point sources towards the edge of the core. These were found to be outside the FWHM (as defined at 250 μm) and so the core was classed as starless and suitable for modelling. Emission from the parent IRDC extends to the west of the core, most evident at 160 and 250 μm, although still visible at 350 μm and through to 500 μm.

A second core is seen to the east of the modelled core in 322.334+0.561 but this core contains an 8 μm point source. A possible third core is also visible to the north-west of 322.334+0.561. However, while in absorption at 8 μm and emission at 250 and 350 μm, no emission is seen at 500 μm. Therefore this third core did not meet our requirements to be labelled as *Herschel*-bright and was not included in our sample.

5.3.13 322.666−0.588

322.666−0.588 contains one of the most circular cores in our selection, with an eccentricity of ∼0.1. Observations of 322.666−0.588 and its core can be seen in Figure 5.13. When viewed at 250 μm, 322.666−0.588 appears to contain only a

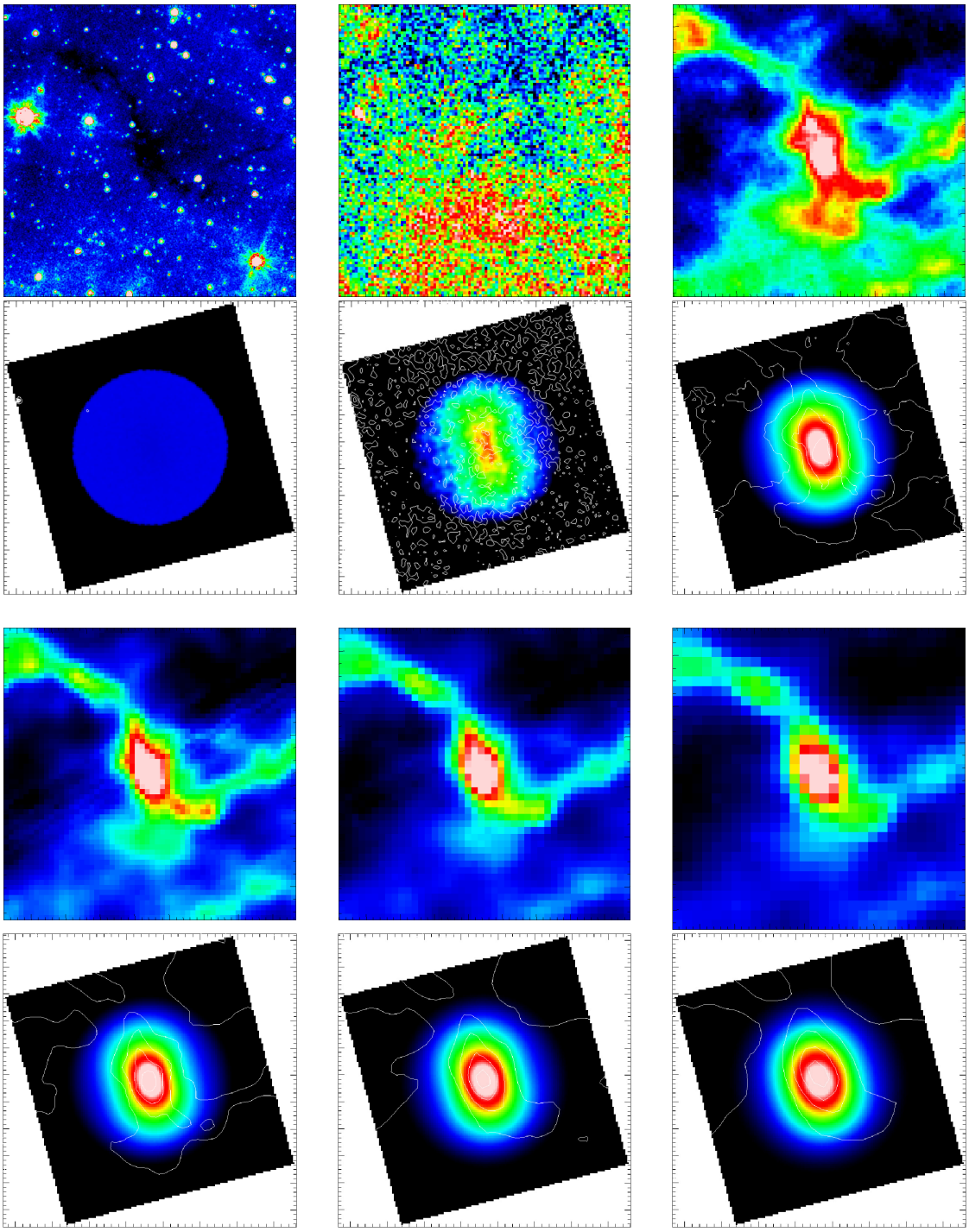

Figure 5.11: 321.753+0.669 - Upper row: Observational images of the infrared dark core at (left-right) *Spitzer* 8 μm, PACS 70 μm and PACS 160 μm. Second row: Modelled images at 8 μm, 70 μm and 160 μm. Third row: Observational at SPIRE 250, 350 and 500 μm. Lower row: Modelled images at 250, 350 and 500 μm. All images are $\sim$0.07$\times$0.07° in size, equivalent to 2.56$\times$2.56 pc.

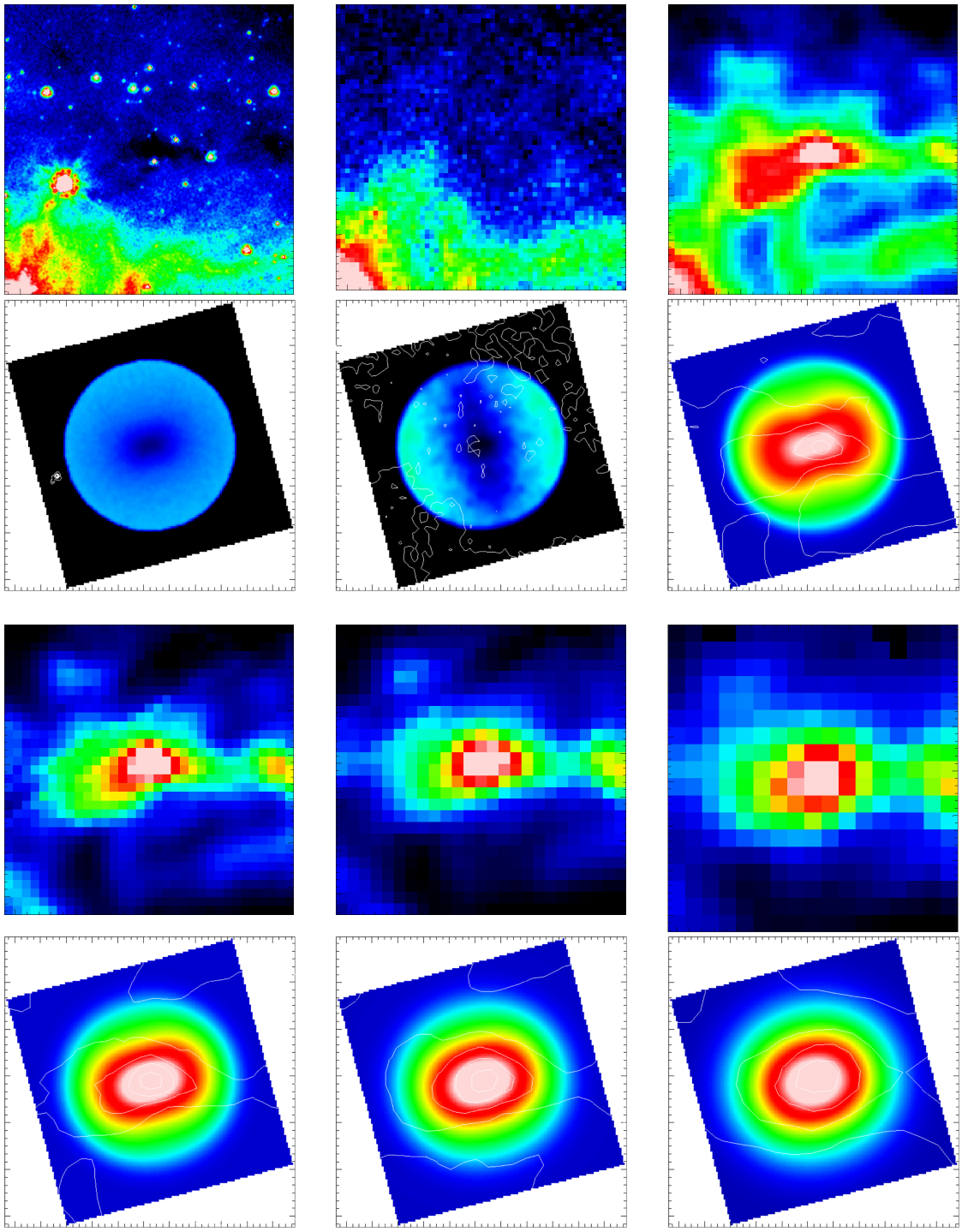

Figure 5.12: 322.334+0.561 - Upper row: Observational images of the infrared dark core at (left-right) *Spitzer* 8 μm, PACS 70 μm and PACS 160 μm. Second row: Modelled images at 8 μm, 70 μm and 160 μm. Third row: Observational at SPIRE 250, 350 and 500 μm. Lower row: Modelled images at 250, 350 and 500 μm. All images are $\sim$0.04$\times$0.04° in size, equivalent to 2.56$\times$2.56 pc.

single core, located at the centre of the images. It, and the parent IRDC, are seen in absorption at 8 μm and in emission at the four longest wavelengths. At 70 μm the noise in the data makes it unclear whether the core or the IRDC is showing any emission. Emission from the parent IRDC can be seen extending towards the east of the central core, and can be seen at 160, 250, 350 and 500 μm. No other IRDCs are seen in Figure 5.13.

5.3.14 322.914−0.321

322.914−0.321 is seen in absorption at 8 μm and in emission from 70 μm to 500 μm (see Figure 5.14). This is one of only three isolated, starless cores which shows clear emission at 70 μm, with a flux density of 2.5 Jy. The starless core we focus on is the bright object seen at the centre of the images. It is possible that 322.914−0.321 contains a second core that is located to the west of the central core. This core has a FWHM of $\sim$20″ and is much smaller than the modelled core which has a FWHM of $\sim$40″. The second core can be seen in the observations at 160 and 250 μm, but not at 350 or 500 μm, where the resolution of the images is lower. It is therefore not isolated at 500 μm and so was not selected for modelling.

A second *Spitzer*-dark and *Herschel*-bright object can be seen at the lower edge of the images on Figure 5.14. This is a separate IRDC, 322.895+0.277, and is not connected to 322.914−0.321. 322.895+0.277 contains a single core but it is not modelled due to the presence of an 8 μm point source. All other sources in the images are *Spitzer*-bright and so have been excluded from this study.

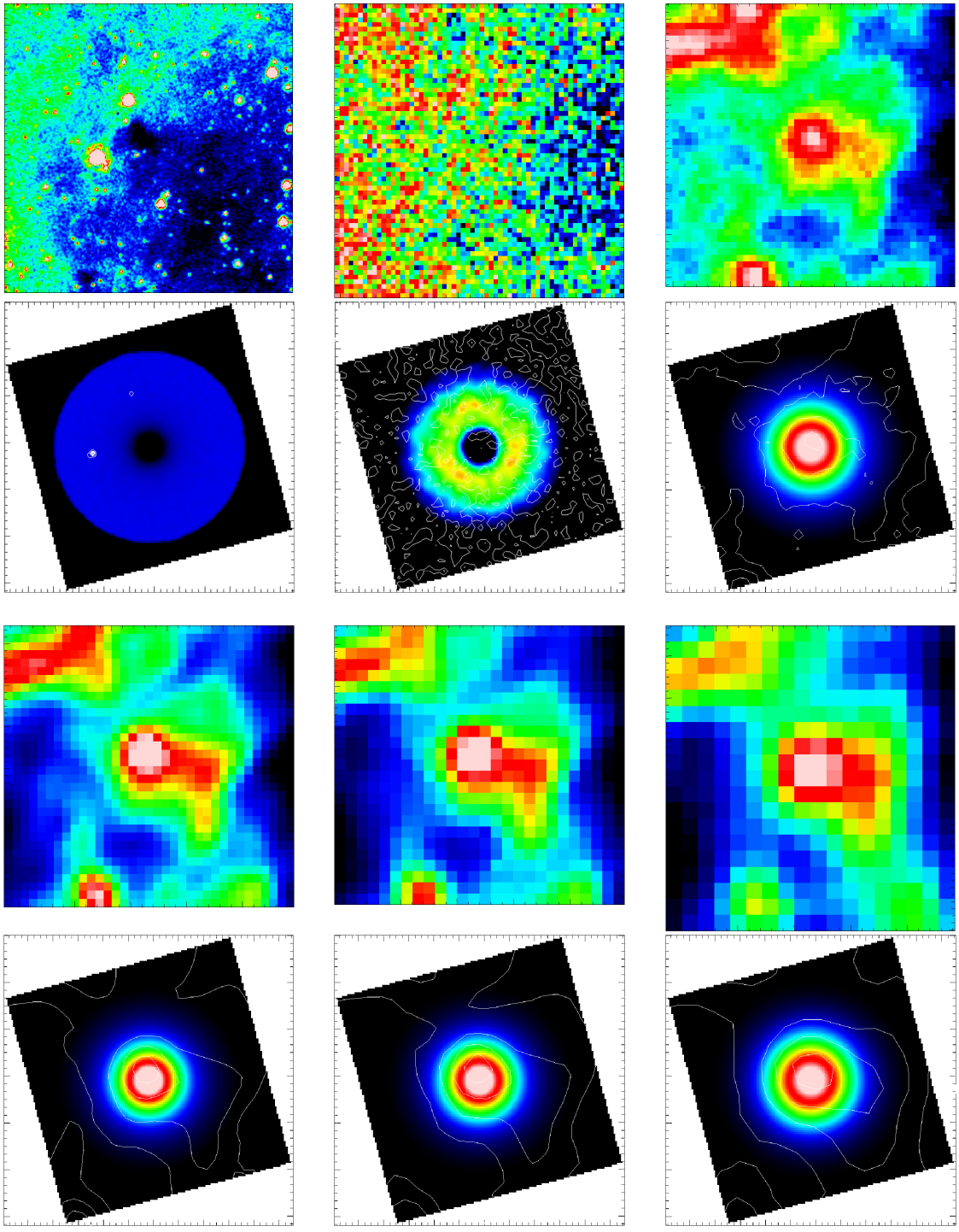

Figure 5.13: 322.666−0.588 - Upper row: Observational images of the infrared dark core at (left-right) *Spitzer* 8 μm, PACS 70 μm and PACS 160 μm. Second row: Modelled images at 8 μm, 70 μm and 160 μm. Third row: Observational at SPIRE 250, 350 and 500 μm. Lower row: Modelled images at 250, 350 and 500 μm. All images are $\sim$0.04×0.04° in size, equivalent to 2.56×2.56 pc.

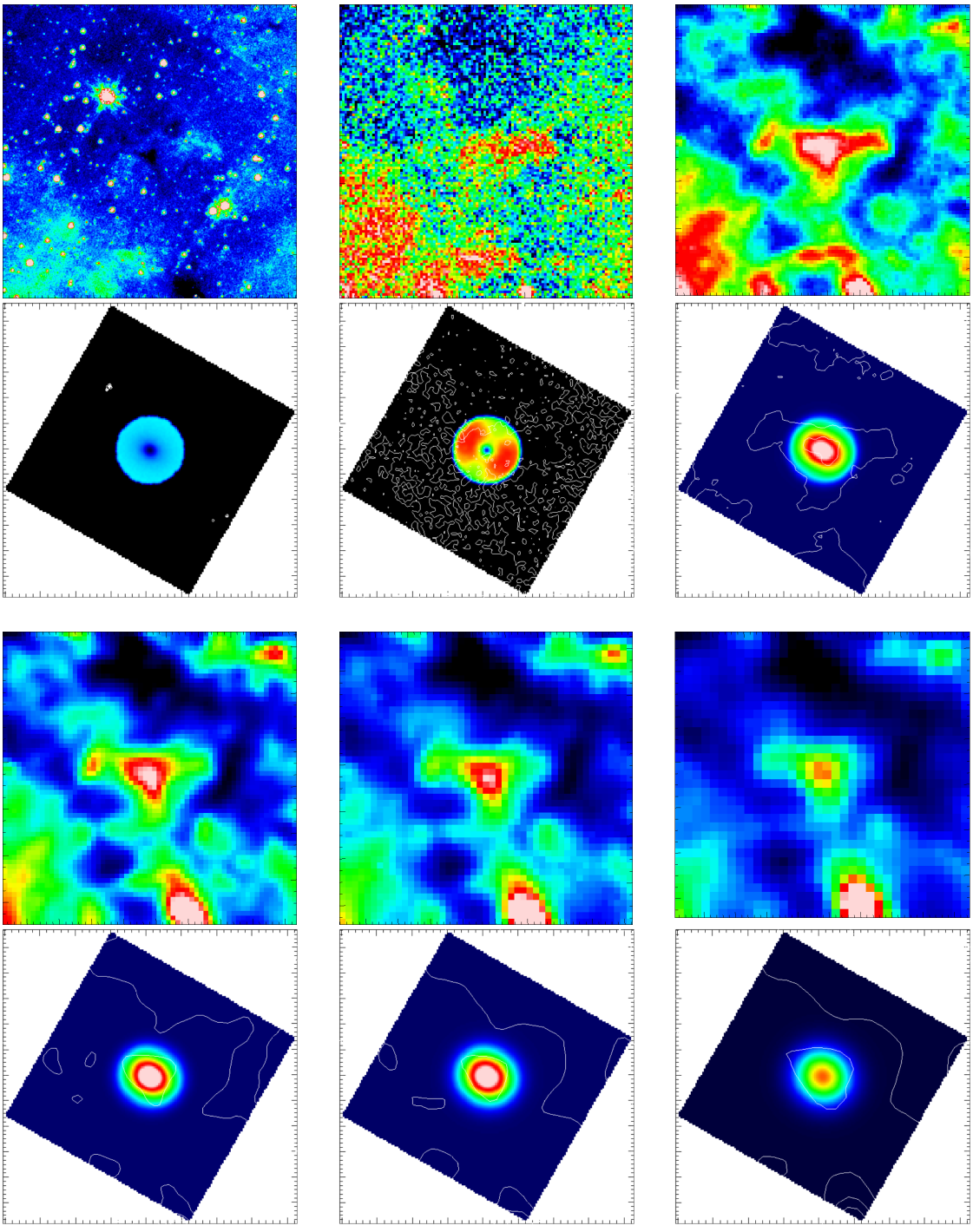

Figure 5.14: 322.914+0.321 - Upper row: Observational images of the infrared dark core at (left-right) *Spitzer* 8 μm, PACS 70 μm and PACS 160 μm. Second row: Modelled images at 8 μm, 70 μm and 160 μm. Third row: Observational at SPIRE 250, 350 and 500 μm. Lower row: Modelled images at 250, 350 and 500 μm. All images are $\sim$0.07$\times$0.07° in size, equivalent to 2.56$\times$2.56 pc.

5.3.15 326.495+0.581

Observations of 326.495+0.581 can be seen in Figure 5.15. At these wavelengths, 326.495+0.581 appears to contain a single core, located in the centre of the images. Both the core and parent cloud are seen in absorption at 8 and 70 μm, and both are seen in emission from 160 to 500 μm. However, at 160 μm the core appears smaller (FWHM $\approx 23''$) than at longer wavelengths (FWHM $\approx 50''$ at 500 μm). This is likely to be due to the decreased resolution at longer wavelengths. Emission that appears to be from the parent cloud at 160 μm appears to be from the core at 500 μm. The size of the core is set from its appearance in the 250 μm data and has a FWHM of $\sim 30''$. Extended emission from the parent IRDC is seen to the north of the core.

No other IRDCs are visible in these observations, although two other emission sources are seen, one to the east of the core and one to the west. However, both are seen in emission at 8 μm and so are not IRDCs.

5.3.16 326.620−0.143

326.620.0.143 appears to contain a single core in the *Herschel* observations – see Figure 5.16. The core and the parent IRDC are seen in absorption at 8 and 70 μm and in emission at 160, 250, 350 and 500 μm. The extended emission from the parent IRDC is most evident at 160 and 250 μm and nearly surrounds the entire core. However, by 350 and 500 μm the resolution of the data is much lower and the extended emission becomes confused with emission from other nearby sources.

A second IRDC is visible in the images to the north of 326.620−0.143. This

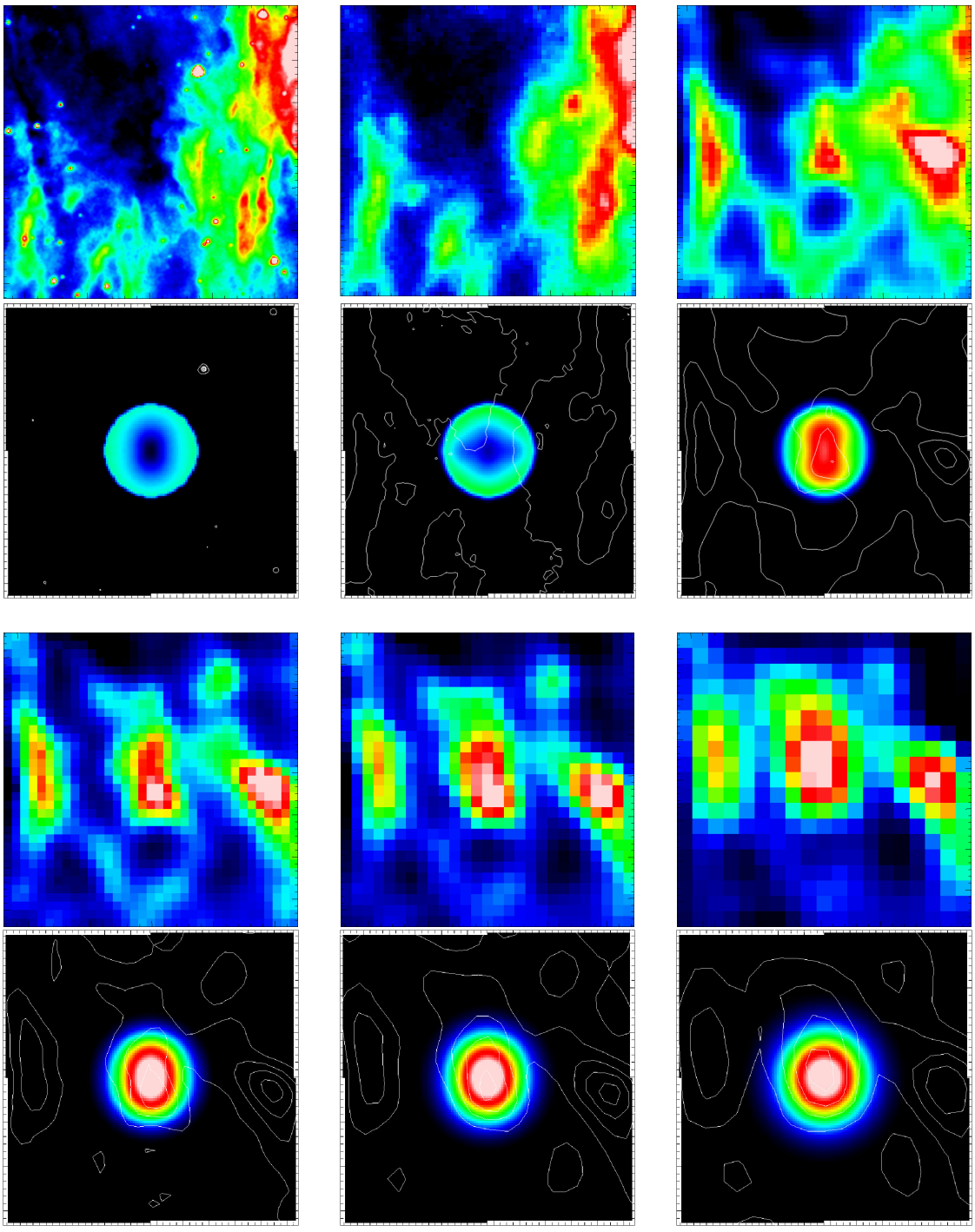

Figure 5.15: 326.495+0.581 - Upper row: Observational images of the infrared dark core at (left-right) *Spitzer* 8 μm, PACS 70 μm and PACS 160 μm. Second row: Modelled images at 8 μm, 70 μm and 160 μm. Third row: Observational at SPIRE 250, 350 and 500 μm. Lower row: Modelled images at 250, 350 and 500 μm. All images are $\sim$0.05$\times$0.05° in size, equivalent to 2.56$\times$2.56 pc.

is named 326.521+0.582 and is labelled as a separate object by PF09. The core in 326.521+0.582 contains an 8 μm point source and so is not modelled. All other emission seen in the FIR is also seen in the MIR.

5.3.17 326.632+0.951

The core in 326.632+0.951 is one of the smallest objects we model with a FWHM of 24″. The observations of 326.632+0.951 are shown in Figure 5.17. The data at 70 μm are particularly stripy in this region. However, as this wavelength is not important for either classification or modelling purposes, this core is included in our sample. The core is seen in absorption at 8 μm and in emission at 160 μm and longwards. The data quality at 70 μm makes it impossible to tell if the core is in absorption or emission at this wavelength.

There are two IRDCS neighbouring 326.632+0.951 each containing a single core. 326.641+0.941 is located to the north-east of 326.632+0.951. The core within was not modelled due to the presence of an 8 μm point source. 326.596+0.957 is located to the south-west of 326.632+0.951, the core in this IRDC was not modelled because it did not meet our isolation criteria at 500 μm. Neither of these IRDCS are connected to 326.632+0.951. The region to the north-west of 326.632+0.951 is seen in absorption at all six wavelengths and so is likely to be a hole in the sky.

5.3.18 326.811+0.656

Observations of 326.811+0.656 can be seen in Figure 5.18. The core selected for modelling is seen in the centre of the images. It is visible in emission at 160, 250,

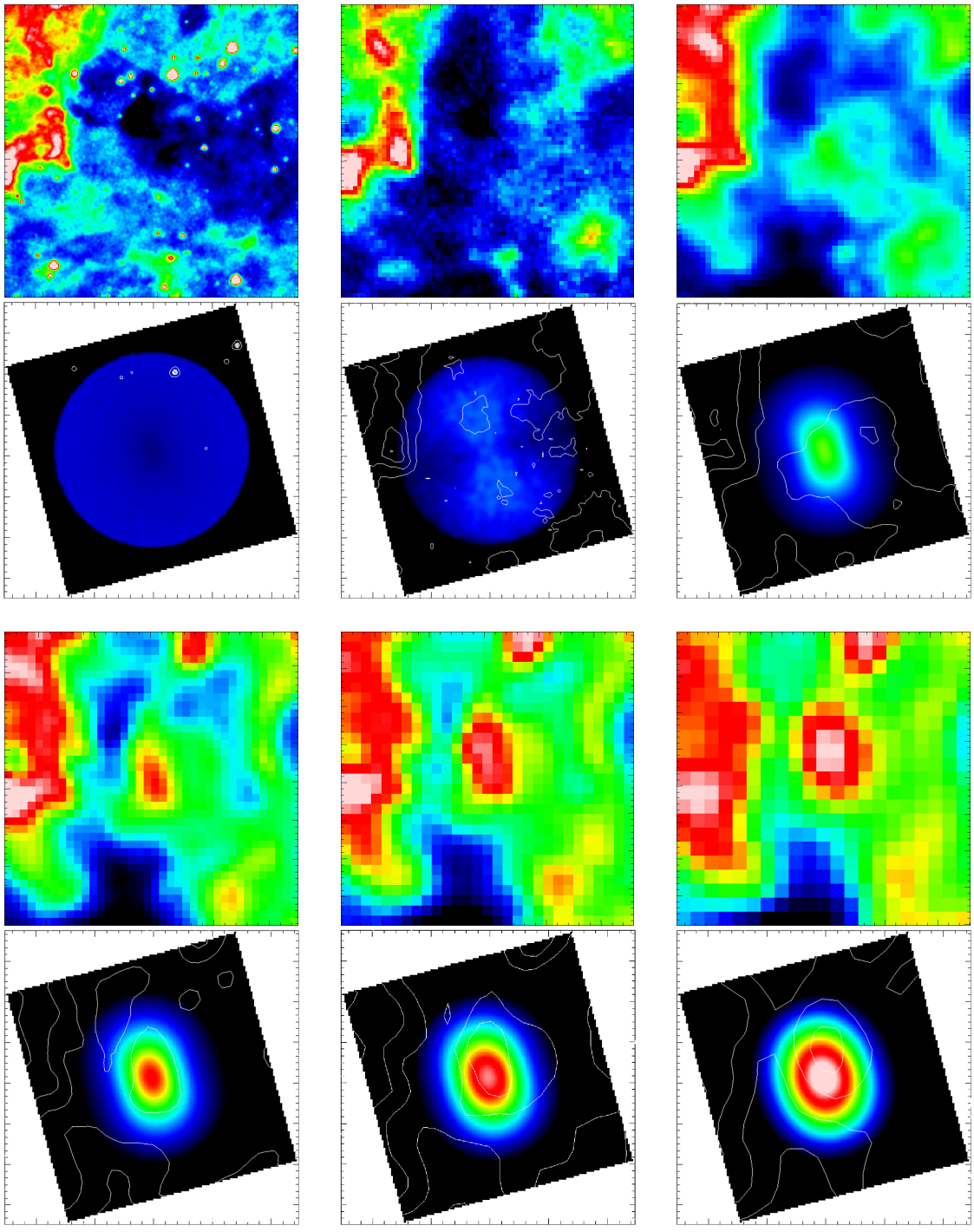

Figure 5.16: 326.620−0.143 - Upper row: Observational images of the infrared dark core at (left-right) *Spitzer* 8 μm, PACS 70 μm and PACS 160 μm. Second row: Modelled images at 8 μm, 70 μm and 160 μm. Third row: Observational at SPIRE 250, 350 and 500 μm. Lower row: Modelled images at 250, 350 and 500 μm. All images are $\sim$0.05$\times$0.05° in size, equivalent to 2.56$\times$2.56 pc.

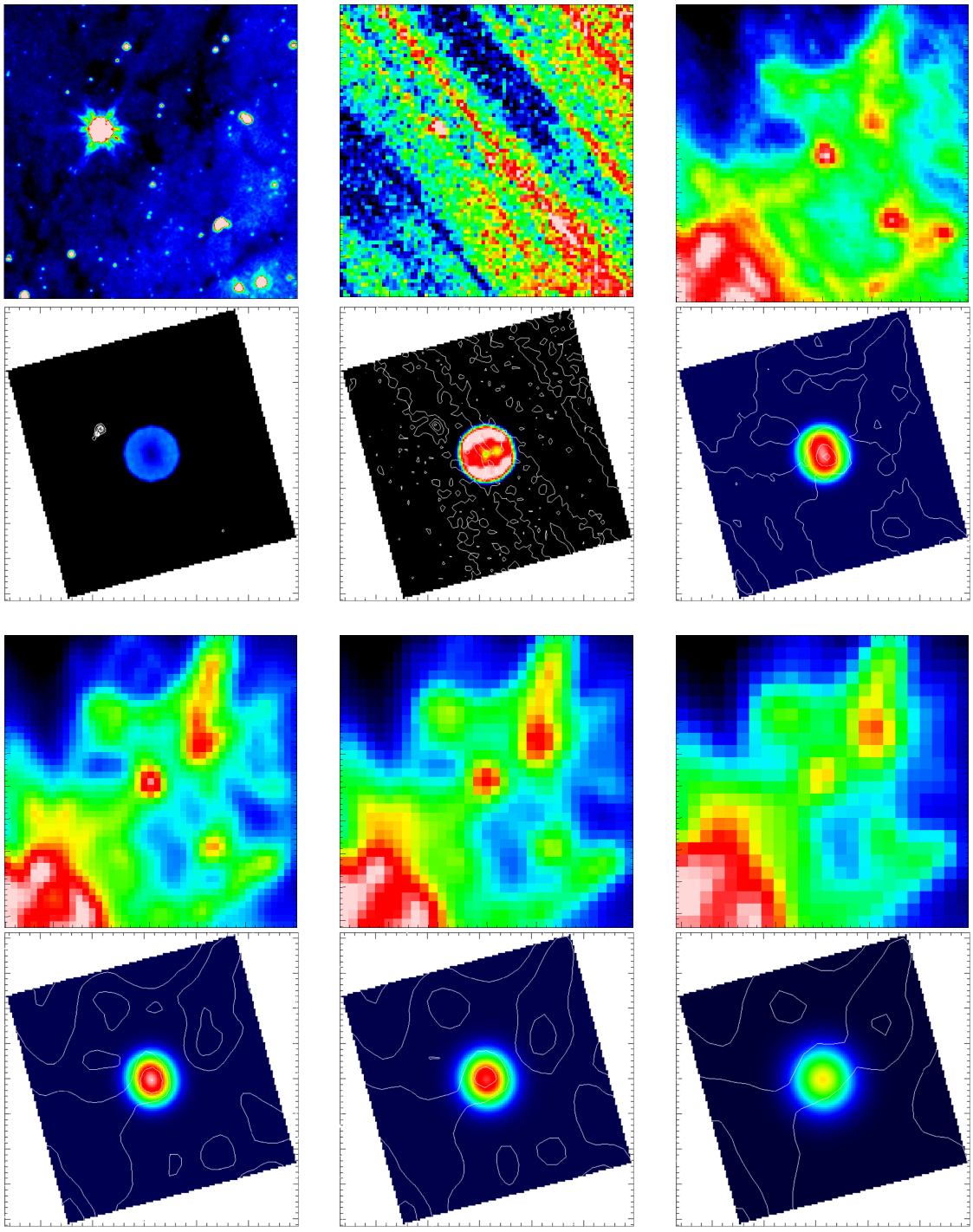

Figure 5.17: 326.632+0.951 - Upper row: Observational images of the infrared dark core at (left-right) *Spitzer* 8 μm, PACS 70 μm and PACS 160 μm. Second row: Modelled images at 8 μm, 70 μm and 160 μm. Third row: Observational at SPIRE 250, 350 and 500 μm. Lower row: Modelled images at 250, 350 and 500 μm. All images are $\sim$0.06$\times$0.06° in size, equivalent to 2.56$\times$2.56 pc.

350 and 500 μm, and in absorption at 8 μm and, albeit only faintly, at 70 μm. The appearance of the core at 160 μm is elongated (e=0.74), changing as the wavelengths increase until it appears much more circular at 500 μm (e=0.46). This is likely to be an effect of the resolution of the images decreasing as the wavelength increases.

A second core exists in the image, to the west of the central core. This second core is in a different IRDC and is not connected to 326.811+0.656. This core was not selected for modelling, as it contains an 8 μm point source. All other emission sources in these images are *Spitzer*-bright.

5.3.19 328.432−0.522

At 70 μm the extended emission from 328.432−0.522 can be seen in emission, although the core at the centre appears to be in absorption. This can be seen in the images of 328.432−0.522 shown in Figure 5.19. This may be explained by the fact that the core is the densest part of the IRDC and therefore also potentially the coldest. If outer parts of the cloud are warmer they may be already be emitting at 70 μm. Both the core and the parent IRDC are seen in absorption at 8 μm and emission in the other four wavelengths. The core itself can be seen in the centre of the images, with the extended emission from the IRDC surrounding it.

Two other IRDCs are visible in these images. 328.400−0.495 which is to the south-west and west of 328.432−0.522. Observations of this IRDC were of insufficient quality to allow it to be modelled. The second IRDC is to the south-east of 328.432−0.522 and is not listed in PF09. As it does not appear to be connected to 328.432−0.522 in the FIR data we consider it a separate object.

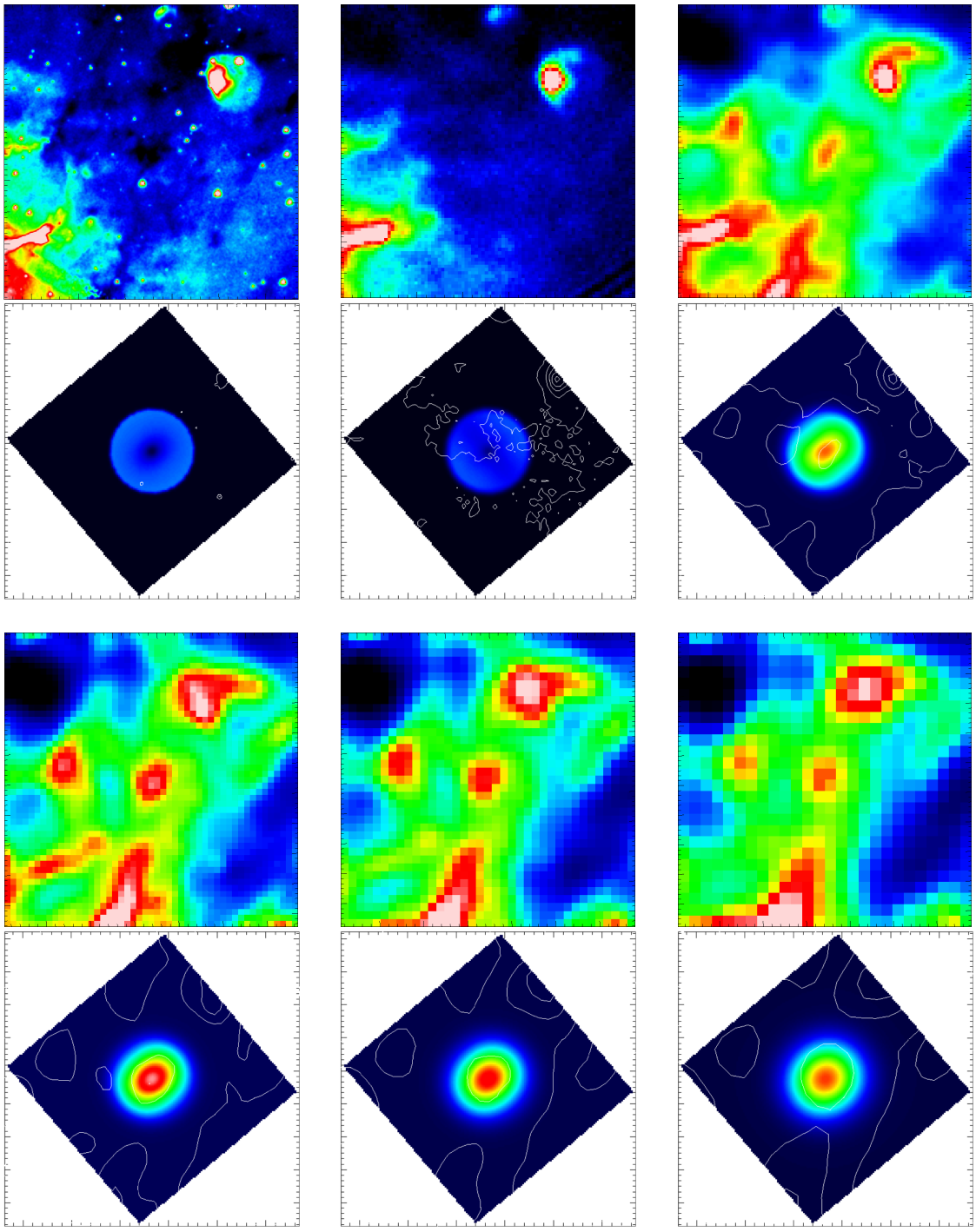

Figure 5.18: 326.811+0.656 - Upper row: Observational images of the infrared dark core at (left-right) *Spitzer* 8 μm, PACS 70 μm and PACS 160 μm. Second row: Modelled images at 8 μm, 70 μm and 160 μm. Third row: Observational at SPIRE 250, 350 and 500 μm. Lower row: Modelled images at 250, 350 and 500 μm. All images are $\sim$0.05$\times$0.05° in size, equivalent to 2.56$\times$2.56 pc.

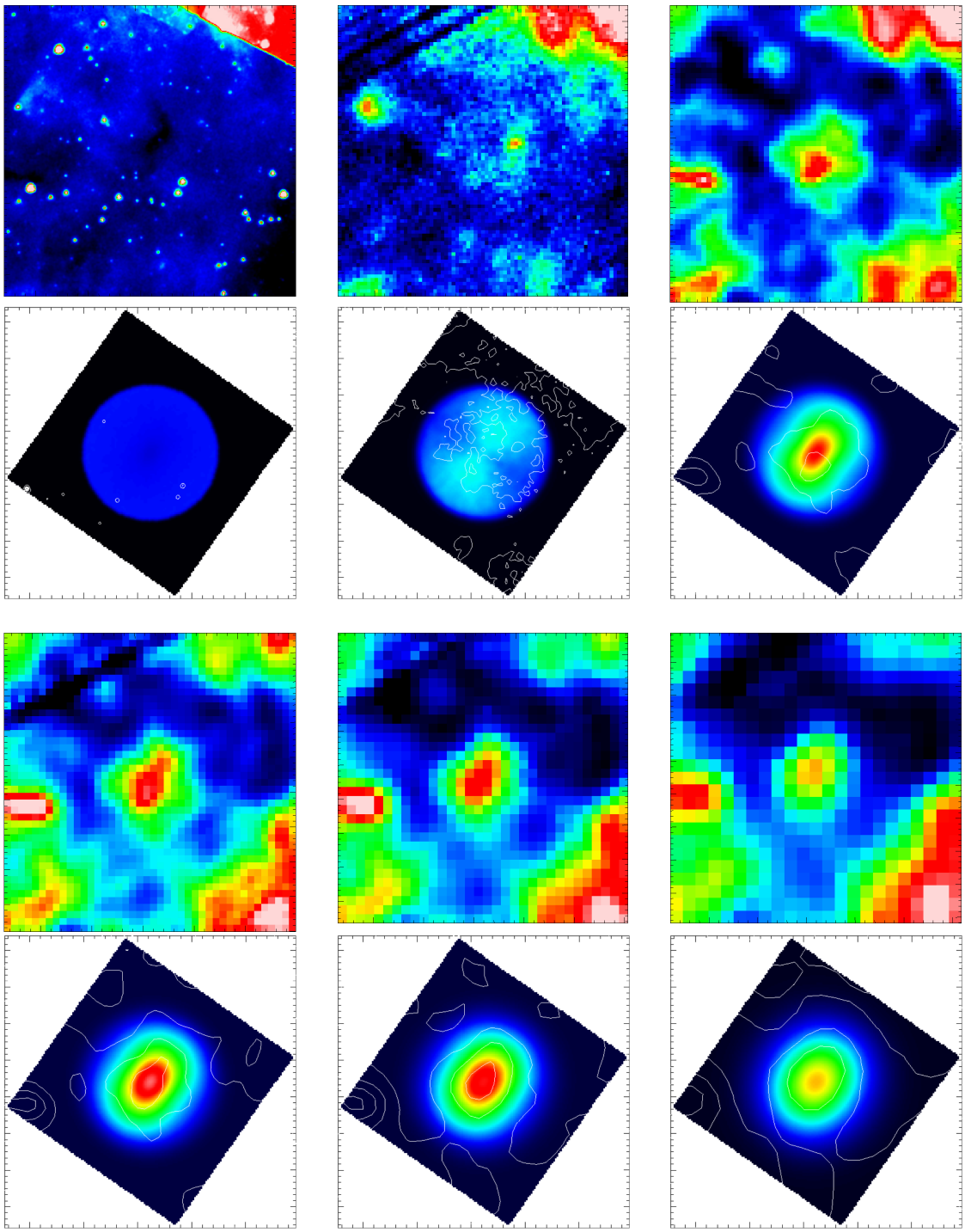

Figure 5.19: 328.432−0.522 - Upper row: Observational images of the infrared dark core at (left-right) *Spitzer* 8 μm, PACS 70 μm and PACS 160 μm. Second row: Modelled images at 8 μm, 70 μm and 160 μm. Third row: Observational at SPIRE 250, 350 and 500 μm. Lower row: Modelled images at 250, 350 and 500 μm. All images are $\sim$0.05×0.05° in size, equivalent to 2.56×2.56 pc.

5.3.20 329.403−0.736

Observations of 329.403−0.736 can be seen in Figure 5.20. 329.403−0.736 can be seen in absorption at 8 and 70 μm, although less clearly at 70 μm than at 8 μm, and in emission at 160, 250, 350 and 500 μm. There is a single core, seen in the centre of the images, and the emission from the parent cloud extends towards the north-west of the image.

A second, and possibly a third, core are visible in Figure 5.20. These can be seen to the west and north, respectively, of the core we modelled. As they are confused with one another at 500 μm they do not meet our criteria for selection for modelling. The possible third core does not appear as a separate object at 500 μm and because of this is not included in our sample of *Spitzer*-dark and *Herschel*-bright objects.

5.4 Distances to the Cores

The distances to the cores are not available in previous literature. As the distance is a required input for PHAETHON, we calculated the distance to each core as follows. The Brand & Blitz (1993) velocity curve was assumed:

$$\frac{\theta}{\theta_0} = a_1 \left(\frac{d_g}{d_{g,0}} \right)^{a_2} + a_3, \tag{5.1}$$

where θ is the core's circular rotation velocity (the velocity at which it orbits the Galactic centre) and d_g is the core's Galacto-centric radius. θ_0 and $d_{g,0}$ are the solar equivalents. Here, the IAU approved values of $\theta_0 = 220\,\mathrm{km\,s^{-1}}$ and $d_{g,0} = 8.5\,\mathrm{kpc}$ are used (e.g. Kerr & Lynden-Bell, 1986). a_1, a_2 and a_3 are constants

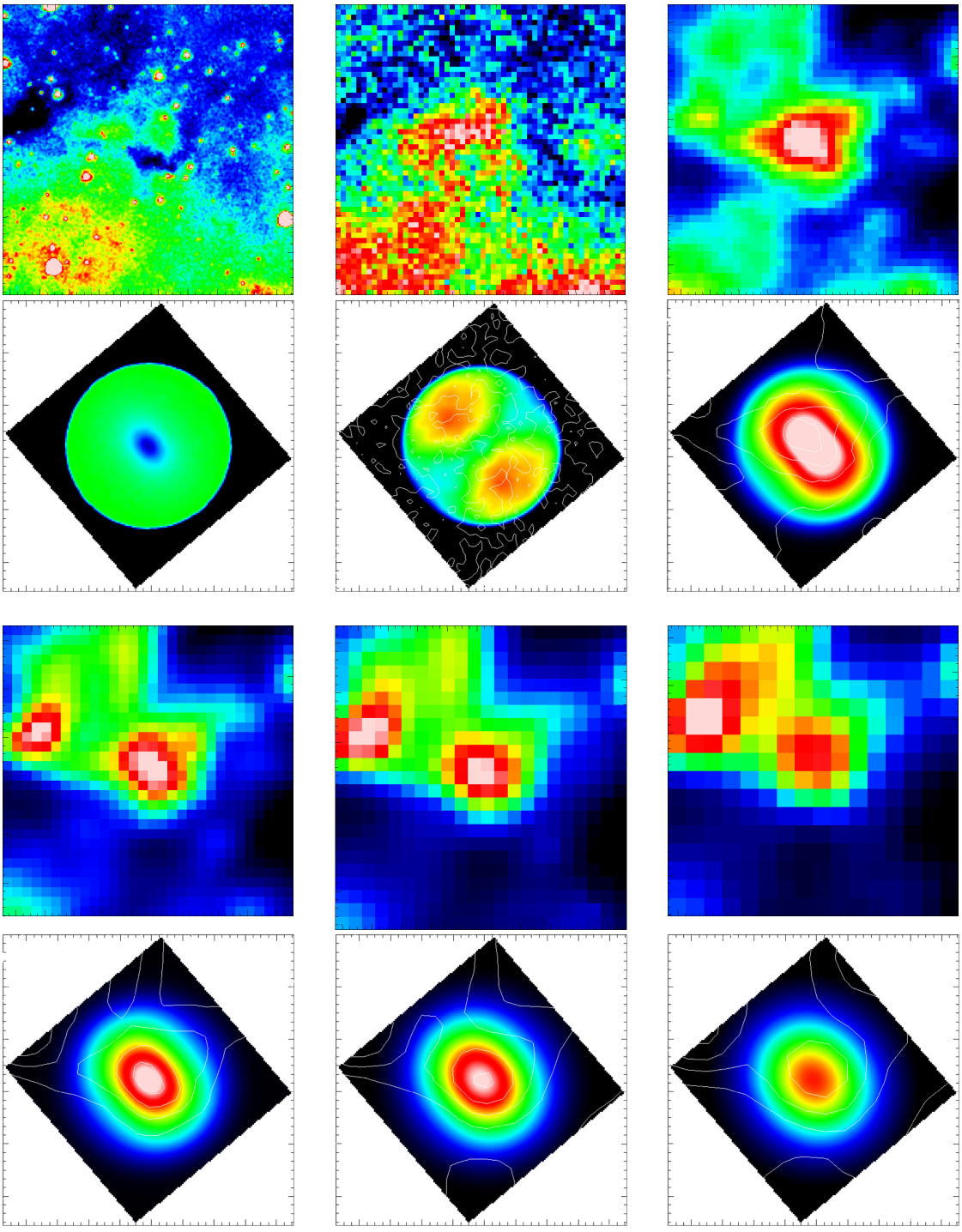

Figure 5.20: 329.403−0.736 - Upper row: Observational images of the infrared dark core at (left-right) *Spitzer* 8 μm, PACS 70 μm and PACS 160 μm. Second row: Modelled images at 8 μm, 70 μm and 160 μm. Third row: Observational at SPIRE 250, 350 and 500 μm. Lower row: Modelled images at 250, 350 and 500 μm. All images are $\sim$0.03×0.03° in size, equivalent to 2.56×2.56 pc.

to be determined.

Brand & Blitz (1993) found that the constants in Equation 5.1 are $a_1 = 1.0069$, $a_2 = 0.0363$ and $a_3 = 0.0065$ for sources in the Southern hemisphere (i.e. those with Galactic longitudes between 180° and 360°). We make the assumption that $\left(\frac{d_g}{d_{g,0}}\right)^{a_2} \approx 1$, valid for $d_g \gtrsim 2.0\,\mathrm{kpc}$, and Equation 5.1 becomes:

$$\theta = \theta_0 \left(a_1 + a_3\right). \tag{5.2}$$

CO velocities were taken from Dame et al. (1987) and used as the cores' radial velocities, V_{LSR}, the cores' velocities along the observer's line of sight. Assuming a circular orbit, V_{LSR} can be related to θ (Brand & Blitz, 1993), via

$$V_{LSR} = \left(\frac{\theta d_{g,0}}{d_g} - \theta_0\right) \sin(l)\cos(b), \tag{5.3}$$

where l and b are the Galactic longitude and latitude of a core. By substituting Equation 5.2 into Equation 5.3, d_g can be found for each core via:

$$d_g = \frac{\theta_0 \left(a_1 + a_3\right) d_{g,0}}{\theta_0 + \left(\frac{V_{LSR}}{\sin(l)\cos(b)}\right)}. \tag{5.4}$$

Once the Galacto-centric distance is known, the helio-centric distance can be calculated (Brand & Blitz, 1993), using the equation:

$$d_h^2 \cos^2(b) - 2 d_{g,0} d_h \cos(b)\cos(l) + \left(d_{g,0}^2 - d_g^2\right) = 0 \tag{5.5}$$

where d_h is the core's helio-centric distance. This is a quadratic equation of the

form:

$$ax^2 + bx + c = 0. \tag{5.6}$$

d_h was therefore calculated using the quadratic formula:

$$x = \frac{-b \pm \sqrt{b^2 - 4ac}}{2a}, \tag{5.7}$$

which, in this specific case, becomes:

$$d_h = \frac{2d_{g,0}\cos(b)\cos(l) \pm \sqrt{\left(2d_{g,0}\cos(b)\cos(l)\right)^2 - 4\cos^2(b)\left(d_{g,0}^2 - d_g\right)}}{2\cos^2(b)}. \tag{5.8}$$

This results in two possible helio-centric distances for each core: one on the near side of the Galaxy and one on the far.

The near/far distance ambiguity exists in all cases. However, each of our cores had to show up in absorption at 8 μm to be considered a candidate IRDC in the first place (PF09). Therefore, most of the Galactic MIR-emitting material must be behind our cores, rather than in front of them, or absorption would not be evident. For this reason, we assume that the near distance is correct for all of the cores. The calculated distance to each core is listed in Table 5.2. The 20 cores modelled here have a mean helio-centric distance of 3.1 kpc.

5.5 Modelling the Cores

Our 20 isolated, starless cores were modelled using Phaethon (Stamatellos & Whitworth 2003, 2005; Stamatellos et al. 2010; see Chapter 3 for further details on Phaethon).

Table 5.2: The physical properties of the modelled cores. Column 1 gives the name of the parent cloud as it appears in PF09. Columns 2 and 3 show the Right Ascension and Declination of the cores in degrees. Column 4 is the calculated kinematic distance from the sun to each core (see Section 5.4). Column 5 shows the interstellar radiation field needed to match the model to core's SED, it is given in terms of multiples of the Black (1994) radiation field. Column 6 is the central density of the core. Column 7 is the core's semi-major axis, as measured at 250 μm. Column 8 is the flattening radius of the core and is set to be one-tenth of the semi-major axis. Column 9 gives the asymmetry factor, a measure of the eccentricity of the core. Column 10 is the mass of each individual core. Columns 11 and 12 show the temperatures at the centre and the surface of each core, respectively, assuming a viewing angle of θ=0 °. The temperatures and masses of the cores are calculated by the model (see text for more details). Column 13 is the χ^2 value for each model. The χ^2 values show the goodness of fit of the model. See text for details.

Name of the Parent IRDC	RA 2000 (°)	Dec 2000 (°)	Distance (pc)	ISRF	$n_0(H_2)$ (cm^{-3})	R_{max} (pc)	R_0 (pc)	Asymmetry factor	Mass ($M_\odot$)	Temperature (K) Centre	Surface	χ^2
305.798−0.097	199.15	−62.83	2900	3.8	3.0×10^4	0.9	0.09	3.0	208	11.0	22.1	1.51
307.495+0.660	202.57	−61.87	3600	0.7	5.0×10^3	0.9	0.09	3.0	34.7	11.3	17.1	1.41
309.079−0.208	206.24	−62.44	3500	1.2	1.3×10^4	0.9	0.09	3.0	90.2	10.3	18.3	2.77
309.111−0.298	206.35	−62.52	3900	5.3	1.7×10^4	0.7	0.07	3.0	53.8	13.5	23.9	1.94
310.297+0.705	208.33	−61.28	4400	2.3	5.6×10^4	0.9	0.09	1.3	75.3	10.1	20.6	2.48
314.701+0.183	217.28	−60.44	3500	1.6	9.5×10^4	0.6	0.06	2.0	103	8.80	19.0	1.83
318.573+0.642	223.84	−58.41	2900	1.8	3.4×10^4	0.5	0.05	3.0	40.5	10.5	19.6	0.75
318.802+0.416	224.43	−58.51	2900	4.6	5.5×10^3	0.6	0.06	3.0	11.3	16.5	23.8	2.16
318.916−0.284	225.26	−59.07	2500	2.2	5.7×10^4	0.4	0.04	3.0	34.7	10.2	20.0	0.72
321.678+0.965	228.59	−56.61	2100	0.6	2.5×10^4	0.6	0.06	3.0	51.4	8.80	16.1	4.04
321.753+0.669	228.99	−56.83	2000	1.6	1.5×10^3	0.8	0.08	3.0	7.31	15.6	20.4	2.32
322.334+0.561	229.99	−56.61	3500	2.0	1.3×10^4	0.9	0.09	3.0	90.2	11.5	20.2	1.45
322.666−0.588	231.65	−57.39	3500	1.3	1.3×10^5	1.0	0.10	1.0	63.9	8.10	19.1	4.35
322.914+0.321	231.11	−56.49	2100	3.7	2.0×10^5	0.4	0.04	1.2	17.9	10.3	22.4	2.14
326.495+0.581	235.97	−54.20	2700	10.4	1.2×10^5	0.4	0.04	2.9	69.6	12.0	26.2	1.02
326.620−0.143	236.91	−54.70	3000	2.2	4.5×10^3	1.0	0.10	3.0	38.8	14.1	20.8	1.58
326.632+0.951	235.77	−53.83	2600	4.0	9.5×10^4	0.3	0.03	2.4	17.5	10.4	23.0	10.12
326.811+0.656	236.32	−53.95	2800	8.5	2.0×10^5	0.3	0.03	1.4	57.4	11.3	25.5	2.07
328.432−0.522	239.72	−53.84	3100	2.8	6.7×10^3	0.8	0.08	2.8	29.6	14.2	21.6	2.18
329.403−0.736	241.19	−53.37	4500	3.0	1.4×10^4	1.0	0.10	2.0	70.1	12.7	21.7	2.51

The input variables of the code are the density profile, the strength of the ambient radiation field, the dust properties of the system, the size of the core and its geometry (i.e. spherical or flattened). The code calculates the temperature profile of the system as well as spectral energy distributions (SEDs – see Figures 5.21 and 5.22) and intensity maps, at different wavelengths and viewing angles — see Figures 5.1–5.20.

All the cores showed some measure of eccentricity in the observations and so were modelled with a flattened geometry. In this case the density profile is given by Equation 3.31.

The FWHM of the major axis of each observed core, as seen at 250 μm, was used as the model core's semi-major axis, R_{max}. The FWHM of the cores have an error of $\pm 15\,\%$, due primarily to the uncertainties in the background levels. R_{max} was calculated using:

$$R_{max} = d_h \times \mathrm{FWHM/rad}, \tag{5.9}$$

where d_h is the helio-centric distance, found via Equation 5.8. The flattening radius, R_0, was set at one tenth of the FWHM. The semi-minor axis of the core was matched as closely as possible to the observations at 250 μm by altering the eccentricity of the modelled core.

The flux density, integrated over twice the FWHM of each core using an elliptical aperture, was measured in all five FIR maps. An SED was plotted for each core. These flux densities have been background subtracted, where the background was defined using an off-cloud, elliptical aperture. For example, in the case of 318.916−0.284, the background aperture was set to the west of the IRDC. The flux densities are shown in Table 5.1 and plotted on SEDs in Figures 5.21 and 5.22.

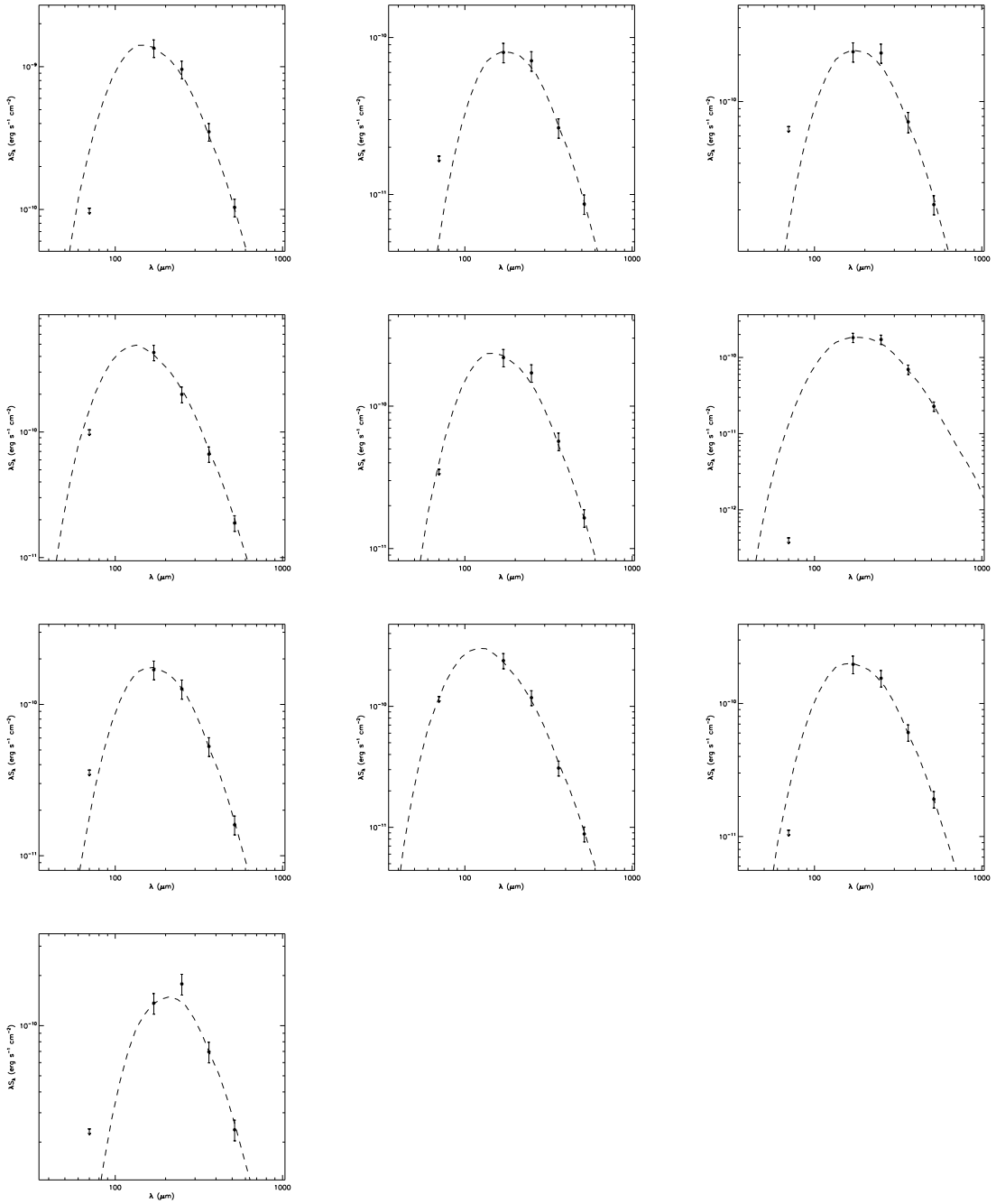

Figure 5.21: SEDs for the modelled cores in (left–right, upper–lower): 305.798−0.097, 307.495+0.660, 309.079−0.208, 309.111−0.298, 310.297+0.705, 314.701+0.183, 318.573+0.642, 318.802+0.416, 318.916−0.284 and 321.678+0.965. The points show the observed flux densities at each of our wavelengths, given in Table 5.1, and the SED output by the modelling is shown as a dashed line. The 70-μm point is used as an upper-limit only.

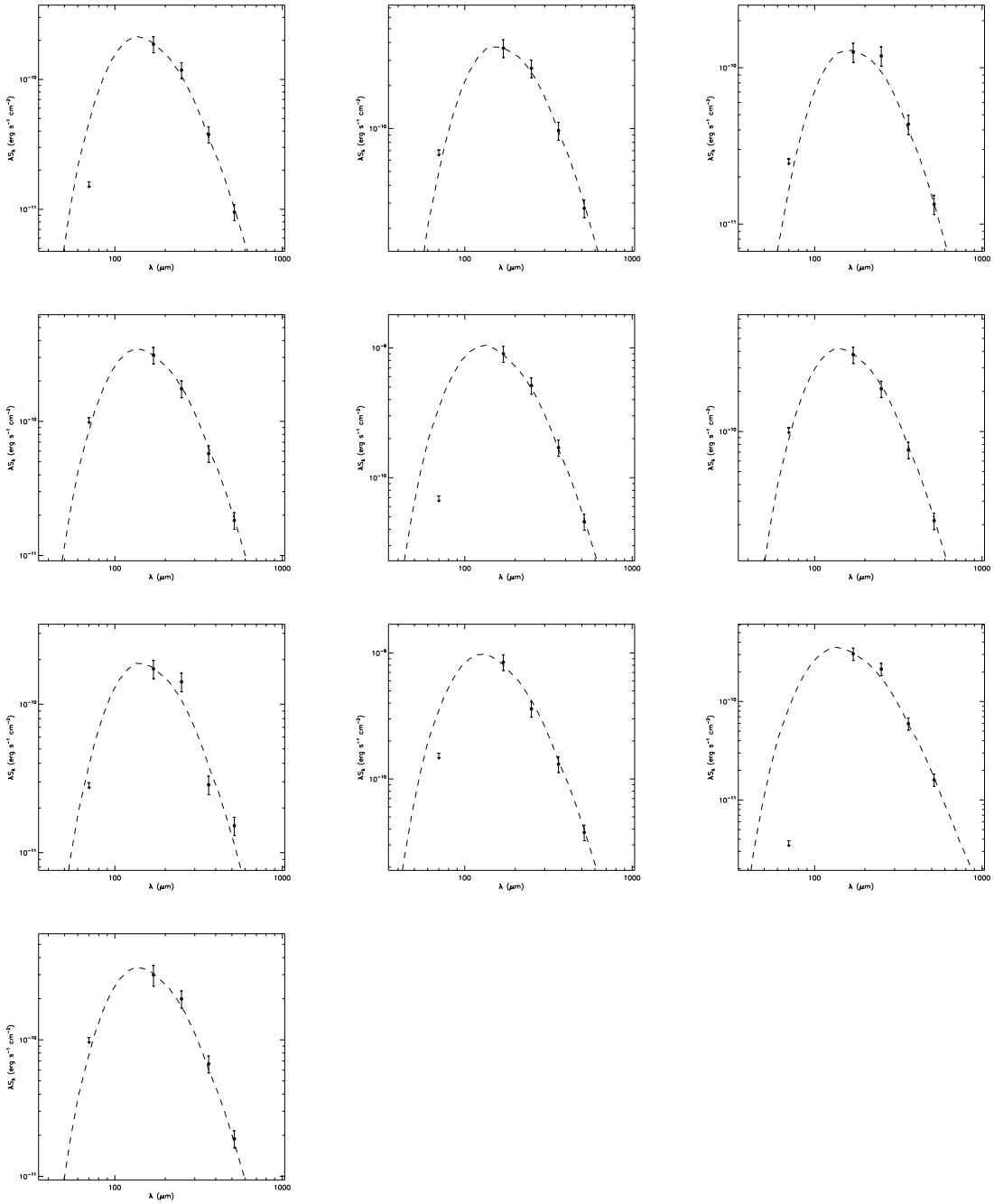

Figure 5.22: SEDs for the modelled cores in (left–right, upper–lower): 321.753+0.669, 322.334+0.561, 322.666−0.588, 322.914−0.321, 326.495+0.581, 326.620−0.143, 326.632+0.951, 326.811+0.656, 328.432−0.522 and 329.403−0.736. The points show the observed flux densities at each of our wavelengths, given in Table 5.1, and the SED output by the modelling is shown as a dashed line. The 70-μm point is used as an upper-limit only.

The central density, $n_0(H_2)$, and ISRF incident on the core were varied until the output model SED matched the observed data. The model SEDs are shown in Figures 5.21 and 5.22 as a dotted line. The final values for $n_0(H_2)$ and the incident ISRF have an uncertainty of $\pm 15\,\%$. As in Chapter 3, this is based on a by-eye estimation of how much they can be varied until the model SED no longer fits the observed SED. The final values for $n_0(H_2)$ and the incident ISRF are listed in Table 5.2.

As was noted in Chapter 3, the internal structure of cores within IRDCs have not yet been observed in detail and our assumption of an elliptical geometry may, therefore, be an over-simplification. If there is structure on smaller scales than we can resolve, this might affect our results.

To test the goodness of fit of the modelled SED to the observed SED the χ^2 value was calculated for each core. A χ^2 that is very high implies the observed data is not a good fit to the observations. On the other hand, if χ^2 is too low then observed values fit too well to the expected data and the fit becomes suspicious. χ^2 was calculated via:

$$\chi^2 = \sum_i \frac{(M_i - O_i)^2}{\sigma_i^2}, \tag{5.10}$$

where M and O are the modelled and observed flux densities respectively and σ is the error on the observed data. Only the flux densities from 160–500 μm were taken into account when calculating χ^2. The 70 μm point was only used as an upper limit and was ignored in this calculation. The final χ^2 values for each model are listed in Table 5.2.

As there are four data points in each SED and two free parameters in the model (the ISRF and central density), there are two degrees of freedom. We aim for a 5% significance level (i.e. only a 5% chance that such a result could have

occurred by chance) and perform a two-sided test (meaning that we have both lower and upper limits on an acceptable value of χ^2). For a 5% significance level, with two degrees of freedom, χ^2 must be between 0.051 and 7.378 (Rouncefield & Holmes, 1993) for the model to be deemed a 'good' fit to the data.

To test the goodness of fit of the modelled to the observed morphology we compared two parameters: the eccentricity; and the FWHM. The eccentricity of the modelled core at 250 μm was compared to the observed eccentricity at 250 μm. A percentage difference of less than 20% was considered a good fit. The eccentricities of the observed and modelled cores are given in Table 5.3. The FWHM of the model and observed cores were also compared. The FWHM of the modelled core is expected to agree, within errors of $\sim$15 %, to the FWHM of the observed core. The FWHM of the observed and modelled cores at 250 μm are given in Table 5.4.

The observations were not deconvolved from the instrument beam before the FWHM of the cores were found. This lead to a small systematic increase in the model FWHM when compared to the observed FWHM. However, nineteen of the twenty model cores have a FWHM in agreement with the observed FWHM and so it can be assumed that the lack of deconvolution had no significant effect of the results of the modelling.

5.6 Models of Isolated, Starless Cores

Figures 5.1–5.20 show the output of the model at wavelengths corresponding to the wavelengths of the observed data. The modelled images have pixels of 0.02×0.02 pc in size. All of the model images have been convolved with the appropriate telescope beam size. For wavelengths where no emission is visible in the model (i.e. at 8 and

Table 5.3: The eccentricities of the cores (to 1 decimal place). Column 2 gives the eccentricity when measured from the data and column 3 shows the eccentricity as measured from the model. Column 4 is the difference between the data and model eccentricities as a percentage of the observed eccentricity to 2 significant figures.

IRDC Name	Eccentricity		Percentage
	Observed	Model	Difference (%)
305.798−0.097	0.9	0.9	0.0
307.495+0.660	0.8	0.9	13
309.079−0.208	0.8	0.9	13
309.111−0.298	0.9	0.9	0.0
310.297+0.705	0.5	0.6	20
314.701+0.183	0.8	0.9	13
318.573+0.642	0.8	0.9	13
318.802+0.416	0.8	0.9	13
318.916−0.284	0.8	0.9	13
321.678+0.965	0.9	0.9	0.0
321.753+0.669	0.9	0.9	0.0
322.334+0.561	0.8	0.9	13
322.666−0.588	0.1	0.1	0.0
322.914+0.321	0.6	0.5	20
326.495+0.581	0.9	0.9	0.0
326.620−0.143	0.9	0.9	0.0
326.632+0.951	0.6	0.9	50
326.811+0.656	0.7	0.7	0.0
328.432−0.522	0.8	0.9	13
329.403−0.736	0.6	0.6	0.0

70 μm), an image showing background radiation is shown. Note that no attempt was made to correctly model the surrounding area, these images are not an accurate representation of the parent cloud but do show, in most cases, the starless cores in absorption as seen in the observations (Stamatellos et al., 2010; Wilcock et al., 2011). Some images appear to show emission at 70 μm. As only the background radiation is shown at this wavelength, this actually implies a lack of absorption by the core at 70 μm, thus allowing emission from the background to be seen, rather than emission from the core itself. Further analysis of the physical parameters of the cores is discussed in Chapter 6.

5.6.1 305.798−0.097

The emission from the parent IRDC, described in Section 5.3.1, is ignored so only the emission from the central core is modelled. The modelled images, shown in Figure 5.1, are each overlaid with contours from the observed data. The size of the modelled core in 305.798−0.097 fits the observed core at all wavelengths. The FWHM of the observed core at 250 μm is 82″, while the modelled core has a FWHM of 62″, in agreement within our prescribed errors. However, the shape of the core is not an ideal match at 160 μm, as the observed core does not appear as a perfect ellipse but is instead almost hourglass-shaped. At 250 μm the model matches the shape of the observations well and the eccentricity of the model is identical to the observed core. The model shows absorption at 8 and 70 μm, in agreement with the observed data.

The model SED, shown in Figure 5.21 fits well with the flux densities at 160, 250, 350 and 500 μm. The fit has a χ^2 equal to 1.51, within the specified limits of a good fit. However, the model appears to over-estimate the flux density at 70 μm showing a flux density in excess of the upper limit measured from the observed data.

5.6.2 307.495+0.660

The model created for the core in 307.495+0.660 shows absorption at 8 and 70 μm (see Figure 5.2), comparable to the absorption seen in the observations. The size and shape of the model fits with the contours from the observed data at all wavelengths, although slightly better at longer wavelengths where the observed core appears as a more regular ellipse. The observed FWHM of the core is 55″ at

Table 5.4: The FWHM of the cores at 250 μm. Column 2 gives the FWHM when measured from the data and column 3 shows the FWHM as measured from the model. Both have errors of $\pm$15 %. See text for details.

IRDC Name	FWHM at 250 μm ($''$)	
	Observed	Model
305.798−0.097	62	82
307.495+0.660	55	59
309.079−0.208	57	65
309.111−0.298	38	43
310.297+0.705	45	38
314.701+0.183	40	45
318.573+0.642	40	44
318.802+0.416	45	45
318.916−0.284	38	42
321.678+0.965	65	72
321.753+0.669	85	79
322.334+0.561	55	63
322.666−0.588	42	40
322.914+0.321	38	42
326.495+0.581	33	39
326.620−0.143	73	73
326.632+0.951	24	31
326.811+0.656	43	43
328.432−0.522	58	57
329.403−0.736	47	51

160 μm and 67$''$ at 500 μm. The model core has a FWHM of 65$''$ at 160 μm and 62$''$ at 500 μm, in agreement with the observed values. The eccentricity of the modelled cores shows only a 13 % difference from the eccentricity of the observed core at 250 μm.

The position of the peak emission appears to shift slightly as the wavelength increases. This could be caused by an asymmetric ISRF, resulting in one side of the core being heated more than the other (Nutter, Ward-Thompson, & Stamatellos, 2009) and thus the position of the modelled core appearing to change as we looks at different temperatures of dust. This means that, while matching the position of the 250 μm core exactly, the modelled core does not match the position of the

observed core at 500 μm.

The SED for the core in 307.495+0.660 is shown in Figure 5.21. For this core the modelled SED fits well with the observed SED at all wavelengths and has a χ^2 of 1.41, well within our boundaries for a 5% significance level. The model is in agreement with the observed flux densities at 160, 250, 350 and 500 μm and below the upper limit set at 70 μm.

5.6.3 309.079−0.208

Absorption is visible in the modelled core at 8 and 70 μm, matching the absorption seen in the observed data. By 160 μm, the model shows the core to be in emission, also matching what is seen in the observations. The size of the core at all wavelengths is based on the apparent size of the core at 250 μm. This core appears much smaller at 160 μm, where the FWHM is 29″, than at 250 μm (see Section 5.3.3). This results in the model of the core, which has a FWHM of ∼65″ at all wavelengths, appearing too large at 160 μm. However, the modelled core is a good fit in the two longest wavelengths, where the core size is comparable to the size at 250 μm. The shape of the model core also agrees with the observed data – see Table 5.3.

The SED for this core is shown in Figure 5.21. At 70 μm the flux density from the model is well below the upper limit measured from the observed data. The flux densities of the model are also in agreement with the observed flux densities measured at 160, 350 and 500 μm. However, at 250 μm the model shows a lower level of flux density than is seen in the data. The resultant χ^2 value of 2.77 is within our boundaries for a good fit to the observed data.

5.6.4 309.111−0.298

The model created for the core in 309.111−0.298 is shown in Figure 5.4. Any emission not from the core was ignored. In particular the extended emission towards the north-east of the core is not considered to be part of the core or its parent IRDC (see Section 5.3.4). In both the observations and the model, the core is seen to be in absorption at 8 and 70 μm and in emission by 160 μm. The FWHM of the modelled core at 250 μm is 43″, in agreement with the observational value of 38″. The decrease in resolution in longer wavelengths means that, at 500 μm, the observed FWHM is 50″. However, the modelled FWHM at 500 μm is 40″, still in agreement with the observed data. The eccentricity of the model is equal to that of the observed core. Again the, position of the centre of the core shifts with increasing wavelength, meaning that the position of the model at 500 μm (which is based on the observed position at 250 μm) does not agree with the position of the observed core. This is possibly due to an asymmetric ISRF.

The SED for the model of the core in 309.111−0.298 is in agreement with the measured flux densities at 160 to 500 μm and shows a good fit (see Table 5.2). However, the model does show a flux density in excess of the upper limit measured from the 70 μm observations.

5.6.5 310.297+0.705

As discussed in Section 5.3.5, this core shows absorption at 8 and 70 μm. The model also shows absorption at these wavelengths – see Figure 5.5. Emission from the parent IRDC, extending to the south and east of the core, is ignored in the modelling. The modelled core fits well with the observed data at all wavelengths

once this extended emission is disregarded. The shape and size of the modelled core match well with the contours from the observed data. The eccentricity of the model agrees with the observed data within the prescribed allowable difference and the FWHM of the modelled and observed cores are also in agreement – see Tables 5.3 and 5.4. The position of the core in 310.297+0.705 again appears to shift at 500 μm, meaning the model does not match the position of the observed core at this wavelength.

The model SED, shown in Figure 5.21, fits well with the measured flux densities at 160, 350 and 500 μm (see Table 5.2). At 70 and 250 μm, however, the model does not agree with the observed flux densities. At 70 μm the model used shows a flux density greater than the upper limit measured from the data and at 250 μm the observed flux density is slightly in excess of the model.

5.6.6 314.701+0.183

Images of the model created for the core in 314.701+0.183 are shown in Figure 5.6. Here, the modelled core clearly shows absorption at 8 and 70 μm in agreement with what is seen in the observed data. As discussed in Section 5.3.6 this core does not show clear emission until 250 μm (although there is some evidence of emission at 160 μm). Our model assumes the core to be in emission from 160 μm. This means that, at 160 μm, our model does not ideally match the observations. This can be seen in Figure 5.6 as the contours from the observed data at 160 μm do not match the shape or position of the modelled core. However, at the three longer wavelengths the shape and extent of the modelled core appear comparable with the observed data - see Tables 5.3 and 5.4.

The model SED, shown in Figure 5.21, fits exactly with the observed flux densities between 160 and 500 μm. The χ^2 value of the fit is 1.83, within the boundaries for an acceptable fit. However, the model predicts a much higher level of emission at 70 μm than is seen in the data.

5.6.7 318.573+0.642

The model created for the core in 318.573+0.642 is shown in Figure 5.7. The core is seen in absorption at 8 μm but is in emission at 70 μm (see Section 5.3.7). Our model assumes the core to be in absorption at 70 μm, which means that the model at 70 μm does not fit the observed data. Emission from the parent IRDC, extending to the south of the core, is ignored in the modelling. The model core fits the observed data well at each of the four longest wavelengths, in agreement with the eccentricity and FWHM of the observed core when the emission from the parent IRDC is disregarded.

The model SED for the core in 318.573+0.642 fits very well with the observed SED with a χ^2 of only 0.75. The model flux densities at 160, 250, 350 and 500 μm are in agreement with the observed data, and the modelled flux density at 70 μm is below the measured upper limit from the observed data.

5.6.8 318.802+0.416

Here, the observed core is in absorption at 8 μm, as discussed in Section 5.3.8, but the data are not good enough to state definitively whether it is in emission or absorption at 70 μm. Our model is in absorption at 8 μm and appears to show

very little absorption at 70 μm, in agreement with the observed data. Emission from the parent cloud, extending to the north-east and south-west, is ignored in the modelling. When considering this the model shows good agreement with the observed data at all wavelengths, the FWHM of both the observed and modelled core is 45″ at 250 μm and the eccentricity shows only a 13 % difference. However, once again, the position of the core at 500 μm is different from its position at 250 μm, meaning that the position of our model at the longer wavelengths does not agree with the position of the observed core.

The SED for this core is shown in Figure 5.21. The model fits well at all wavelengths with $\chi^2 = 2.16$, well within our boundaries for an acceptable fit. The modelled flux density at 70 μm is below the upper limit measured from the observations, and the modelled flux densities at 160, 250, 350 and 500 μm fit well with the observed data.

5.6.9 318.916−0.284

This core was particularly difficult to model, as the appearance of the core depends heavily on the wavelength at which it is viewed. This has resulted in a core that, while being a good fit to the appearance of the observed data at 250 μm, is not an ideal match at other wavelengths. This is especially true at 160 μm, as our model predicts that the core should be showing emission by this point, and the data show very little emission from the core itself. Images of the modelled core are shown in Figure 5.9. At 8 and 70 μm the modelled core shows absorption, in agreement with what is seen in the observed data at these wavelengths. At 250 μm the observed core had an eccentricity of 0.8 and a FWHM of 38″. At the same wavelength, the modelled core had an eccentricity of 0.9 and a FWHM of 42″, in good agreement

with the observations.

The modelled SED for this core, shown in Figure 5.21, fits well with the SED from the observed data. The flux densities from the four longest wavelengths agree with those measured from the data and the χ^2 value is within our assigned boundaries (see Table 5.2). However, the modelled 70 μm flux density is greater than the upper limit measured from the observations.

5.6.10 321.678+0.965

Images of the model created for the core in 321.678+0.965 are shown in Figure 5.10. As discussed in Section 5.3.10, the data for this core is of particularly bad quality at 70 and 160 μm. This means that the model can only be a rough estimate of the observations at these wavelengths, as it can not replicate the diminished quality of the observed data. At 8 μm the model, like the data, is seen in absorption. The emission from the parent cloud, noted in Section 5.3.10, is ignored in the modelling of the core. The modelled core in this case is an especially good match to the shape and size of the observed core with identical eccentricities at 250 μm. The size of the modelled core is also an acceptable fit to the observed core with a FWHM of 72 and 80″ at 250 μm and 500 μm, respectively. The observed core had a FWHM of 65 and 83″ at 250 μm and 500 μm.

The modelled SED is shown in Figure 5.21. At 70 μm the modelled flux density fits well below the observed upper limit. Similarly, the modelled flux densities at 160, 350 and 500 μm are again in good agreement with the observed flux densities. However, the modelled flux density at 250 μm is not in agreement with the observed data, and is much lower than expected. This results in a $\chi^2 = 4.04$, within our

boundaries for an acceptable fit but one of the worst fits overall.

5.6.11 321.753+0.669

The modelled core shows absorption at 8 μm, in agreement with what is seen in the observations – see Figure 5.11. The images do not make it clear that there is absorption in the model at 8 μm. This is due to the scaling used. At 70 μm the model shows only a very low amount of absorption. It is not clear from the observations whether the observed core shows emission or absorption at this wavelength (see Section 5.3.11). The size of the model matches the apparent size of the observed core – see Table 5.4. The shape of the modelled core is also a good match to the observed data, showing an identical eccentricity, although the observed core shows a more complex shape than could be ideally modelled using an ellipse. This is most likely due to the effect of smaller cores in the same IRDC distorting the shape of the core we focus on and exemplifies why we have tried to choose the more isolated cores for modelling.

The model SED is shown in Figure 5.22. The model is in good agreement with the observed data at 160, 250, 350 and 500 μm (see Table 5.2) but at 70 μm the modelled flux density is greater than the measured upper limit from the observed data.

5.6.12 322.334+0.561

The model for the core in 322.334+0.561 shows the core to be in absorption at 8 and 70 μm, in agreement with what is seen in the observed data. By 160 μm

and through to at least 500 μm, the core is seen in emission in both the observed data and the model. We once again ignore the emission from the parent cloud, extending towards the south-west and the east (see Section 5.3.12). The model fits well with the observed shape and size of the core at 250, 350 and 500 μm. The eccentricities differed by 13 % and the modelled core has a FWHM comparable to the observed FWHM – see Table 5.4. However, at 160 μm there are nearby sources that are not seen in the longer wavelengths, which affect the appearance of the core. As such, the model does not fit the shape of the observed core at 160 μm as well as at the longer wavelengths. This can be seen from the contours on the model in Figure 5.12.

The SED for the model of the core within 322.334+0.561 is in good agreement with the observed data (see Table 5.2). All four of the modelled longer wavelength flux densities agree with the observed data and the modelled 70 μm flux density is below the observed upper limit. The SED for the core in 322.334+0.561 is shown in Figure 5.22.

5.6.13 322.666−0.588

322.666−0.588 is one of the more circular cores that we model, as mentioned in Section 5.3.13. Nevertheless, there was still some eccentricity measured in the data and so a flattened density profile was still used. Images of the model created for the core in 322.666−0.588 are shown in Figure 5.13. It is unclear whether the core is in emission or absorption at 70 μm, although clear absorption can be seen in the observed data at 8 μm. Both wavelengths are seen in absorption in the modelled data. The size and shape of the model fit well with the observed data at all wavelengths – see Tables 5.3 and 5.4. However, the position of the observed

core again appears to shift slightly at different wavelengths, with the result that the centre of the model at 500 μm does not coincide with the centre of the observed core.

The model SED shows good agreement with the observed data at 70, 160, 350 and 500 μm. However, at 250 μm the modelled flux density is lower than the measured flux density from the observed data. The χ^2 value is 4.35 and it is one of the worse fits in our sample but is still within our boundaries for an acceptable fit.

5.6.14 322.914−0.321

The modelled data show absorption at both 8 and 70 μm. This fits with the observed data at 8 μm, where the core is seen in absorption, but not at 70 μm, where the core is seen in emission. All other wavelengths show emission in both the model and observed data – see Figure 5.14. The shape of this core was particularly difficult to model, as it appears almost triangular in the observed data, possibly due to the influence of the second core in 322.914−0.321. The semi-major axis was taken to extend from the north-west to the south-east and the core was assumed to be an ellipse, similar to the other starless cores. The eccentricity and size of the core is well matched by the model at all wavelengths – see Tables 5.3 and 5.4.

The SED for both the model core and the observed core are shown in Figure 5.22. The modelled core is a good fit to the observed data, with χ^2=2.14. The model flux densities at 160, 250, 350 and 500 μm are all in agreement with the observed flux densities and the model flux density at 70 μm falls below the upper limit measured from the data.

5.6.15 326.495+0.581

Both the model core and observed core show absorption at 8 and 70 μm – see Figure 5.15 – and emission at 160 μm and longwards. The appearance of the core at 160 μm is different to that at the three longer wavelengths (see Section 5.3.15). This means that the shape of the core, while matching the observed data well at 250, 350 and 500 μm (where the eccentricities are identical and equal to 0.9), is not an ideal fit to the observed core at 160 μm, where the eccentricity is only 0.7. The size of the core is a good fit at all wavelengths – see Table 5.4. However, the observed core at 500 μm has a different centre than at 250 μm. This means that the centre of the model and the observed core do not coincide at 500 μm.

The model SED at 160, 250, 350 and 500 μm, shown in Figure 5.22, fits well with the measurements taken from the data. However, at 70 μm the model flux density is much higher than the upper limit measured from the observations.

5.6.16 326.620−0.143

Images of the model created for the core in 326.620−0.143 are shown in Figure 5.16. Absorption is seen in both the observations and the model at 8 μm, with a decreased level of absorption at 70 μm. Once again, the shape of our model at 160 μm is not an exact match for the observations, due to the differences in the observed data between 160 and 250 μm. The eccentricity at 160 μm is 0.7, while at 250 μm is 0.9, a 29 % difference. At 250 μm the model appears to be a good fit to the observed data, exactly matching the shape and size of the core in the observed data – see Tables 5.3 and 5.4. However, at the longer wavelengths the emission from the core appears to shift slightly northwards. This means that, while the

contours are a good match for the physical properties of the core, the position is not.

The modelled flux densities are a good fit for the observed flux densities (see Table 5.2), with the model SED in agreement with all four of the longest wavelength flux densities and also with the upper limit at 70 μm. The SED for the model of 326.620−0.143 is shown in Figure 5.22.

5.6.17 326.632+0.951

The model for the core in 326.632+0.951 is the poorest fit to the observed data at the four longer wavelengths, however it was the best fit possible with PHAETHON. The data quality at 70 μm makes it impossible to ascertain whether the core in 326.632+0.951 is in emission or absorption, as discussed in Section 5.3.17. The model we create shows absorption at 70 and 8 μm and emission at 160μm and beyond. The size of the model matches the observed core at the four longer wavelengths – see Table 5.4. However, the eccentricity shows a 50 % difference, outside our acceptable margin. All emission from neighbouring IRDCs was ignored when modelling the core – see Section 5.3.17. Only the emission seen to be coming directly from the core is modelled.

The model SED of the core in 326.632+0.951 is one of the poorest fits of our 20 modelled cores. The χ^2 value is greater than 7.378, see Table 5.2, outside of the boundaries for a 5 % significance. However, it is within the boundaries of a 10 % significance level (where χ^2 must be between 0.010 and 10.597; Rouncefield & Holmes, 1993). Only the 160 μm flux density is in agreement with the observed data. The model flux densities at 250, 350 and 500 μm are either above or below

the observed data and the 70 μm flux density is above the measured upper limit. This SED was, nevertheless, the best fit possible to the observed data. This may be indicating that this core has a more complex morphology than the model allows.

5.6.18 326.811+0.656

The model created for the core in 326.811+0.656, is shown in Figure 5.18. The core is seen in absorption in both the model and the observations at 8 and 70 μm. The model shows a smaller amount of absorption at 70 μm than at 8 μm, in agreement with the observed data. The observed core is far more elongated at 160 μm than in the three longer wavelengths, with an eccentricity of 0.9 compared to 0.7 at 250 μm. This means that the shape is not an ideal match at this wavelength. At 250, 350 and 500 μm the modelled core is a good fit to the size of the observations, both show a FWHM of 43″ at 250 μm and 50″ at 500 μm. The shape of the modelled core at 250 μm matches the observed core, showing identical eccentricities – see Table 5.3.

The model SED, seen in Figure 5.22, is a good fit to the observed SED at 160–500 μm (see Table 5.2), with all the model flux densities in agreement with all four observed data points. However, at 70 μm the model shows a flux density greater than that of the upper limit measured from the observations.

5.6.19 328.432−0.522

Both the observed core and the model show absorption at 8 and 70 μm and emission at 160 to 500 μm, as seen in Figure 5.19. The modelled core at 160 μm appears

more elongated than the observed core. This is due to differences in the appearance of the observed core at 160 and 250 μm. The observed core has an eccentricity of 0.4 at 160 μm and 0.8 at 250 μm, while the modelled core has an eccentricity of 0.9 at all wavelengths. By 250 μm the shape of the core is a better match to the observational data, with only a 13 % difference in eccentricities. It remains a good approximation of the observations at 350 and 500 μm where the eccentricity is comparable to that at 250 μm. The size of the modelled core in the three longest wavelengths is also a good fit to the observed data contours, the observed FWHM at 250 μm is 58″ and the model FWHM is 57″.

The modelled SED for the core in 328.432−0.522, shown in Figure 5.22, is a good fit to the observed SED at 160 to 500 μm and results in a χ^2 value of 2.18. However, at 70 μm the model predicts a flux greater than the upper limit of the observed data.

5.6.20 329.403−0.736

The core in 329.403−0.736 is seen is absorption at 8 and 70 μm in the model, in agreement with what is seen in the observed data (see Section 5.3.20). At 160, 250, 350 and 500 μm the core is seen in emission in the model, also in agreement with the observed data. The size and shape of the model fits well with the observed core at all wavelengths with both the eccentricities and FWHM of the model agreeing with the data to within our prescribed boundaries – see Tables 5.3 and 5.4. However, the shape of the modelled core is a better match to the observations at 350 and 500 μm where the core is better modelled by an ellipse. At 160 and 250 μm the appearance of the core in the observed data is slightly more complex, although the model is still a good approximation.

The SED for the model of the core in 329.403−0.736 is shown in Figure 5.22. The SED is an excellent fit at all wavelengths with the flux densities at 160 to 500 μm in agreement with the observed flux densities and the modelled flux density at 70 μm below the measured upper limit, it has a χ^2 value of 1.25.

5.7 Summary

Twenty starless, isolated cores were found in the Hi-GAL data and modelled using PHAETHON. To be classified as starless the core must have no 8 or 24 μm point sources within its FWHM. To then also be classified as isolated it must have a $>3\sigma$ dip between its peak flux and the peak flux of all neighbouring sources. Starless, isolated cores are more likely to have simple internal structures and so were most suited for modelling with PHAETHON.

The distance to each core was calculated using the Brand & Blitz (1993) velocity curve and CO data. We found an average helio-centric distance of 3.1 kpc for this sample. This was then used to calculate the size of each core. The flux density of each core was measured at 70, 160, 250, 350 and 500 μm, and an SED created.

A model of each of the 20 isolated, starless, cores was created using PHAETHON. The parameters for each core were found by matching the size and shape of the modelled core to that of the observed core at 250 μm and by altering the ISRF and central density of the model until the SED of the modelled core matched that of the observed core.

In general, we found that the model matched the physical appearance of the

observed cores well, particularly at 250 and 350 μm. This was tested through a comparison of the eccentricities and FWHM of the observed and modelled cores. At 160 μm the resolution of the observations is much higher than at longer wavelengths. This meant that, for some of our cores, the appearance was more complex than could be modelled by an ellipse, or significantly different from that at 250 μm. This resulted in a model which did not exactly fit with the appearance of the core at 160 μm.

The SEDs of the models also fit well to the observed flux densities. This was especially true at the wavelengths where we had definite measurements of flux density from the observed data. This was tested via a χ^2 analysis, where a χ^2 value between 0.051 and 7.378 was considered a good fit. At 70 μm not all of our cores were in emission by this wavelengths, so we used the flux density as an upper limit only. It was found that in half of our cores the modelled flux density at 70 μm exceeded the upper limit measured from the observed data.

Chapter 6

Discussion

6.1 The Evolution and Lifetimes of Cores

In Chapter 4, 972 cores were identified in the *Herschel*-bright IRDCs. Each was searched for evidence of 8 and 24 μm point sources and placed into an evolutionary sequence based on the presence or absence of said sources (Chambers et al., 2009). 170 cores showed no MIR point sources at either 8 or 24 μm and were deemed starless. They are thought to be the youngest observable stage of a core. 149 had a 24 μm point source but no 8 μm point source, indicating that they belong in an intermediate phase. Finally, 653 cores showed evidence of an 8 μm point source within their radius. An 8 μm point source is indicative of PAH emission (see Chapter 1) and implies that a core is in the final evolutionary stage.

6.1.1 Statistical Comparison with Previous Work

Previous studies of cores have performed a similar analysis, albeit with a much smaller number of sources. Here, the relative numbers of cores in the three different evolutionary stages are compared with two previous studies: Chambers et al. (2009) with 190 candidate cores; and Parsons et al. (2009) with 205 cores.

6.1.1.1 Comparison with Chambers et al. (2009)

The relative number of cores with no embedded MIR point sources, compared to those with 8 and 24 μm point sources (see Table 6.1), can be used for comparison with previous findings. Chambers et al. (2009) labelled cores with no embedded MIR point sources as quiescent, those with a 24 μm point source and one other form of star formation tracer (maser activity or an extended green object indicative of collapse) as active, and those with an 8 μm point source as red. They also identified blue cores (with 3.6 μm emission) and intermediate cores (those with a single star formation tracer). However, when considering the evolutionary sequence of IRDC cores they only included the red, active and quiescent stages. We equate their quiescent cores to our starless cores, their active cores to our cores with a 24 μm point source but no 8 μm point source and their red cores to the ones in our sample which show 8 μm emission.

Chambers et al. (2009) had a sample of 190 candidate cores. Of these, 49 were classified as blue or intermediate and are ignored here. Of the remaining 141 they found $\sim$25 % ($\pm$8%) to be red, $\sim$26 % ($\pm$8%) to be active and $\sim$49 % ($\pm$8%) to be quiescent. Our sample consists of 972 cores, of which, 67% ($\pm$3%) have an 8 μm point source, 15% ($\pm$3%) have only a 24 μm point source and 18% ($\pm$3%)

Table 6.1: IRDC core statistics. The left side of the Table refers to the work presented in this thesis and gives the numbers of cores found for each stage. The right side of the table refers to the work presented in Chambers et al. (2009) and gives the numbers of cores found in their equivalent classes.

This work			Chambers et al. (2009)		
Core Type	Number of Cores	Percentage (%)	Core Type	Number of Cores	Percentage (%)
8μm source	653	67	Red	35	25
24μm source only	149	15	Active	37	26
Starless	170	18	Quiescent	69	49
Total	972		Total	141	

are starless. The number of cores in each stage are summarised in Table 6.1.

It can be seen that there is a much larger fraction of quiescent cores in the Chambers et al. (2009) sample than in ours. This could be due to the effect of some fraction of their initial sample of candidate IRDCs not being genuine, as they had no FIR data in which to separate out the holes in the sky. Interestingly, though, because they see 51 % of their cores having other star formation tracers, then only a maximum of 49 % (±8 %) of their cores could be false, compared to up to 62 % (±3 %) in our full sample (although note that some of their associations could be chance alignments). However, the much smaller numbers in the Chambers et al. (2009) sample make a more detailed comparison difficult. The errors quoted in brackets here are simply the random ($\sqrt{n}$) errors, and there may also be systematic effects at work.

6.1.1.2 Comparison with Parsons et al. (2009)

Parsons et al. (2009) cross-matched the candidate IRDCs of Simon et al. (2006a) with 850 μm emission seen in Submillimeter Common-User Bolometer Array (SCUBA; Cunningham et al. 1994) observations and found that 25 % of the candidate IRDCs

were not seen in emission at 850 μm. This is a smaller percentage than we found to be *Herschel*-dark.

They identify 205 cores that were detected by SCUBA and which also appeared in the GLIMPSE survey. They found that 70 % had embedded 24 μm point sources, and 30 % did not. They made no distinction between those 24 μm sources that also had 8 μm point sources and those that did not. Hence their 30 % needs to be compared to the percentage of starless cores in our sample (18 %), and their 70 % should be compared to the sum of the cores which show any kind of MIR emission (82 %). Given the very different sizes of the samples (the simple random $\sqrt{n}$ errors on their numbers are $\sim \pm 10$ %), these are also consistent with the percentages we find.

6.1.2 Relative Lifetimes

A simple evolutionary picture for a core within an IRDC is given by Chambers et al. (2009). This entails a quiescent, starless core evolving first into a core with an embedded 24 μm point source and eventually into a core with an 8 μm point source.

If each starless core evolves into a corresponding star-forming core with one or more embedded 24 μm point sources, and each of these evolves into a core with the same number of embedded 8 μm point sources, then we can equate the relative numbers of cores in each phase with theoretical lifetimes. We thus produce a statistical lifetime for each of the evolutionary stages of a core and from this calculate the total lifetime of a core. These results are summarised in Table 6.2.

The intermediate phase (containing a 24 μm point source but no 8 μm point

Table 6.2: The lifetimes of the different phases of cores. Column 2 gives the statistical lifetimes calculated from the work presented in this thesis. Column 3 gives the equivalent lifetimes calculated by Chambers et al. (2009).

Source Type	Statistical Lifetime (years)	Equivalent Lifetime from Chambers et al. (2009)
Cores with 8 μm source	$\sim 9\times10^5$	$\sim 4\times10^5$
Cores with 24 μm source only	2×10^5	2×10^5
Cores with no MIR source	$\sim 2.3\times10^5$	–

source) can be theoretically equated with the main accretion phase for massive protostar formation. A starless core has not yet begun active star formation and no accretion is evident, while an 8 μm point source indicates the beginning of an HII region and accretion stopping. Any accretion must therefore take place in the 24 μm only phase. The canonical accretion timescale of a high mass star was calculated by Zinnecker & Yorke (2007) and estimated to be $\sim 2\times10^5$ years. Thus we assume that the 24 μm-only stage of a core will last for approximately 2×10^5 years.

Hence we calculate, from the ratio of the number of starless cores to the number of cores with only a 24 μm point source, that the lifetime of the starless phase of cores is $\sim 2.3\times10^5$ years ($\pm 0.3\times10^5$ years). Similarly, the lifetime of the phase with an embedded 8 μm source would then be $\sim 9\times10^5$ years ($\pm 1\times10^5$ years). The entire IRDC lifetime (after core formation) is therefore the sum of the lifetimes of all three phases: $\sim 1.3\times10^6$ years ($\pm 0.2\times10^6$ years). The errors given here are, again, simply the random ($\sqrt{n}$) errors.

These calculations assume that every starless core develops into a single core with a 24 μm point source and that every 24 μm-only core evolves into a single core with an 8 μm point source. If starless cores, for example, fragment and develop into more than one star-forming core these calculations would no longer be valid.

However, they do at least give an upper limit on the lifetime of a core.

One clear result that comes from the relative numbers of cores in each phase is that only about one-fifth of cores do not contain embedded point sources. If this corresponds to the starless phase of cores, then we would conclude that a typical core only spends around one-fifth of its lifetime without any seed of a protostar within it.

Chambers et al. (2009) also assume a lifetime of 2×10^5 years for their active phase (equivalent to our 24 μm-only stage). They thus derive a lifetime of $\sim4\times10^5$ years ($\pm1\times10^5$ years) for their quiescent cores (equivalent to our starless cores) — see Table 6.2. These numbers are roughly consistent with our calculations when accounting for the difference in sample sizes. Chambers et al. (2009) do not calculate a lifetime for their red cores (equivalent to our cores with an 8 μm source).

The 8 μm emission is believed to arise from PAH emission and to be excited by very high energy photons (Chambers et al. 2009). Such high-energy photons are presumed to be emitted from HCHII and UCHII regions. Hence the phase where a core contains an embedded 8 μm point source should roughly correlate with the combined HCHII and UCHII phases. The UCHII lifetime is not well known, although recent estimates put it at several $\times10^5$ years (e.g. Kaper et al. 2011). Similarly, McKee & Tan (2002) look at stars in typical regions of high mass star formation and find timescales of a few $\times10^5$ years for the combined HCHII and UCHII phases. Both these results are consistent with our estimated lifetime of the phase in which a core has an embedded 8 μm point source ($\sim9\times10^5$ years).

6.2 Revised Numbers of Galactic IRDCs

In Chapter 4 we took a selection of *Spitzer*-dark candidate IRDCs (from a MIR catalogue; PF09) and viewed them at FIR wavelengths. We presume that a genuine IRDC should be both *Herschel*-bright (in emission at 250, 350 and 500 μm) and *Spitzer*-dark (in absorption at 8 μm). Only 40% of the candidate IRDCs were found to be *Herschel*-bright.

Using PHAETHON, we modelled several IRDCs of different sizes and masses and placed them into the Hi-GAL data in areas of differing background and confusion. We estimated that any IRDC whose major axis is $\leq 26''$ (corresponding to 0.4 pc at a distance of 3.1 kpc) with a peak column density less than $4\times10^{22}\,\mathrm{cm}^{-2}$ in an area where the background level is greater than $1300\,\mathrm{MJy\,sr}^{-1}$ at 250 μm is not likely to be found to be *Herschel*-bright, regardless of whether it is a genuine IRDC or not. IRDCs meeting these criteria accounted for an estimated 20 % of the PF09 *Spitzer*-dark regions. These sources are not be expected to be *Herschel*-bright even if they are genuine IRDCs. As such we can not definitively state whether these small and diffuse objects are actual IRDCs or holes in the sky. This adds an additional 20 % uncertainty onto our figures.

This means that 40–60 % of the MIR-selected candidate IRDCs are genuine, or 50±10 %. If this holds for the entire Galactic Plane, there are therefore approximately half the number of IRDCs in the Galaxy than had been previously estimated.

The *Spitzer*-dark and *Herschel*-dark objects are those which show absorption throughout the infrared and account for the remaining 50±10 % of the sample. Regions of the sky that have been found to be dark throughout the electromagnetic

spectrum have been found previously (e.g. Stanke et al., 2010). We refer to these objects as holes in the sky. The research presented here implies that holes in the sky may be far more common than was previously realised.

6.2.1 The Role of IRDCs and their Cores in Galactic Star Formation

Rathborne et al. (2006) estimated the rate of star formation in IRDCs to be approximately $2\,M_{\odot}\,yr^{-1}$ (see Section 1.2.4). They state that this is close enough to the total Galactic star formation rate ($\sim 1 - 2\,M_{\odot}yr^{-1}$; Murray & Rahman 2010; Robitaille & Whitney 2010; Chomiuk & Povich 2011) to conclude that the majority of stars in our Galaxy form in IRDCs.

However, this calculation was performed using the numbers available from Simon et al. (2006a) and an estimate of the IRDC lifetime. The Simon et al. (2006a) catalogue was based purely on MIR observations. We have shown that numbers of IRDCs based upon MIR data alone are over-estimated by a factor of $\sim$2. We also find that only 80% of our *Herschel*-bright IRDCs show evidence of a core at FIR wavelengths. We calculate here a new estimate of the star formation rate in cores using the revised figures of the number of cores and our estimate of the lifetime of cores (Section 6.1.2).

First, we estimated the fraction of the Galaxy that was observed in our study. We have examined the *Spitzer*-dark objects between Galactic longitudes of 300 and 330^{o} and Galactic latitudes of $\pm 1^{o}$. We make the assumption that all the *Spitzer*-dark objects observed in this region are within 8 kpc of the Sun. 8 kpc is the approximate distance of the Sun to the Galactic centre. IRDCs with a helio-

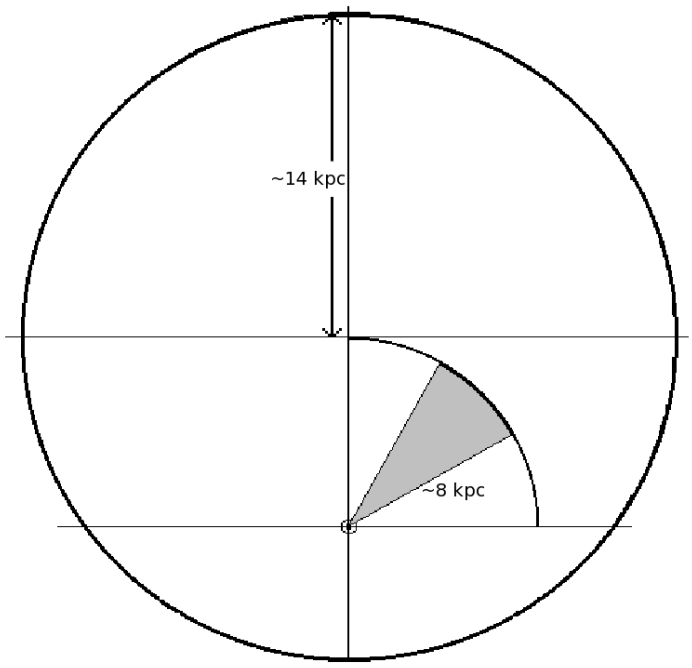

Figure 6.1: A sketch of the Galaxy (not drawn to scale). The position of the Sun is marked with '⊙'. The shaded area is the approximate region which was searched for *Herschel*-bright and *Spitzer*-dark objects.

centric distance greater than 8 kpc are unlikely to be seen by either *Spitzer* or *Herschel*. The approximate area searched is shown as the shaded region in Figure 6.1.

The region shaded in Figure 6.1 is the region we searched for IRDCs, it has the same area as the shaded region in Figure 6.2, which represents one twelfth of the Solar Circle. The two shaded regions have an equal area. The region we searched is therefore equivalent to one-twelfth of the inner Galaxy (i.e. within the Solar Circle).

We thus estimated the total number of cores in the Solar Circle. The region we searched is $\sim 8.3\,\%$ of the Solar Circle and contains 3171 *Spitzer*-dark regions (Peretto & Fuller, 2009). Assuming this is typical of the entire inner Galaxy, we

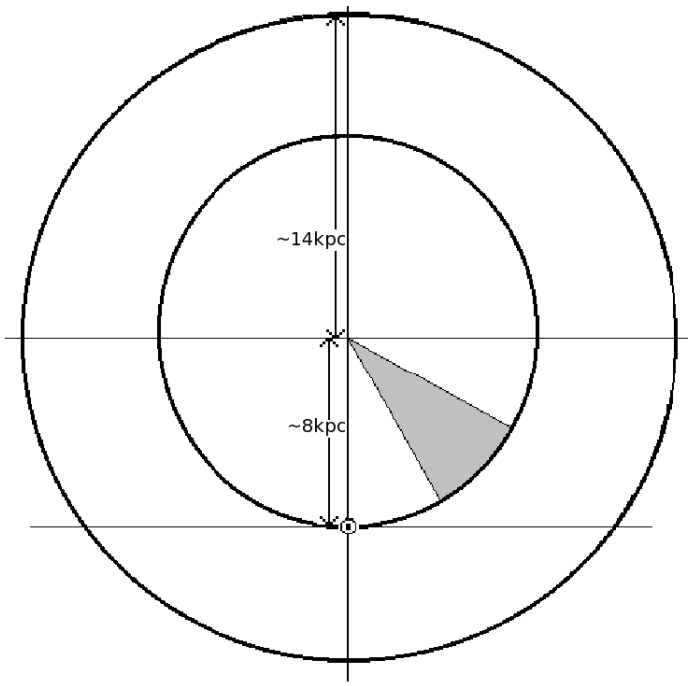

Figure 6.2: A sketch of the Galaxy, with the Solar Circle marked (not drawn to scale). The position of the Sun is marked with '⊙'. The shaded region shows one twelfth of the Solar Circle and is equal in area to the region which we searched for IRDCs.

estimate that there are ∼38,000 *Spitzer*-dark regions in the stellar disk. We found that ∼50±10 % of the *Spitzer*-dark regions were genuine IRDCs. This implies a maximum of 19,000±4,000 genuine IRDCs in the inner Milky Way.

Of the IRDCs we found to be *Herschel*-bright, ∼ 80% contained at least one core (i.e. 966/1205). We thus calculate that there is a maximum of ∼15,000±3,000 genuine IRDCs which contain at least a single core inside the Solar Circle. Of the 966 IRDCs that showed evidence of containing cores, only ∼1% showed evidence of multiple cores at 250 μm. The remaining 99% showed only a single peak in the 250 μm observation and so contained only a single core. Therefore, we estimate that there are roughly the same number of cores in the inner Galaxy as there are IRDCs with embedded cores.

We can estimate the average mass of an individual core. We modelled 20 starless cores, and found an average mass of $58\,M_\odot$ (see Section 6.3.3). However, these cores are a small subset of all cores in that they are only the youngest, most isolated cores. Our estimate of the number of cores includes cores of all stages of evolution and those cores that would be classed as confused. Rathborne et al. (2006) estimate the mass of 190 cores from all stages of evolution and find their median mass to be $140\,M_\odot$. If we take the average mass of a core to be $140\,M_\odot$, then we can estimate the total mass of cores in the Solar Circle via Equation 1.2. We find the total mass contained in cores to be $\sim (2 \pm 0.4) \times 10^6\,M_\odot$.

We can then estimate the rate of star formation taking place in cores via Equation 1.3. We use the same value for star formation rate efficiency as Rathborne et al. (2006), that is 0.2, typical for star forming clumps. It should be noted that estimates for star formation efficiency vary by up to a factor of 10 (e.g. Murray & Rahman 2010). Our calculations are heavily dependent on the star formation efficiency and a change in efficiency will alter the star formation rate in cores by a similar amount (e.g. doubling the star formation efficiency will double the star formation rate in cores).

Instead of using the Rathborne et al. (2006) estimate for the lifetime, we use the value calculated in Section 6.1.2 for the total lifetime of a core (i.e. 1.3×10^6 years). Substituting these values into Equation 1.3 gives the star formation rate inside cores to be $\sim 0.34 \pm 0.07\,M_\odot\,yr^{-1}$ within the inner Galaxy.

We then calculate the Galactic star formation rate inside cores. Figure 6.3 shows the star formation rate of the Galaxy as a function of Galactic radius (Zhukovska, 2008). By estimating the area under the best-fit line from 0 kpc to 8 kpc and comparing it to the area from 8 kpc to 14 kpc we calculate that $\sim$84 % of

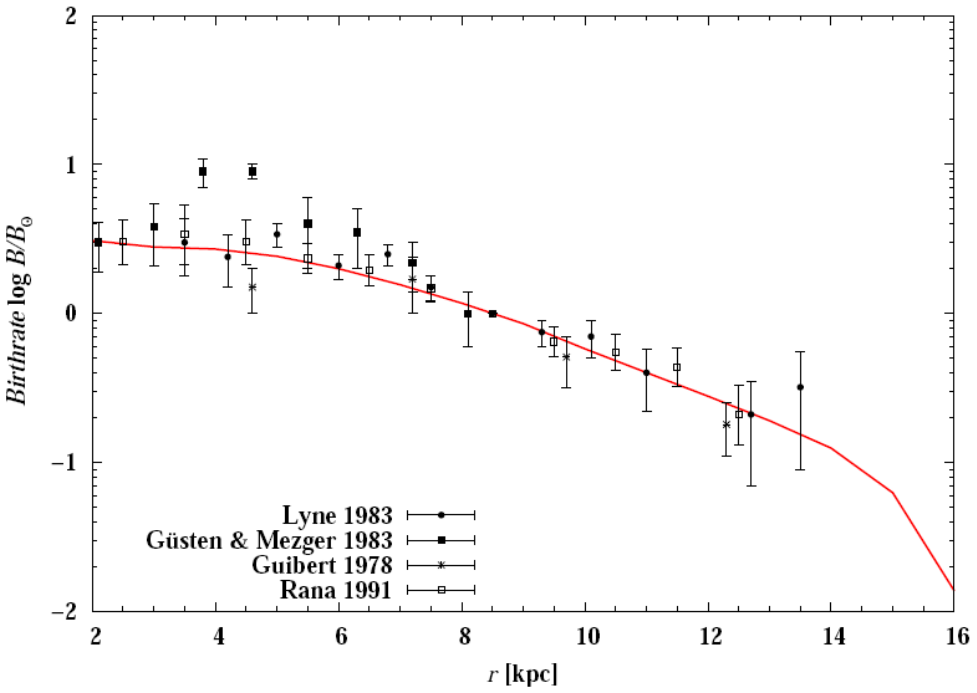

Figure 6.3: The present star formation rate of the Galactic disk as a function of Galactocentric distance. The red line shows a best fit to the datapoints (Zhukovska, 2008). We assume that the star formation rate is approximately constant for the inner 2 kpc of the Galaxy.

Galactic star formation occurs within the Solar Circle. If this is true for the star formation rate in IRDC cores then the total Galactic star formation rate occurring in cores is $\sim 0.41 \pm 0.08\,\mathrm{M}_{\odot}\,\mathrm{yr}^{-1}$. Our calculation of the rate of star formation occurring in cores, using new estimates of numbers and lifetime, is significantly less than was previously estimated (Rathborne et al., 2006).

Our value of the rate of star formation in cores ($\sim 0.41 \pm 0.08\,\mathrm{M}_{\odot}\,\mathrm{yr}^{-1}$) is much lower than the Galactic rate of star formation ($\sim 1-2\,\mathrm{M}_{\odot}\mathrm{yr}^{-1}$). We therefore infer that, contrary to the findings of Rathborne et al. (2006), not all star formation in our Galaxy is occurring in cores or IRDCs. For the current star formation rate in the Galaxy to be achieved, there must be star formation taking place in addition to that occurring in IRDC cores.

6.2.2 Holes in the Sky

Stanke et al. (2010) find a dark patch in the NGC1999 reflection nebula (see Figure 1.4). We call this dark patch a hole in the sky. This hole is visible at optical wavelengths and throughout the infrared. Furthermore, their observations place an upper limit of $2.4{\times}10^{-2}\,\mathrm{M}_{\odot}$ on the mass of the dark patch, while the mass needed to produce such an absorption feature would be several tenths to a few $\mathrm{M}_{\odot}$. They state that the dark patch is a cavity in the nebula caused by protostellar jets.

Of 3171 *Spitzer*-dark sources, we find that ∼40–60 % are both *Spitzer*-dark and *Herschel*-dark and thus show no emission throughout the MIR and FIR. Approximately one third of these regions are thought to be too small and too diffuse to be seen by *Herschel* even if they are genuine IRDCs. We therefore state that a minimum of 40 % of all *Spitzer*-dark regions, or 66% of the *Spitzer*-dark and *Herschel*-dark regions, are candidates to be holes in the sky. Further observations at other wavelengths are needed to ensure that there is no emission throughout the EM spectrum.

The list of *Spitzer*-dark and *Herschel*-dark sources can be found in Appendix B. These 1966 objects show no emission at 8, 24, 70, 160, 250, 350 or 500 μm. Around 1300 are believed to be holes in the sky, a factor of ∼1000 more than has been previously identified – only one was previously known.

6.3 Physical Properties of Starless Cores

In Chapter 5, models were produced of 20 of the most isolated starless cores and their physical properties were derived. The relationships between these parameters

are now discussed.

6.3.1 Distance

Fourth quadrant IRDCs have a typical Galacto-centric distance of 6 kpc (Jackson et al., 2008) and a mean helio-centric distance of 4 kpc (Peretto & Fuller, 2010). The mean helio-centric distance to our isolated cores is 3.1 kpc, slightly closer than Peretto & Fuller (2010) found. This is due to a selection bias of our isolation criterion. This can be seen in Figures 6.4 and 6.5, where we compare the radii (see Section 6.3.2) and the masses (see Section 6.3.3) of the cores, respectively, to their helio-centric distance. Only cores with a high mass or large radius were seen as isolated at greater distances. This is due to the angular resolution of *Herschel*. Using our lowest datapoints, a cutoff is extrapolated, shown as a dashed line in Figure 6.4. Below this a core is unlikely to be selected for modelling due to our isolation criterion.

6.3.2 Radius

The minimum detectable core radii were set by the FWHM at 250 μm. The radii range from 0.3 to 1.0 pc, with a mean of 0.7 and a median of 0.8 pc. The distribution of the radii is shown in Figure 6.6.

The radii measured here are in agreement with previous studies of cores which found the radii to be between 0.05 and 1.0 pc (see Section 1.3.1). Rathborne et al. (2006) found the median radius of 190 cores to be 0.55 pc. This is slightly lower than is calculated in this work. However, we are using a factor of ten fewer cores

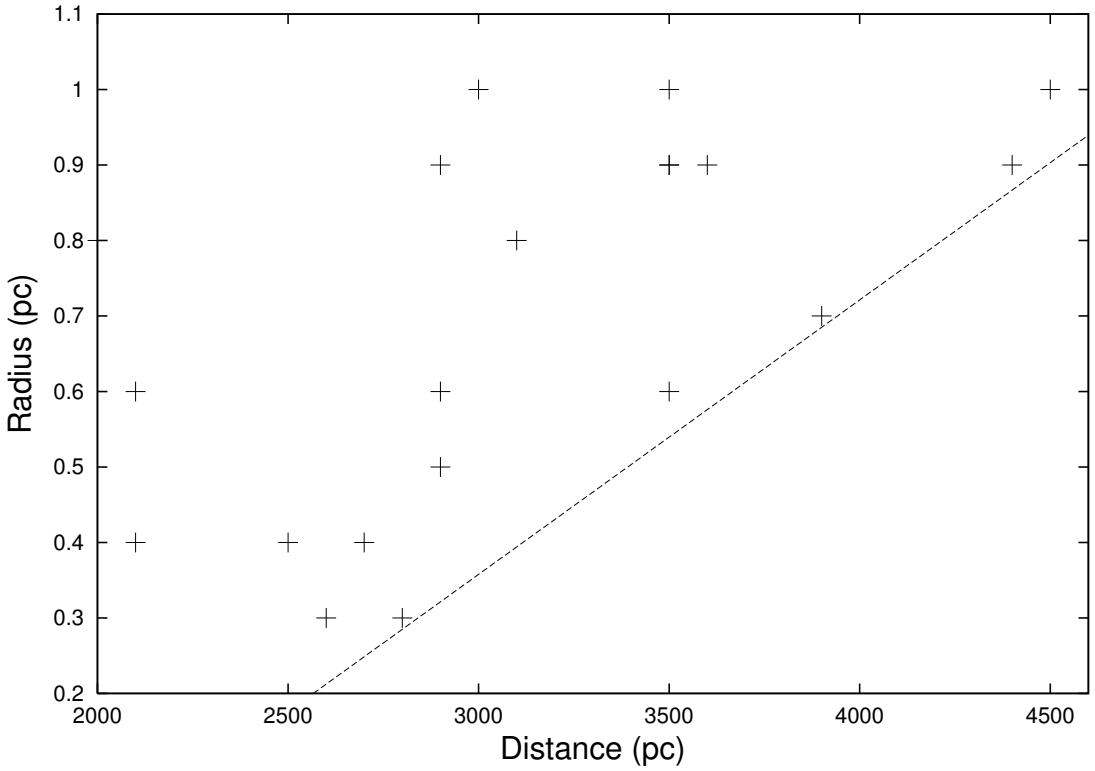

Figure 6.4: Radius versus the helio-centric distance to the cores. The dashed line shows the cutoff point for a core's radius – a core with a radius below this line will not have been selected for modelling due to our 'isolated' criterion (see Chapter 5).

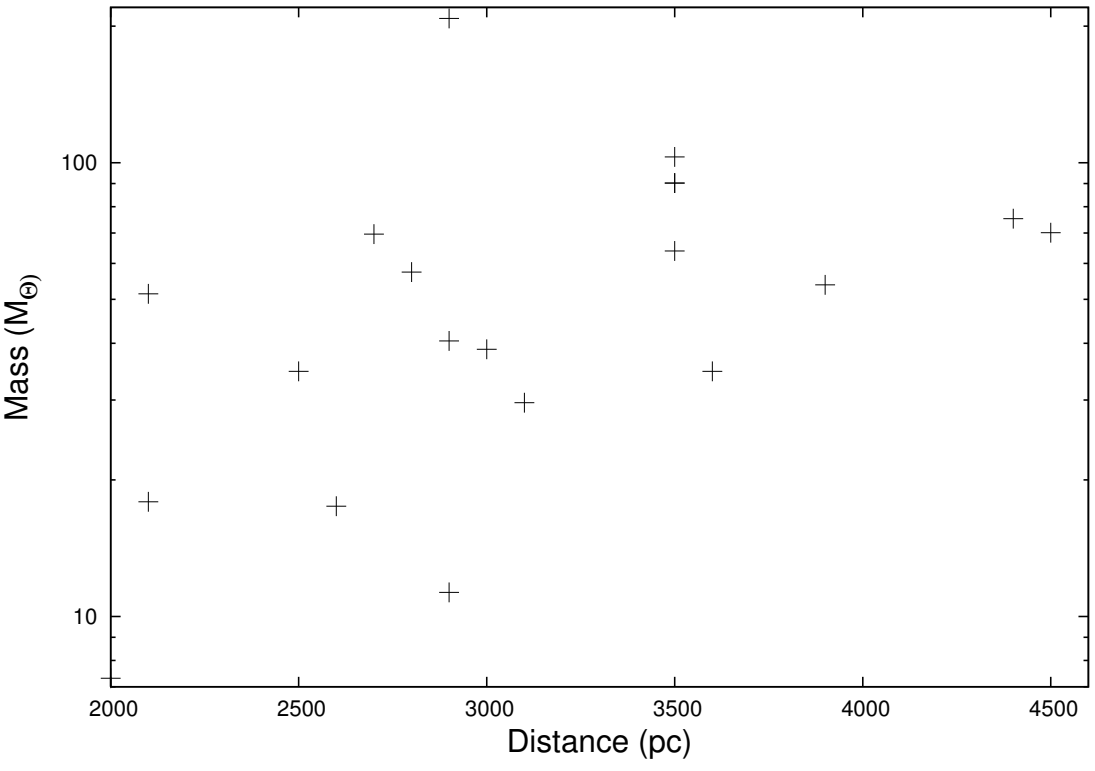

Figure 6.5: Mass plotted against the helio-centric distance to the cores.

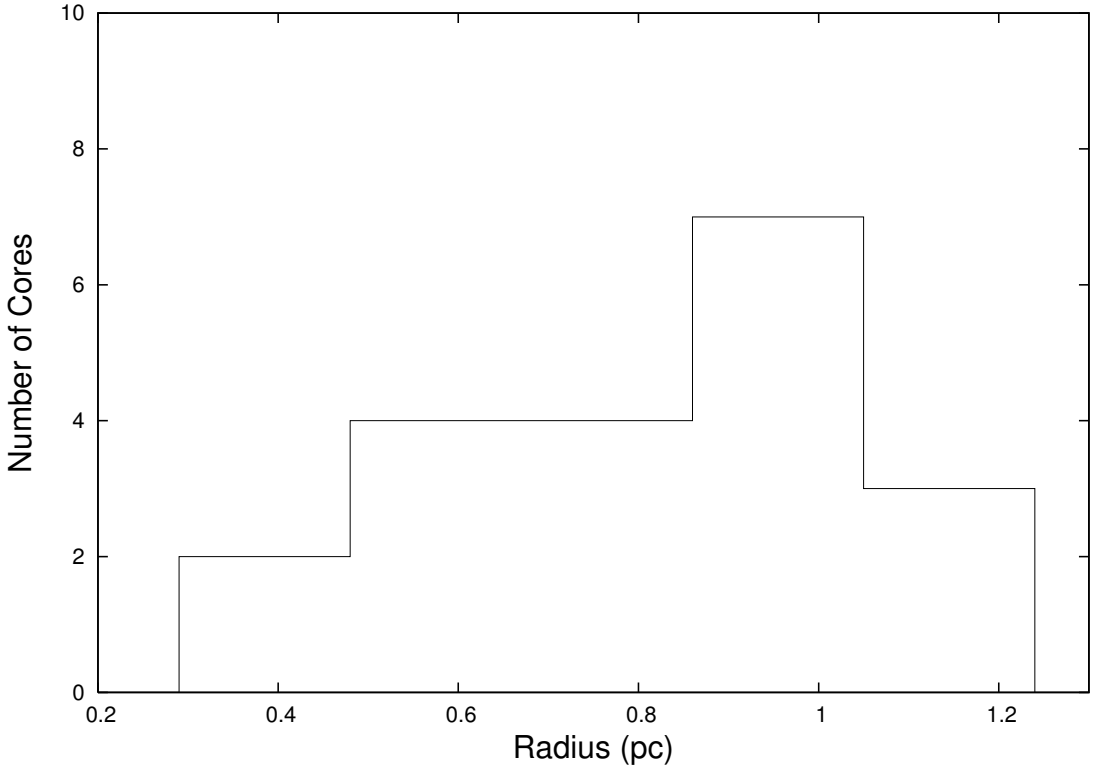

Figure 6.6: Histogram showing the distribution of the radii of the starless cores.

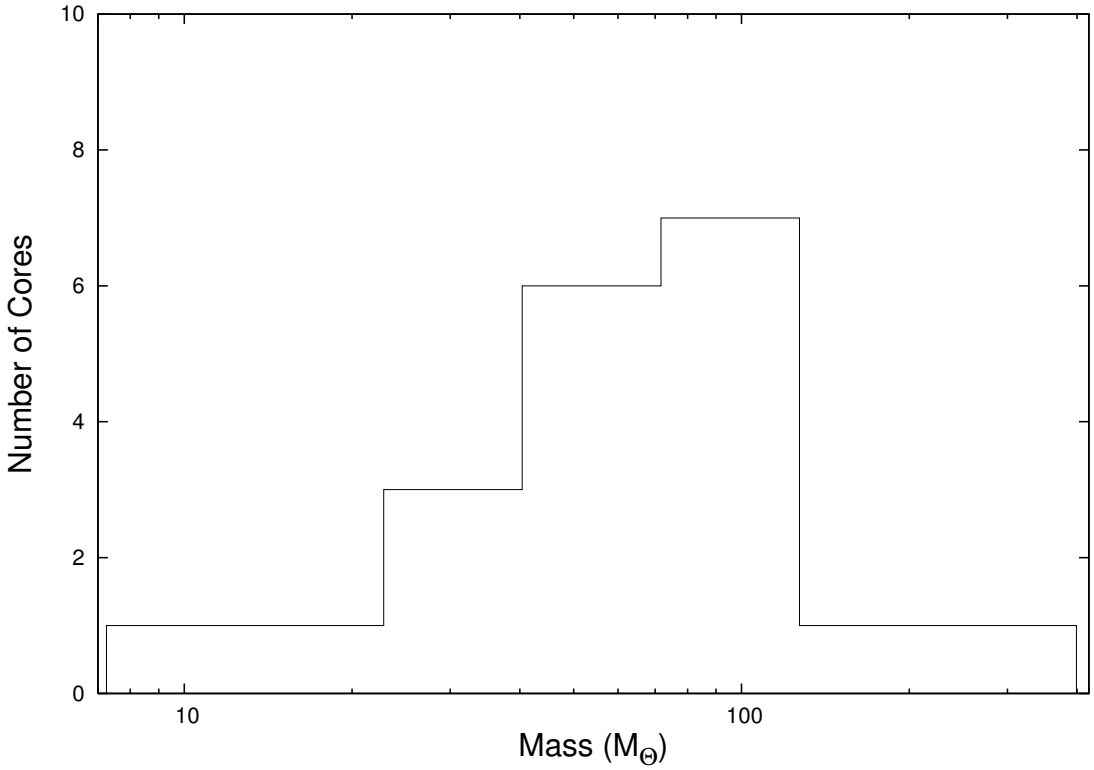

Figure 6.7: Histogram showing the distribution of the masses of the starless cores. Note that the x-axes uses a logarithmic scale.

and our isolation criteria biases us towards larger cores.

6.3.3 Mass

The core masses were calculated within the PHAETHON code using an opacity of $\kappa_{500\,\mu m}$=0.03 $\mathrm{cm^2\,g^{-1}}$ (Ossenkopf & Henning, 1994). Our 20 cores have masses in the range ∼7-200 $\mathrm{M_\odot}$, with a mean of 58 $\mathrm{M_\odot}$ and a median of 53 $\mathrm{M_\odot}$. Their distribution is shown in Figure 6.7.

Rathborne et al. (2006) calculated the masses of 140 cores and found a range between 10 and 2100 $\mathrm{M_\odot}$, with a median of 120 $\mathrm{M_\odot}$. They also find that 67 % of their cores have a mass between 30 and 300 $\mathrm{M_\odot}$. By choosing only a few of the youngest, most nearby cores, we are more likely to only pick those with lower masses, so this discrepancy is most likely a selection effect.

Figures 6.8 and 6.9 shows the masses of our cores plotted against their radii and central densities. The masses of the cores do not appear to be correlated with either parameter. The correlation coefficient between the mass and radius is r=0.33 and between mass and central density is -0.04. The correlation coefficient, r, is the Pearson-product moment correlation coefficient. It was calculated via:

$$r = \frac{\sum_{n=1}^{i}(x_i - \bar{x})(y_i - \bar{y})}{\sqrt{\sum_{n=1}^{i}(x_i - \bar{x})^2 \times \sum_{n=1}^{i}(y_i - \bar{y})^2}} \tag{6.1}$$

(Pearson, 1920), where x and y are two variables and $\bar{x}$ and $\bar{y}$ are the mean of those variables. r=+1 implies a positive correlation between the two variables and r=−1 a negative correlation. The closer the value of $|r|$ is to one, the stronger the relationship between the two variables. A lower value implies a weaker relationship

until r=0 signifies no relationship at all. p is the level of significance, i.e. p<0.05 implies a >95 % confidence that a relationship exists. In the work presented here, with 18 degrees of freedom, p<0.05 if $|r| > 0.44$ (Pearson, 1920). Hence correlation coefficients of 0.33 and -0.04 are not significant.

6.3.4 Temperature

When selecting our sources the aim was to pick the youngest subset of cores: those which show no internal MIR source and which were thus deemed to be starless. The lack of a MIR source makes it unlikely that these cores have any significant heating from within. The cores are, instead, heated by external radiation on their surfaces. This external heating results in a temperature gradient throughout each core, decreasing from surface to centre. Temperatures in individual cores have been observed to vary by up to 15 K (Peretto et al., 2010; Wilcock et al., 2011). It should be noted that the temperature profiles of the cores are not linear but rather show an exponential relationship with distance from the centre of the core. Two example temperature profiles are shown in Figure 6.10.

In Table 5.2, the temperature at the centre of the core (T_c) and at the surface (T_s) are given. These have averages of 11 and 21 K respectively. The dust temperatures in flattened cores show a variation at different directions within the cores. The cores have lower temperatures in their midplanes ($\theta = 90\,^\circ$) than in the direction perpendicular to their midplanes ($\theta = 0\,^\circ$). The surface temperatures quoted are those seen at $\theta = 0\,^\circ$. This gives the maximum temperature visible in the cores. The surface temperatures show a greater range (varying by over 10 K) than the central temperatures (which have a range of less than 7 K). Figures 6.11–6.13 show the distribution of surface temperature, central temperature and the range of the

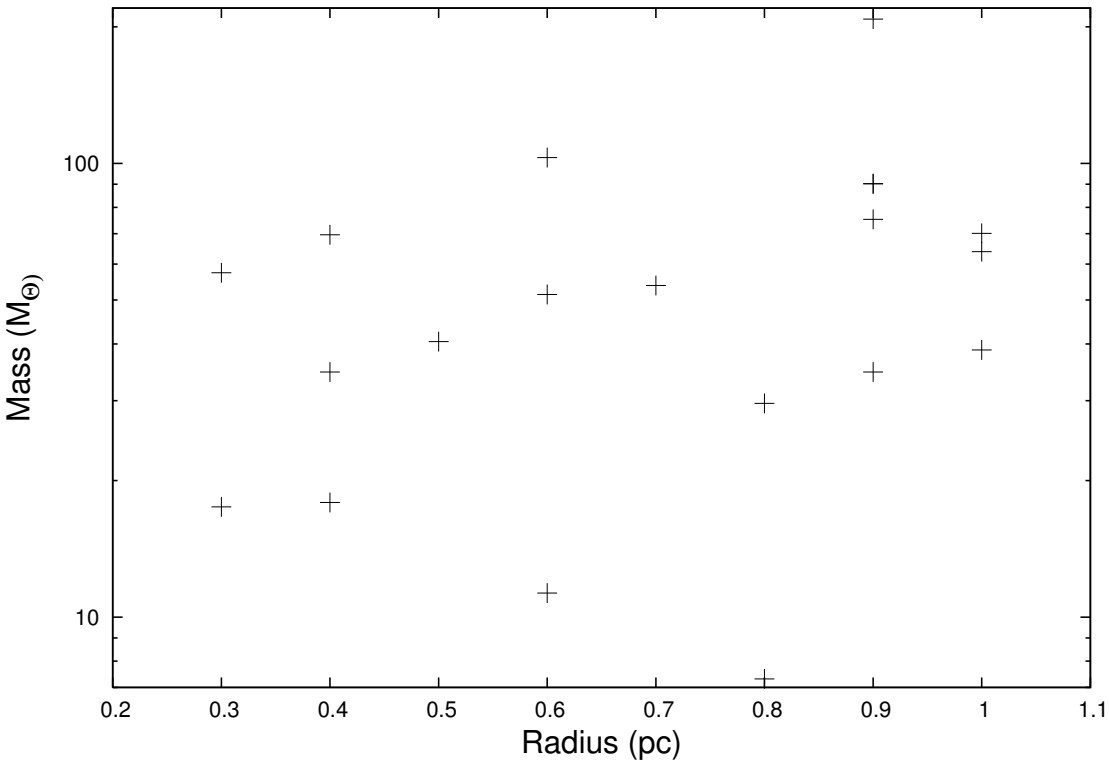

Figure 6.8: The masses of the core plotted against their radius. No correlation is seen.

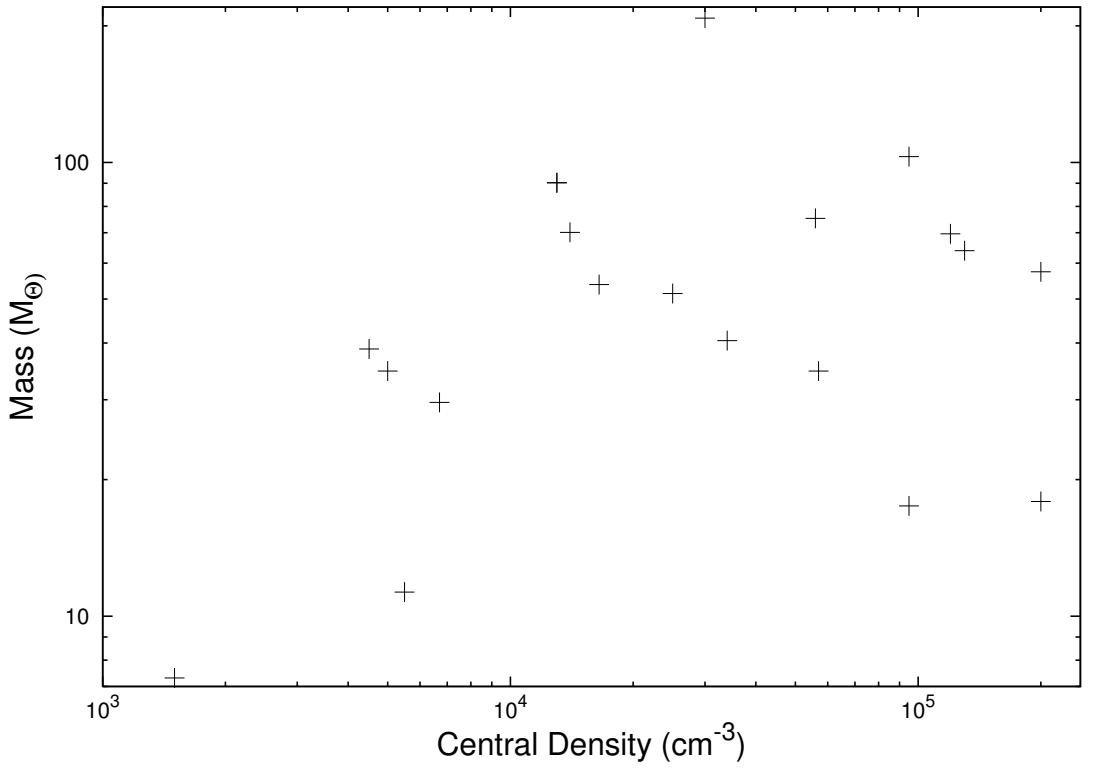

Figure 6.9: The masses of the core plotted against their central density. No correlation is seen.

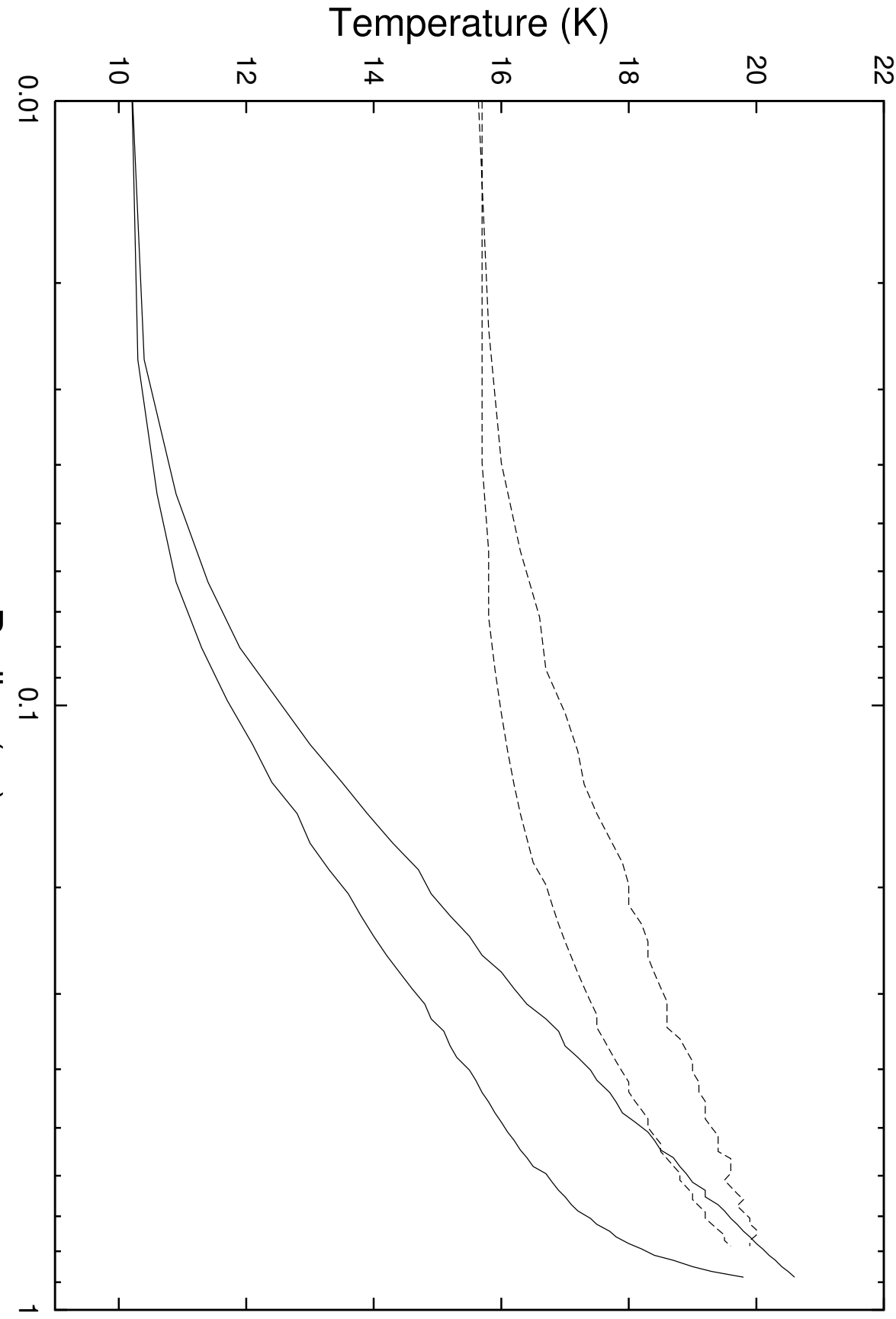

Figure 6.10: Temperature profiles of two typical cores. The solid line shows core 310.297+0.705 and the dashed line shows core 321.753+0.669. The top line of each pair shows a direction of θ=0°, perpendicular to the midplane of the core, and the lower line shows θ=90°, along the midplane of the core.

temperatures observed in each core.

6.3.4.1 Surface Temperature

Figure 6.14 shows the ISRF surrounding each core plotted against the surface temperature. The surface temperature is seen to be strongly dependent on the amount of radiation falling on the core. As the major source of heating for a core is from external radiation, this is as expected. The higher the local ISRF, the more radiation will fall on the core and the higher its surface temperature will be. The two show an exponential relationship, with increasing amounts of radiation needed to heat the surface of the core to greater temperatures. The correlation coefficient between ISRF and T_s is r=0.99, p<0.05, indicating a strong positive correlation.

The dotted line in Figure 6.14 shows the best-fit canonical relationship:

$$\ln(G_{IS}) = (5.8 \pm 0.2)\ln(T_s) - (16.8 \pm 0.6), \tag{6.2}$$

where G_{IS} is the radiation field found in the vicinity of the core in multiples of the Black (1994) radiation field.

To determine the physicality of this best-fit relationship, we consider the relationship between the temperature of the core as a function of radius and the interstellar radiation field. This can be described by the equation:

$$G_{IS}\ \exp(\frac{-AM}{R^2}) = BT^{4+\beta}, \tag{6.3}$$

where A and B are constants, M is the mass external to radius R, T is the temperature at radius R and β is the dust emissivity index. The power of four derives

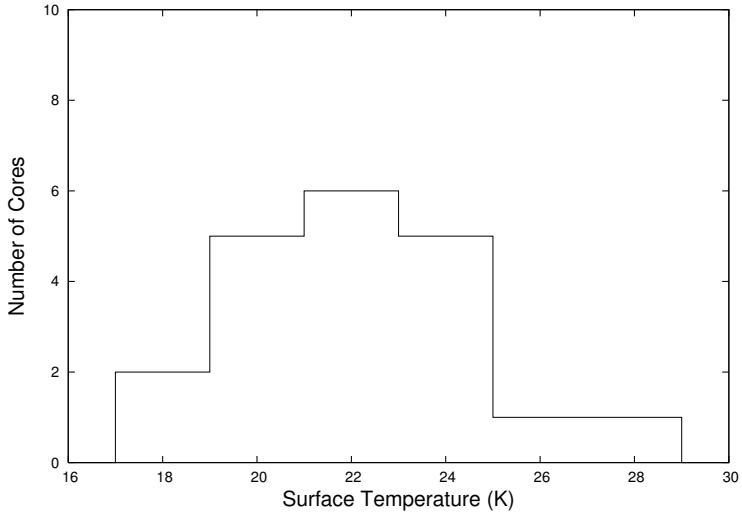

Figure 6.11: Histogram showing the distribution of the surface temperatures of the cores.

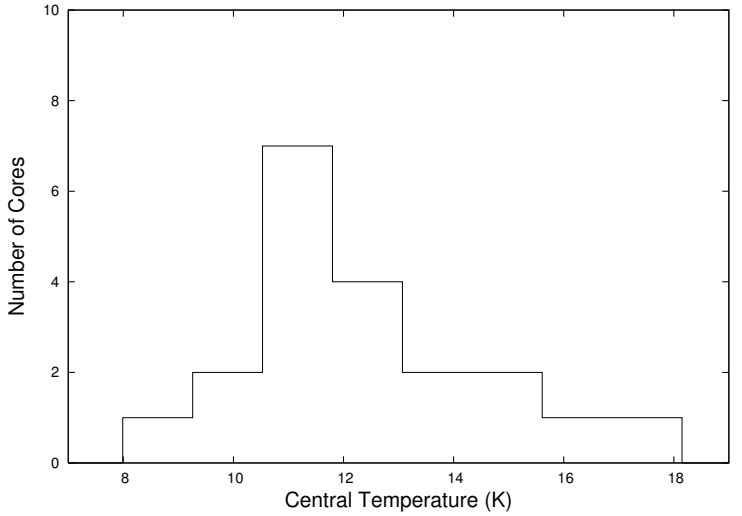

Figure 6.12: Histogram showing the distribution of the temperatures found in the centre of the cores.

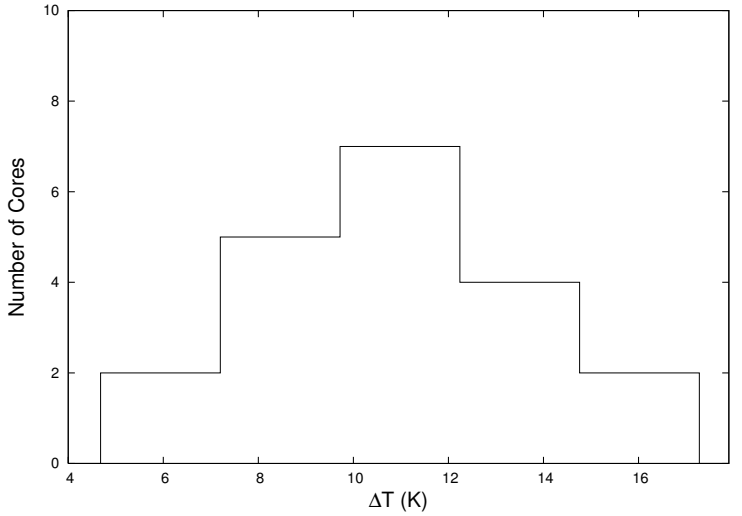

Figure 6.13: Histogram showing the distribution of the range of temperatures found in the cores.

from the Stefan-Boltzmann law (Stefan, 1879; Boltzmann, 1884), where the total radiant heat energy is proportional to T^4 for blackbodies. Here we must also include the dust emissivity index as the cores are not ideal blackbodies.

Equation 6.3 can be re-written as:

$$\ln\left(\frac{G_{IS}}{T^{4+\beta}}\right) - A\frac{M}{R^2} = \ln(B), \tag{6.4}$$

Therefore, at the surface of the core (where column density, M/R^2, is zero) Equation 6.4 becomes:

$$\ln\left(G_{IS}\right) = (4+\beta)\ln\left(\mathrm{T}_s\right) + B. \tag{6.5}$$

The form of the canonical relationship (Equation 6.2) is in excellent agreement with Equation 6.5. The multiple of temperature from Equation 6.2 was 5.8±0.2. We find the dust emissivity index by subtracting four from this value and thus find β=1.8±0.2, in agreement with the expected value of $\beta = 1.85$ (Ossenkopf & Henning, 1994).

From Equation 6.2, we extrapolate that for a core to have a surface temperature over 30 K the ISRF would need to be over 20 times that of the solar neighbourhood and for a surface temperature over 40 K the ISRF would have to be 100 times greater. Most cores will therefore have a surface temperature lower than 30 K. The majority of our cores have surface temperatures less than 25 K.

Similarly, a core with a surface temperature less than 10 K would need to be situated in a radiation field of only one-hundredth of the solar value. This makes lower surface temperatures very unlikely (although not impossible). All of our cores had surface temperatures greater than 16 K.

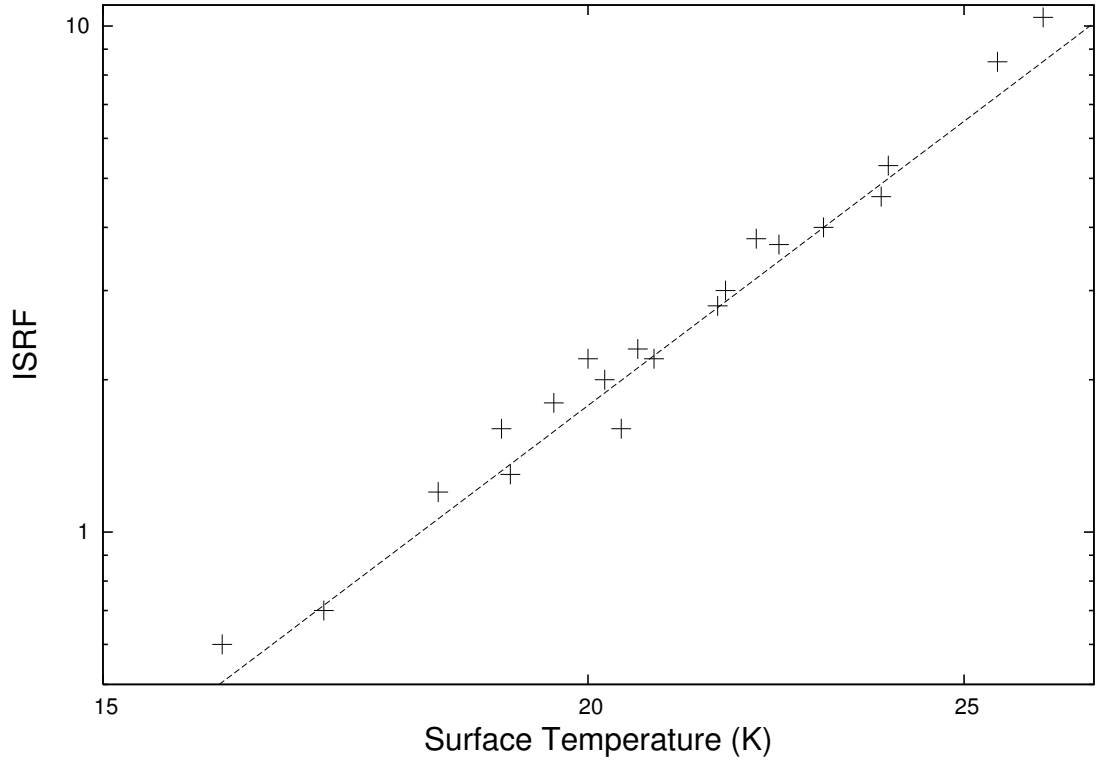

Figure 6.14: A log-log plot of ISRF in multiples of the Black (1994) radiation field against the surface temperature. The dashed line shows the relation between the surface temperature and ISRF as described in Equation 6.2.

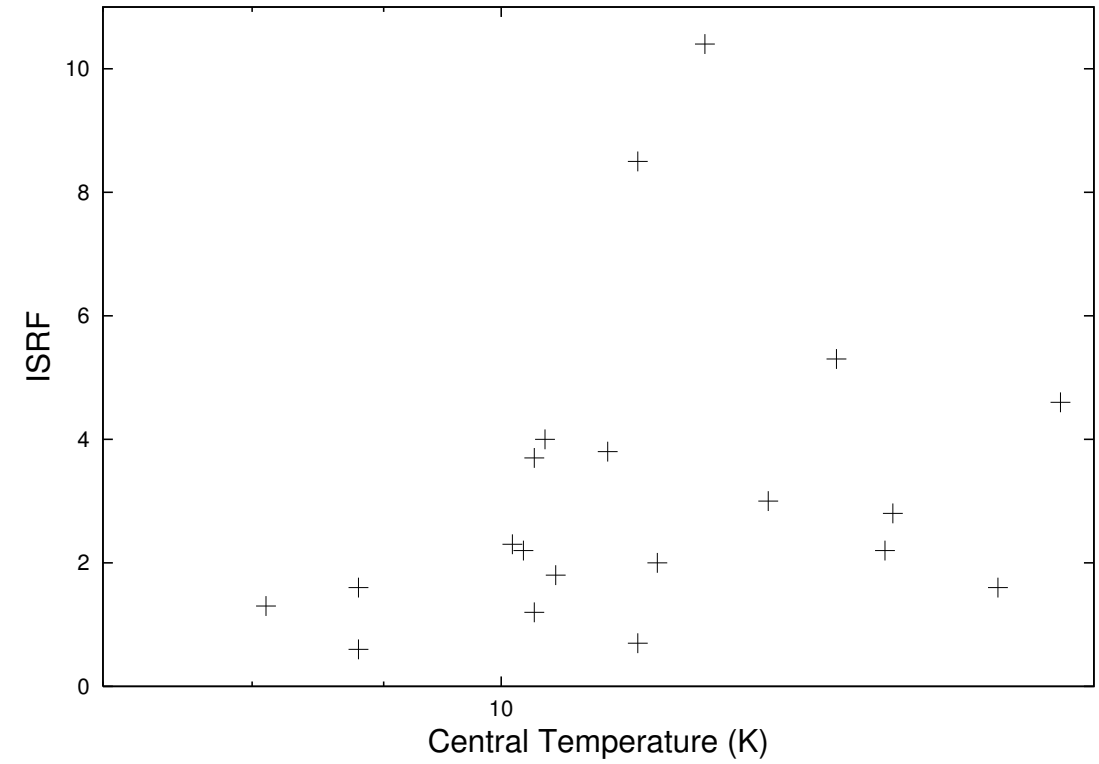

Figure 6.15: The ISRF in multiples of the Black (1994) radiation field plotted against the central temperature.

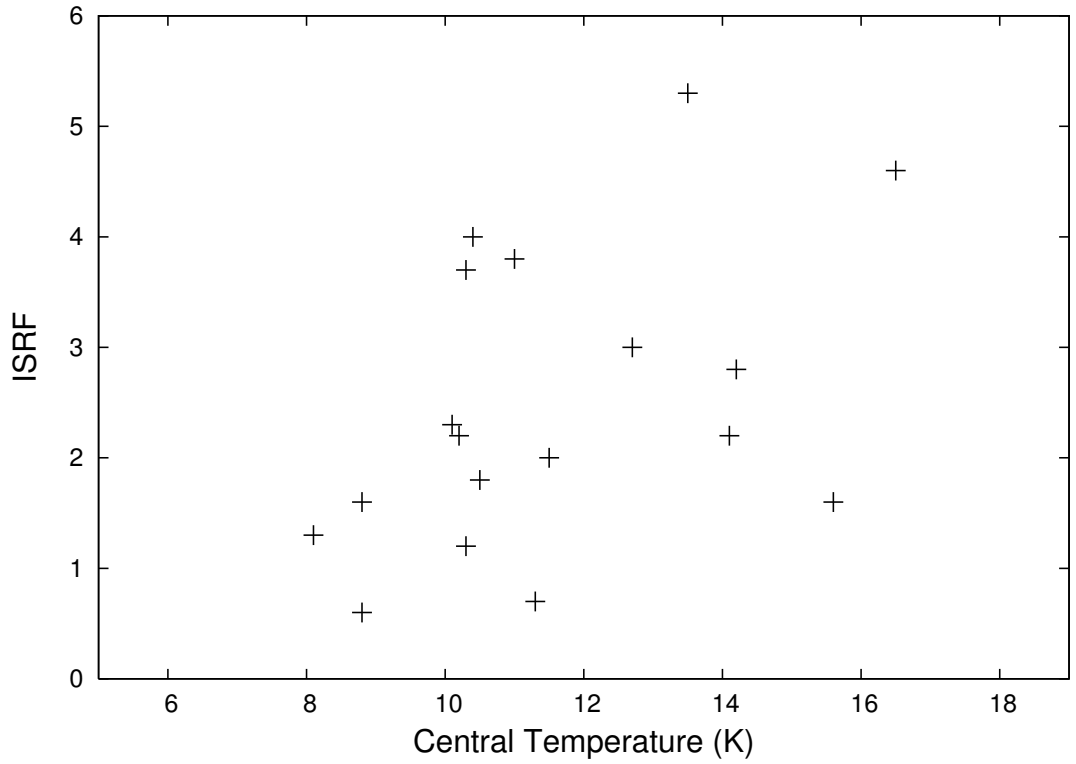

Figure 6.16: The ISRF in multiples of the Black (1994) radiation field plotted against the central temperature with the two cores with the highest ISRF removed.

6.3.4.2 Central Temperature

The temperatures at the centres of the cores vary according to different criteria to those at the surface. For instance, the central temperatures of the cores do not appear to show any direct linear dependency on the ISRF ($r = 0.24$) – see Figure 6.15. Instead, the temperature at the centre of the core appears to be determined by its mass and central density, as shown in Figures 6.17 and 6.18.

However, if we ignore the two outlying points in Figure 6.15, the central temperature shows a positive correlation with the ISRF (r=0.45, p<0.05). This is shown on Figure 6.16. The two outlying cores are those within 326.495+0.581

and 326.811+0.656. These are the cores with the highest local ISRF (10.4 and 8.5 times the solar value, respectively) and the largest temperatures ranges (14.25 and 14.2 K, respectively). However, they also have central densities towards the higher end of our range (a few $\times 10^5\,\mathrm{cm}^{-3}$). Hence more of the ISRF is attenuated before reaching the core centres.

The central temperature shows an inverse linear relationship with central density with a correlation coefficient of $r = -0.46$, $p<0.05$. As radiation impinges onto the surface of a core it will heat the outer layers first, giving the temperature gradient visible in all cores. In denser cores the radiation will have a greater probability of being absorbed in the outer layers and less will travel through the core to heat the centre. Thus, denser cores have a lower central temperature than cores with a lower density.

The masses of the cores show no relation to the temperature at the surface of the core but do show an anti-correlation with the central temperatures, $r = -0.50$, $p<0.05$. Cores with high masses have a lower central temperature. This is due to the same effect that causes the central temperature to vary with density. As mentioned in Section 6.3.3, mass and central density show no correlation with one another. This implies that their relationships with central temperature must be independent of each other.

Figure 6.19 shows the central temperature plotted against the surface temperature. The two show a broad correlation ($r = 0.44$, $p<0.05$), implying that cores with a similar central density, have a higher central temperature if there is a greater ISRF. However, the cores with highest surface temperatures do not necessarily have the highest central temperatures. For example, cores in 307.495+0.660 and 326.811+0.656 have vastly different surface temperatures but identical central

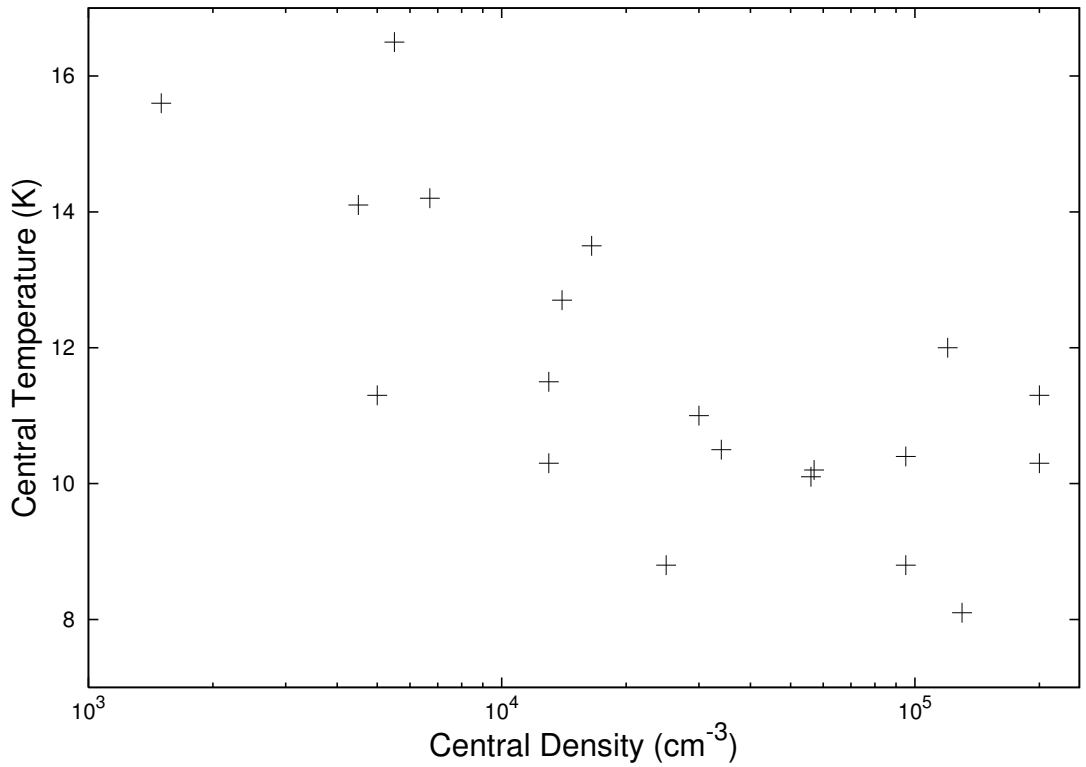

Figure 6.17: The central density of the cores plotted against their central temperatures. Note central density is given on a log scale.

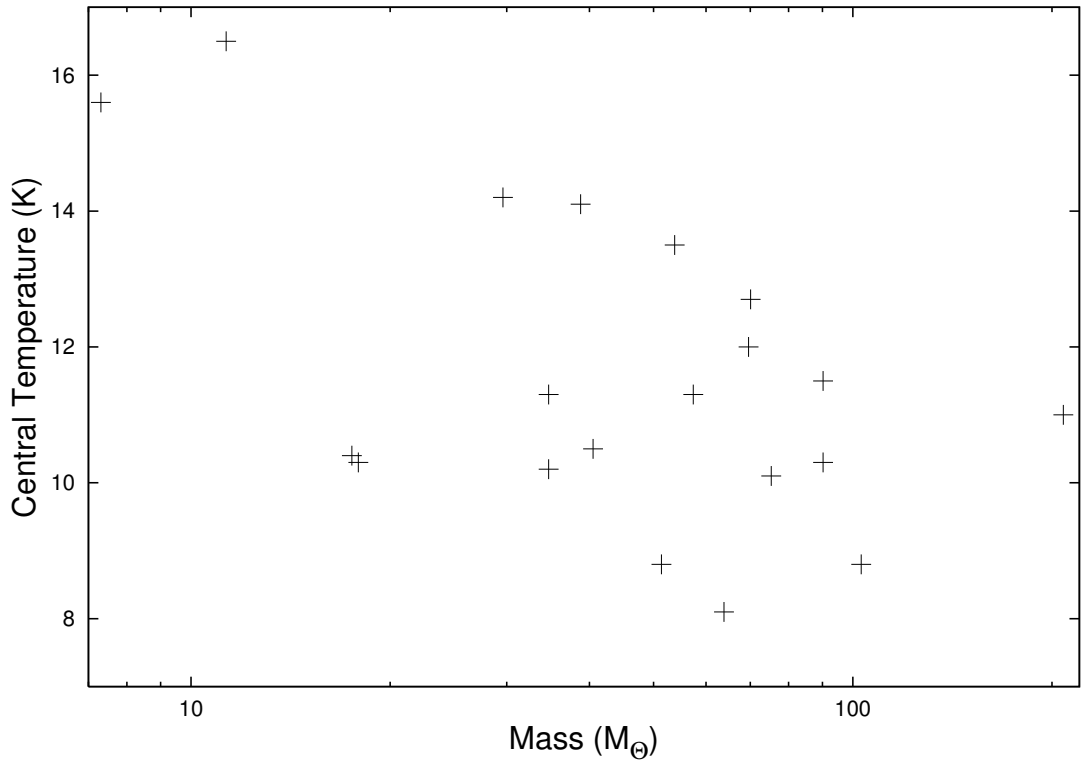

Figure 6.18: The mass of the cores plotted against their central temperatures. Note that mass is shown on a log scale.

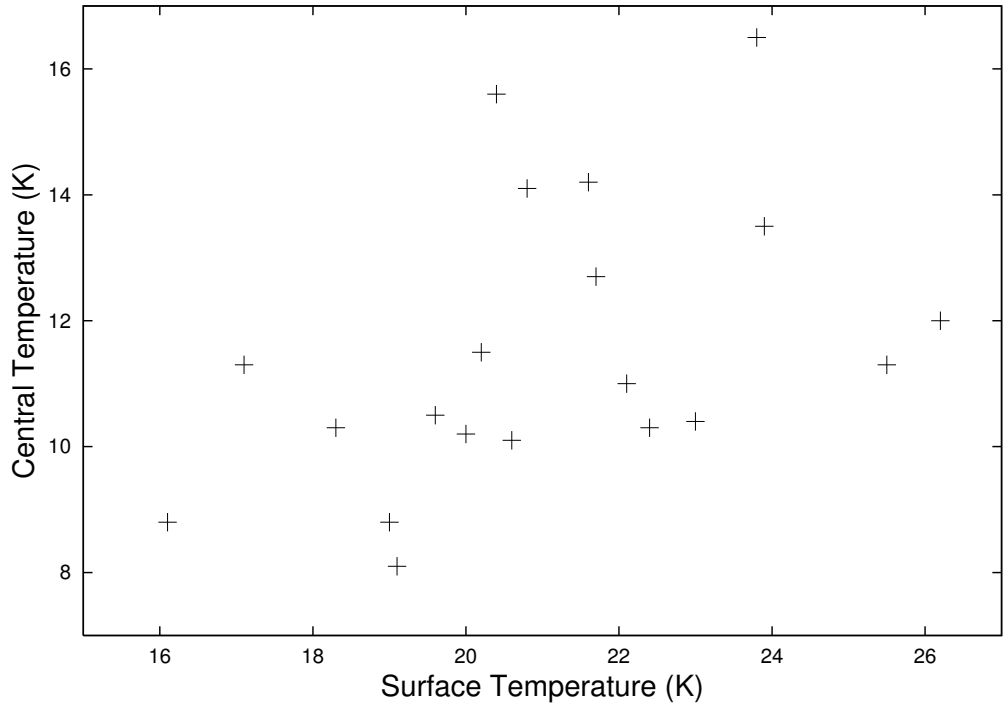

Figure 6.19: The temperature at the centre of the core versus the temperature at the surface of the core.

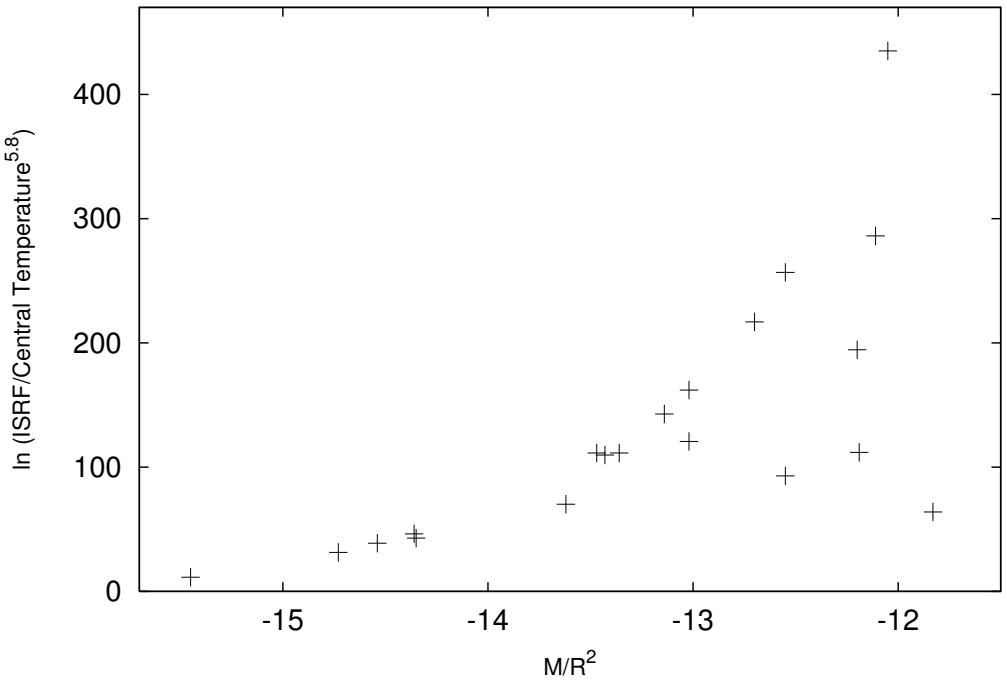

Figure 6.20: The relationship shown in Equation 6.4 plotted for our twenty cores. β=1.8 is assumed.

temperatures, see Table 5.2.

Equation 6.4 can be simplified to Equation 6.5 at the surface of a core but at the centre of a core, where the column density is not zero, the M/R^2 term is non-negligible and so must be included. We make the assumption that β=1.8, which was shown to be the best-fit value for the cores in Section 6.3.4.1, and is compatible with the Ossenkopf & Henning (1994) value of 1.85. Equation 6.4 therefore becomes:

$$\ln\left(\frac{G_{IS}}{T_c^{5.8}}\right) - A\frac{M}{R^2} = \ln(B). \tag{6.6}$$

This relationship is plotted in Figure 6.20 and shows a positive correlation (r=0.64). The correlation between $G_{IS}/T_c^{5.8}$ and M/R^2 shows that Equation 6.3 holds at all radii within the cores, and confirms that β=1.8±0.2 is a sensible assumption for the cores.

6.3.4.3 Temperature Range

The range of temperatures in each core, ΔT, is found via

$$\Delta\mathrm{T} = \mathrm{T}_s - \mathrm{T}_c. \tag{6.7}$$

ΔT is indicative of a core's temperature profile. A core with a high ΔT will show a steeper profile than a core with a lower ΔT. Figure 6.10 shows the temperature profiles of two cores with similar radii. The core in 310.297+0.705 has ΔT= 10.5 K and a far steeper profile than the core in 321.753+0.669 which has ΔT= 4.8 K.

ΔT appears to be dependent on the central density of a core (r = 0.81, p<0.05) and the surrounding ISRF (r = 0.71, p<0.05), but not with its mass (r = 0.27).

These relationships are shown in Figures 6.21, 6.22 and 6.23, respectively. A possible exponential relation between ΔT and the ISRF can be seen. This is similar to the relationship between ISRF and the surface temperature.

The strongest relation is that between ΔT and the core central density. The difference between the temperature at the surface and centre of a core clearly increases as the central density increases. Radiation passing through denser material has a greater probability of being absorbed in the surface layers of the core, and so less radiation passes through to (and heats) the centre of the core. Therefore, if two cores are situated within areas of equivalent ISRFs then, while the surface temperatures would be the same, the denser core would have a colder centre and exhibit a wider range of temperature.

ΔT also shows a weak inverse correlation with the core's radius (r=–0.55, p<0.05) – see Figure 6.24. The larger the size of the core, the smaller the temperature difference between the surface and the centre. This is the opposite of what one would generally expect and, as it is a weak relationship, is not likely to be a direct result but rather a side effect of the fact that our smallest cores have the highest densities.

6.3.5 Central Density

The central densities of the cores vary from $1.5\times10^3\,\mathrm{cm}^{-3}$ to $2.0\times10^5\,\mathrm{cm}^{-3}$, with a mean of $2.0\times10^4\,\mathrm{cm}^{-3}$. The central density of the core is a variable input to the Phaethon code, by which we mean that it is not set by the observational data as with radius and distance. Altering the central density of a core mostly affects the longer wavelength end of the SED (i.e. 350 and 500 μm). Figure 6.25 shows the

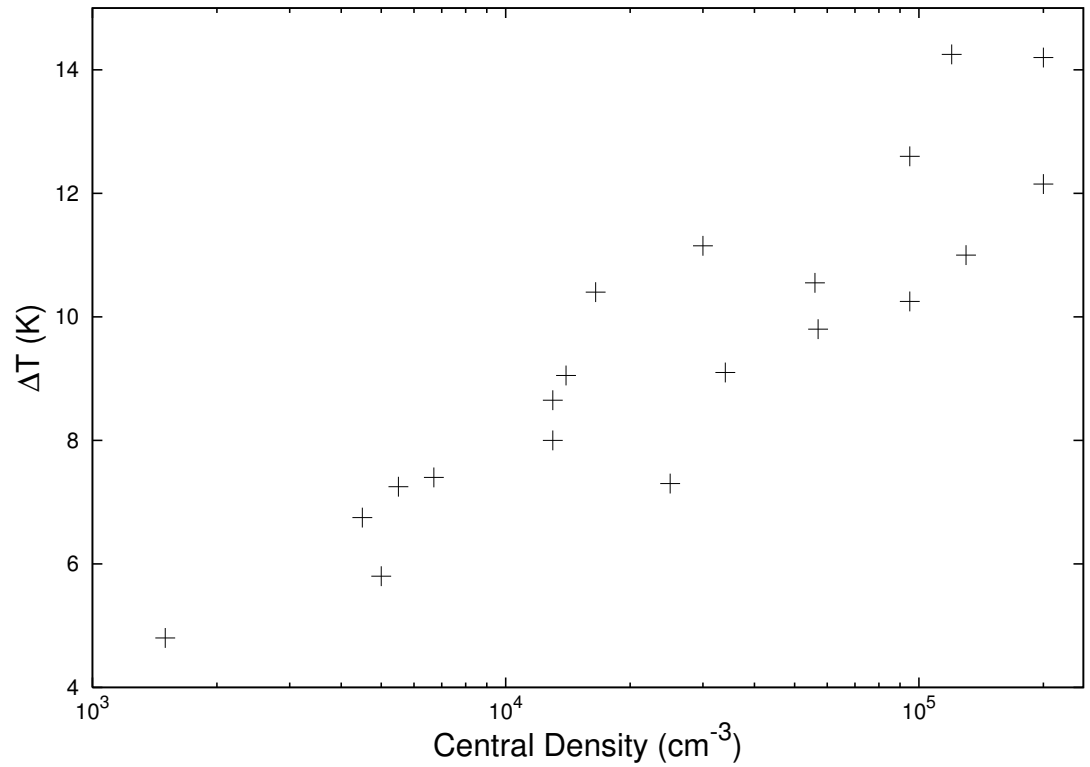

Figure 6.21: The central density of the cores plotted against the difference between the surface and central temperatures (ΔT)

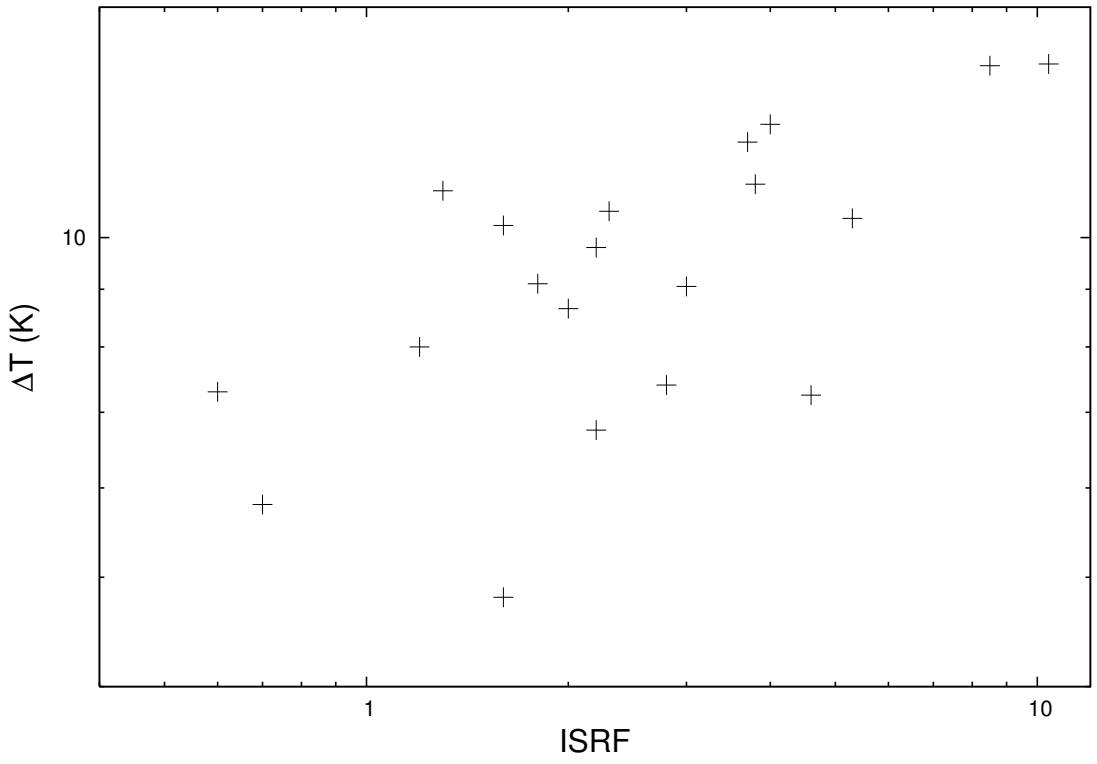

Figure 6.22: The ISRF in multiples of the Black (1994) radiation field plotted against ΔT. This is shown on a log-log scale.

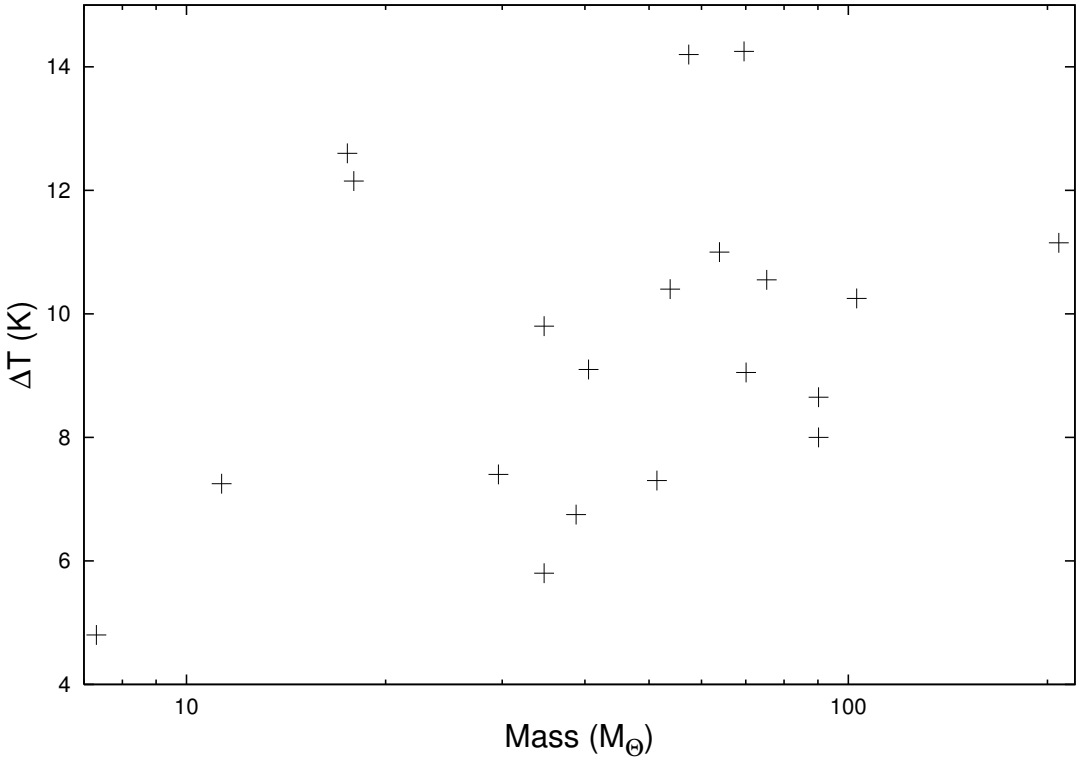

Figure 6.23: ΔT plotted against the masses of the cores

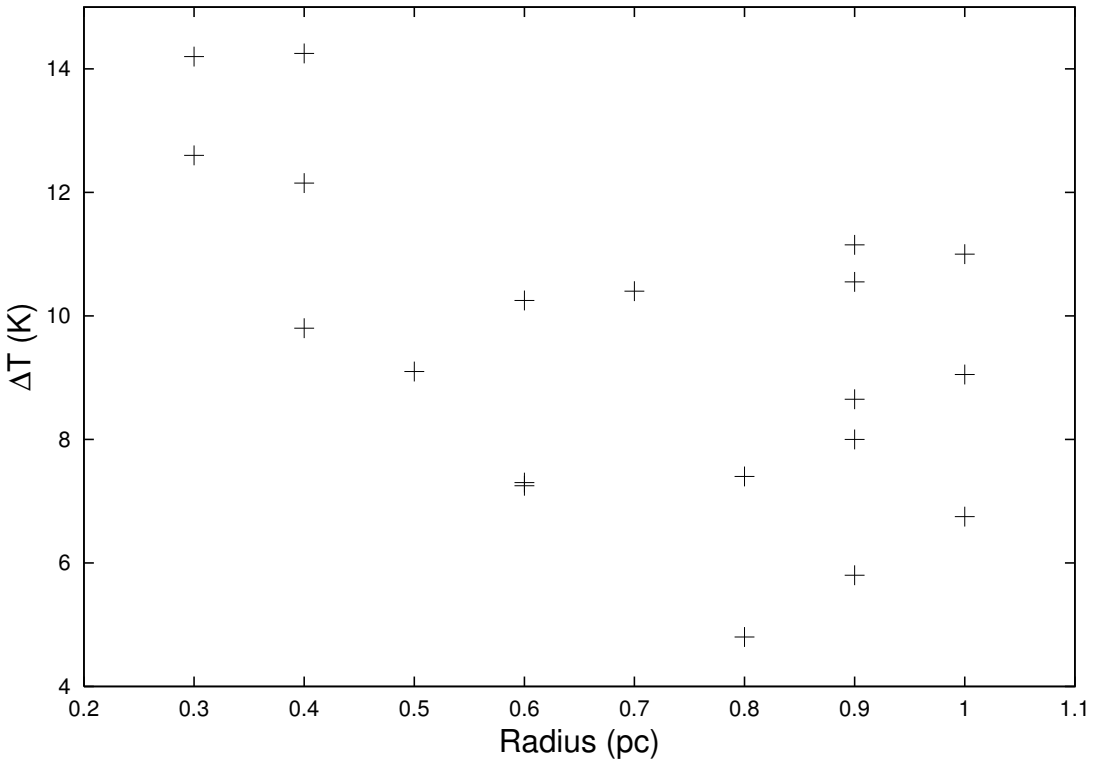

Figure 6.24: ΔT plotted against the radius of the cores.

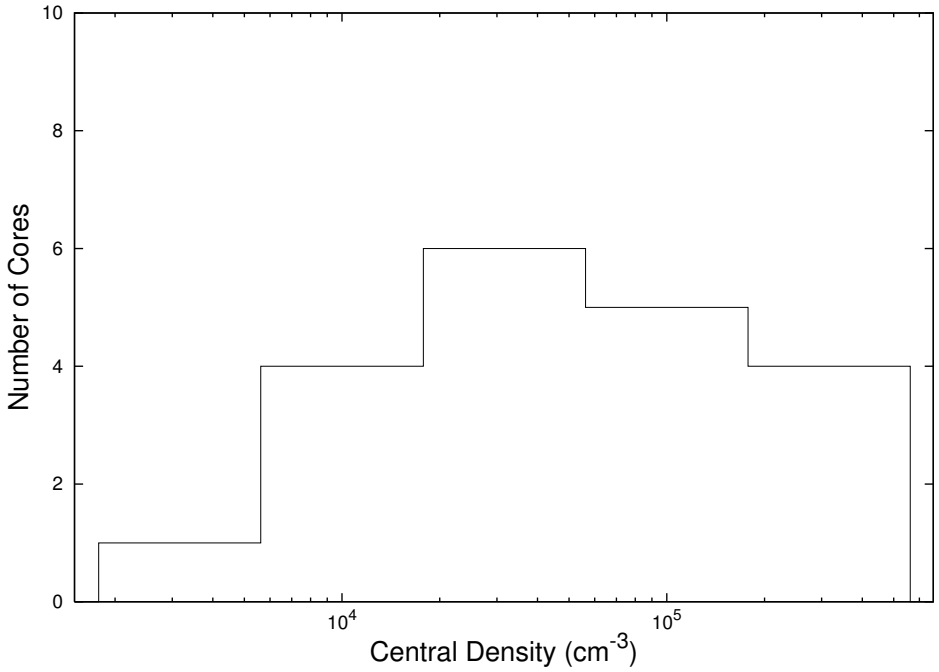

Figure 6.25: Histogram showing the distribution of the central density of the starless cores. Note that the x-axis uses a logarithmic scale.

distribution of central densities. The density profile of each core is calculated via Equation 3.31. This results in the density at the surface of the core (where it is at its lowest) directly correlating with the maximum, central density. It is simply an input definition of the model. This is shown in Figure 6.26. The surface densities range from 0.1 to 20 cm^{-3}.

Figure 6.27 shows the central density of each core plotted against its radius. There is no obvious correlation between the two but there is a noticeable lack of cores in the lower left-hand corner, i.e those with both a low central density and a small radius. This is likely to be a selection effect. This implies that either: small, low density cores do not show up as a distinct peak against their parent cloud; they do not block enough MIR background emission to show a significant dip at 8 μm; or that they are simply fainter and so are more likely to be confused at 500 μm.

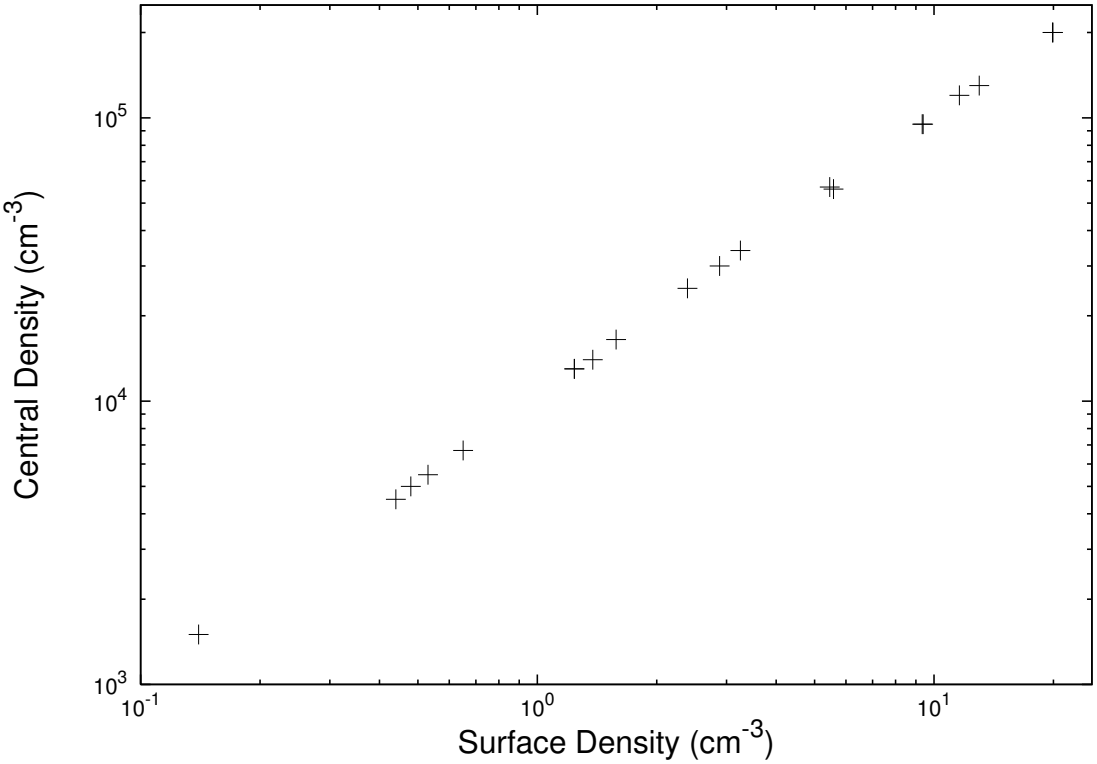

Figure 6.26: Central versus surface density.

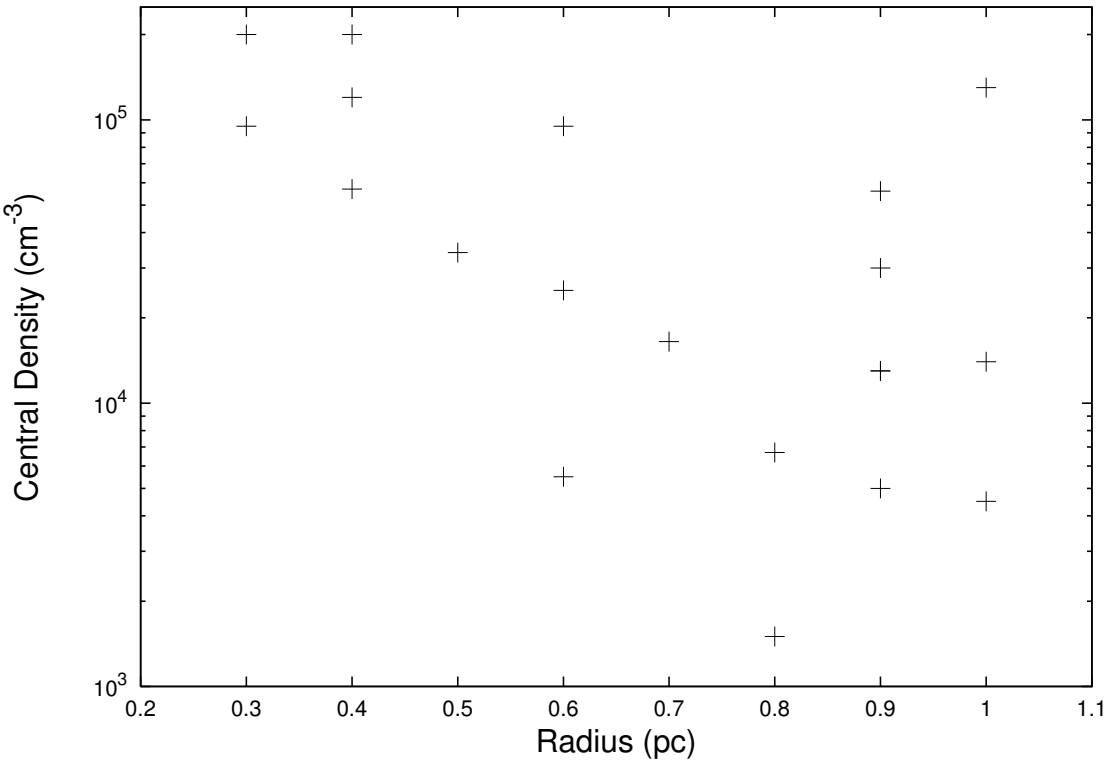

Figure 6.27: Central density versus core radius.

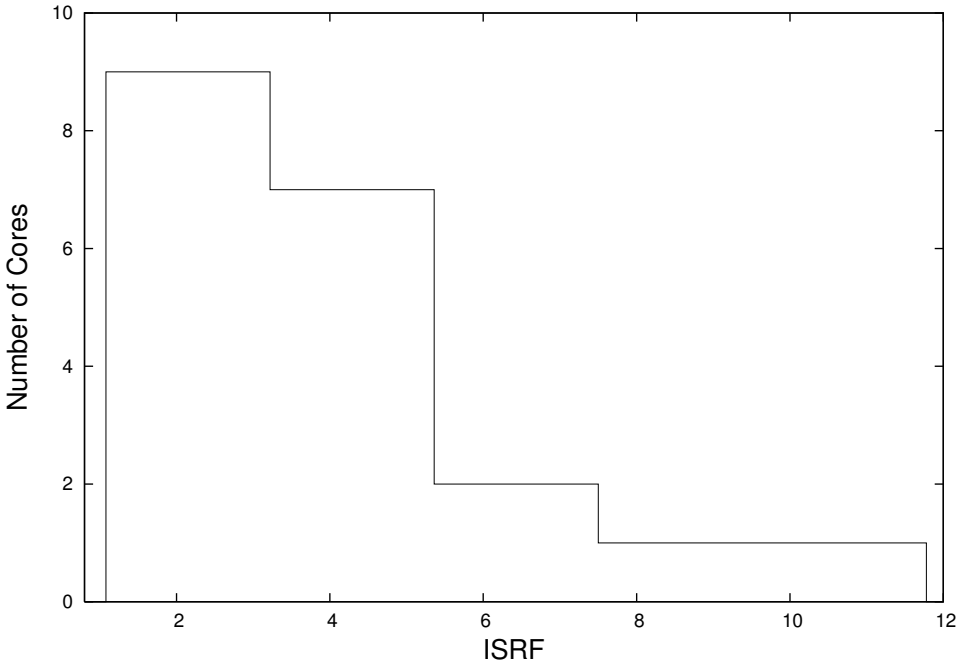

Figure 6.28: Histogram showing the distribution of the ISRF surrounding the starless cores.

This latter theory was tested by creating two model cores that would reside in the lower left of Figure 6.27. Both had a radius of 0.3 pc, equal to the smallest core we model. One had a central density of $2 \times 10^3\,\mathrm{cm}^{-3}$ and the other had $2 \times 10^4\,\mathrm{cm}^{-3}$. We placed them both at a distance of 3.1 kpc, gave them an ISRF of 3.2 times the Black (1994) radiation field and an asymmetry factor of 2.5 (these are the average parameters of our modelled cores). The resulting objects have masses of $0.4\,\mathrm{M}_\odot$ and $3.9\,\mathrm{M}_\odot$. These modelled cores were then added into the Hi-GAL data. This was done in a similar fashion to the modelled IRDCs in Section 4.4. Both model cores were placed in the same four locations with varying confusion and background levels. They were then observed in the same way as our original 20 starless cores. If the model cores could be seen in emission and met our criteria for isolation then we could state that it is possible that real cores of a similar size and density could have been selected for modelling. However, even in unconfused

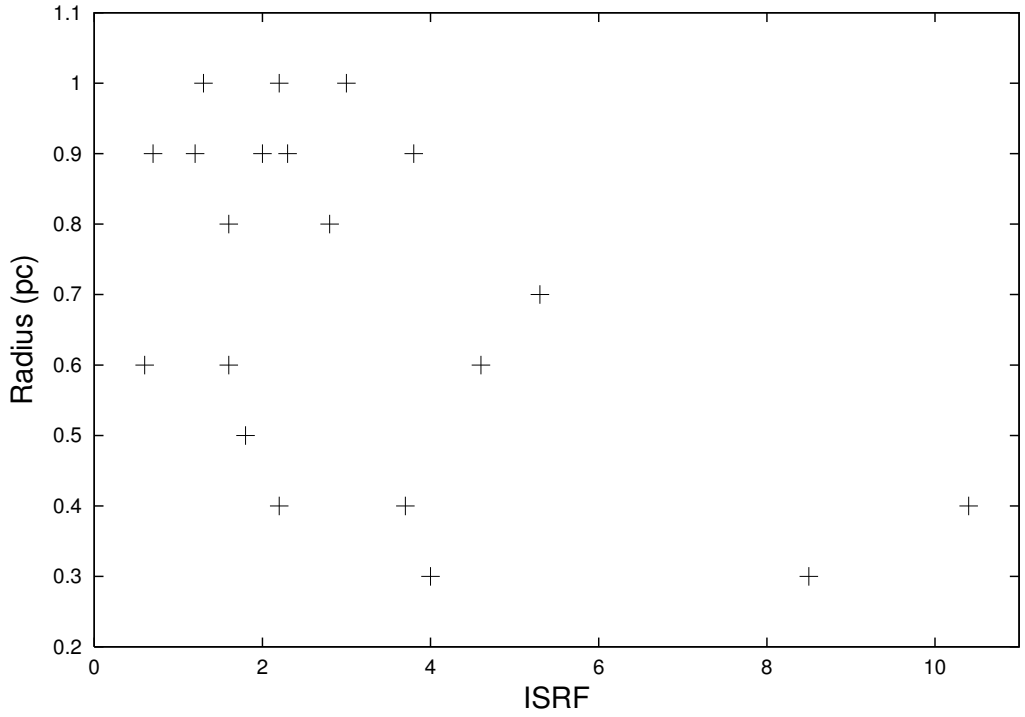

Figure 6.29: Core radius versus ISRF – in multiples of the Black (1994) radiation field.

regions with very low background levels, neither model core met our criteria for isolation at 500 μm. Such cores would not have been selected for modelling. As such, any similar cores in the data are also unlikely to have been selected.

6.3.6 The Interstellar Radiation Field

The ISRF for each core is quoted in terms of multiples of the Black (1994) radiation field. The Black (1994) radiation field models the ISRF in the solar neighbourhood and measures a value of $1.3 \times 10^{-16}\,\mathrm{erg\,s^{-1}\,cm^{-2}\,Hz^{-1}\,sr^{-1}}$ at 500 μm. Along with the central density, the ISRF is one of the variable inputs of the PHAETHON code (see Section 5.5), and mostly affects the SED at shorter wavelengths (i.e. 70 and 160 μm). The ISRF around our cores ranges from 0.6 to 10.4 times the Black (1994) field, with an average multiple of 3.2. Figure 6.28 shows the distribution of

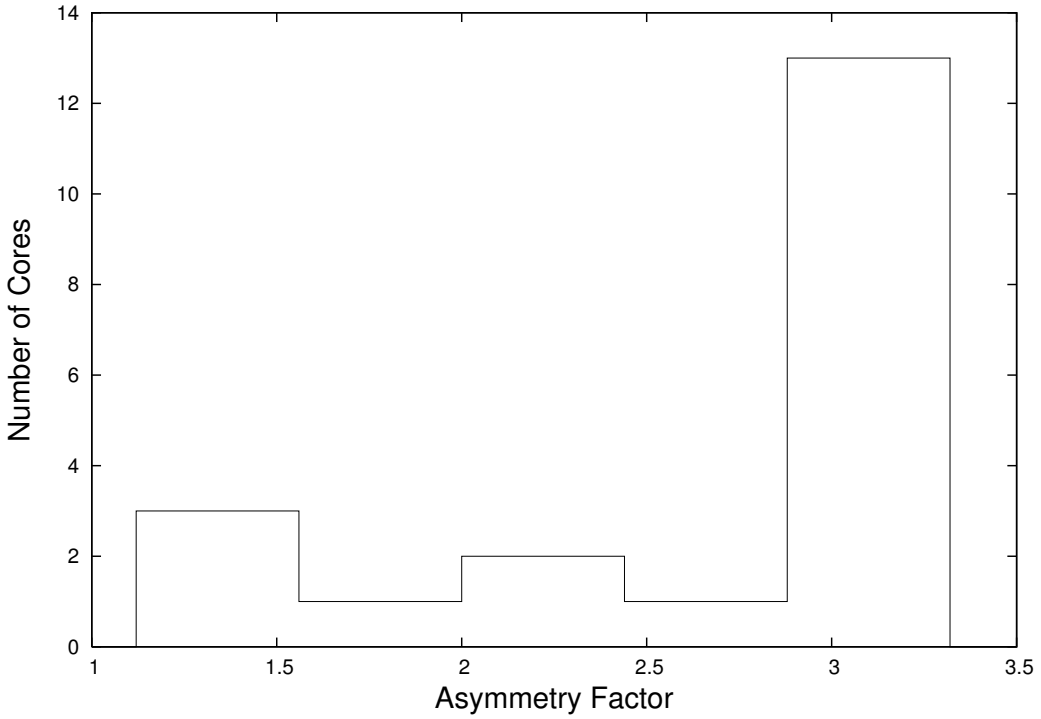

Figure 6.30: Histogram showing the distribution of the asymmetry factor of the starless cores.

the ISRF surrounding the cores.

The amount of radiation incident on our cores is typically greater than that which is observed in the solar neighbourhood. This is consistent with the inner Galactic Plane generally having a stronger radiation field than that of the solar neighbourhood. However, two of the cores do show a radiation field lower than the solar value. These are the cores in 307.495+0.660 and 321.678+0.965 (see Table 5.2). There are two possible explanations for this: either they simply exist in an area which has a particularly low ISRF; or the ISRF surrounding the parent IRDC is consistent with other cores but the parent cloud is absorbing most of the radiation. The latter could be caused by the IRDC being especially dense, or by the cores being buried particularly deeply within the parent cloud. Either case would make it difficult for radiation to penetrate far enough to affect the cores.

Figure 6.29 shows a plot of core radius versus ISRF. We detect cores of all sizes with ISRFs at the lower end of our scale but our modelled sample doesn't include any cores with a high ISRF and a large radius. If radiation pressure were forcing the cores to condense then we would expect the central density to increase as the radius decreased. While our smaller cores do tend to have densities at the higher end of our range, the larger cores have both low and high densities. This is due to the selection effect discussed in Section 6.3.5. We therefore dismiss radiation pressure as the reason why we detect no large cores in areas of high ISRF. Instead, we consider that in areas with a high radiation field the outer layers of large cores may 'boil away' due to the large amounts of energy being absorbed. This would explain why we only see small cores in areas of high ISRF and why there is no significant increase in the density of these cores.

6.3.7 Asymmetry Factor

The asymmetry factor input to the model controls the shape of the core. A value of 1.0 would result in a circular core. The ellipticity of the core is increased by raising the asymmetry factor up to a maximum of 3.0. Most IRDC cores are elongated and have a high eccentricity. 80 % of our cores have an asymmetry factor greater than 2 (corresponding to an aspect ratio of $\sim 1:4$) – see Table 5.2. Figure 6.30 shows the distribution of the asymmetry factor of the cores, with a clear bias towards more elliptical cores. It is also possible that some of our more circular cores could be elongated but viewed end-on.

Table 6.3: The mean values of the physical properties of the 20 modelled cores.

Physical Property	Mean
Helio-centric Distance (pc)	3100
Radius (pc)	0.7
Mass ($M_\odot$)	58.3
Surface Temperature (K)	21.1
Central Temperature (K)	11.5
ΔT (K)	9.5
Central Density (cm^{-3})	5.6×10^4
ISRF	3.2
Asymmetry Factor	2.5

6.3.8 Mean Core Properties

Table 6.3 shows the mean values of each of the nine physical properties discussed in Sections 6.3.1–6.3.7. The mean physical properties reiterate the fact that starless cores are dense, elongated, objects and, when found in the Galactic Plane, have a local ISRF greater than that which is found in the solar neighbourhood. Within the cores, the temperature decreases from surface to centre, typically by $\sim$10 K. The mean asymmetry factor is 2.5, corresponding to an aspect ratio of $\sim$1:3.

6.4 Principal Component Analysis

6.4.1 Principal Component Analysis Assuming a Linear Relationship

We have analysed the results of our modelling, first looking at each of the parameters individually and then in pairs. Now, we analyse our parameters as a whole through principal component analysis. This was performed using the eight major

physical properties of the cores: distance; central temperature; surface temperature; local ISRF; central density; radius; asymmetry factor; and mass.

As these parameters have different units, the results had to be standardised before the analysis could be performed. This was done via:

$$A_s = \frac{\left(A - \overline{A}\right)}{\sigma}, \tag{6.8}$$

where A_s is the standardised result, A is the actual result, $\overline{A}$ is the mean of the parameter and σ its standard deviation. This ensured that all parameters were dimensionless, with a mean of zero and a standard deviation of one.

The covariance matrix for the eight parameters was then calculated. An $n \times n$ covariance matrix gives the covariances between a set of n parameters. There are 8 parameters and so an 8×8 matrix was used. The covariance is defined as the mean value of the product of the deviations of two variables (e.g. x and y) from their respective means. The covariance between two parameters was thus calculated using the equation:

$$S_{xy} = \frac{\sum_{i=1}^{N} \left(x_i - \overline{x}\right) . \left(y_i - \overline{y}\right)}{N - 1}, \tag{6.9}$$

where N is the total number of datapoints, in this case 20 for the 20 cores. As the mean of each parameter ($\overline{x}$ and $\overline{y}$) was zero, this was simplified to:

$$S_{xy} = \frac{\sum_{i=1}^{N} x_i . y_i}{N - 1}. \tag{6.10}$$

The eigenvectors and eigenvalues of the covariance matrix were then calculated. Our 8×8 matrix resulted in eight eigenvalues (shown in Table 6.4) and eight eigenvectors. Each eigenvector contained eight coefficients (see Table 6.5 in order

Table 6.4: The eigenvalues of the covariance matrix.

Number	Eigenvalue	Percentage of Total (%)	Cumulative Percentage (%)
1	2.98	37.16	37.2
2	2.05	25.61	62.8
3	1.51	18.80	81.6
4	0.94	11.71	93.3
5	0.37	4.67	98.0
6	0.11	1.32	99.3
7	0.03	0.41	99.7
8	0.03	0.31	100.0

of decreasing value) and is paired with one of the initial parameters (e.g. the first eigenvector is associated with the distance of each core). Each eigenvalue is paired with one coefficient in each eigenvector (i.e. the first eigenvalue corresponds to eigenvector component x_1). The values of each coefficient in all eight eigenvectors form one principal component – for example, the column labelled x_1 in Table 6.5 is the first principal component and that labelled x_2 is the second.

The principal components were then selected using the eigenvalue-one criterion. The eigenvalue-one criterion states that any eigenvalue which is greater than 1 is influential and should be kept, while those with a value less than 1 are to be discarded (Hatcher, 1994). We thus kept the first three eigenvalues and so the first three principal components (i.e. x_1, x_2 and x_3 in Table 6.5, which are also shown in Table 6.6). These three principal components account for $\sim$82 % of the total variance in the data. Each principal component contains eight loadings, which are coupled with one of the initial parameters (e.g. the first coefficient in each principal component relates to the distance of each core).

For each principal component, it was then determined which loadings were most significant. A loading with a higher value will have more effect on the final

Table 6.5: The eigenvectors of the covariance matrix. Each row contains a single vector and each column contains one coefficient of that vector.

	x_1	x_2	x_3	x_4	x_5	x_6	x_7	x_8
Distance	0.24	0.20	0.58	0.31	−0.63	−0.07	0.15	0.22
T_s	−0.45	−0.24	0.42	0.02	0.05	−0.24	−0.70	0.14
T_c	0.01	−0.62	0.21	0.29	0.35	−0.29	0.50	0.16
ISRF	−0.48	−0.17	0.36	−0.16	−0.13	0.57	0.29	−0.41
Central Density	−0.48	0.37	−0.06	0.06	0.19	0.21	0.23	0.70
Radius	0.47	0.06	0.34	0.19	0.51	0.55	−0.25	0.08
Asymmetry Factor	0.23	−0.52	−0.12	−0.49	−0.31	0.29	−0.07	0.49
Mass	0.13	0.27	0.43	−0.71	0.27	−0.32	0.19	0.00

scores and is considered more important. Each component was normalised, so the highest loading had a value of 1 and the others had decreasing values in order of significance. Any normalised loading with a value greater than 0.6 was considered significant (Joliffe, 1986). This resulted in any loading greater than ∼0.28, ∼0.37 and ∼0.35 being selected for the first, second and third principal components, respectively. The loadings considered to be important to each principal component are highlighted in Table 6.6.

Each principal component can be interpreted based on their loadings, only those loadings which were ruled to be significant are analysed here. In the first principal component (PC1; Table 6.6) the surface temperature, ISRF, central density and radius all contribute. The latter with a positive sign and the other three have a negative, meaning that this component contrasts the ISRF, surface temperature and central density of a core with its size. Thus, large cores with low temperatures, in low areas of ISRF and with a low central density will score high in this index. These parameters are those which were shown to affect the temperature gradient of a core (see Section 6.3.4). PC1 can therefore be viewed as an index of the temperature gradient within the cores; those cores with a shallow

Table 6.6: The principal components of our analysis. Loadings which were considered significant have been highlighted in bold (see text for details).

	PC1	PC2	PC3
Distance	0.24	0.20	**0.58**
T_s	**−0.45**	−0.24	**0.42**
T_c	0.01	**−0.62**	0.21
ISRF	**−0.48**	−0.17	**0.36**
Central Density	**−0.48**	**0.37**	−0.06
Radius	**0.47**	0.06	0.34
Asymmetry Factor	0.23	**−0.52**	−0.12
Mass	0.13	0.27	**0.43**

temperature gradient will have a high PC1 score.

In the second principal component (PC2; Table 6.6) the central temperature, central density and asymmetry factor are the biggest contributors. Central temperature and asymmetry factor both have a negative sign and the central density a positive sign. The cores that score highest in PC2 will be the more circular cores with a low central temperature and high central density. The latter two parameters are known to be strongly inversely correlated, the central temperature depends greatly on the central density (see Figure 6.17). As it is dependent upon the shape and the density of the core, the second principal component is possibly a measure of the internal structure of the material that makes up the core.

Finally, the third principal component (PC3; Table 6.6) is affected most by the helio-centric distance of each core as well its surface temperature, surrounding ISRF and mass. All the significant coefficients in PC3 have a positive sign. Cores that have a high score for PC3 will be far from the Sun with a hot surface (the surface temperature was seen to depend almost exclusively on the ISRF, see Section 6.3.4.1) and a high mass. This component implies that there is a cluster of cores with high helio-centric distances that have high masses and high surface

temperatures. However, this is likely to be due to our selection criteria. Instrument constraints (sensitivity and resolution) mean that if a core has a higher than average distance then it must be larger, and possibly brighter, than a nearby core to be selected for modelling. Figure 6.5 shows that only high mass cores are selected if they have a large helio-centric distance. Those cores with slightly higher temperatures will be brighter at 250 μm (Equation 2.1) and so more easily detectable at greater distances. Hence, we may ultimately discard PC3 as being an observational selection effect.

The final scores for the twenty modelled cores were then calculated. Each core gets three scores, one for each principal component. The scores were calculated via:

$$C = \sum_{i=1}^{n} x_i \, A_{s,i}, \tag{6.11}$$

where C is the core's final score in the principal component, x_i is the i^{th} coefficient and $A_{s,i}$ is the standardised result associated with the i^{th} parameter (i.e. $C = x_1$ $\times$ the distance to the core + $x_2 \times T_s + x_3 \times T_c$ + ... + $x_8 \times$ mass).

The final scores for each principal component were plotted against one another (see Figures 6.31–6.33). PC1 and PC2 show a strong, positive correlation with r=0.78, p<0.05. A plot of PC1 against PC2 is shown in Figure 6.31 and represents over $\sim$ 60 % of the variation of the modelled cores. Cores with a high score on PC1 are likely to have a shallow temperature gradient (i.e. low central density, low ISRF and surface temperature and a large radius), while PC2 tracks the internal structure of the core. The correlation appears strongest for those cores with a high score for PC1 and PC2. The correlation at the lowest values appears much weaker. The cores situated in the top right-hand corner of the graph are those with a low surface and central temperature, lower central density and a larger radius (hence a

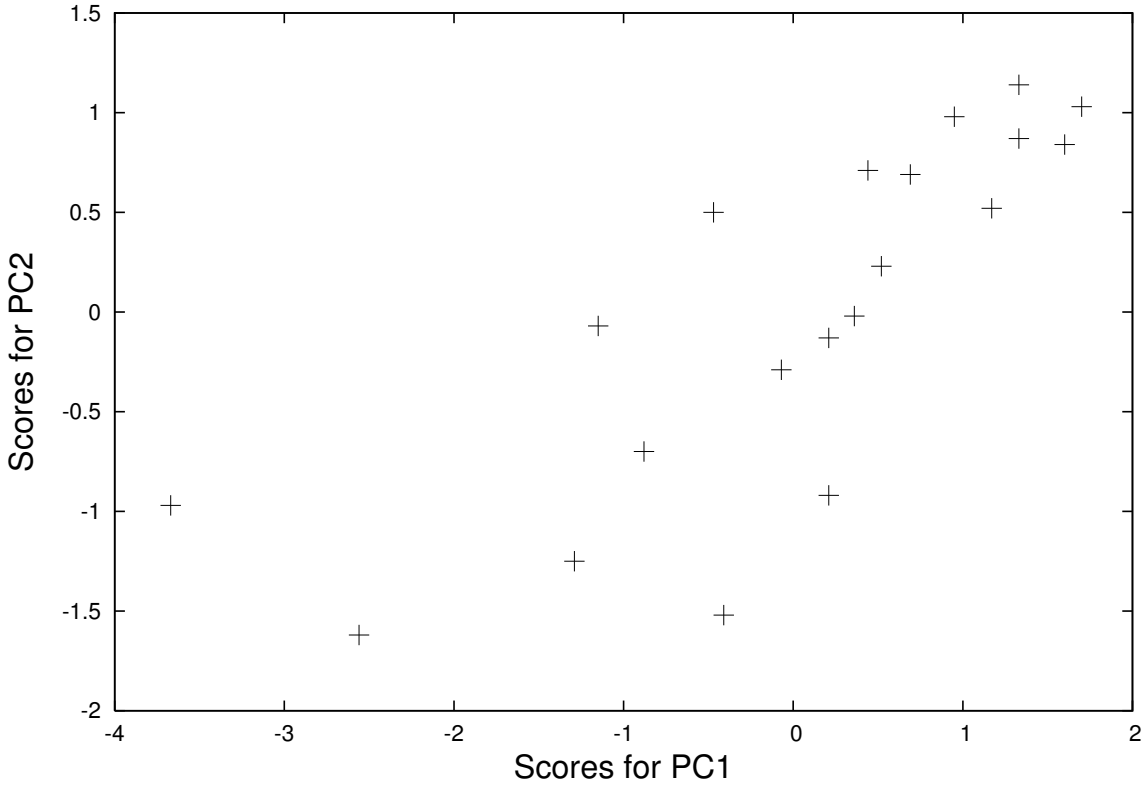

Figure 6.31: The final scores of each core for PC1 plotted against those for PC2.

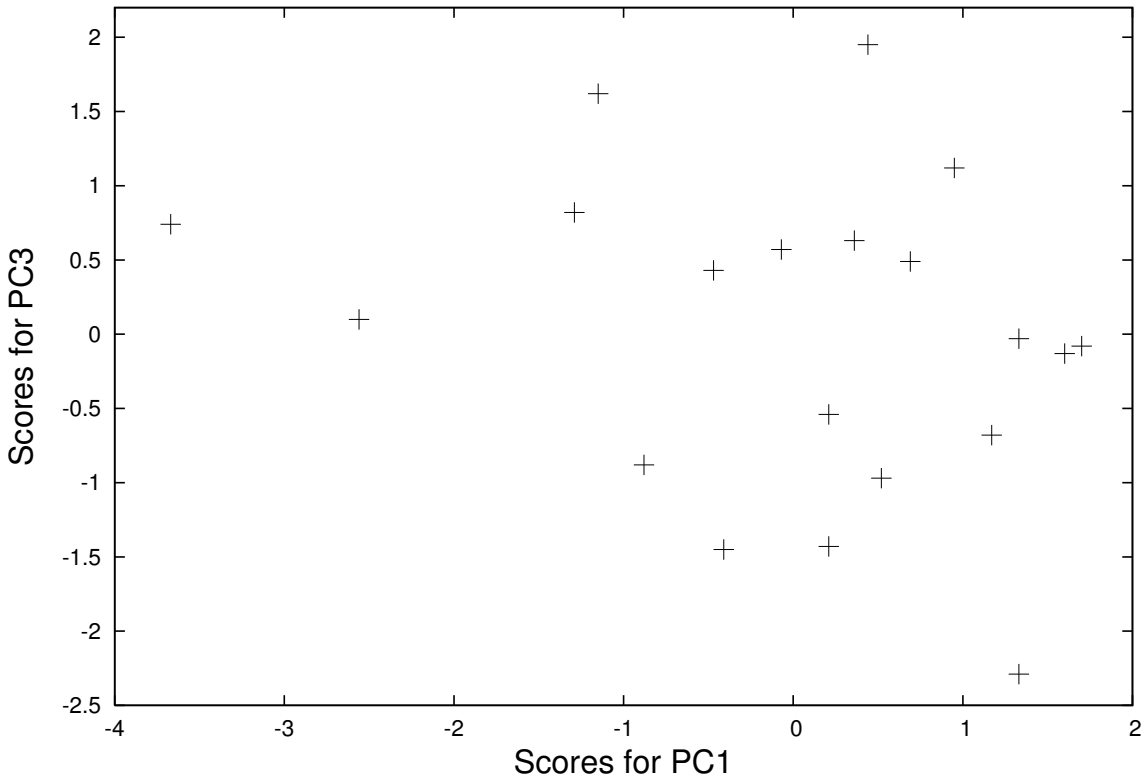

Figure 6.32: The final scores of each core for PC1 plotted against those for PC3.

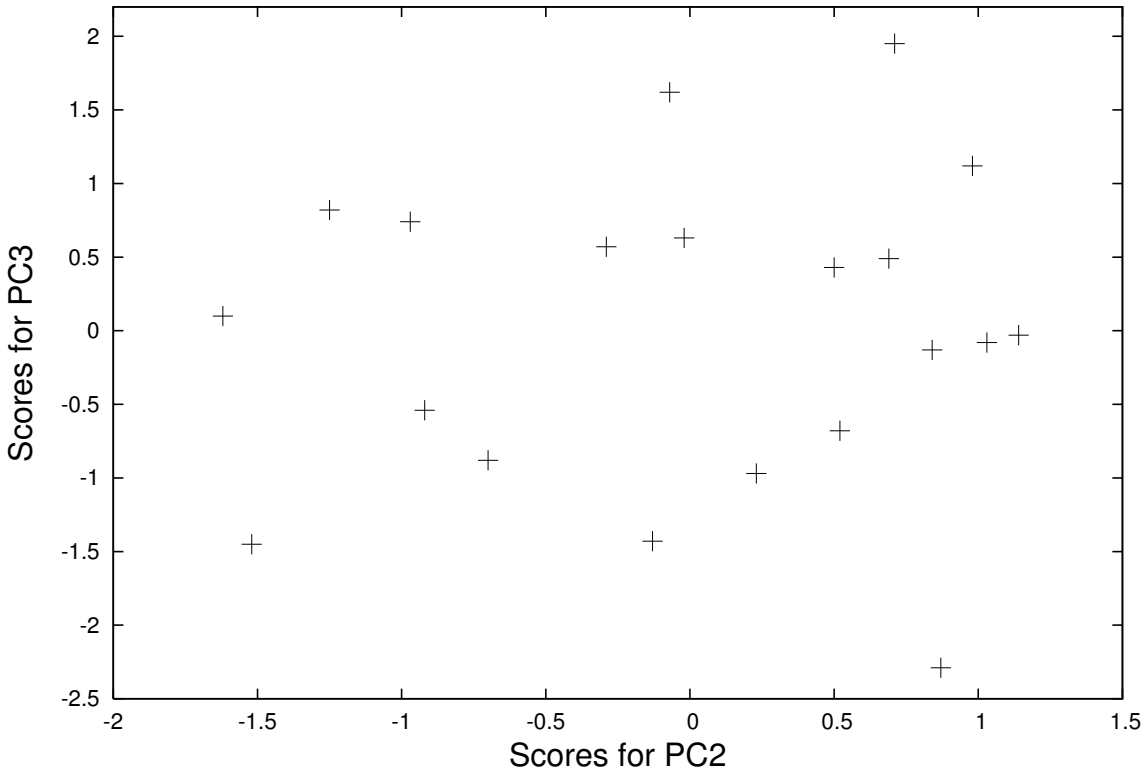

Figure 6.33: The final scores of each core for PC2 plotted against those for PC3.

shallow temperature gradient). These cores also appear to have a typically higher mass, with an average mass of $\sim$50 $M_{\odot}$, compared to those in the lower left-hand corner which have an average of $\sim$30 $M_{\odot}$.

Neither PC1 nor PC2 shows a correlation with PC3, with r=$-$0.26 and 0.09, respectively (see Figures 6.32 and 6.33). Nor does either graph appear to show any clusters of cores. This confirms our suspicion that PC3 is purely a selection effect. Our analysis therefore implies that the internal temperature gradient and density structure are the most significant parameters in determining how a core appears in our data.

Table 6.7: The eigenvectors of the covariance matrix formed from the log values of the eight major physical parameters. Each row contains a single vector and each column contains one coefficient of that vector.

	$x_{1_{log}}$	$x_{2_{log}}$	$x_{3_{log}}$	$x_{4_{log}}$	$x_{5_{log}}$	$x_{6_{log}}$	$x_{7_{log}}$	$x_{8_{log}}$
Distance	0.18	0.19	0.64	0.14	−0.71	0.03	0.00	0.00
T_s	−0.50	−0.21	0.34	0.02	0.14	0.26	−0.45	−0.55
T_c	−0.03	−0.59	0.24	0.14	0.06	−0.46	0.54	−0.25
ISRF	−0.52	−0.15	0.34	−0.09	0.12	0.11	0.09	0.74
Central Density	−0.40	0.47	−0.08	−0.08	−0.04	0.30	0.67	−0.28
Radius	0.49	−0.01	0.36	0.26	0.52	0.52	0.18	0.02
Asymmetry Factor	0.21	−0.40	−0.04	−0.77	−0.22	0.38	0.11	−0.05
Mass	0.10	0.41	0.41	−0.54	0.38	−0.45	−0.05	−0.08

6.4.2 Principal Component Analysis Assuming a Logarithmic Relationship

Using principal component analysis the initial eight parameters have been reduced into three principal components which account for ∼80 % of the variation in the data. However, ideally, we would hope for our eight parameters to be reduced to two components describing ∼90 % of the variation. Our results imply that there may be a more complex relationship between the parameters than our linear analysis allows for. The same analysis was therefore performed on the log values of the eight physical parameters. This will allow for a power-law relationship between the parameters, as seen between surface temperature and ISRF (see Section 6.3.4.1), where previously only a linear relationship would have been accounted for. A second covariance matrix was calculated from the logarithmic values and the new eigenvectors and eigenvalues found as before. The new eigenvectors and eigenvalues are shown in Tables 6.7 and 6.8, respectively.

Using the same criteria as before, it was found that the first three principal components are the most significant. These account for ∼85 % of the variance

Table 6.8: The eigenvalues of the covariance matrix formed from the log values of the eight major physical parameters.

Number	Eigenvalue_{log}	Percentage of Total (%)	Cumulative Percentage (%)
1	2.78	34.75	34.75
2	2.5	31.24	66
3	1.64	20.43	86.43
4	0.77	9.62	96.05
5	0.27	3.37	99.42
6	0.04	0.5	99.92
7	0.01	0.08	100
8	0	0	100

Table 6.9: The principal components of our second (logarithmic) analysis. Loadings which were considered significant have been highlighted in bold (see text for details).

	PC1_{log}	PC2_{log}	PC3_{log}
Distance	0.18	0.19	**0.64**
T_s	**−0.5**	−0.21	0.34
T_c	−0.03	**−0.59**	0.24
ISRF	**−0.52**	−0.15	0.34
Central Density	**−0.4**	**0.47**	−0.08
Radius	**0.49**	−0.01	0.36
Asymmetry Factor	0.21	**−0.4**	−0.04
Mass	0.1	**0.41**	**0.41**

in the data. The three principal components found when assuming a logarithmic relationship between the parameters are shown in Table 6.9, where the significant loadings are highlighted.

For the first principal component the loadings considered significant are the same as those in the initial analysis — that is surface temperature, ISRF, central density and radius. All four also have the same sign as before. This implies that the first principle component likely still refers to the temperature gradient inside the core. However, in this analysis the central density has less impact than previously.

In the case of the second principal component, central temperature, central density and asymmetry factor are all still considered important but the loading of mass has increased and now must also be considered. The addition of mass to the second principal component does not change its interpretation. This component is still likely a measure of the internal structure and density of the core.

The third principal component shows the most drastic change from the first analysis. Mass and distance are still considered significant but neither surface temperature nor ISRF have a normalised loading over 0.6. Surface temperature and ISRF are therefore no longer considered significant when evaluating what the component represents. Nevertheless, the most likely interpretation of this component is still an observational selection effect. Only the more massive cores are detectable by *Herschel* at greater distances. However, in this case, the core's surface temperature does not appear to play any major role in determining whether the object is observable and isolated.

Figures 6.34–6.36 show the scores for the new principle components plotted against one another. In the first analysis PC1 and PC2 showed a strong positive correlation but neither exhibited a linear correlation with PC3. In this case, $PC2_{log}$ shows no correlation with either $PC1_{log}$ or $PC3_{log}$, with r=–0.15 and 0.31, respectively. However, $PC1_{log}$ and $PC3_{log}$ show a strong negative correlation. We interpret $PC1_{log}$ as an indicator of the temperature gradient within the core. A correlation between $PC1_{log}$ and $PC3_{log}$ implies that temperature may play a role in whether the core is observable by *Herschel*. This was implied in the previous analysis where surface temperature was significant in PC3.

The second analysis results show approximately the same results as the initial analysis: that the internal temperature gradient and density structure are the

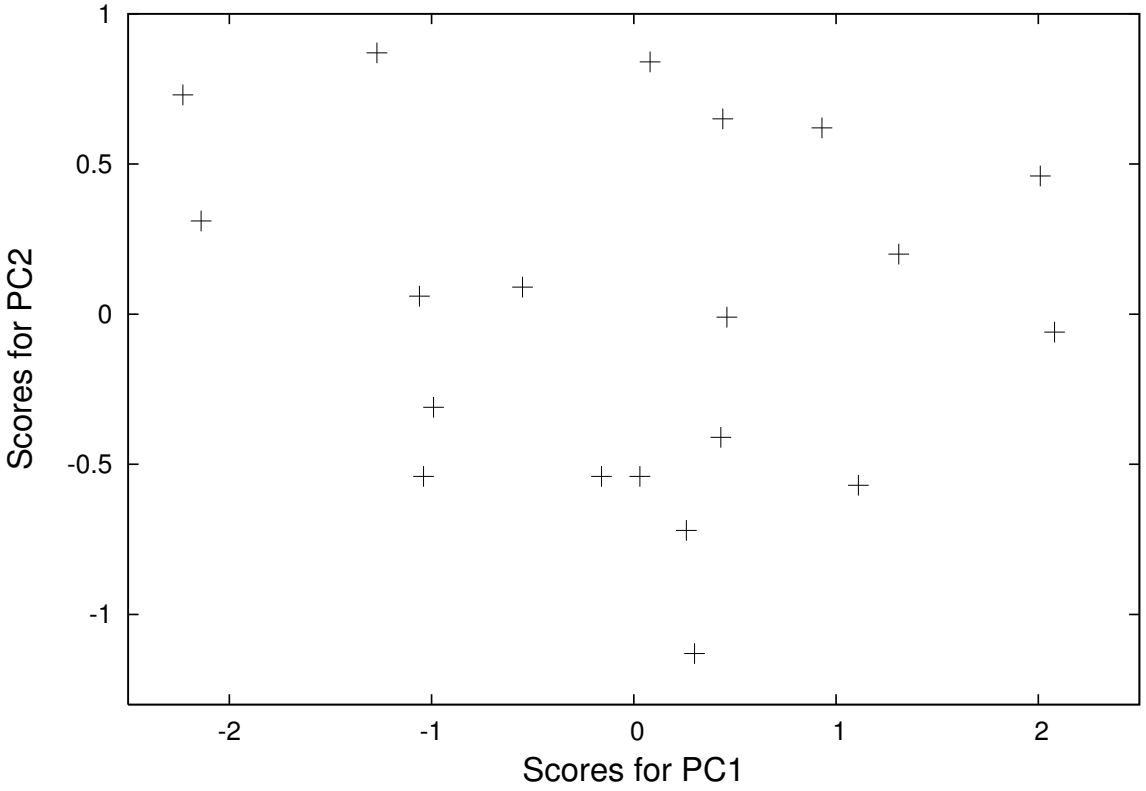

Figure 6.34: The final scores of each core for $PC1_{log}$ plotted against those for $PC2_{log}$.

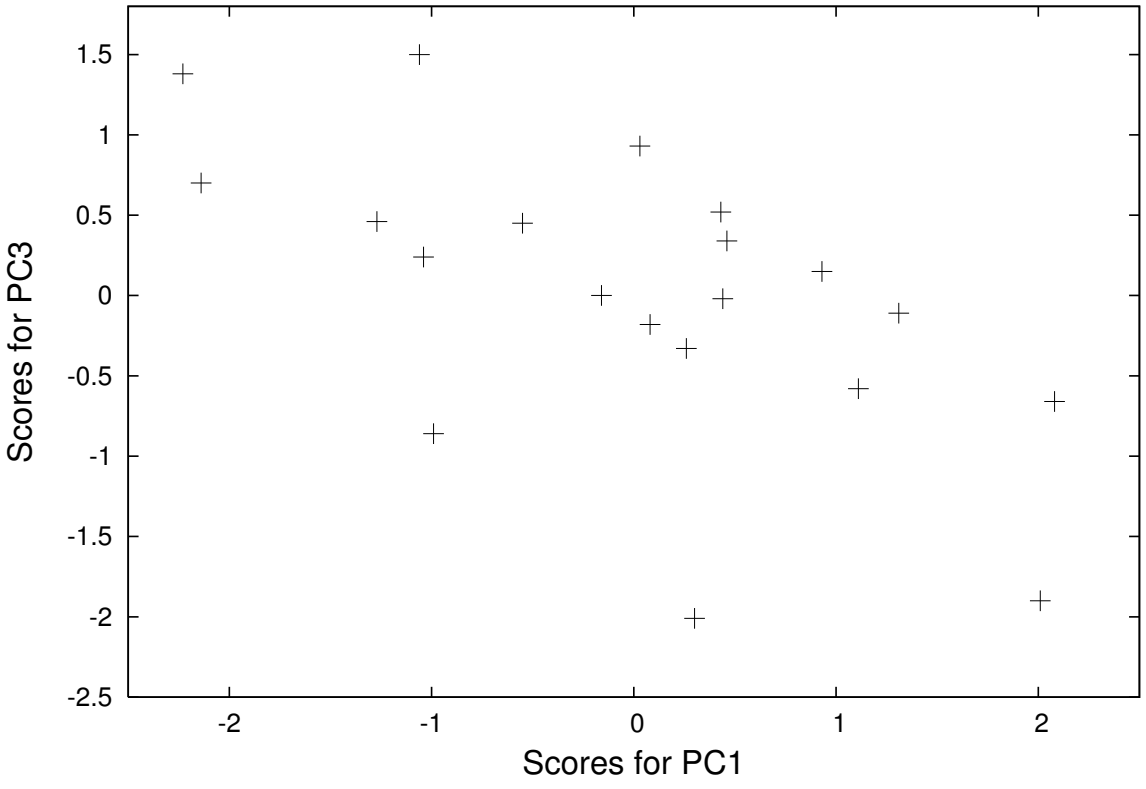

Figure 6.35: The final scores of each core for $PC1_{log}$ plotted against those for $PC3_{log}$.

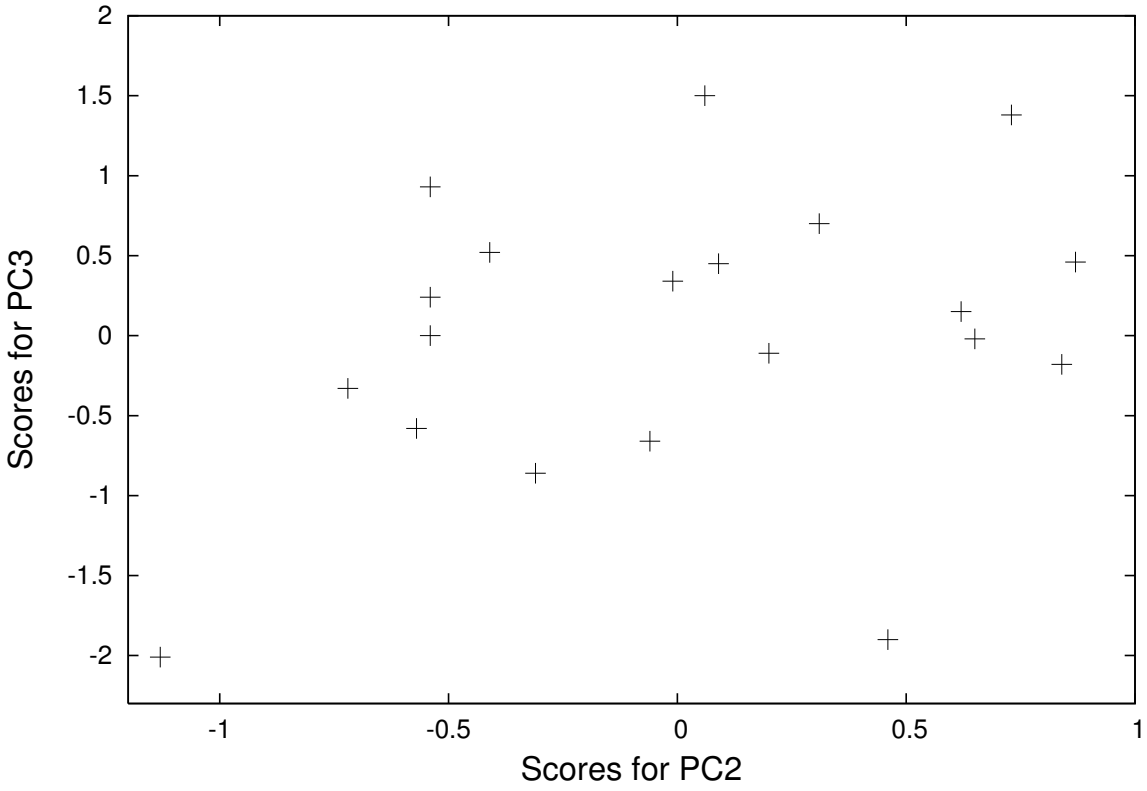

Figure 6.36: The final scores of each core for $PC2_{log}$ plotted against those for $PC3_{log}$.

most significant parameters in determining how a core appears in our data. The compression ratio is not any greater, three principal components are still necessary to describe a minimum of 80 % of the variance in the data. As such, if there is a more complex relationship between the physical parameters, it is not described any better by a logarithmic relationship than by a linear relationship.

Chapter 7

Summary and Future Work

7.1 Thesis summary

In this thesis, data from the *Herschel* Space Observatory have been presented. Specifically, the data used were taken as part of the *Herschel* Infrared Galactic Plane Survey (Hi-GAL), a *Herschel* open-time key project. Hi-GAL aims to perform observations of the entire Galactic Plane, $-180° \leq l \leq +180°$, $|b| \leq 1°$ (Molinari et al., 2010b), in a series of $2\,° \times 2°$ tiles. Observations have been taken at five wavelengths: 70, 160, 250, 350 and 500 μm. As such, Hi-GAL serves as a longer wavelength counterpart to previous high resolution MIR Galactic Plane surveys (e.g. GLIMPSE, MIPSGAL, ATLASGAL etc). The work shown here has focussed on the region $l = 300 - 330\,°$, $|b| < 1°$, which was the first region to be observed.

We have used Hi-GAL data to study the earliest observable stages of high mass star formation: IRDCs and the cores embedded within them. High mass stars affect their environments on a Galactic scale but their formation processes

are, as yet, poorly understood. IRDCs are the suspected birth-places of high mass stars and are cold, with temperatures typically around 15 K. Their SEDs thus peak at $\sim$200 μm, ideal for study with *Herschel*. Through our study of IRDCs, it was hoped to gain insight into the earliest stages of high mass star formation.

7.2 Numbers and Lifetimes of IRDCs and their Cores

There are currently two catalogues of IRDCs: Simon et al. (2006a) who use 8 μm MSX data; and Peretto & Fuller (2009) who use 8 μm *Spitzer* GLIMPSE data. This work used the latter catalogue, which identified the candidate IRDCs as connected structures with an apparent mean 8 μm opacity greater than 0.35, an apparent peak opacity above 0.7 and a diameter greater than $4''$. This catalogue contains 11,303 candidate IRDCs in the regions $10^\circ < l < 65^\circ$ and $295^\circ < l < 350^\circ$ with $|b| < 1^\circ$, of which 3171 lie in the area $l = 300^\circ - 330^\circ$.

Of 3171 candidate IRDCs that were catalogued from their MIR absorption in *Spitzer* data (*Spitzer*-dark regions), 1205 were found which appear to be *Herschel*-bright — approximately 38% of the PF09 candidate IRDCs. The objects that were found to be *Herschel*-dark as well as *Spitzer*-dark are possibly minima in the infrared background. These regions are candidates for the type of object we refer to as a 'hole in the sky' — areas which show no emission throughout the EM spectrum. We note, however, that some of the *Herschel*-dark objects may be genuine IRDCs but too small and diffuse to be seen in emission by *Herschel*. We estimate that $\sim$20 % of the original *Spitzer*-dark candidates fall into this category. Thus, we find that 40–60 % (i.e. 50$\pm$10%) of the *Spitzer*-dark regions are genuine

IRDCs. This suggests that IRDC searches based solely on MIR data may overestimate the total number of IRDCs in the Galaxy by up to a factor as high as $\sim$2.

The revised number of Galactic IRDCs has implications for the role of IRDCs and cores in Galactic star formation. We estimated the area we searched for IRDCs as a fraction of the inner Galaxy. From this we approximated the number of *Spitzer*-dark regions in the inner Galaxy, assuming the region we searched was typical. Using our numbers as a guide, we then extrapolated how many of these *Spitzer*-dark regions are also *Herschel*-bright and so are likely to be genuine IRDCs. The number of IRDC cores was found and, assuming an average mass of $140\,\mathrm{M}_{\odot}$, the total mass of cores in the inner Galaxy was calculated. The rate of star formation in these cores was found to be $\sim$$0.34\,\mathrm{M}_{\odot}\,\mathrm{yr}^{-1}$, using an estimated star formation efficiency of 0.2 and our core lifetime of 1.3×10^{6} years. From this figure and using the profile of the star formation rate in the Galaxy as a function of Galacto-centric radius, we extrapolated that the Galactic star formation rate occurring in cores is $\sim$$0.41\,\mathrm{M}_{\odot}\,\mathrm{yr}^{-1}$, compared to the total Galactic star formation rate of 1–$2\,\mathrm{M}_{\odot}\,\mathrm{yr}^{-1}$. This leads to the conclusion that a significant fraction of Galactic star formation must be occurring outside of IRDCs. This is contrary to some previous findings (Rathborne et al., 2006).

966 of the 1205 *Herschel*-bright IRDCs have one or more discernible peaks at $250\,\mu$m, indicating the formation of dense cores within these IRDCs. In total, we find 972 cores in our sample. The *Spitzer* data were then examined to see whether the cores contained either an 8 or a $24\,\mu$m point source. 653 are seen to harbour one or more $8\,\mu$m point sources, and of the remainder, a further 149 contained one or more $24\,\mu$m point sources. When accounting for differences in sample size, these results are roughly comparable with those from previous surveys (e.g. Chambers

et al., 2009; Parsons et al., 2009).

We equated the presence of a 24 μm point source to the typical accretion timescale for high-mass stars of $\sim 2\times10^5$ years. Using the relative numbers of cores in the starless and 24 μm-only phases the lifetime of $\sim 2.3\times10^5$ years was derived for a starless core. Similarly, the lifetime of a core with an 8 μm point source was calculated to be $\sim 9\times10^5$ years. The presence of an 8 μm point source was equated to the combined HCHII and UCHII phase. Estimates of the lifetime for a HCHII and UCHII region are in agreement with the timescale calculated here of $\sim 9\times10^5$ years for a core with an 8 μm point source. The total lifetime for IRDCs with cores was found to be $\sim 1.3\times10^6$ years.

7.3 The Physical Properties of Cores

Using data from *Spitzer* and *Herschel*, 20 isolated, starless, cold cores were modelled with the PHAETHON radiative transfer code (Stamatellos & Whitworth, 2003, 2005). A flattened radial density profile was assumed for all. The FWHM of each core was measured at 250 μm and used as the core's radius. The radial distance for which the central density is constant was set to one tenth of this value. The central density and surrounding ISRF were varied until the model SED matched the observed SED at 160, 250, 350 and 500 μm. The other physical parameters of the cores (i.e. temperature and mass) were found as outputs of the model.

The cores were found to have masses ranging from approximately ten to a few hundred solar masses and radii from 0.3 to 1 pc, in agreement with previous surveys of cores (e.g. Rathborne et al., 2006; Butler & Tan, 2009). The masses of the cores did not correlate well with their size or central density. 16 out of 20

isolated cores showed high levels of ellipticity. The central densities of the cores ranged from 1.5×10^3 to $2.0\times10^5\,\mathrm{cm}^{-3}$, also in agreement with previous findings (e.g. Peretto & Fuller, 2009; Peretto et al., 2010).

The temperature at the surface of a core was seen to depend almost entirely on the level of the ISRF surrounding the core. A canonical best-fit relationship was found and showed a logarithmic, positive correlation between the ISRF and surface temperature. This was proven to agree with the expected form of the theoretical relationship between ISRF, temperature, radius and mass. The best-fit relation was also shown to provide a sensible estimate of the dust emissivity index, in agreement with previous estimates in similar objects. This was also shown to hold true at the centre of the cores. The central temperature was seen to have an inverse, linear dependency on the density and mass of the core. A core with a high column density is likely to have a lower central temperature.

The temperature of each core was shown to decrease from surface to centre. The temperature change was typically $\sim$10 K (although changes of up to 14 K were seen in some of the models), consistent with previous observations (e.g. Peretto et al., 2010; Stamatellos et al., 2010). The range of temperatures from centre to edge in any one core was found to correlate strongly with the central density of that core. Low density cores exhibit a much smaller range of temperatures and thus a shallower temperature profile than higher density cores. The cores situated in a high ISRF (and thus with a high surface temperature) are also likely to show a greater range of temperature from centre to edge.

No large cores were found within an area of comparatively high ISRF. There appears to be no correlation between the ISRF surrounding a core and its central density. Hence, we rule out radiation pressure as the cause. Instead, we consider

that the outer layers of cores in areas of high radiation may be evaporated due to the high levels of energy being absorbed, leaving only smaller cores in high-ISRF regions.

A principal component analysis of the eight major parameters (distance, central temperature, surface temperature, ISRF, central density, radius, asymmetry factor and mass) was also performed. This enabled us to analyse the parameters as a whole rather than one-by-one or in pairs. The analysis was performed twice: once assuming a linear relationship between the parameters; and once assuming a logarithmic relationship. Both analyses yielded similar results. It was found that the first three principal components were most significant, although the third was eventually ruled out as being due to a selection effect. The first and second principal components are believed to represent the temperature gradient within a core and its density structure, respectively. Together, they account for around 60 % of the variation in the modelled cores. These are therefore the most important parameters in determining how a core appears in our data. Neither the linear nor logarithmic analysis yielded an ideal compression ratio. It is therefore likely that the physics between the parameters is more complex than either of these relationships predict.

7.4 Future work

Studies of IRDCs and the cores within them gives us insight into the very earliest stages of high mass star formation. This research has focused on expanding our knowledge about the processes behind massive star formation. Continued research into this area will continue to increase our understanding of massive stars.

IRDCs have been traditionally identified as regions of high contrast against the mid-infrared background, where, due to their low temperatures, they are seen in absorption. However, with the launch of *Herschel*, high resolution observations of the Galactic Plane in the FIR are now available. Large scale searches for IRDCs at the wavelengths where IRDCs are seen in emission have been performed at resolutions where the cores residing within are visible.

Observing these cores in both the mid-infrared and far-infrared means that the youngest (those that fall into the starless or quiescent category) have been identified. Additionally, those which are unconfused with regards to their surroundings are also identified. By selecting the starless cores, the most likely candidates for observing the earliest phase of high mass star formation are found. By selecting only the isolated, starless cores only the young candidates with simple structures and no contamination from more evolved nearby sources are used.

These young, isolated cores are ideal candidates for further observation. Previous studies have generally been concerned with the differences between the evolutionary stages of the cores (e.g. Chambers et al., 2009; Battersby et al., 2011; Zhang et al., 2011). By selecting only the youngest cores it would be possible to gain further insight into the very beginnings of the evolution of a high mass star. For instance, spectral line observations would enable the confirmation of whether or not these cores are, as yet, undergoing any form of star formation and comparisons of continuum observations between the FIR and sub-mm would increase our knowledge of their structure and formation.

The cores within IRDCs have typical masses up to a few hundred solar masses. Objects of this mass are not likely to create a single star, but rather a cluster of stars. High resolution observations (e.g. using ALMA) would determine whether

the cores have begun to fragment into sub-structures, indicating that they are in the process of forming double, triple, or multiple systems. Binary and multiple star formation among high-mass stars is a common but little understood phenomenon.

Using *Herschel* observations, it has been found that many IRDCs do not show any discernible peak in their FIR emission, and thus have no cores visible in the FIR. These objects could represent an even younger stage of high mass star formation than cores. Further observations at higher resolutions could confirm their lack of structure or, possibly, make apparent cores that are not visible in the FIR. Comparisons of the chemical composition of these regions to the more evolved cores would indicate whether these areas are likely to eventually form high mass stars.

Thus far, 60 square degrees of the Hi-GAL data have been searched for *Spitzer*-dark and *Herschel*-bright objects. If the entirety of the proposed region is observed before the helium supply onboard *Herschel* is depleted there will be 720 square degrees of data. Twelve times the amount of data used in this thesis that will be available for further study. The major source of error when looking for *Spitzer*-dark and *Herschel*-bright regions, putting aside instrument limitations, was human error (we estimated this to be $\sim$3 %). This type of by-eye examination is also time-consuming. However, it does ultimately lead to better results than an automated routine. This makes further examination of IRDCs in the Hi-GAL data an ideal citizen-science project (e.g. Galaxy Zoo; Raddick et al. 2007). Numerous individuals looking over the same data would reduce the human error and the time required for such an undertaking. This would be a logical continuation of the work in this thesis.

Appendix A

Integrating the Density Profile

We use a flattened geometry for all our cold cores, which means all of our modelled cold cores have the density profile described in Equation 3.31. We make the assumption that $\sin(\theta) = 1$ and Equation 3.35 becomes

$$N(H_2) = \rho_0 \int_0^R \frac{1 + A\left(\frac{r}{R_0}\right)^2}{\left[1 + \left(\frac{r}{R_0}\right)^2\right]^2} \, dr. \tag{A.1}$$

We substitute

$$q = \frac{r}{R_0} \tag{A.2}$$

$$dq = \frac{1}{R_0} \, dr \tag{A.3}$$

into Equation A.1 giving

$$N(H_2) = \rho_0 R_0 \int_0^{\frac{R}{R_0}} \frac{1 + Aq^2}{(1+q^2)^2} \, dq \tag{A.4}$$

$$= \rho_0 R_0 \left[\int_0^{\frac{R}{R_0}} \frac{1}{(1+q^2)^2} \, dq\right] + \rho_0 R_0 \left[\int_0^{\frac{R}{R_0}} \frac{Aq^2}{(1+q^2)^2} \, dq\right] \tag{A.5}$$

$$= \rho_0 R_0 \left[F + G\right] \tag{A.6}$$

where

$$F = \int_0^{\frac{R}{R_0}} \frac{1}{(1+q^2)^2} \, dq \tag{A.7}$$

and

$$G = \int_0^{\frac{R}{R_0}} \frac{Aq^2}{(1+q^2)^2}\, dq. \tag{A.8}$$

First we solve for F by making the substitution

$$q = \tan(u) \tag{A.9}$$
$$dq = \sec^2(u)\, du. \tag{A.10}$$

into Equation A.7.

$$F = \int_0^{\arctan\left(\frac{R}{R_0}\right)} \frac{1}{(1+\tan^2(u))^2}\, \sec^2(u)\, du. \tag{A.11}$$

Using the following trigonometric identities in turn

$$\tan^2(x) + 1 = \sec^2(x) \tag{A.12}$$
$$\sec(x) = \frac{1}{\cos(x)} \tag{A.13}$$
$$\cos^2(x) = \frac{1+\cos(2x)}{2} \tag{A.14}$$
$$\sin(2x) = 2\sin(x)\cos(x) \tag{A.15}$$

Equation A.11 becomes

$$F = \int_0^{\arctan\left(\frac{R}{R_0}\right)} \frac{1}{\sec^4(u)} \sec^2(u)\, du \tag{A.16}$$
$$= \int_0^{\arctan\left(\frac{R}{R_0}\right)} \frac{1}{\sec^2(u)}\, du \tag{A.17}$$
$$= \int_0^{\arctan\left(\frac{R}{R_0}\right)} \cos^2(u)\, du \tag{A.18}$$
$$= \frac{1}{2}\int_0^{\arctan\left(\frac{R}{R_0}\right)} 1 + \cos(2u)\, du \tag{A.19}$$
$$= \frac{1}{2}\left[u + \frac{1}{2}\sin(2u)\right]_0^{\arctan\left(\frac{R}{R_0}\right)} \tag{A.20}$$
$$= \frac{1}{2}\left[u + \sin(u)\cos(u)\right]_0^{arctan\left(\frac{R}{R_0}\right)}. \tag{A.21}$$

Equation A.9 can be re-arranged to give

$$\tan(u) = \frac{q}{1} \tag{A.22}$$

which implies

$$\sin(u) = \frac{q}{\sqrt{1+q^2}} \tag{A.23}$$

$$\cos(u) = \frac{1}{\sqrt{1+q^2}} \tag{A.24}$$

and by substituting Equations A.22–A.24 back into Equation A.21 we find

$$F = \frac{1}{2}\left[\arctan(q) + \frac{q}{1+q^2}\right]_0^{\frac{R}{R_0}} \tag{A.25}$$

We then solve A.8 in a similar fashion:

$$G = \int_0^{\frac{R}{R_0}} \frac{Aq^2}{\left(1+q^2\right)^2}\, dq. \tag{A.26}$$

Substitute in Equations A.9 and A.10 and using the trigonometric identities in Equations A.12–A.15 along with

$$\tan(x) = \frac{\sin(x)}{\cos(x)} \tag{A.27}$$

$$\cos(2x) = 1 - 2\sin^2(x) \tag{A.28}$$

we find

$$G = A\int_0^{\arctan\left(\frac{R}{R_0}\right)} \frac{\tan^2(u)}{\left(1+\tan^2(u)\right)^2}\sec^2(u)\, du \tag{A.29}$$

$$= A\int_0^{\arctan\left(\frac{R}{R_0}\right)} \frac{\tan^2(u)}{\sec^2(u)}\, du \tag{A.30}$$

$$= A\int_0^{\arctan\left(\frac{R}{R_0}\right)} \frac{\sin^2(u)}{\cos^2(u)}\cos^2(u)\, du \tag{A.31}$$

$$= A\int_0^{\arctan\left(\frac{R}{R_0}\right)} \sin^2(u)\, du \tag{A.32}$$

$$= \frac{A}{2}\int_0^{\arctan\left(\frac{R}{R_0}\right)} 1 - \cos(2u)\, du \tag{A.33}$$

$$= \frac{A}{2}\left[u - \frac{1}{2}\sin(2u)\right]_0^{\arctan\left(\frac{R}{R_0}\right)} \tag{A.34}$$

$$= \frac{A}{2}\left[u - \sin(u)\cos(u)\right]_0^{\arctan\left(\frac{R}{R_0}\right)}. \tag{A.35}$$

Substituting Equations A.22–A.24 into Equation A.35 results in

$$G = \frac{1}{2}\left[\arctan(q) - \frac{q}{1+q^2}\right]_0^{\frac{R}{R_0}}. \tag{A.36}$$

Substituting Equations A.25 and A.36 back into Equation A.6 gives

$$\begin{aligned} N(H_2) &= \frac{\rho_0 R_0}{2}\left[\frac{q}{q^2+1} + \arctan(q) + A\,\arctan(q) - \frac{Aq}{1+q^2}\right]_0^{\frac{R}{R_0}} && \text{(A.37)}\\ &= \frac{\rho_0 R_0}{2}\left[(A+1)\arctan\left(\frac{R}{R_0}\right) + \frac{(1-A)\frac{R}{R_0}}{1+\left[\frac{R}{R_0}\right]^2}\right] && \text{(A.38)}\\ &= \frac{\rho_0 R_0}{2}\left[(A+1)\arctan\left(\frac{R}{R_0}\right) - \frac{(A-1)RR_0}{R_0^2+R^2}\right] && \text{(A.39)}\\ &= \frac{\rho_0 R_0^2}{2}\left[\frac{(A+1)}{R_0}\arctan\left(\frac{R}{R_0}\right) - \frac{(A-1)R}{R_0^2+R^2}\right]. && \text{(A.40)} \end{aligned}$$

Appendix B

Spitzer-Dark and Herschel-Dark Sources

Table B.1 gives the names (column 1) and positions (columns 2 and 3), according to PF09, of the *Spitzer*-dark regions that were also found to be *Herschel*-dark. These objects are candidates for the type of region we call a hole in the sky. The smallest and most diffuse of these sources may be genuine IRDCs as they, theoretically, would not exhibit enough emission to be classed as *Herschel*-bright.

Table B.1: A list of *Spitzer*-dark regions that have been identified as *Herschel*-dark.

Name of *Spitzer*-dark and *Herschel*-dark Region	Right Ascension 2000.0 (°)	Declination 2000.0 (°)
300.180−0.093	186.82	−62.84
300.197−0.138	186.85	−62.88
300.205−0.352	186.83	−63.10
300.213−0.109	186.89	−62.86
300.243−0.126	186.96	−62.88
300.249−0.469	186.90	−63.22
300.257−0.253	186.96	−63.00
300.292−0.255	187.04	−63.01
300.305−0.226	187.07	−62.98
300.316−0.247	187.09	−63.00
300.334−0.265	187.13	−63.02
300.339−0.205	187.15	−62.96
300.343−0.184	187.16	−62.94
300.343−0.227	187.15	−62.98
300.395−0.197	187.27	−62.96
300.403−0.309	187.27	−63.07
300.406−0.060	187.32	−62.82
300.413−0.310	187.29	−63.07
300.436−0.109	187.38	−62.87
300.456−0.218	187.40	−62.99

continued on next page

Name of *Spitzer*-dark and *Herschel*-dark Region	Right Ascension 2000.0 (°)	Declination 2000.0 (°)
300.464−0.076	187.45	−62.84
300.500−0.212	187.50	−62.98
300.644+0.041	187.86	−62.74
300.743+0.128	188.09	−62.66
300.761+0.071	188.12	−62.72
300.936+0.940	188.63	−61.87
300.940+0.937	188.63	−61.87
300.962+0.885	188.67	−61.92
300.963+0.831	188.67	−61.98
300.977+0.890	188.71	−61.92
300.979+0.896	188.71	−61.91
301.004+0.899	188.76	−61.91
301.058+0.050	188.76	−62.76
301.062−0.015	188.76	−62.83
301.111−0.287	188.83	−63.10
301.119−0.290	188.85	−63.11
301.147−0.228	188.92	−63.05
301.166−0.181	188.97	−63.00
301.184−0.173	189.01	−62.99
301.192−0.245	189.02	−63.07
301.195−0.199	189.03	−63.02
301.199−0.193	189.04	−63.01
301.260+0.434	189.25	−62.39
301.279−0.221	189.21	−63.05
301.515+0.278	189.78	−62.56
301.521+0.340	189.81	−62.50
301.639−0.217	190.01	−63.06
301.649−0.272	190.02	−63.12
301.656−0.339	190.03	−63.18
301.666−0.239	190.06	−63.08
301.702−0.418	190.13	−63.26
301.714−0.423	190.15	−63.27
301.759+0.272	190.31	−62.58
301.861+0.677	190.57	−62.17
302.040+0.277	190.92	−62.58
302.044−0.045	190.91	−62.90
302.058−0.067	190.94	−62.93
302.078+0.061	190.99	−62.80
302.121−0.024	191.08	−62.89
302.132+0.935	191.16	−61.93
302.141+0.082	191.13	−62.78
302.147+0.102	191.15	−62.76
302.164+0.036	191.18	−62.83
302.204+0.917	191.31	−61.95
302.214+0.900	191.33	−61.96
302.242+0.387	191.37	−62.48
302.323+0.155	191.53	−62.71
302.366+0.898	191.66	−61.97
302.378+0.272	191.66	−62.59
302.388+0.261	191.68	−62.61
302.403+0.303	191.71	−62.56

continued on next page

Name of *Spitzer*-dark and *Herschel*-dark Region	Right Ascension 2000.0 (°)	Declination 2000.0 (°)
302.412−0.100	191.72	−62.97
302.446−0.805	191.76	−63.67
302.462−0.751	191.80	−63.62
302.463−0.723	191.81	−63.59
302.476−0.002	191.86	−62.87
302.486−0.076	191.88	−62.95
302.486−0.758	191.86	−63.63
302.515−0.810	191.92	−63.68
302.519−0.746	191.93	−63.62
302.526−0.855	191.94	−63.72
302.575+0.236	192.08	−62.63
302.606+0.192	192.15	−62.68
302.627+0.264	192.20	−62.61
302.673+0.213	192.30	−62.66
302.676−0.079	192.30	−62.95
302.679+0.019	192.31	−62.85
302.718+0.151	192.39	−62.72
302.773+0.208	192.51	−62.66
302.818−0.861	192.60	−63.73
302.874−0.877	192.73	−63.75
302.928−0.409	192.85	−63.28
303.017+0.173	193.05	−62.70
303.047−0.894	193.12	−63.77
303.109−0.887	193.26	−63.76
303.139−0.822	193.33	−63.69
303.223−0.817	193.52	−63.69
303.305−0.888	193.71	−63.76
303.334−0.795	193.77	−63.66
303.341−0.735	193.78	−63.60
303.418−0.659	193.95	−63.53
303.425−0.582	193.96	−63.45
303.498−0.776	194.14	−63.64
303.509−0.677	194.16	−63.54
303.514−0.709	194.17	−63.58
303.544−0.499	194.23	−63.36
303.569−0.588	194.29	−63.45
303.580−0.677	194.31	−63.54
303.587−0.592	194.33	−63.46
303.645−0.751	194.47	−63.61
303.691−0.685	194.56	−63.55
303.882−0.692	194.99	−63.55
304.006+0.281	195.19	−62.57
304.015+0.309	195.21	−62.54
304.268−0.386	195.83	−63.23
304.423−0.014	196.13	−62.85
304.458+0.012	196.20	−62.82
304.539+0.341	196.34	−62.49
304.566+0.325	196.40	−62.50
304.612−0.930	196.66	−63.75
304.671+0.247	196.64	−62.57
304.703+0.270	196.70	−62.55

continued on next page

Name of *Spitzer*-dark and *Herschel*-dark Region	Right Ascension 2000.0 (°)	Declination 2000.0 (°)
304.712+0.600	196.68	−62.22
304.749−0.854	196.96	−63.67
304.750−0.803	196.96	−63.62
304.772+0.215	196.86	−62.60
304.785−0.835	197.04	−63.65
304.795+0.326	196.90	−62.49
304.885+0.296	197.09	−62.51
304.943+0.270	197.22	−62.53
304.961+0.184	197.27	−62.62
304.969+0.033	197.32	−62.77
304.975+0.269	197.29	−62.53
304.994+0.091	197.36	−62.71
304.997+0.034	197.38	−62.76
305.015+0.227	197.39	−62.57
305.016−0.039	197.43	−62.84
305.029+0.124	197.43	−62.67
305.031+0.217	197.42	−62.58
305.036+0.077	197.45	−62.72
305.039+0.061	197.46	−62.73
305.042+0.164	197.45	−62.63
305.046+0.058	197.48	−62.74
305.047−0.006	197.49	−62.80
305.056+0.199	197.48	−62.60
305.057+0.116	197.49	−62.68
305.059+0.259	197.48	−62.54
305.061−0.205	197.55	−63.00
305.062−0.191	197.56	−62.99
305.066+0.035	197.53	−62.76
305.068−0.069	197.55	−62.86
305.070+0.329	197.49	−62.47
305.074−0.098	197.57	−62.89
305.074−0.173	197.58	−62.97
305.074+0.235	197.51	−62.56
305.075−0.133	197.57	−62.93
305.075+0.113	197.54	−62.68
305.076−0.036	197.56	−62.83
305.077−0.208	197.59	−63.00
305.083+0.206	197.54	−62.59
305.090+0.004	197.58	−62.79
305.094−0.172	197.62	−62.96
305.098−0.310	197.65	−63.10
305.112−0.180	197.66	−62.97
305.113−0.090	197.65	−62.88
305.117−0.236	197.68	−63.03
305.123−0.270	197.70	−63.06
305.132−0.124	197.70	−62.91
305.134−0.241	197.72	−63.03
305.149+0.193	197.68	−62.60
305.151+0.002	197.72	−62.79
305.156+0.235	197.69	−62.55
305.161+0.354	197.68	−62.43

continued on next page

Name of *Spitzer*-dark and *Herschel*-dark Region	Right Ascension 2000.0 (°)	Declination 2000.0 (°)
305.165+0.264	197.70	−62.52
305.166−0.291	197.80	−63.08
305.166+0.027	197.75	−62.76
305.171−0.004	197.76	−62.79
305.182−0.039	197.79	−62.82
305.188+0.203	197.76	−62.58
305.188+0.402	197.73	−62.38
305.189−0.346	197.86	−63.13
305.193−0.046	197.82	−62.83
305.204+0.249	197.79	−62.54
305.209+0.024	197.84	−62.76
305.213+0.233	197.81	−62.55
305.221+0.228	197.83	−62.55
305.222+0.256	197.83	−62.53
305.236−0.335	197.96	−63.12
305.236+0.406	197.84	−62.38
305.247+0.168	197.90	−62.61
305.265+0.284	197.92	−62.50
305.270−0.018	197.98	−62.80
305.270−0.050	197.99	−62.83
305.280−0.263	198.05	−63.04
305.283+0.385	197.94	−62.39
305.302+0.274	198.00	−62.50
305.320+0.319	198.03	−62.46
305.328+0.181	198.07	−62.59
305.338+0.165	198.10	−62.61
305.356+0.037	198.16	−62.73
305.361+0.180	198.14	−62.59
305.363−0.025	198.18	−62.80
305.364+0.215	198.14	−62.56
305.370+0.191	198.16	−62.58
305.371−0.097	198.21	−62.87
305.374−0.215	198.24	−62.99
305.387+0.232	198.19	−62.54
305.389+0.189	198.20	−62.58
305.393+0.234	198.20	−62.53
305.398+0.231	198.21	−62.54
305.406−0.137	198.30	−62.90
305.406+0.402	198.20	−62.37
305.407+0.206	198.24	−62.56
305.410−0.070	198.30	−62.84
305.434+0.061	198.32	−62.70
305.440+0.387	198.28	−62.38
305.460+0.222	198.35	−62.54
305.470+0.109	198.39	−62.65
305.480−0.384	198.51	−63.14
305.488+0.247	198.40	−62.51
305.490+0.407	198.38	−62.35
305.506+0.315	198.43	−62.44
305.513+0.338	198.44	−62.42
305.525−0.320	198.59	−63.08

continued on next page

Name of *Spitzer*-dark and *Herschel*-dark Region	Right Ascension 2000.0 (°)	Declination 2000.0 (°)
305.534−0.006	198.55	−62.76
305.538+0.332	198.50	−62.42
305.541−0.034	198.57	−62.79
305.551−0.391	198.67	−63.15
305.553+0.283	198.54	−62.47
305.554−0.264	198.65	−63.02
305.554+0.063	198.58	−62.69
305.557−0.009	198.60	−62.76
305.562−0.103	198.63	−62.86
305.563+0.036	198.61	−62.72
305.565−0.020	198.62	−62.77
305.565+0.083	198.60	−62.67
305.567+0.371	198.55	−62.38
305.570−0.008	198.63	−62.76
305.572−0.089	198.65	−62.84
305.574−0.077	198.66	−62.83
305.576+0.298	198.59	−62.46
305.577−0.005	198.65	−62.76
305.583+0.020	198.66	−62.73
305.583+0.290	198.60	−62.46
305.588+0.008	198.67	−62.74
305.590−0.075	198.69	−62.83
305.591−0.316	198.74	−63.07
305.592−0.024	198.68	−62.78
305.594−0.347	198.75	−63.10
305.595+0.358	198.62	−62.39
305.600+0.000	198.70	−62.75
305.602+0.056	198.69	−62.69
305.604+0.005	198.70	−62.75
305.616−0.077	198.75	−62.83
305.617+0.142	198.70	−62.61
305.634−0.076	198.78	−62.82
305.642+0.366	198.72	−62.38
305.643−0.296	198.85	−63.04
305.664−0.127	198.86	−62.87
305.674−0.091	198.88	−62.84
305.675+0.392	198.78	−62.35
305.676+0.130	198.84	−62.61
305.682+0.052	198.86	−62.69
305.682+0.174	198.84	−62.57
305.684+0.217	198.83	−62.53
305.685−0.044	198.89	−62.79
305.697−0.129	198.93	−62.87
305.708+0.068	198.92	−62.67
305.715−0.045	198.96	−62.79
305.726+0.111	198.95	−62.63
305.741−0.097	199.02	−62.83
305.763−0.227	199.10	−62.96
305.783−0.272	199.15	−63.01
305.802+0.321	199.07	−62.41
305.804+0.338	199.07	−62.39

continued on next page

Name of *Spitzer*-dark and *Herschel*-dark Region	Right Ascension 2000.0 (°)	Declination 2000.0 (°)
305.807−0.193	199.19	−62.92
305.821−0.240	199.23	−62.97
305.832+0.078	199.18	−62.65
305.833+0.050	199.19	−62.68
305.838−0.121	199.24	−62.85
305.852−0.071	199.26	−62.80
305.863−0.043	199.28	−62.77
305.881+0.317	199.24	−62.41
305.889+0.120	199.30	−62.60
305.907−0.171	199.40	−62.89
305.909−0.134	199.40	−62.85
305.940+0.091	199.41	−62.63
305.949−0.068	199.47	−62.78
305.958−0.037	199.48	−62.75
305.971+0.020	199.50	−62.69
305.989−0.068	199.56	−62.78
306.001−0.058	199.58	−62.77
306.005−0.189	199.62	−62.90
306.010+0.008	199.58	−62.70
306.021+0.153	199.58	−62.56
306.033−0.208	199.68	−62.92
306.037−0.020	199.65	−62.73
306.038−0.046	199.66	−62.75
306.045+0.075	199.65	−62.63
306.046−0.068	199.68	−62.77
306.048+0.127	199.64	−62.58
306.055−0.046	199.69	−62.75
306.070−0.307	199.79	−63.01
306.124−0.126	199.86	−62.82
306.126−0.113	199.86	−62.81
306.131−0.112	199.88	−62.81
306.141−0.333	199.95	−63.03
306.151+0.150	199.86	−62.55
306.170−0.362	200.02	−63.05
306.181+0.133	199.93	−62.56
306.232+0.124	200.04	−62.56
306.241+0.152	200.05	−62.53
306.244+0.170	200.05	−62.52
306.256−0.012	200.12	−62.70
306.270+0.155	200.11	−62.53
306.286+0.111	200.16	−62.57
306.305−0.318	200.31	−63.00
306.315−0.326	200.33	−63.00
306.344−0.353	200.40	−63.03
306.348−0.048	200.33	−62.72
306.426−0.008	200.49	−62.67
306.523+0.060	200.68	−62.59
307.048−0.836	202.09	−63.41
307.089−0.840	202.18	−63.41
307.126−0.729	202.23	−63.30
307.143−0.872	202.31	−63.43

continued on next page

Name of *Spitzer*-dark and *Herschel*-dark Region	Right Ascension 2000.0 (°)	Declination 2000.0 (°)
307.490−0.827	203.06	−63.34
307.511−0.688	203.06	−63.20
307.564−0.605	203.14	−63.11
307.605−0.635	203.24	−63.13
307.749+0.480	203.17	−62.00
307.790+0.330	203.30	−62.15
308.050−0.406	204.13	−62.83
308.098−0.460	204.25	−62.87
308.131−0.317	204.27	−62.73
308.370+0.843	204.33	−61.54
308.411+0.440	204.57	−61.93
308.528+0.541	204.77	−61.81
308.543+0.333	204.89	−62.01
308.566+0.048	205.05	−62.29
308.574+0.143	205.03	−62.19
308.575+0.468	204.90	−61.87
308.602+0.416	204.98	−61.92
308.613+0.650	204.91	−61.69
308.615−0.304	205.30	−62.63
308.619−1.031	205.62	−63.34
308.623+0.467	205.00	−61.87
308.639+0.611	204.98	−61.72
308.640+0.662	204.96	−61.67
308.656+0.760	204.95	−61.57
308.662+0.631	205.02	−61.70
308.688+0.440	205.15	−61.88
308.689+0.417	205.16	−61.90
308.710+0.455	205.19	−61.86
308.714+0.480	205.19	−61.84
308.722+0.648	205.13	−61.67
308.725+0.503	205.20	−61.81
308.729+0.484	205.21	−61.83
308.732+0.420	205.25	−61.89
308.739+0.780	205.12	−61.54
308.749+0.759	205.15	−61.56
308.797+0.182	205.48	−62.11
308.806+0.679	205.30	−61.62
308.818+0.726	205.30	−61.58
308.883+0.667	205.46	−61.62
308.950+0.124	205.83	−62.14
308.988+0.169	205.89	−62.09
309.028−0.412	206.22	−62.65
309.039−0.413	206.25	−62.65
309.057−0.040	206.12	−62.28
309.059+0.219	206.01	−62.03
309.062−0.264	206.23	−62.50
309.082−0.250	206.27	−62.48
309.102+0.157	206.13	−62.08
309.103−0.201	206.29	−62.43
309.111−0.203	206.31	−62.43
309.128−0.528	206.49	−62.74

continued on next page

Name of *Spitzer*-dark and *Herschel*-dark Region	Right Ascension 2000.0 (°)	Declination 2000.0 (°)
309.135+0.128	206.21	−62.10
309.136−0.223	206.37	−62.44
309.137−0.411	206.46	−62.63
309.144−0.389	206.46	−62.60
309.146−0.537	206.53	−62.75
309.147+0.230	206.19	−62.00
309.152−0.055	206.33	−62.27
309.152−0.397	206.48	−62.61
309.153−0.367	206.47	−62.58
309.172−0.222	206.44	−62.43
309.176−0.287	206.48	−62.50
309.179+0.057	206.33	−62.16
309.193−0.302	206.52	−62.51
309.196−0.011	206.40	−62.22
309.208−0.453	206.63	−62.65
309.218−0.417	206.63	−62.61
309.223−0.470	206.67	−62.67
309.225−0.454	206.66	−62.65
309.237−0.459	206.69	−62.65
309.238−0.556	206.74	−62.75
309.243−0.481	206.71	−62.67
309.256−0.431	206.72	−62.62
309.279−0.649	206.87	−62.83
309.324−0.412	206.85	−62.59
309.356+0.647	206.44	−61.54
309.380−0.129	206.84	−62.30
309.395+0.482	206.59	−61.70
309.399−0.582	207.09	−62.74
309.429−0.575	207.15	−62.72
309.530−0.742	207.45	−62.86
309.545−0.706	207.47	−62.83
309.555+0.712	206.82	−61.44
309.641+0.503	207.09	−61.62
309.673+0.517	207.15	−61.60
309.748+0.123	207.49	−61.97
309.863+0.337	207.62	−61.74
309.868+0.324	207.64	−61.75
309.902+0.476	207.64	−61.59
309.913+0.230	207.78	−61.83
309.924+0.371	207.73	−61.69
309.937+0.290	207.80	−61.77
309.937+0.608	207.65	−61.46
309.957+0.335	207.82	−61.72
309.977+0.559	207.75	−61.50
309.997+0.455	207.84	−61.59
309.998+0.267	207.94	−61.77
310.005+0.446	207.86	−61.60
310.009+0.453	207.87	−61.59
310.013−0.581	208.39	−62.60
310.019+0.404	207.91	−61.64
310.024−0.249	208.25	−62.27

continued on next page

Name of *Spitzer*-dark and *Herschel*-dark Region	Right Ascension 2000.0 (°)	Declination 2000.0 (°)
310.061−0.591	208.50	−62.59
310.074−0.258	208.36	−62.27
310.079−0.228	208.35	−62.24
310.083−0.244	208.37	−62.25
310.088−0.237	208.38	−62.24
310.100−0.247	208.41	−62.25
310.108−0.252	208.42	−62.25
310.110−0.333	208.47	−62.33
310.118−0.255	208.45	−62.25
310.132+0.774	207.96	−61.25
310.137+0.740	207.99	−61.28
310.144+0.560	208.09	−61.45
310.146+0.779	207.99	−61.24
310.147+0.384	208.19	−61.63
310.154+0.539	208.12	−61.47
310.156+0.752	208.02	−61.27
310.172+0.734	208.06	−61.28
310.180−0.221	208.56	−62.21
310.201+0.207	208.38	−61.78
310.203+0.386	208.30	−61.61
310.207+0.409	208.29	−61.59
310.228−0.167	208.63	−62.14
310.233−0.029	208.57	−62.01
310.253−0.017	208.61	−61.99
310.344−0.528	209.06	−62.46
310.372−0.570	209.14	−62.50
310.374−0.578	209.15	−62.51
310.390−0.277	209.03	−62.21
310.401−0.353	209.09	−62.28
310.500−0.053	209.13	−61.96
310.505−0.059	209.15	−61.97
310.514−0.034	209.15	−61.94
310.550−0.083	209.25	−61.98
310.713+0.254	209.41	−61.61
310.724+0.808	209.14	−61.07
310.725+0.195	209.46	−61.67
310.725+0.269	209.42	−61.60
310.755+0.827	209.19	−61.05
310.787−0.359	209.89	−62.19
310.794−0.377	209.92	−62.20
310.795−0.404	209.93	−62.23
310.833+0.400	209.57	−61.44
310.846+0.483	209.55	−61.36
310.893+0.325	209.73	−61.50
310.948+0.484	209.76	−61.33
310.961+0.463	209.80	−61.35
310.986−0.287	210.26	−62.07
310.992+0.738	209.71	−61.07
311.007+0.400	209.92	−61.40
311.010+0.419	209.92	−61.38
311.012+0.459	209.90	−61.34

continued on next page

Name of *Spitzer*-dark and *Herschel*-dark Region	Right Ascension 2000.0 (°)	Declination 2000.0 (°)
311.013+0.109	210.10	−61.68
311.015+0.448	209.91	−61.35
311.024+0.726	209.78	−61.08
311.032+0.700	209.81	−61.10
311.039+0.533	209.91	−61.26
311.042+0.449	209.97	−61.34
311.054+0.702	209.85	−61.09
311.060+0.767	209.83	−61.03
311.065+0.696	209.88	−61.10
311.065+0.816	209.81	−60.98
311.077+0.708	209.90	−61.08
311.086+0.540	210.01	−61.24
311.105−0.407	210.58	−62.15
311.117+0.730	209.96	−61.05
311.139+0.705	210.02	−61.07
311.150+0.667	210.06	−61.10
311.158+0.110	210.39	−61.64
311.165+0.968	209.93	−60.81
311.172−0.419	210.72	−62.14
311.174−0.443	210.74	−62.17
311.175+0.786	210.05	−60.98
311.176+0.274	210.33	−61.47
311.181−0.406	210.73	−62.13
311.182−0.391	210.73	−62.11
311.186+1.026	209.94	−60.75
311.187+0.841	210.04	−60.92
311.190+0.696	210.13	−61.06
311.192+0.455	210.26	−61.29
311.200−0.329	210.73	−62.05
311.202−0.024	210.55	−61.75
311.206+0.225	210.42	−61.51
311.217+0.864	210.09	−60.89
311.220+0.944	210.05	−60.82
311.230+0.392	210.38	−61.35
311.232+0.999	210.05	−60.76
311.235+0.738	210.19	−61.01
311.237+0.105	210.55	−61.62
311.238+0.942	210.09	−60.81
311.241−0.363	210.83	−62.07
311.248+0.839	210.16	−60.91
311.266+1.041	210.09	−60.71
311.270−0.056	210.71	−61.77
311.273+0.174	210.59	−61.54
311.276+0.269	210.54	−61.45
311.278−0.351	210.90	−62.05
311.281+1.031	210.13	−60.72
311.285+0.969	210.17	−60.77
311.296+0.979	210.18	−60.76
311.324+1.007	210.23	−60.73
311.328−0.293	210.97	−61.98
311.340+0.691	210.43	−61.03

continued on next page

Name of *Spitzer*-dark and *Herschel*-dark Region	Right Ascension 2000.0 (°)	Declination 2000.0 (°)
311.340+0.827	210.35	−60.90
311.341+0.645	210.46	−61.07
311.343+0.869	210.34	−60.86
311.369+0.879	210.38	−60.84
311.376+0.483	210.62	−61.22
311.380−0.536	211.22	−62.20
311.388−0.044	210.94	−61.72
311.409+0.747	210.54	−60.96
311.412+0.618	210.61	−61.08
311.426+0.881	210.50	−60.82
311.428+0.370	210.79	−61.31
311.437+0.356	210.81	−61.32
311.441+0.688	210.63	−61.00
311.442+0.749	210.60	−60.94
311.447+0.436	210.79	−61.24
311.449+0.336	210.85	−61.34
311.451−0.492	211.34	−62.14
311.467+0.749	210.65	−60.94
311.468+0.394	210.85	−61.28
311.470+0.788	210.63	−60.90
311.482+0.450	210.85	−61.22
311.486+0.392	210.89	−61.28
311.494+0.372	210.92	−61.29
311.501+0.251	211.00	−61.41
311.506−0.447	211.42	−62.08
311.509+0.805	210.70	−60.87
311.516−0.417	211.43	−62.05
311.519−0.460	211.46	−62.09
311.522+0.503	210.90	−61.16
311.561+0.329	211.08	−61.32
311.564+0.260	211.12	−61.38
311.585+0.270	211.16	−61.37
311.592+0.306	211.15	−61.33
311.599−0.499	211.65	−62.10
311.600+0.231	211.21	−61.40
311.602+0.269	211.19	−61.36
311.610+0.410	211.13	−61.22
311.624+0.270	211.24	−61.35
311.625+0.312	211.21	−61.31
311.645+0.224	211.31	−61.39
311.668+0.189	211.37	−61.42
311.676+0.243	211.36	−61.37
311.682+0.173	211.41	−61.43
311.686+0.330	211.33	−61.28
311.722−0.500	211.90	−62.07
311.736−0.048	211.65	−61.63
311.757−0.334	211.87	−61.90
311.764+0.109	211.61	−61.47
311.768−0.652	212.09	−62.20
311.772+0.075	211.65	−61.50
311.776−0.188	211.82	−61.75

continued on next page

Name of *Spitzer*-dark and *Herschel*-dark Region	Right Ascension 2000.0 (°)	Declination 2000.0 (°)
311.784−0.259	211.88	−61.82
311.795−0.005	211.74	−61.57
311.795−0.291	211.92	−61.84
311.805−0.327	211.96	−61.88
311.809+0.063	211.73	−61.50
311.820−0.753	212.26	−62.28
311.823−0.239	211.94	−61.79
311.828−0.205	211.93	−61.75
311.836+0.124	211.75	−61.43
311.840+0.074	211.79	−61.48
311.842+0.145	211.75	−61.41
311.862+0.854	211.37	−60.73
311.863+0.091	211.82	−61.46
311.867+0.217	211.75	−61.34
311.875−0.691	212.33	−62.20
311.880+0.123	211.84	−61.42
311.884+0.096	211.86	−61.45
311.885−0.201	212.04	−61.73
311.889−0.186	212.04	−61.72
311.889+0.122	211.85	−61.42
311.890+0.386	211.70	−61.17
311.893+0.109	211.87	−61.43
311.899+0.169	211.85	−61.37
311.914+0.034	211.96	−61.50
311.917+0.052	211.95	−61.48
311.927−0.273	212.17	−61.79
311.935+0.248	211.87	−61.29
311.943−0.221	212.17	−61.73
311.951−0.272	212.22	−61.78
311.971−0.754	212.57	−62.23
311.976+0.144	212.01	−61.37
311.984−0.762	212.60	−62.24
312.012+0.036	212.15	−61.47
312.014−0.563	212.53	−62.04
312.035−0.659	212.64	−62.13
312.047−0.685	212.68	−62.15
312.070+0.070	212.25	−61.42
312.072−0.808	212.81	−62.26
312.080−0.766	212.80	−62.21
312.090+0.314	212.14	−61.18
312.096−0.646	212.75	−62.09
312.098−0.774	212.84	−62.22
312.108−0.499	212.68	−61.95
312.109−0.530	212.71	−61.98
312.121−0.015	212.40	−61.48
312.122−0.881	212.96	−62.31
312.124+0.311	212.21	−61.17
312.125−0.536	212.74	−61.98
312.128−0.210	212.54	−61.67
312.133−0.205	212.55	−61.66
312.145+0.003	212.44	−61.46

continued on next page

Name of *Spitzer*-dark and *Herschel*-dark Region	Right Ascension 2000.0 (°)	Declination 2000.0 (°)
312.157+0.002	212.46	−61.46
312.158−0.715	212.92	−62.14
312.160−0.116	212.54	−61.57
312.166−0.152	212.58	−61.60
312.181−0.211	212.65	−61.65
312.186−0.684	212.96	−62.10
312.187−0.142	212.62	−61.59
312.187−0.828	213.06	−62.24
312.187−0.850	213.07	−62.26
312.198−0.057	212.58	−61.50
312.202−0.071	212.60	−61.51
312.206−0.200	212.69	−61.64
312.221−0.872	213.16	−62.27
312.226−0.208	212.73	−61.64
312.227−0.709	213.06	−62.11
312.233+0.748	212.16	−60.72
312.240−0.841	213.18	−62.24
312.241−0.786	213.14	−62.18
312.270−0.903	213.28	−62.28
312.271−0.787	213.20	−62.17
312.274−0.799	213.22	−62.19
312.279−0.801	213.23	−62.19
312.282−0.872	213.28	−62.25
312.283−0.896	213.30	−62.27
312.285+0.024	212.70	−61.40
312.357+0.033	212.84	−61.37
312.387−0.013	212.93	−61.40
312.391−0.505	213.26	−61.87
312.400−0.515	213.28	−61.88
312.402−0.532	213.30	−61.89
312.428−0.438	213.29	−61.79
312.453+0.611	212.67	−60.79
312.508−0.009	213.17	−61.36
312.604+0.039	213.33	−61.29
312.616+0.025	213.36	−61.29
312.716+0.054	213.54	−61.24
312.723+0.045	213.56	−61.24
312.757−0.698	214.13	−61.94
312.770−0.775	214.21	−62.01
312.857−0.473	214.17	−61.69
312.879+0.230	213.75	−61.02
312.882−0.476	214.22	−61.69
312.903+0.209	213.81	−61.03
312.922−0.425	214.27	−61.62
312.932−0.442	214.30	−61.64
312.991−0.437	214.41	−61.61
313.006−0.491	214.48	−61.66
313.171−0.396	214.74	−61.52
313.174−0.389	214.74	−61.51
313.263−0.284	214.85	−61.38
313.264−0.707	215.15	−61.78

continued on next page

Name of *Spitzer*-dark and *Herschel*-dark Region	Right Ascension 2000.0 (°)	Declination 2000.0 (°)
313.294−0.714	215.21	−61.77
313.334−0.506	215.14	−61.56
313.341−0.921	215.46	−61.95
313.346−0.458	215.13	−61.52
313.346+0.629	214.39	−60.49
313.361+0.283	214.65	−60.81
313.393−0.580	215.31	−61.61
313.426+0.188	214.84	−60.88
313.455+0.217	214.87	−60.84
313.460+0.148	214.93	−60.91
313.479−0.088	215.13	−61.12
313.516−0.032	215.17	−61.06
313.530−0.533	215.55	−61.52
313.599−0.167	215.42	−61.16
313.652+0.563	215.02	−60.45
313.664−0.787	216.00	−61.72
313.671−0.309	215.66	−61.26
313.678+0.081	215.40	−60.89
313.680+0.676	214.99	−60.33
313.692+0.608	215.06	−60.39
313.703+0.103	215.43	−60.87
313.705−0.507	215.87	−61.44
313.709−0.226	215.68	−61.17
313.716−0.237	215.70	−61.18
313.718−0.079	215.59	−61.03
313.724+0.606	215.13	−60.39
313.726+0.399	215.27	−60.58
313.743−0.858	216.21	−61.75
313.752+0.547	215.22	−60.43
313.752+0.712	215.11	−60.28
313.753−0.085	215.66	−61.03
313.756+0.299	215.40	−60.66
313.774−0.863	216.27	−61.75
313.789−0.255	215.86	−61.17
313.793−0.250	215.86	−61.17
313.793+0.079	215.62	−60.86
313.795−0.287	215.89	−61.20
313.803−0.296	215.91	−61.21
313.805+0.159	215.59	−60.78
313.809+0.213	215.56	−60.73
313.810+0.135	215.62	−60.80
313.817+0.176	215.60	−60.76
313.817+0.714	215.23	−60.25
313.829+0.174	215.63	−60.76
313.855+0.849	215.21	−60.11
313.868+0.808	215.26	−60.15
313.872+0.052	215.79	−60.86
313.901+0.702	215.40	−60.24
313.905+0.941	215.24	−60.01
313.914−0.061	215.96	−60.95
313.995+0.788	215.51	−60.12

continued on next page

Name of *Spitzer*-dark and *Herschel*-dark Region	Right Ascension 2000.0 (°)	Declination 2000.0 (°)
314.012+0.090	216.04	−60.77
314.037+0.646	215.69	−60.24
314.059+0.830	215.61	−60.06
314.062+0.414	215.90	−60.45
314.067+0.828	215.62	−60.06
314.068+0.406	215.92	−60.46
314.068+0.836	215.62	−60.05
314.072+0.564	215.82	−60.31
314.084−0.036	216.27	−60.86
314.092+0.463	215.93	−60.39
314.093+0.281	216.06	−60.56
314.109+0.563	215.89	−60.29
314.114+0.524	215.92	−60.33
314.115+0.312	216.07	−60.53
314.116+0.457	215.97	−60.39
314.123+0.386	216.04	−60.46
314.132+0.938	215.67	−59.93
314.137+0.857	215.73	−60.01
314.161+0.444	216.07	−60.39
314.165+0.539	216.01	−60.30
314.167+0.578	215.99	−60.26
314.176+0.223	216.25	−60.59
314.182+0.430	216.12	−60.39
314.185+0.214	216.28	−60.59
314.189+0.925	215.78	−59.93
314.190+0.260	216.26	−60.55
314.201+0.348	216.21	−60.46
314.208+0.493	216.12	−60.32
314.210+0.757	215.94	−60.08
314.215+0.311	216.27	−60.49
314.226+0.251	216.33	−60.55
314.235+0.397	216.24	−60.41
314.247+0.562	216.15	−60.25
314.255+0.644	216.10	−60.17
314.257−0.225	216.74	−60.98
314.260+0.067	216.53	−60.70
314.266+0.112	216.51	−60.66
314.267+0.426	216.28	−60.37
314.269+0.497	216.24	−60.30
314.270+0.119	216.51	−60.65
314.281+0.089	216.55	−60.68
314.290+0.017	216.62	−60.74
314.292+0.451	216.31	−60.33
314.294+0.114	216.56	−60.65
314.300+0.039	216.63	−60.72
314.301−0.058	216.70	−60.81
314.301+0.031	216.63	−60.72
314.304+0.025	216.64	−60.73
314.305−0.005	216.67	−60.76
314.305−0.059	216.71	−60.81
314.306+0.073	216.61	−60.68

continued on next page

Name of *Spitzer*-dark and *Herschel*-dark Region	Right Ascension 2000.0 (°)	Declination 2000.0 (°)
314.310+0.102	216.60	−60.65
314.318−0.027	216.71	−60.77
314.320−0.034	216.72	−60.78
314.326−0.164	216.83	−60.90
314.330−0.378	216.99	−61.10
314.340+0.270	216.53	−60.49
314.342+0.098	216.66	−60.65
314.352−0.042	216.79	−60.77
314.357−0.163	216.88	−60.89
314.376−0.009	216.81	−60.73
314.399+0.040	216.81	−60.68
314.524+0.336	216.83	−60.36
314.603−0.287	217.45	−60.91
314.656−0.113	217.42	−60.73
314.708+0.184	217.29	−60.43
314.714−0.301	217.67	−60.88
314.724−0.274	217.67	−60.85
314.730−0.317	217.71	−60.89
314.755−0.019	217.53	−60.61
314.757−0.026	217.54	−60.61
314.802−0.149	217.72	−60.71
314.984+0.033	217.93	−60.47
315.037−0.121	218.14	−60.59
315.057−0.096	218.16	−60.56
315.112−0.185	218.34	−60.62
315.320−0.231	218.76	−60.59
315.324−0.308	218.83	−60.66
315.346−0.269	218.84	−60.61
315.673−0.655	219.77	−60.84
315.674−0.652	219.77	−60.83
315.690−0.634	219.78	−60.81
315.690−0.634	219.78	−60.81
315.987−0.597	220.31	−60.66
316.337−0.410	220.80	−60.34
316.377−0.494	220.94	−60.40
316.406−0.422	220.93	−60.32
316.409−0.450	220.96	−60.35
316.419−0.265	220.82	−60.17
316.450−0.271	220.89	−60.17
316.454−0.259	220.88	−60.15
316.484−0.613	221.24	−60.46
316.488+0.263	220.51	−59.66
316.504−0.260	220.98	−60.13
316.511−0.559	221.24	−60.40
316.532−0.601	221.32	−60.43
316.541−0.268	221.05	−60.13
316.559+0.048	220.82	−59.83
316.583+0.038	220.87	−59.83
316.599+0.040	220.90	−59.82
316.601−0.191	221.09	−60.03
316.611−0.825	221.66	−60.60

continued on next page

Name of *Spitzer*-dark and *Herschel*-dark Region	Right Ascension 2000.0 (°)	Declination 2000.0 (°)
316.619−0.195	221.13	−60.03
316.623−0.067	221.03	−59.91
316.626−0.007	220.99	−59.85
316.637+0.024	220.98	−59.82
316.640+0.048	220.96	−59.80
316.641−0.153	221.14	−59.98
316.641−0.401	221.35	−60.20
316.643−0.347	221.30	−60.15
316.649−0.375	221.34	−60.18
316.649−0.421	221.38	−60.22
316.659−0.309	221.30	−60.11
316.665−0.135	221.16	−59.95
316.668+0.035	221.03	−59.80
316.687+0.136	220.98	−59.70
316.699−0.219	221.30	−60.02
316.729−0.161	221.30	−59.95
316.730+0.173	221.02	−59.65
316.731−0.443	221.54	−60.20
316.734−0.131	221.28	−59.92
316.745−0.054	221.24	−59.85
316.750+0.127	221.10	−59.68
316.751−0.121	221.31	−59.90
316.757+0.109	221.12	−59.69
316.760+0.061	221.17	−59.73
316.765+0.062	221.18	−59.73
316.770−0.065	221.29	−59.85
316.770+0.272	221.01	−59.54
316.771−0.133	221.35	−59.91
316.786−0.044	221.30	−59.82
316.788−0.225	221.46	−59.98
316.795+0.198	221.12	−59.60
316.803+0.297	221.05	−59.50
316.816−0.030	221.35	−59.79
316.821−0.062	221.38	−59.82
316.825+0.013	221.33	−59.75
316.830−0.034	221.37	−59.79
316.833−0.018	221.37	−59.78
316.856+0.407	221.05	−59.38
316.876−0.017	221.44	−59.76
316.876+0.332	221.15	−59.44
316.879+0.034	221.40	−59.71
316.887−0.050	221.49	−59.78
316.893+0.401	221.12	−59.37
316.895+0.444	221.09	−59.33
316.900+0.300	221.22	−59.46
316.904+0.054	221.43	−59.68
316.911+0.575	221.01	−59.21
316.923−0.110	221.61	−59.82
316.925+0.256	221.30	−59.49
316.925+0.366	221.21	−59.39
316.935+0.342	221.25	−59.41

continued on next page

Name of *Spitzer*-dark and *Herschel*-dark Region	Right Ascension 2000.0 (°)	Declination 2000.0 (°)
316.935+0.517	221.10	−59.25
316.937+0.454	221.16	−59.30
316.959+0.332	221.30	−59.41
316.961+0.400	221.25	−59.34
316.970+0.328	221.32	−59.40
316.985+0.363	221.32	−59.37
316.991+0.328	221.36	−59.40
317.000+0.358	221.35	−59.36
317.001+0.388	221.33	−59.34
317.020−0.066	221.74	−59.74
317.026+0.314	221.43	−59.39
317.034+0.472	221.32	−59.25
317.039+0.546	221.26	−59.18
317.045+0.212	221.55	−59.48
317.059+0.311	221.49	−59.38
317.081+0.000	221.80	−59.65
317.098+0.183	221.67	−59.48
317.104+0.219	221.65	−59.45
317.120+0.308	221.61	−59.36
317.167+0.326	221.67	−59.32
317.179+0.226	221.78	−59.41
317.202+0.196	221.85	−59.42
317.213+0.275	221.80	−59.35
317.214+0.255	221.82	−59.37
317.232+0.166	221.92	−59.44
317.259+0.264	221.89	−59.34
317.271+0.199	221.96	−59.39
317.276+0.103	222.06	−59.48
317.284+0.285	221.91	−59.31
317.285+0.234	221.96	−59.35
317.288+0.278	221.93	−59.31
317.293−0.450	222.57	−59.97
317.308+0.331	221.92	−59.26
317.316−0.194	222.38	−59.73
317.323+0.223	222.04	−59.35
317.329+0.265	222.01	−59.31
317.333−0.238	222.45	−59.76
317.340−0.217	222.45	−59.74
317.341+0.315	221.99	−59.26
317.342+0.105	222.17	−59.45
317.342+0.113	222.16	−59.44
317.346+0.147	222.14	−59.41
317.350−0.336	222.57	−59.84
317.351−0.001	222.28	−59.54
317.357+0.246	222.08	−59.31
317.370+0.346	222.02	−59.22
317.383+0.140	222.21	−59.40
317.388+0.431	221.98	−59.13
317.400−0.137	222.48	−59.64
317.402−0.285	222.62	−59.77
317.407−0.389	222.72	−59.86

continued on next page

Name of *Spitzer*-dark and *Herschel*-dark Region	Right Ascension 2000.0 (°)	Declination 2000.0 (°)
317.410+0.118	222.28	−59.40
317.411+0.498	221.96	−59.06
317.417−0.609	222.93	−60.05
317.418−0.350	222.70	−59.82
317.423−0.152	222.54	−59.64
317.427+0.221	222.22	−59.30
317.428+0.637	221.87	−58.93
317.429−0.671	223.01	−60.10
317.436−0.267	222.66	−59.74
317.440+0.500	222.01	−59.05
317.444+0.597	221.93	−58.96
317.451−0.128	222.57	−59.61
317.463+0.625	221.94	−58.92
317.464−0.064	222.53	−59.55
317.464−0.403	222.83	−59.85
317.467−0.067	222.54	−59.55
317.472+0.065	222.43	−59.42
317.473+0.439	222.12	−59.09
317.492−0.700	223.15	−60.10
317.495−0.440	222.92	−59.87
317.495+0.281	222.29	−59.22
317.519+0.354	222.27	−59.14
317.519+0.621	222.04	−58.90
317.539−0.700	223.23	−60.08
317.550−0.705	223.25	−60.08
317.570−0.405	223.02	−59.80
317.576−0.944	223.52	−60.28
317.582+0.089	222.61	−59.35
317.585−0.718	223.33	−60.08
317.587−0.115	222.80	−59.54
317.601+0.048	222.68	−59.38
317.617−0.833	223.49	−60.16
317.632−0.080	222.84	−59.48
317.642−0.175	222.95	−59.57
317.652+0.123	222.70	−59.29
317.667−0.132	222.95	−59.52
317.696−0.050	222.93	−59.43
317.699+0.126	222.78	−59.27
317.700+0.078	222.83	−59.31
317.706−0.367	223.23	−59.71
317.724−0.914	223.76	−60.19
317.734+0.090	222.87	−59.29
317.742−0.057	223.02	−59.42
317.750−0.043	223.02	−59.40
317.772−0.040	223.06	−59.39
317.797−0.922	223.89	−60.16
317.816+0.175	222.94	−59.17
317.823−0.816	223.84	−60.06
317.832+0.154	222.99	−59.19
317.851+0.100	223.07	−59.22
317.862−0.734	223.84	−59.96

continued on next page

Name of *Spitzer*-dark and *Herschel*-dark Region	Right Ascension 2000.0 (°)	Declination 2000.0 (°)
317.874+0.221	223.01	−59.11
317.877−0.320	223.49	−59.59
317.887−0.249	223.44	−59.52
317.907−0.821	224.00	−60.02
317.910−0.233	223.47	−59.50
317.923−0.671	223.89	−59.88
317.931−0.725	223.95	−59.92
317.949−0.902	224.15	−60.07
317.960−0.613	223.90	−59.81
317.961−0.788	224.06	−59.97
317.973−0.954	224.24	−60.11
317.976−0.806	224.11	−59.98
317.987+0.041	223.36	−59.22
317.996−0.763	224.10	−59.93
318.013−0.790	224.16	−59.95
318.014+0.070	223.38	−59.18
318.027−0.829	224.22	−59.97
318.038+0.086	223.41	−59.15
318.043−0.888	224.30	−60.02
318.045+0.076	223.43	−59.16
318.053−0.776	224.22	−59.91
318.083−0.735	224.23	−59.86
318.084+0.108	223.47	−59.11
318.091+0.093	223.50	−59.12
318.132−0.938	224.50	−60.02
318.137+0.079	223.59	−59.11
318.158−0.646	224.28	−59.75
318.162−0.769	224.40	−59.86
318.165−0.614	224.26	−59.72
318.166+0.892	222.93	−58.38
318.192−0.387	224.10	−59.50
318.192−0.640	224.33	−59.73
318.214+0.048	223.75	−59.11
318.223−0.612	224.36	−59.69
318.255−0.537	224.35	−59.61
318.292−0.603	224.48	−59.65
318.319−0.731	224.64	−59.75
318.322−0.750	224.66	−59.77
318.397−0.134	224.23	−59.19
318.559−0.201	224.57	−59.17
318.611+0.653	223.89	−58.39
318.700−0.237	224.85	−59.14
318.700−0.791	225.36	−59.62
318.718−0.312	224.94	−59.19
318.727−0.740	225.36	−59.56
318.731−0.721	225.35	−59.55
318.734+0.651	224.10	−58.33
318.749−0.240	224.93	−59.11
318.900−0.299	225.25	−59.09
318.926+0.702	224.38	−58.20
318.930−0.242	225.24	−59.03

continued on next page

Name of *Spitzer*-dark and *Herschel*-dark Region	Right Ascension 2000.0 (°)	Declination 2000.0 (°)
318.935−0.188	225.20	−58.98
318.938−0.242	225.26	−59.03
318.953−0.124	225.17	−58.92
318.957−0.199	225.25	−58.98
319.044−0.348	225.54	−59.07
319.068+0.453	224.84	−58.35
319.071−0.374	225.61	−59.08
319.080−0.368	225.62	−59.07
319.092−0.406	225.67	−59.10
319.108+0.766	224.63	−58.06
319.117−0.444	225.75	−59.12
319.119−0.388	225.70	−59.07
319.121−0.334	225.65	−59.02
319.127−0.300	225.63	−58.99
319.149−0.424	225.79	−59.09
319.161−0.465	225.85	−59.11
319.177−0.366	225.78	−59.02
319.190−0.295	225.74	−58.95
319.197−0.265	225.72	−58.92
319.201−0.408	225.86	−59.05
319.206−0.224	225.70	−58.88
319.216−0.370	225.85	−59.01
319.217+0.834	224.75	−57.95
319.235−0.007	225.55	−58.68
319.249−0.248	225.79	−58.88
319.251+0.875	224.77	−57.89
319.267+0.868	224.80	−57.89
319.286−0.304	225.91	−58.91
319.303+0.042	225.61	−58.60
319.328+0.914	224.86	−57.82
319.334+0.036	225.67	−58.59
319.348+0.033	225.70	−58.59
319.391−0.344	226.12	−58.90
319.406−0.040	225.86	−58.62
319.412+0.042	225.80	−58.55
319.426+0.010	225.85	−58.57
319.497−0.453	226.40	−58.94
319.499−0.020	226.00	−58.56
319.723−0.122	226.47	−58.54
319.859+0.818	225.82	−57.65
319.882+0.810	225.87	−57.65
319.886−0.174	226.79	−58.51
319.886+0.753	225.93	−57.70
319.888−0.186	226.81	−58.51
319.910+0.796	225.93	−57.65
319.958+0.710	226.08	−57.70
320.011+0.746	226.14	−57.64
320.011+0.773	226.11	−57.62
320.013+0.826	226.07	−57.57
320.014+0.724	226.16	−57.66
320.037+0.832	226.10	−57.55

continued on next page

Name of *Spitzer*-dark and *Herschel*-dark Region	Right Ascension 2000.0 (°)	Declination 2000.0 (°)
320.063+0.747	226.22	−57.62
320.084+0.673	226.32	−57.67
320.153+0.771	226.35	−57.55
320.160+0.780	226.35	−57.54
320.164+0.831	226.31	−57.49
320.166−0.357	227.43	−58.52
320.172+0.792	226.36	−57.52
320.177−0.158	227.26	−58.35
320.181+0.713	226.44	−57.59
320.218−0.126	227.29	−58.30
320.218+0.501	226.70	−57.75
320.219+0.430	226.77	−57.81
320.228−0.158	227.34	−58.32
320.228+0.144	227.05	−58.06
320.233−0.924	228.10	−58.98
320.236−0.555	227.74	−58.66
320.243−0.293	227.49	−58.43
320.251−0.190	227.41	−58.34
320.251−0.563	227.77	−58.66
320.252+0.447	226.81	−57.78
320.256−0.475	227.69	−58.58
320.261−0.332	227.56	−58.45
320.262−0.361	227.59	−58.48
320.262+0.467	226.80	−57.76
320.272+0.148	227.12	−58.03
320.284+0.287	227.01	−57.91
320.291+0.408	226.91	−57.80
320.296−0.203	227.49	−58.33
320.296+0.117	227.19	−58.05
320.302−0.334	227.63	−58.43
320.303−0.287	227.59	−58.39
320.304+0.185	227.14	−57.99
320.304+0.398	226.94	−57.80
320.321−0.327	227.66	−58.42
320.322+0.469	226.90	−57.73
320.327−0.783	228.12	−58.81
320.329+0.186	227.18	−57.97
320.334−0.761	228.10	−58.79
320.336−0.152	227.51	−58.26
320.338+0.158	227.22	−57.99
320.354+0.260	227.15	−57.89
320.354+0.260	227.15	−57.89
320.358+0.179	227.23	−57.96
320.363−0.189	227.59	−58.28
320.363+0.209	227.21	−57.93
320.374+0.119	227.31	−58.01
320.377−0.262	227.69	−58.34
320.388−0.160	227.61	−58.24
320.389+0.180	227.28	−57.95
320.405+0.091	227.39	−58.02
320.409+0.169	227.32	−57.95

continued on next page

Name of *Spitzer*-dark and *Herschel*-dark Region	Right Ascension 2000.0 (°)	Declination 2000.0 (°)
320.415+0.152	227.35	−57.96
320.423−0.835	228.33	−58.80
320.447+0.226	227.33	−57.88
320.453−0.084	227.64	−58.14
320.457+0.112	227.46	−57.97
320.466−0.261	227.83	−58.29
320.470+0.114	227.48	−57.96
320.486−0.880	228.47	−58.81
320.596−0.194	227.98	−58.16
320.599+0.249	227.56	−57.78
320.624+0.459	227.40	−57.59
320.631+0.195	227.66	−57.81
320.643+0.159	227.71	−57.84
320.648+0.301	227.59	−57.71
320.654+0.274	227.62	−57.73
320.668+0.244	227.67	−57.75
320.674+0.234	227.69	−57.76
320.677+0.238	227.69	−57.75
320.679+0.244	227.69	−57.74
320.680+0.274	227.66	−57.72
320.681+0.251	227.69	−57.74
320.685+0.253	227.69	−57.73
320.692+0.194	227.76	−57.78
320.692+0.442	227.52	−57.57
320.696+0.205	227.75	−57.77
320.702+0.201	227.77	−57.77
320.706+0.459	227.53	−57.55
320.723+0.176	227.83	−57.78
320.735+0.291	227.74	−57.68
320.742+0.238	227.80	−57.72
320.743+0.266	227.77	−57.69
320.753+0.136	227.91	−57.80
320.762+0.696	227.40	−57.31
320.778+0.208	227.88	−57.73
320.785+0.720	227.41	−57.28
320.789+0.362	227.76	−57.59
320.790+0.214	227.90	−57.71
320.800+0.126	228.00	−57.78
320.804+0.199	227.93	−57.72
320.807+0.388	227.76	−57.56
320.809+0.271	227.87	−57.66
320.818+0.213	227.94	−57.70
320.830+0.259	227.92	−57.65
320.850+0.167	228.04	−57.72
320.891−0.415	228.67	−58.20
320.897+0.921	227.40	−57.05
320.911−0.428	228.72	−58.20
320.911−0.777	229.07	−58.50
320.929−0.406	228.73	−58.17
320.980−0.785	229.19	−58.47
320.997−0.500	228.93	−58.22

continued on next page

Name of *Spitzer*-dark and *Herschel*-dark Region	Right Ascension 2000.0 (°)	Declination 2000.0 (°)
320.998−0.819	229.25	−58.49
321.035−0.522	229.01	−58.22
321.040−0.625	229.12	−58.30
321.057−0.572	229.10	−58.25
321.062−0.615	229.15	−58.28
321.067−0.558	229.10	−58.23
321.068−0.552	229.09	−58.23
321.075−0.581	229.14	−58.25
321.076−0.482	229.04	−58.16
321.076−0.602	229.16	−58.26
321.080−0.524	229.09	−58.20
321.095−0.608	229.20	−58.26
321.097−0.523	229.11	−58.19
321.103−0.630	229.23	−58.27
321.106−0.611	229.22	−58.26
321.142−0.630	229.29	−58.25
321.153−0.604	229.28	−58.23
321.184−0.570	229.30	−58.18
321.185−0.551	229.28	−58.16
321.192−0.594	229.34	−58.20
321.218−0.661	229.45	−58.24
321.374−0.293	229.33	−57.84
321.520+0.122	229.15	−57.41
321.550+0.115	229.20	−57.40
321.560+0.121	229.21	−57.39
321.650−0.001	229.48	−57.45
321.693−0.033	229.58	−57.45
321.708+0.063	229.50	−57.36
321.730−0.678	230.28	−57.98
321.739−0.572	230.19	−57.88
321.769−0.085	229.75	−57.46
321.769−0.528	230.19	−57.83
321.802+0.010	229.70	−57.36
321.803−0.104	229.82	−57.46
321.803−0.657	230.38	−57.92
321.881−0.852	230.70	−58.04
321.909−0.893	230.79	−58.06
321.934−0.052	229.97	−57.34
321.936−0.003	229.93	−57.30
322.023+0.851	229.23	−56.53
322.027−0.256	230.32	−57.46
322.034−0.074	230.15	−57.31
322.036+0.788	229.31	−56.58
322.043+0.624	229.48	−56.71
322.063−0.077	230.20	−57.29
322.084−0.061	230.22	−57.27
322.093−0.658	230.83	−57.76
322.111+0.537	229.67	−56.75
322.116+0.528	229.68	−56.75
322.125−0.142	230.36	−57.31
322.149+0.639	229.63	−56.64

continued on next page

Name of *Spitzer*-dark and *Herschel*-dark Region	Right Ascension 2000.0 (°)	Declination 2000.0 (°)
322.162+0.615	229.67	−56.66
322.181+0.601	229.71	−56.66
322.247+0.621	229.79	−56.61
322.303+0.578	229.92	−56.61
322.385+0.181	230.44	−56.90
322.385+0.234	230.39	−56.86
322.391+0.531	230.10	−56.60
322.489+0.645	230.14	−56.45
322.489+0.645	230.14	−56.45
322.525+0.645	230.20	−56.44
322.628+0.175	230.82	−56.77
322.659−0.710	231.77	−57.50
322.803−0.460	231.73	−57.21
323.163+0.143	231.66	−56.51
323.202+0.095	231.77	−56.52
323.206+0.185	231.68	−56.45
323.218+0.139	231.75	−56.48
323.248−0.388	232.33	−56.90
323.303−0.375	232.40	−56.86
323.348−0.383	232.48	−56.84
323.378+0.099	232.03	−56.42
323.380−0.058	232.19	−56.55
323.416−0.452	232.65	−56.85
323.442−0.078	232.31	−56.53
323.471−0.081	232.35	−56.52
323.477+0.490	231.78	−56.04
323.489−0.229	232.53	−56.63
323.504−0.379	232.71	−56.74
323.508−0.124	232.45	−56.53
323.514−0.470	232.82	−56.81
323.545−0.199	232.58	−56.57
323.545+0.357	232.02	−56.11
323.580−0.417	232.86	−56.73
323.620+0.003	232.49	−56.36
323.688−0.318	232.92	−56.59
323.738−0.270	232.94	−56.52
323.752−0.356	233.06	−56.58
323.882−0.159	233.04	−56.35
323.898+0.059	232.84	−56.16
323.910+0.380	232.53	−55.89
323.913+0.003	232.92	−56.20
323.922−0.013	232.95	−56.20
323.936+0.396	232.55	−55.86
324.076−0.852	234.06	−56.80
324.085−0.829	234.05	−56.78
324.117−0.852	234.12	−56.78
324.121−0.919	234.20	−56.83
324.142+0.232	233.02	−55.88
324.142+0.266	232.99	−55.85
324.158+0.453	232.82	−55.69
324.159+0.434	232.84	−55.70

continued on next page

Name of *Spitzer*-dark and *Herschel*-dark Region	Right Ascension 2000.0 (°)	Declination 2000.0 (°)
324.173+0.443	232.85	−55.69
324.182+0.246	233.07	−55.84
324.187+0.410	232.91	−55.71
324.396−0.413	234.06	−56.26
324.396−0.936	234.62	−56.68
324.539+0.303	233.53	−55.59
324.623+0.402	233.54	−55.46
324.633+0.779	233.18	−55.15
324.990+0.109	234.37	−55.48
325.049−0.089	234.66	−55.61
325.081+0.007	234.61	−55.51
325.110+0.014	234.64	−55.49
325.114+0.312	234.34	−55.25
325.122+0.047	234.62	−55.46
325.137+0.079	234.61	−55.42
325.206+0.024	234.77	−55.42
325.239+0.160	234.67	−55.30
325.283−0.176	235.09	−55.54
325.377+0.053	234.98	−55.30
325.471−1.015	236.26	−56.09
325.504+0.420	234.77	−54.93
325.512+0.409	234.80	−54.93
325.524+0.377	234.85	−54.95
325.537+0.446	234.79	−54.89
325.555+0.199	235.08	−55.08
325.687+0.512	234.93	−54.75
325.703+0.326	235.15	−54.89
325.724+0.460	235.04	−54.77
325.743−0.575	236.16	−55.58
325.758+0.429	235.12	−54.77
325.765+0.428	235.13	−54.77
325.766+0.226	235.34	−54.93
325.772−0.717	236.36	−55.67
325.795+0.530	235.07	−54.67
325.811−0.610	236.29	−55.57
325.820+0.464	235.17	−54.70
325.831−0.650	236.37	−55.59
325.846+0.184	235.50	−54.91
325.855+0.165	235.53	−54.92
325.856−0.190	235.91	−55.21
325.865+0.284	235.42	−54.82
325.867−0.154	235.88	−55.17
325.911+0.000	235.78	−55.02
325.926+0.054	235.74	−54.97
325.946−0.187	236.03	−55.15
325.958−0.469	236.35	−55.36
325.996+0.106	235.79	−54.88
326.005−0.523	236.47	−55.38
326.055−0.485	236.50	−55.32
326.058−0.568	236.59	−55.38
326.074−0.252	236.28	−55.12

continued on next page

Name of *Spitzer*-dark and *Herschel*-dark Region	Right Ascension 2000.0 (°)	Declination 2000.0 (°)
326.084−0.387	236.43	−55.22
326.093+0.803	235.20	−54.27
326.099+0.711	235.30	−54.34
326.109−0.526	236.62	−55.32
326.112−0.403	236.49	−55.22
326.113+0.886	235.14	−54.19
326.120+0.669	235.37	−54.36
326.128−0.503	236.62	−55.29
326.132+0.617	235.44	−54.40
326.136−0.473	236.60	−55.26
326.136+0.933	235.12	−54.14
326.146−0.338	236.47	−55.15
326.147+0.757	235.32	−54.28
326.155+0.689	235.40	−54.32
326.156−0.377	236.52	−55.17
326.163+0.584	235.52	−54.40
326.164−0.426	236.59	−55.20
326.189+0.961	235.16	−54.09
326.200−0.510	236.73	−55.25
326.200+0.536	235.62	−54.42
326.207−0.539	236.77	−55.27
326.210−0.374	236.60	−55.13
326.241−0.646	236.93	−55.33
326.244−0.452	236.73	−55.18
326.247−0.609	236.90	−55.30
326.249+0.594	235.62	−54.34
326.252+0.581	235.64	−54.35
326.254+0.345	235.89	−54.54
326.264−0.489	236.79	−55.19
326.265−0.295	236.59	−55.04
326.265−0.483	236.79	−55.19
326.280−0.588	236.92	−55.26
326.282+0.625	235.64	−54.30
326.284−0.483	236.81	−55.18
326.297−0.068	236.39	−54.84
326.306+0.900	235.39	−54.06
326.308−0.435	236.80	−55.12
326.310+0.897	235.40	−54.06
326.312−0.179	236.53	−54.92
326.312+0.644	235.66	−54.27
326.313−0.485	236.86	−55.16
326.314−0.069	236.41	−54.83
326.314+0.902	235.39	−54.06
326.315+0.893	235.41	−54.07
326.320−0.501	236.88	−55.17
326.328+0.910	235.41	−54.04
326.329+0.363	235.98	−54.48
326.331+0.635	235.69	−54.26
326.359+0.695	235.67	−54.20
326.361−0.142	236.55	−54.86
326.365−0.455	236.89	−55.10

continued on next page

Name of *Spitzer*-dark and *Herschel*-dark Region	Right Ascension 2000.0 (°)	Declination 2000.0 (°)
326.365+0.790	235.58	−54.12
326.365+0.934	235.43	−54.00
326.367−0.240	236.67	−54.93
326.371−0.558	237.02	−55.18
326.373+0.017	236.40	−54.73
326.373+0.940	235.44	−53.99
326.373+0.940	235.44	−53.99
326.376−0.507	236.97	−55.14
326.376+0.488	235.91	−54.35
326.377+0.363	236.04	−54.45
326.377+0.810	235.58	−54.09
326.381−0.326	236.78	−54.99
326.385−0.424	236.89	−55.07
326.389+0.029	236.41	−54.71
326.402−0.481	236.97	−55.10
326.403−0.765	237.28	−55.32
326.408+0.810	235.62	−54.08
326.412−0.215	236.70	−54.89
326.412+0.897	235.53	−54.00
326.414+0.680	235.76	−54.17
326.415+0.760	235.68	−54.11
326.416+0.042	236.43	−54.68
326.417+0.895	235.54	−54.00
326.420−0.537	237.06	−55.13
326.426−0.655	237.20	−55.22
326.429−0.364	236.88	−54.99
326.429+0.815	235.64	−54.06
326.435+0.726	235.74	−54.13
326.440−0.391	236.93	−55.01
326.441−0.469	237.01	−55.07
326.444+0.061	236.45	−54.65
326.445−0.231	236.76	−54.88
326.445−0.646	237.21	−55.20
326.451−0.432	236.99	−55.03
326.455−0.227	236.77	−54.87
326.455+0.535	235.97	−54.27
326.458+0.744	235.75	−54.10
326.459+0.029	236.50	−54.66
326.459+0.874	235.62	−53.99
326.460−0.526	237.10	−55.10
326.461+0.891	235.61	−53.98
326.462−0.195	236.75	−54.84
326.463−0.442	237.02	−55.03
326.473−0.750	237.36	−55.27
326.473+0.827	235.69	−54.02
326.475−0.350	236.93	−54.95
326.476+0.706	235.82	−54.12
326.478−0.061	236.63	−54.72
326.480+0.753	235.77	−54.08
326.483+0.595	235.94	−54.20
326.490+0.629	235.92	−54.17

continued on next page

Name of *Spitzer*-dark and *Herschel*-dark Region	Right Ascension 2000.0 (°)	Declination 2000.0 (°)
326.491−0.171	236.76	−54.80
326.491+0.683	235.86	−54.13
326.494+0.693	235.86	−54.12
326.495−0.508	237.13	−55.06
326.497−0.763	237.41	−55.26
326.501−0.489	237.12	−55.04
326.508−0.611	237.26	−55.14
326.508+0.545	236.03	−54.23
326.516−0.116	236.74	−54.74
326.518−0.662	237.33	−55.17
326.521−0.219	236.85	−54.82
326.523−0.453	237.11	−55.00
326.535−0.639	237.33	−55.14
326.536−0.054	236.70	−54.68
326.537−0.676	237.37	−55.17
326.537+0.931	235.67	−53.90
326.538+0.894	235.71	−53.93
326.540+0.559	236.06	−54.19
326.549−0.053	236.72	−54.67
326.553−0.114	236.79	−54.72
326.555−0.019	236.69	−54.64
326.559−0.531	237.24	−55.04
326.563−0.037	236.72	−54.65
326.567+0.778	235.87	−54.00
326.570−0.144	236.84	−54.73
326.578−0.501	237.24	−55.01
326.586+0.955	235.71	−53.85
326.587+0.431	236.25	−54.27
326.588−0.461	237.21	−54.97
326.597+0.953	235.73	−53.85
326.598−0.098	236.83	−54.68
326.600+0.598	236.10	−54.13
326.607+0.518	236.19	−54.19
326.611−0.345	237.11	−54.86
326.617+0.566	236.15	−54.14
326.625+0.504	236.23	−54.19
326.626+0.336	236.41	−54.32
326.626+0.578	236.15	−54.13
326.627+0.534	236.20	−54.16
326.628+0.468	236.27	−54.21
326.630−0.642	237.46	−55.08
326.632+0.594	236.14	−54.11
326.635+0.480	236.27	−54.20
326.636−0.673	237.50	−55.11
326.636+0.501	236.25	−54.18
326.641+0.562	236.19	−54.13
326.642+0.415	236.35	−54.25
326.644−0.579	237.41	−55.03
326.644+0.550	236.21	−54.14
326.646+0.448	236.32	−54.22
326.646+0.975	235.77	−53.80

continued on next page

Name of *Spitzer*-dark and *Herschel*-dark Region	Right Ascension 2000.0 (°)	Declination 2000.0 (°)
326.651+0.369	236.41	−54.28
326.652+0.423	236.35	−54.23
326.653+0.468	236.31	−54.20
326.653+0.478	236.29	−54.19
326.657−0.459	237.30	−54.92
326.661+0.573	236.21	−54.11
326.662+0.734	236.04	−53.98
326.664−0.099	236.92	−54.64
326.666−0.127	236.95	−54.66
326.666+0.711	236.07	−54.00
326.667+0.422	236.37	−54.23
326.667+0.878	235.90	−53.86
326.668+0.035	236.78	−54.53
326.669−0.119	236.95	−54.65
326.669−0.302	237.15	−54.79
326.669−0.787	237.67	−55.17
326.670−0.413	237.27	−54.88
326.672+0.585	236.21	−54.09
326.673+0.068	236.75	−54.50
326.673+0.300	236.51	−54.32
326.674+0.466	236.34	−54.19
326.675−0.386	237.24	−54.86
326.676+0.008	236.82	−54.55
326.677+0.892	235.90	−53.85
326.678+0.549	236.25	−54.12
326.679−0.734	237.63	−55.13
326.683−0.581	237.47	−55.00
326.686−0.321	237.19	−54.80
326.690−0.104	236.96	−54.63
326.691−0.605	237.50	−55.02
326.691+0.431	236.39	−54.20
326.693−0.459	237.35	−54.90
326.696+0.849	235.97	−53.87
326.701−0.505	237.41	−54.93
326.703−0.801	237.73	−55.16
326.705+0.854	235.97	−53.86
326.707+0.371	236.48	−54.24
326.708−0.404	237.31	−54.85
326.715−0.098	236.99	−54.61
326.715+0.372	236.49	−54.24
326.716−0.226	237.13	−54.71
326.717+0.011	236.87	−54.52
326.718−0.041	236.93	−54.56
326.721+0.442	236.42	−54.18
326.722−0.019	236.91	−54.54
326.722+0.354	236.52	−54.25
326.723+0.545	236.32	−54.09
326.725−0.724	237.68	−55.09
326.726+0.598	236.27	−54.05
326.727−0.004	236.90	−54.52
326.727−0.688	237.64	−55.06

continued on next page

Name of *Spitzer*-dark and *Herschel*-dark Region	Right Ascension 2000.0 (°)	Declination 2000.0 (°)
326.733+0.555	236.32	−54.08
326.739+0.432	236.46	−54.17
326.742−0.115	237.04	−54.60
326.744−0.123	237.06	−54.61
326.745−0.821	237.81	−55.15
326.747−0.532	237.50	−54.93
326.748−0.434	237.40	−54.85
326.748+0.448	236.45	−54.16
326.749−0.738	237.73	−55.09
326.751+0.663	236.23	−53.98
326.752−0.543	237.52	−54.93
326.756+0.527	236.38	−54.09
326.757+0.438	236.48	−54.16
326.757+0.480	236.43	−54.12
326.762−0.531	237.52	−54.92
326.763−0.083	237.04	−54.56
326.764−0.513	237.50	−54.90
326.764+0.392	236.54	−54.19
326.764+0.726	236.19	−53.93
326.767+0.422	236.51	−54.16
326.769+0.545	236.38	−54.07
326.771+0.729	236.19	−53.92
326.773−0.474	237.47	−54.86
326.773−0.665	237.68	−55.01
326.777+0.742	236.19	−53.91
326.783−0.707	237.74	−55.04
326.784+0.690	236.25	−53.94
326.785+0.709	236.23	−53.93
326.787−0.079	237.07	−54.55
326.788−0.130	237.12	−54.59
326.788+0.716	236.23	−53.92
326.791+0.652	236.30	−53.97
326.796−0.084	237.08	−54.54
326.796−0.093	237.09	−54.55
326.796+0.386	236.58	−54.17
326.799−0.098	237.10	−54.55
326.799−0.536	237.58	−54.90
326.804+0.676	236.29	−53.94
326.807−0.086	237.10	−54.54
326.808−0.576	237.63	−54.92
326.815+0.543	236.44	−54.04
326.817−0.019	237.04	−54.48
326.817+0.708	236.27	−53.91
326.826−0.753	237.85	−55.05
326.831+0.549	236.46	−54.02
326.833−0.737	237.84	−55.03
326.833+0.588	236.42	−53.99
326.834+0.582	236.43	−54.00
326.835−0.069	237.12	−54.51
326.836+0.068	236.97	−54.40
326.836+0.667	236.34	−53.93

continued on next page

Name of *Spitzer*-dark and *Herschel*-dark Region	Right Ascension 2000.0 (°)	Declination 2000.0 (°)
326.838−0.046	237.10	−54.49
326.839+0.132	236.91	−54.35
326.844−0.005	237.06	−54.45
326.845+0.682	236.34	−53.91
326.847+0.576	236.45	−53.99
326.848−0.024	237.09	−54.47
326.850+0.433	236.61	−54.10
326.851+0.499	236.54	−54.05
326.854+0.136	236.93	−54.34
326.855−0.357	237.46	−54.72
326.860−0.676	237.81	−54.97
326.865−0.011	237.10	−54.44
326.865+0.119	236.96	−54.34
326.869−0.144	237.25	−54.55
326.872+0.491	236.58	−54.05
326.881−0.106	237.22	−54.51
326.883−0.048	237.16	−54.46
326.883−0.186	237.31	−54.57
326.891+0.540	236.55	−53.99
326.892−0.098	237.23	−54.50
326.892+0.548	236.54	−53.99
326.898−0.095	237.23	−54.49
326.901+0.537	236.57	−53.99
326.903−0.168	237.32	−54.54
326.908+0.457	236.66	−54.05
326.909+0.534	236.58	−53.99
326.909+0.718	236.39	−53.84
326.912−0.094	237.25	−54.48
326.914−0.019	237.17	−54.42
326.914−0.155	237.32	−54.53
326.914+0.349	236.78	−54.13
326.918−0.176	237.35	−54.54
326.920+0.789	236.33	−53.78
326.928−0.193	237.38	−54.55
326.931+0.567	236.58	−53.95
326.932+0.549	236.60	−53.96
326.933−0.299	237.50	−54.63
326.935−0.110	237.30	−54.48
326.935+0.770	236.37	−53.79
326.938+0.561	236.59	−53.95
326.944+0.100	237.09	−54.31
326.946+0.356	236.82	−54.11
326.950+0.072	237.12	−54.33
326.953+0.440	236.74	−54.03
326.954−0.014	237.22	−54.39
326.954+0.040	237.16	−54.35
326.956−0.597	237.85	−54.85
326.959−0.379	237.62	−54.67
326.979−0.067	237.31	−54.42
326.980+0.049	237.19	−54.33
326.984−0.088	237.34	−54.43

continued on next page

Name of *Spitzer*-dark and *Herschel*-dark Region	Right Ascension 2000.0 (°)	Declination 2000.0 (°)
326.984+0.074	237.17	−54.30
326.989−0.222	237.49	−54.53
326.993−0.051	237.31	−54.40
326.996−0.074	237.34	−54.41
326.997−0.080	237.35	−54.42
327.014−0.077	237.37	−54.40
327.015+0.052	237.23	−54.30
327.018−0.106	237.41	−54.42
327.019−0.036	237.33	−54.37
327.030−0.244	237.57	−54.52
327.030−0.440	237.78	−54.68
327.039−0.009	237.33	−54.33
327.043−0.309	237.66	−54.57
327.050−0.112	237.46	−54.41
327.052+0.025	237.31	−54.30
327.053−0.075	237.42	−54.38
327.064+0.040	237.31	−54.28
327.075−0.114	237.49	−54.39
327.083−0.172	237.56	−54.44
327.088+0.065	237.32	−54.25
327.090−0.160	237.56	−54.42
327.099−0.164	237.58	−54.42
327.101−0.276	237.70	−54.50
327.105−0.190	237.61	−54.44
327.120−0.320	237.77	−54.53
327.127−0.425	237.90	−54.60
327.127−0.614	238.10	−54.75
327.138−0.228	237.70	−54.44
327.146−0.682	238.20	−54.79
327.155−0.356	237.86	−54.53
327.184−0.538	238.10	−54.66
327.207+0.258	237.27	−54.02
327.263−0.760	238.45	−54.78
327.277−0.387	238.06	−54.48
327.306−0.566	238.29	−54.60
327.307−0.510	238.23	−54.56
327.336−0.102	237.83	−54.22
327.338−0.758	238.54	−54.73
327.342−0.741	238.53	−54.71
327.367−0.449	238.24	−54.47
327.377−0.540	238.36	−54.53
327.386−0.414	238.23	−54.43
327.392+0.447	237.32	−53.76
327.395−0.594	238.44	−54.57
327.397+0.439	237.33	−53.76
327.414+0.036	237.78	−54.06
327.443−0.400	238.29	−54.39
327.453−0.726	238.66	−54.63
327.463−0.845	238.81	−54.72
327.512−0.728	238.74	−54.59
327.526−0.843	238.89	−54.67

continued on next page

Name of *Spitzer*-dark and *Herschel*-dark Region	Right Ascension 2000.0 (°)	Declination 2000.0 (°)
327.529+0.643	237.29	−53.52
327.544−0.806	238.87	−54.63
327.551−0.835	238.91	−54.65
327.576−0.404	238.47	−54.30
327.595−0.333	238.42	−54.24
327.597−0.651	238.77	−54.48
327.604−0.633	238.76	−54.46
327.623−0.385	238.51	−54.26
327.648−0.336	238.49	−54.21
327.655−0.391	238.56	−54.24
327.658+0.798	237.30	−53.32
327.667−0.351	238.54	−54.20
327.667−0.828	239.06	−54.57
327.691−0.343	238.56	−54.18
327.703−0.551	238.80	−54.34
327.705−0.558	238.81	−54.34
327.707−0.466	238.71	−54.27
327.707+0.894	237.26	−53.21
327.718+0.896	237.27	−53.20
327.721+0.606	237.58	−53.43
327.725−0.520	238.80	−54.30
327.729−0.443	238.72	−54.24
327.730−0.419	238.69	−54.22
327.731+0.536	237.67	−53.48
327.733−0.686	238.99	−54.42
327.733+0.592	237.61	−53.43
327.736−0.366	238.64	−54.17
327.742−0.662	238.97	−54.40
327.746+0.545	237.68	−53.46
327.748+0.056	238.20	−53.84
327.758−0.717	239.06	−54.43
327.760+0.515	237.73	−53.47
327.768−0.344	238.66	−54.14
327.777−0.009	238.31	−53.87
327.779−0.578	238.93	−54.31
327.779−0.603	238.96	−54.33
327.788−0.646	239.02	−54.35
327.799−0.268	238.62	−54.06
327.803−0.460	238.83	−54.20
327.803−0.755	239.16	−54.43
327.803+0.076	238.25	−53.79
327.813−0.321	238.69	−54.09
327.816−0.692	239.10	−54.37
327.820−0.270	238.65	−54.04
327.835−0.617	239.05	−54.30
327.840−0.561	238.99	−54.26
327.843−0.549	238.98	−54.24
327.890−0.611	239.11	−54.26
327.892−0.805	239.33	−54.41
327.893−0.392	238.88	−54.09
327.894+0.455	237.97	−53.44

continued on next page

Name of *Spitzer*-dark and *Herschel*-dark Region	Right Ascension 2000.0 (°)	Declination 2000.0 (°)
327.896+0.585	237.83	−53.33
327.917−0.155	238.65	−53.89
327.919−0.650	239.19	−54.27
327.927−0.196	238.71	−53.92
327.939+0.022	238.49	−53.74
327.943−0.038	238.56	−53.79
327.953−0.109	238.65	−53.84
327.954+0.374	238.13	−53.46
327.977−0.071	238.64	−53.79
327.978−0.170	238.75	−53.87
327.981+0.510	238.02	−53.34
327.984−0.108	238.69	−53.82
327.997+0.377	238.18	−53.43
328.004+0.528	238.03	−53.31
328.008−0.640	239.30	−54.21
328.017−0.101	238.72	−53.79
328.021+0.547	238.03	−53.29
328.058+0.362	238.28	−53.41
328.061−0.054	238.73	−53.72
328.061−0.275	238.97	−53.89
328.065+0.347	238.30	−53.41
328.068−0.028	238.71	−53.70
328.072−0.319	239.03	−53.92
328.078−0.594	239.34	−54.13
328.091+0.529	238.14	−53.26
328.107−0.563	239.34	−54.09
328.109+0.002	238.73	−53.65
328.110+0.503	238.20	−53.26
328.118−0.565	239.36	−54.08
328.119−0.008	238.75	−53.65
328.124+0.606	238.10	−53.17
328.131+0.015	238.74	−53.63
328.136−0.051	238.82	−53.67
328.136+0.613	238.11	−53.16
328.141−0.433	239.24	−53.96
328.147+0.587	238.15	−53.17
328.152+0.016	238.77	−53.61
328.156−0.674	239.53	−54.14
328.158+0.567	238.19	−53.18
328.158+0.619	238.13	−53.14
328.161+0.309	238.47	−53.38
328.177−0.316	239.16	−53.85
328.177+0.625	238.15	−53.13
328.190−0.514	239.40	−53.99
328.197+0.285	238.54	−53.38
328.198+0.295	238.53	−53.37
328.199−0.588	239.49	−54.05
328.203−0.461	239.36	−53.95
328.214−0.358	239.26	−53.86
328.214−0.578	239.50	−54.03
328.219−0.374	239.28	−53.87

continued on next page

Name of *Spitzer*-dark and *Herschel*-dark Region	Right Ascension 2000.0 (°)	Declination 2000.0 (°)
328.224−0.691	239.64	−54.11
328.228+0.265	238.60	−53.37
328.230+0.256	238.61	−53.38
328.245+0.248	238.64	−53.37
328.268−0.296	239.26	−53.78
328.268+0.517	238.39	−53.15
328.276−0.274	239.25	−53.76
328.277−0.551	239.55	−53.97
328.293−0.416	239.42	−53.85
328.298−0.317	239.32	−53.77
328.301−0.611	239.65	−54.00
328.307+0.408	238.55	−53.21
328.312−0.527	239.57	−53.93
328.314−0.413	239.45	−53.84
328.323−0.527	239.58	−53.92
328.325−0.406	239.45	−53.82
328.328+0.455	238.53	−53.16
328.332−0.530	239.60	−53.91
328.334−0.523	239.59	−53.91
328.348−0.458	239.54	−53.85
328.371−0.534	239.65	−53.89
328.387−0.564	239.71	−53.90
328.420+0.091	239.04	−53.38
328.426+0.061	239.07	−53.40
328.448−0.329	239.53	−53.69
328.507+0.417	238.80	−53.08
328.545+0.274	239.00	−53.16
328.553−0.517	239.87	−53.76
328.561−0.517	239.88	−53.76
328.566+0.270	239.03	−53.15
328.573−0.502	239.88	−53.74
328.573−0.507	239.88	−53.74
328.576−0.483	239.86	−53.72
328.584−0.513	239.90	−53.74
328.590+0.269	239.06	−53.14
328.592−0.540	239.94	−53.75
328.597−0.126	239.50	−53.44
328.656−0.359	239.83	−53.57
328.728+0.398	239.10	−52.95
328.739+0.389	239.12	−52.95
328.755+0.714	238.80	−52.69
328.798+0.625	238.95	−52.73
328.818−0.109	239.76	−53.28
328.828+0.674	238.93	−52.67
328.833−0.545	240.26	−53.60
328.834+0.755	238.86	−52.61
328.850−0.556	240.29	−53.60
328.867−0.568	240.33	−53.59
328.871+0.248	239.44	−52.97
328.894−0.595	240.39	−53.60
328.920−0.560	240.39	−53.55

continued on next page

Name of *Spitzer*-dark and *Herschel*-dark Region	Right Ascension 2000.0 (°)	Declination 2000.0 (°)
328.925+0.346	239.40	−52.86
328.930+0.290	239.47	−52.90
328.935−0.126	239.93	−53.22
328.938+0.215	239.56	−52.95
328.946−0.591	240.45	−53.56
328.948+0.711	239.05	−52.57
328.984+0.560	239.25	−52.66
328.990−0.438	240.34	−53.42
329.012+0.720	239.12	−52.52
329.048−0.132	240.08	−53.15
329.053+0.358	239.55	−52.77
329.054+0.949	238.93	−52.32
329.054+0.967	238.91	−52.30
329.068−0.301	240.29	−53.26
329.093−0.316	240.33	−53.26
329.098−0.281	240.30	−53.23
329.117−0.277	240.32	−53.21
329.122−0.492	240.57	−53.37
329.161−0.365	240.47	−53.25
329.168−0.360	240.48	−53.24
329.174−0.316	240.44	−53.20
329.186−0.317	240.45	−53.20
329.204−0.587	240.77	−53.39
329.214−0.236	240.40	−53.12
329.215+0.301	239.82	−52.71
329.229−0.736	240.97	−53.48
329.230−0.428	240.63	−53.25
329.257−0.745	241.02	−53.47
329.260−0.314	240.54	−53.14
329.268+0.130	240.07	−52.80
329.271+0.070	240.14	−52.85
329.283−0.389	240.65	−53.19
329.309+0.122	240.13	−52.78
329.323−0.540	240.87	−53.27
329.334−0.546	240.89	−53.27
329.354−0.540	240.91	−53.25
329.361+0.151	240.16	−52.73
329.368−0.437	240.81	−53.17
329.387−0.066	240.43	−52.87
329.401−0.298	240.70	−53.04
329.407−0.194	240.60	−52.96
329.409−0.298	240.71	−53.03
329.414−0.757	241.23	−53.38
329.423−0.185	240.61	−52.94
329.427+0.151	240.25	−52.68
329.441+0.830	239.54	−52.16
329.452+0.118	240.31	−52.69
329.453−0.161	240.62	−52.90
329.472+0.156	240.30	−52.65
329.472+0.873	239.53	−52.11
329.474+0.235	240.21	−52.59

continued on next page

Name of *Spitzer*-dark and *Herschel*-dark Region	Right Ascension 2000.0 (°)	Declination 2000.0 (°)
329.474+0.261	240.19	−52.57
329.486+0.208	240.26	−52.60
329.492+0.221	240.25	−52.59
329.513+0.210	240.29	−52.58
329.528+0.727	239.75	−52.18
329.533+0.240	240.28	−52.55
329.551+0.717	239.79	−52.17
329.555+0.696	239.82	−52.19
329.573+0.071	240.51	−52.65
329.592+0.239	240.36	−52.51
329.602+0.279	240.32	−52.47
329.603−0.418	241.09	−53.00
329.603+0.105	240.51	−52.60
329.605+0.975	239.59	−51.94
329.607+0.037	240.59	−52.65
329.615−0.400	241.08	−52.97
329.635+0.846	239.76	−52.02
329.638+0.947	239.66	−51.94
329.639−0.449	241.16	−53.00
329.662−0.489	241.24	−53.01
329.662+0.085	240.61	−52.58
329.688−0.073	240.81	−52.68
329.692−0.341	241.11	−52.88
329.711−0.338	241.13	−52.86
329.717+0.785	239.93	−52.01
329.817+0.143	240.74	−52.43
329.864+0.106	240.83	−52.43
329.866−0.758	241.79	−53.07
329.888+0.433	240.51	−52.17
329.938+0.965	240.01	−51.73
329.949−0.020	241.08	−52.47
329.964+0.962	240.04	−51.72
329.985+0.926	240.11	−51.73

Bibliography

Ade P. A. R., Pisano G., Tucker C., Weaver S., 2006, in Presented at the Society of Photo-Optical Instrumentation Engineers (SPIE) Conference, Vol. 6275, Society of Photo-Optical Instrumentation Engineers (SPIE) Conference Series

Agnese P., Buzzi C., Rey P., Rodriguez L., Tissot J.-L., 1999, in Presented at the Society of Photo-Optical Instrumentation Engineers (SPIE) Conference, Vol. 3698, B. F. Andresen & M. Strojnik Scholl , ed, Society of Photo-Optical Instrumentation Engineers (SPIE) Conference Series, p. 284

Agnese P., Cigna C., Pornin J.-L., Accomo R., Bonnin C., Colombel N., Delcourt M., Doumayrou E., Lepennec J., Martignac J., Reveret V., Rodriguez L., Vigroux L. G., 2003, in Presented at the Society of Photo-Optical Instrumentation Engineers (SPIE) Conference, Vol. 4855, T. G. Phillips & J. Zmuidzinas , ed, Society of Photo-Optical Instrumentation Engineers (SPIE) Conference Series, p. 108

Altenhoff W., Mezger P., Wendker H., Weserhout G., 1960, Veroff. Sternwarte, Bonn, 59, 48

Alves J., Lombardi M., Lada C. J., The mass function of dense molecular cores and the origin of the IMF, 2007, A&A, 462, L17

André P., Belloche A., Motte F., Peretto N., The initial conditions of star formation in the Ophiuchus main cloud: Kinematics of the protocluster condensations, 2007, A&A, 472, 519

Arthur S. J., Hoare M. G., Hydrodynamics of Cometary Compact H II Regions, 2006, ApJS, 165, 283

Baes M., Piasecki S., 2007, in IAU Symposium, Vol. 238, V. Karas & G. Matt , ed, IAU Symposium, p. 321

Baes M., Stamatellos J. I., D. Davies, Whitworth A., Sabtini S., Roberts S., Linder S. M., Evans R., 2005, NEWA, 10, 523

Battersby C., Bally J., Ginsburg A., Bernard J. ., Brunt C., Fuller G. A., Martin P., Molinari S., Mottram J., Peretto N., Testi L., Thompson M. A., Characterizing Precursors to Stellar Clusters with Herschel, 2011, ArXiv e-prints

Battersby C., Bally J., Jackson J. M., Ginsburg A., Shirley Y. L., Schlingman W., Glenn J., 2010, ApJ, 721, 222

Baumgardt H., Klessen R. S., The role of stellar collisions for the formation of massive stars, 2011, MNRAS, 413, 1810

Beaulieu J.-P., Tinetti G., Kipping D. M., Ribas I., Barber R. J., Cho J. Y.-K., Polichtchouk I., Tennyson J., Yurchenko S. N., Griffith C. A., Batista V., Waldmann I., Miller S., Carey S., Mousis O., Fossey S. J., Aylward A., Methane in the Atmosphere of the Transiting Hot Neptune GJ436B?, 2011, ApJ, 731, 16

Beichmann C., Neugebauer G., Habling H., Clegg P., Chester T., 1988, IRAS Catalogs & Atlases: Explanatory Supplement. Washington DC:GPO

Belgacem M., Ravera L., Caux E., Cais P., Cros A., 2003, New Astronomy, 9, 483

Benjamin R., Churchwell E., Babler B. L., Bania T. M., Clemens D. P., Cohen M., Dickey J. M., Indebetouw R., Jackson J. M., Kobulnicky H. A., Lazarian A., Marston A. P., Mathis J. S., Meade M. R., Seager S., Stolovy S. R., Watson C., Whitney B. A., Wolff M. J., Wolfire M. G., 2003, PASP, 113, 953

Benjamin R. A., Churchwell E., Haffner M., GLIMPSE team , 2006, in Bulletin of the American Astronomical Society, Vol. 38, American Astronomical Society Meeting Abstracts, p. 242.05

Bertout C., Genova F., A kinematic study of the Taurus-Auriga T association, 2006, A&A, 460, 499

Beuther H., Churchwell E., McKee C., Tan J., 2006, Protostars and Planets V. in press

Bisbas T. G., Wünsch R., Whitworth A. P., Hubber D. A., Walch S., Radiation-driven Implosion and Triggered Star Formation, 2011, ApJ, 736, 142

Bjorkman J. E., Wood K., Radiative Equilibrium and Temperature Correction in Monte Carlo Radiation Transfer, 2001, ApJ, 554, 615

Blaauw A., 1991, in NATO ASI Ser, Vol. 342, C.J. L., D. K. N., ed, The Physics of Star Fromation and Early Stellar Evolution, p. 125

Black J. H., 1994, in Astronomical Society of the Pacific Conference Series, Vol. 58, Cutri R. M., Latter W. B., ed, The First Symposium on the Infrared Cirrus and Diffuse Interstellar Clouds, p. 355

Blake G. A., Sutton E. C., Masson C. R., Phillips T. G., Molecular abundances in OMC-1 - The chemical composition of interstellar molecular clouds and the influence of massive star formation, 1987, ApJ, 315, 621

Bodenheimer P., Tenorio-Tagle G., Yorke H. W., The gas dynamics of H II regions. II - Two-dimensional axisymmetric calculations, 1979, ApJ, 233, 85

Boltzmann L., Ableitung des Stefan'schen Gesetzes, betreffend die Abhngigkeit der Warmestrahlung von der Temperatur aus der electromagnetischen Lichttheorie, 1884, Annalen der Physik und Chemie, 22, 291

Bonnell I. A., Bate M. R., Clarke C. J., Pringle J. E., Accretion and the stellar mass spectrum in small clusters, 1997, MNRAS, 285, 201

Bonnell I. A., Bate M. R., Zinnecker H., On the formation of massive stars, 1998, MNRAS, 298, 93

Bonnell I. A., Clarke C. J., Bate M. R., Pringle J. E., Accretion in stellar clusters and the initial mass function, 2001, MNRAS, 324, 573

Brand J., Blitz L., 1993, A&A, 257, 67

Butler M. J., Tan J., 2009, ApJ, 696, 484

Campbell B., VLA observations of collimated outflow at NGC 7538 IRS 1, 1984, ApJ, 282, L27

Carey S., Clark F., Egan M., Price S., Shipman R., Kuchar T., 1998, ApJ, 508, 721

Carey S., Feldman P., Redman R., Egan M., MacLeod J., Price S., 2000, ApJ, 543, 157

Carey S., Noriega Crespo A., Mizuno D. R., Shenoy S., Paladini R., Kraemer K. E., Price S. D., Flagey N., Ryan E., Ingalls J. G., Kuchar T. A., Pinheiro Goncalves D., Indebetouw R., Billot N., et al. , 2009, PASP, 121, 76

Carral P., Kurtz S. E., Rodrguez L. F., Pree C. D., Hofner P., 1997, ApJL, 486, L103

Carroll B. W., Ostlie D. A., 1996, An Introduction to Modern Astrophysics. Addison-Wesley Publishing Company

Cesaroni R., 2005, IAUS, 227, 59

Cesaroni R., Beltrán M. T., Zhang Q., Beuther H., Fallscheer C., Dissecting a hot molecular core: the case of G31.41+0.31, 2011, A&A, 533, A73

Cesaroni R., Churchwell E., Hofner P., Walmsley C. M., Kurtz S., Hot ammonia towards compact HII regions, 1994, A&A, 288, 903

Cesaroni R., Felli M., Testi L., Walmsley C. M., Olmi L., The disk-outflow system around the high-mass (proto)star IRAS 20126+4104., 1997, A&A, 325, 725

Cesaroni R., Felli M., Walmsley C. M., High density molecular clumps around protostellar candidates., 1999, A&AS, 136, 333

Cesaroni R., Walmsley C. M., Köempe C., Churchwell E., 1991, A&A, 252, 278

Chambers E., Jackson M., Rathborne J., Simon R., 2009, ApJS, 181, 360

Charles L. C., Michel F., ed, 2002, Charles L. C., Michel F., ed, SFChem 2002: Chemistry as a Diagnostic of Star Formation. NRC Press, Ottawa, Canada

Chattopadhyay G., Glenn J., Bock J., Rownd B. K., Caldwell M., Griffin M., 2003, IEEE Transactions on Microwave Theory and Techniques, 51

Cherednichenko S., Drakinsky V., Berg D., 2005, in Proc. Europ. Microwave Assoc., Vol. 1, THz HEB heterodyne recievers for space and ground based radio astronomy, p. 3

Cherednichenko S., Kroug M., Khosropanah P., Adam A., Merkel H., Kollberg E., Loudkov D., Voronov G., Gol'tsman H.-W., Richter H., 2002, Physica C, 372, 427

Chomiuk L., Povich M. S., Toward a Unification of Star Formation Rate Determinations in the Milky Way and Other Galaxies, 2011, AJ, 142, 197

Churchwell E., 1999, in Lada C., Kylafis N., ed, In the Origin of Stars and Planets. Kluwer: Dordrecht, The Netherlands

Churchwell E., 2002, ARA&A, 40, 27

Churchwell E., Felli M., Mezger P. G., A Search at 15 GHz for Compact H II Regions in Regions of Possible Star Formation, 1969, Astrophys. Lett., 4, 33

Crespin A., Lebonnois S., Hourdin F., Eymet V., Fournier R., Forget F., 2006, in Bulletin of the American Astronomical Society, Vol. 38, AAS/Division for Planetary Sciences Meeting Abstracts #38, p. 515

Cunningham C. R., Gear W. K., Duncan W. D., Hastings P. R., Holland W. S., 1994, in Society of Photo-Optical Instrumentation Engineers (SPIE) Conference Series, Vol. 2198, D. L. Crawford & E. R. Craine , ed, Society of Photo-Optical Instrumentation Engineers (SPIE) Conference Series, p. 638

Cyganowski C. J., Whitney B. A., Holden E., Braden E., Brogan C. L., Churchwell E., Indebetouw R., Watson D. F., Babler B. L., Benjamin R., Gomez M., Meade M. R., Povich M. S., Robitaille T. P., Watson C., A Catalog of Extended Green Objects in the GLIMPSE Survey: A New Sample of Massive Young Stellar Object Outflow Candidates, 2008, AJ, 136, 2391

Dale J. E., Bonnell I. A., Whitworth A. P., Ionization-induced star formation - I. The collect-and-collapse model, 2007, MNRAS, 375, 1291

Dame T. M., Ungerechts H., Cohen R. S., de Geus E. J., Grenier I. A., May J., Murphy D. C., Nyman L., Thaddeus P., A Composite CO Survey of the Entire Milky Way, 1987, APJ, 322

De Buizer J. M., Radomski J. T., Telesco C. M., Piña R. K., A Search for Mid-Infrared Emission from Hot Molecular Core Candidates, 2003, ApJ, 598, 1127

De Buizer J. M., Vacca W., Direct Spectroscopic Identification of the Origin of 'Green Fuzzy' Emission in Star Formation Regions, 2010, A&A, 140, 196

De Buizer J. M., Watson A. M., Radomski J. T., Piña R. K., Telesco C. M., Mid-Infrared Detection of a Hot Molecular Core in G29.96-0.02, 2002, ApJ, 564, L101

de Graauw T. et al., The Herschel-Heterodyne Instrument for the Far-Infrared (HIFI), 2010, AAP, 518, L6

de la Fuente E., Kurtz S. E., Rodriguez-Rico C. A., Trinidad M. A., Araya E., Kemp S., Porras A., Hofner P., Franco J., 2010, in IAU Symposium, Vol. 262, G. Bruzual & S. Charlot , ed, IAU Symposium, p. 319

de Pree C., Wilner D., Deblasio J., Mercer A., Davis L., 2005, ApJ, 624, 101

de Pree C. G., Goss W. M., Gaume R. A., Ionized Gas in Sagittarius B2 Main on Scales of 0.065 Arcsecond (600 AU), 1998, ApJ, 500, 847

de Pree C. G., Rodriguez L. F., Goss W. M., 1995, RMxAA, 31, 39

de Vicente P., Martín-Pintado J., Neri R., Rodríguez-Franco A., On the Heating Source of the Orion KL Hot Core, 2002, ApJ, 574, L163

Deharveng L., Zavagno A., Schuller F., Caplan J., Pomarès M., De Breuck C., Star formation around RCW 120, the perfect bubble, 2009, A&A, 496, 177

Delorme Y., Salez M., Lecomt B., Peron I., Dauplay F., Feret A., Spatazza J., Krieg J.-M., Schuster K., 2005, Int.Symp. on Space THz Technology, 16

Desai K. M., Chu Y.-H., Gruendl R. A., Dluger W., Katz M., Wong T., Chen C.-H. R., Looney L. W., Hughes A., Muller E., Ott J., Pineda J. L., Supernova Remnants and Star Formation in the Large Magellanic Cloud, 2010, AJ, 140, 584

Dessart L., Hillier D. J., Synthetic line and continuum linear-polarization signatures of axisymmetric Type II supernova ejecta, 2011, MNRAS, 415, 3497

Devine K. E., Chandler C. J., Brogan C., Churchwell E., Indebetouw R., Shirley Y., Borg K. J., Very Large Array Observations of the Infrared Dark Cloud G19.30+0.07, 2011, ApJ, 733, 44

Di Francesco J., Evans II N. J., Caselli P., Myers P., Shirley Y., Aikawa A., Tafalla M., An Observational Perspective of Low-Mass Dense Cores I: Internal Physical and Chemical Properties, 2007, Protostars and Planets V

Dobbs C. L., Bonnell I. A., Clark P. C., Centrally condensed turbulent cores: massive stars or fragmentation?, 2005, MNRAS, 360, 2

Dohlen K., Origne A., Pouliquen D., Swinyard B. M., 2000, in Presented at the Society of Photo-Optical Instrumentation Engineers (SPIE) Conference, Vol. 4013, J. B. Breckinridge & P. Jakobsen , ed, Society of Photo-Optical Instrumentation Engineers (SPIE) Conference Series, p. 119

Dopita M. A., Fischera J., Crowley O., Sutherland R. S., Christiansen J., Tuffs R. J., Popescu C. C., Groves B. A., Kewley L. J., Compact h ii regions: What lies within?, 2006, ApJ, 639, 788

Drimmel R., Evidence for a two-armed spiral in the Milky Way, 2000, A&A, 358, L13

Drimmel R., Spergel D., 2001, ApJ, 556, L181

Duband L., Clerc L., Ercolani E., Guillemet L., Vallcorba R., Herschel Flight Models Sorption Coolers, 2008, Cryogenics, 48, 95

Dyson J. E., Williams R. J. R., Redman M. P., Clumpy Ultra Compact HII Regions - Part One - Fully Supersonic Wind-Blown Models, 1995, MNRAS, 277, 700

Egan M., Shipman R., Price S., Carey S., Clark F., Cohen M., 1998, ApJ, 494, 199

Elmegreen B. G., 1998, in ASP Conf. Ser., Vol. 83, Woodward C. E., Shull J. M., Thronson H. A., ed, The Origin of Stars and Planetary Systems, p. 148

Elmegreen B. G., Lada C. J., Sequential formation of subgroups in OB associations, 1977, ApJ, 214, 725

Ercolano B., Barlow M. J., Storey P. J., Liu X.-W., MOCASSIN: a fully three-dimensional Monte Carlo photoionization code, 2003, MNRAS, 340, 1136

Evans N. J., II, Rawlings J. M. C., Shirley Y. L., Mundy L. G., 2001, ApJ, 557, 193

Favre C., Despois D., Brouillet N., Baudry A., Combes F., Guélin M., Wootten A., Wlodarczak G., $HCOOCH_3$ as a probe of temperature and structure in Orion-KL, 2011, A&A, 532, A32

Forster J. R., Caswell J. L., Okumura S. K., Ishiguro M., Hasegawa T., Molecules and masers near compact H II regions, 1990, A&A, 231, 473

Furuya R. S., Cesaroni R., Shinnaga H., Infall, outflow, and rotation in the G19.61-0.23 hot molecular core, 2011, A&A, 525, A72

Garay G., Faúndez S., Mardones D., Bronfman L., Chini R., Nyman L., Discovery of Four New Massive and Dense Cold Cores, 2004, ApJ, 610, 313

Garay G., Lizano S., Massive Stars: Their Environment and Formation, 1999, PASP, 111, 1049

Garay G., Rodriguez L., Moran J., Churchwell E., 1993, ApJ, 418, 368

Garnett D., Kennicutt R., 2004, ApJL, 607, L21

Gaume R., Claussen M., de Pree C., Goss W., Mehringer D., 1995, ApJ, 449, 663

Glauser A. M., Ménard F., Pinte C., Duchêne G., Güdel M., Monin J.-L., Padgett D. L., Multiwavelength studies of the gas and dust disc of IRAS 04158+2805, 2008, A&A, 485, 531

Gomez Y., Garay G., Lizano S., Warm Molecular Gas Associated with Cometary H II Regions, 1995, ApJ, 453, 727

Goodwin S. P., Nutter D., Kroupa P., Ward-Thompson D., Whitworth A. P., The relationship between the prestellar core mass function and the stellar initial mass function, 2008, A&A, 477, 823

Gratiy S., 2009, Ph.D. thesis, The Pennsylvania State University

Griffin M. J., 1999, Nuclear Instruments and Methods in Physics Research A, 444, 397

Griffin M. J., Abergel A., Ade P., André P., Baluteau J., Bock J., Franceschini A., Gear W., Glenn J., Lellouch E., Naylor D., Olofsson G., Perez Fournon I., Rowan Robinson M., Saraceno P., Smith A., Swinyard B., Vigroux L., Wright G., 2010, A&A, 518, L3

Griffin M. J., Bock J. J., Gear W. K., Relative performance of filled and feedhorn-coupled focal-plane architectures, 2002, Appl. Opt., 41, 6543

Gunther C., Guillet B., Kouadio F., Routoure J.-M., Mechin L., 2009, in VIII Semetro

Güver T., Özel F., The relation between optical extinction and hydrogen column density in the Galaxy, 2009, MNRAS, 2050

Habing H., 1968, Bull. Astron. Inst. Neth., 19, 421

Hadhazy A., 2010, Spitzer spies a 'flying dragon' smoldering with secret star birth

Hatcher L., 1994, A step-by-step approach to using SAS for factor analysis and structural equation modelling. SAS Institute Inc.

Henning T., Michel B., Stognienko R., 1995, Planet Space Sci., 43, 1333

Henyey L. G., Greenstein J. L., Diffuse radiation in the Galaxy, 1941, ApJ, 93, 70

Herschel W., A: Investigation of the Powers of the Prismatic Colours to Heat and Illuminate Objects; With Remarks, That Prove the Different Refrangibility of Radiant Heat. to Which is Added, an Inquiry into the Method of Viewing the Sun Advantageously, with Telescopes of Large Apertures and High Magnifying Powers. by William Herschel, LL. D. F. R. S., 1800a, Royal Society of London Philosophical Transactions Series I, 90, 255

Herschel W., B: Experiments on the Refrangibility of the Invisible Rays of the Sun. by William Herschel, LL. D. F. R. S., 1800b, Royal Society of London Philosophical Transactions Series I, 90, 284

Herschel Observer's Manual , 2011, Herschel Consortium, HERSCHEL-DOC-0876, Version 4.0

HIFI Observer's Manual , 2011, HIFI Consortium, HERSCHEL-DOC-0784, Version 2.4

Hildebrand R., 1983, QJRAS, 24, 267

Ho P. T. P., Haschick A. D., Molecular clouds associated with compact H II regions. III - Spin-up and collapse in the core of G10.6 - 0.4, 1986, ApJ, 304, 501

Hoare M. G., Kurtz S. E., Lizano S., Keto E., Hofner P., Ultracompact Hii Regions and the Early Lives of Massive Stars, 2007, Protostars and Planets V, 181

Hollenbach D., Johnstone D., Lizano S., Shu F., 1994, ApJ, 428, 654

Hughes A. M., Andrews S. M., Wilner D. J., Meyer M. R., Carpenter J. M., Qi C., Hales A. S., Casassus S., Hogerheijde M. R., Mamajek E. E., Wolf S., Henning T., Silverstone M. D., Structure and Composition of Two Transitional Circumstellar Disks in Corona Australis, 2010, AJ, 140, 887

Hunter T. R., Testi L., Zhang Q., Sridharan T. K., Molecular Jets and H_2O Masers in the AFGL 5142 Hot Core, 1999, AJ, 118, 477

Indebetouw R., Mathis J. S., Babler B. L., Meade M. R., Watson C., Whitney B. A., Wolff M., Wolfire M. G., Cohen M., T. M. Bania T. M., Benjamin R. A., Clemens D. P., Dickey J. M., Jackson J. M., Kobulnicky H. A., Marston A. P., Mercer E. P., Stauffer J. R., Stolovy S. R., E. C., 2005, ApJ, 619, 931

Jackson B. D., de Lange G., Zijlstra T., Kroug M., Kooi J. W., Stern J. A., Klapwijk T. M., 2006, IEEE Trans. on Microwave Theory and Techniques, 54, 547

Jackson B. D., de Lange G., Zijlstra T., Kroug M., Stern J. A., Klapwijk T. M., 2005, Journal of Applied Physics, 97, 113904

Jackson J., Finn S., Rathborne J., Chambers E., Simon R., 2008, ApJ, 680, 349

Jiménez-Serra I., Caselli P., Tan J. C., Hernandez A. K., Fontani F., Butler M. J., van Loo S., Parsec-scale SiO emission in an infrared dark cloud, 2010, MNRAS, 406, 187

Joliffe I. T., 1986, Principle Component Analysis. New York: Springer-Verlag

Jørgensen J. K., Johnstone D., van Dishoeck E. F., Doty S. D., The effect of a strong external radiation field on protostellar envelopes in Orion, 2006, A&A, 449, 609

Kaper L., Ellerbroek L. E., Ochsendorf B. B., Caballero Pouroutidou R. N., Studying the formation of massive stars with VLT/X-shooter, 2011, Astronomische Nachrichten, 332, 232

Kasen D., Thomas R. C., Röpke F., Woosley S. E., Multidimensional radiative transfer calculations of the light curves and spectra of Type Ia supernovae, 2008, Journal of Physics Conference Series, 125, 012007

Kaufman M. J., Hollenbach D. J., Tielens A. G. G. M., High-Temperature Molecular Cores near Massive Stars and Application to the Orion Hot Core, 1998, ApJ, 497, 276

Kerr F. J., Lynden-Bell D., Review of galactic constants, 1986, MNRAS, 221, 1023

Kessler M. F., Metcalfe L., Salama A., The Infrared Space Observatory (ISO), 1992, Space Sci. Rev., 61, 45

Keto E., 2002, ApJ, 568, 753

Keto E., 2003, ApJ, 599, 1196

Kim K.-T., Koo B.-C., Radio continuum and recombination line study of ultracompact h ii regions with extended envelopes, 2001, The Astrophysical Journal, 549, 979

Kirk J., Ward-Thompson D., Andre P., 2005, MNRAS, 360, 1506

Kirk J. M. et al., 2010, A&A, 518, L82

Kraft S., Frenzl O., Charlier O., Cronje T., Katterloher R. O., Rosenthal D., Groezinger U., Beeman J. W., 2000, in Presented at the Society of Photo-Optical Instrumentation Engineers (SPIE) Conference, Vol. 4013, J. B. Breckinridge & P. Jakobsen , ed, Society of Photo-Optical Instrumentation Engineers (SPIE) Conference Series, p. 233

Kraft S., Merken P., Creten Y., Putzeys J., Van Hoof C. A., Katterloher R. O., Rosenthal D., Rumitz M., Groezinger U., Hofferbert R., Beeman J. W., 2001, in Presented at the Society of Photo-Optical Instrumentation Engineers (SPIE) Conference, Vol. 4540, H. Fujisada, J. B. Lurie, & K. Weber , ed, Society of Photo-Optical Instrumentation Engineers (SPIE) Conference Series, p. 374

Krumholz M., Matzner C., McKee C., 2006, ApJ, 653, 361

Krumholz M. R., Klein R. I., McKee C. F., Radiation-Hydrodynamic Simulations of Collapse and Fragmentation in Massive Protostellar Cores, 2007, ApJ, 656, 959

Krumholz M. R., Matzner C. D., McKee C. F., The Global Evolution of Giant Molecular Clouds. I. Model Formulation and Quasi-Equilibrium Behavior, 2006, ApJ, 653, 361

Krumholz M. R., McKee C. F., Klein R. I., 2007, Nature, 438, 332

Kurtz S., 2002, ASPC, 267, 81

Kurtz S., 2005, IAUS, 227, 111

Kurtz S., Cesaroni R., Churchwell E., Hofner P., Walmsley C. M., Hot Molecular Cores and the Earliest Phases of High-Mass Star Formation, 2000, Protostars and Planets IV, 299

Kurtz S., Churchwell E., Wood D. O. S., Ultracompact H II regions. 2: New high-resolution radio images, 1994, ApJS, 91, 659

Larson R., 1981, MNRAS, 194, 809

Lefevre J., Bergeat J., Daniel J.-Y., Numerical simulation of radiative transfer in circumstellar dust shells. I - Spherical shells, 1982, A&A, 114, 341

Lefevre J., Daniel J.-Y., Bergeat J., Numerical simulation of radiative transfer in circumstellar dust shells. II - Ellipsoidal shells, 1983, A&A, 121, 51

Li D., Goldsmith P. F., Menten K., Massive Quiescent Cores in Orion. I. Temperature Structure, 2003, ApJ, 587, 262

Lizano S., Canto J., Garay G., Hollenbach D., Photoevaporated Flows from H II Regions, 1996, ApJ, 468, 739

Longdon N., ed, 1984, ESA Special Publication, Vol. 1070, European Space Science : Horizon 2000

Lucy L. B., Computing radiative equilibria with Monte Carlo techniques, 1999, A&A, 344, 282

Lugo J., Lizano S., Garay G., 2004, ApJ, 614, 807

Lumsden S. L., Hoare M. G., Oudmaijer R. D., Richards D., The population of the Galactic plane as seen by MSX, 2002, MNRAS, 336, 621

Lupton R., 1993, Statistics in Theory and Practice. Princeton University Press, Princeton

Mac Low M.-M., van Buren D., Wood D. O. S., Churchwell E., Bow shock models of ultracompact H II regions, 1991, ApJ, 369, 395

Maccone C., 2002, Acta Astronautica, 5, 185

Markwardt C., 2008, in ASP Conference Series, Vol. 411, Bohlender D., Dowler P., Durand D., ed, Astronomical Data Analysis Software and Systems XVIII, p. 251

Marseille M. G., van der Tak F. F. S., Herpin F., Jacq T., Tracing early evolutionary stages of high-mass star formation with molecular lines, 2010a, A&A, 522, A40

Marseille M. G. et al., Water abundances in high-mass protostellar envelopes: Herschel observations with HIFI, 2010b, A&A, 521, L32

Marshall D. J., Joncas G., Jones A. P., Distribution and Characteristics of Infrared Dark Clouds Using Genetic Forward Modelling, 2009, ApJ, 706, 727

Mathis J. S., Rumpl W., Nordsieck K. H., The size distribution of interstellar grains, 1977, ApJ, 217, 425

Matzner C., 2002, ApJ, 556, 302

McKee C. F., Tan J. C., Massive star formation in 100,000 years from turbulent and pressurized molecular clouds, 2002, Nature, 416, 59

McKee C. F., Tan J. C., The Formation of Massive Stars from Turbulent Cores, 2003, ApJ, 585, 850

McLeod A., Palouš J., Whitworth A., 2011, in IAU Symposium, Vol. 270, Alves J., Elmegreen B. G., Girart J. M., Trimble V., ed, Computational Star Formation, p. 355

Melnick G. J. et al., Herschel observations of EXtra-Ordinary Sources (HEXOS): Observations of H_2O and its isotopologues towards Orion KL, 2010, A&A, 521, L27

Mezger P., Henderson A., 1967, ApJ, 147, 471

Mihos J. C., Richstone D. O., Bothun G. D., Models of star formation in interacting and merging disk galaxies, 1992, ApJ, 400, 153

Millar T. J., Herbst E., Charnley S. B., The formation of oxygen-containing organic molecules in the Orion compact ridge, 1991, ApJ, 369, 147

Mills E., Morris M., Lane H., C.C. ad Dong, Wang Q., Cotera A., Stolovy S. R., Properties of the Compact HII Region Complex G000.02-00.07, 2011, ApJ, 735, 85

Minier V., Ellingsen S. P., Norris R. P., Booth R. S., The protostellar mass limit for 6.7 GHz methanol masers. I. A low-mass YSO survey, 2003, A&A, 403, 1095

Misselt K. A., Gordon K. D., Clayton G. C., Wolff M. J., The DIRTY Model. II. Self-consistent Treatment of Dust Heating and Emission in a Three-dimensional Radiative Transfer Code, 2001, ApJ, 551, 277

Molinari S. et al., 2010a, A&A, 518, L100

Molinari S., Swinyard B., Bally J., Bernard J.-P., Martin P., Moore T., Noriega Crespo A., Plume R., Testi L., Zavagno A., 2010b, PASP, 122, 314

Murakami H. et al., The Infrared Astronomical Mission AKARI, 2007, PASJ, 59, 369

Murray N., Rahman M., Star Formation in Massive Clusters Via the Wilkinson Microwave Anisotropy Probe and the Spitzer Glimpse Survey, 2010, ApJ, 709, 424

Niccolini G., Woitke P., Lopez B., High precision Monte Carlo radiative transfer in dusty media, 2003, A&A, 399, 703

Nummelin A., Bergman P., Hjalmarson Å., Friberg P., Irvine W. M., Millar T. J., Ohishi M., Saito S., A Three-Position Spectral Line Survey of Sagittarius B2 between 218 and 263 GHZ. II. Data Analysis, 2000, ApJS, 128, 213

Nutter D., Kirk J., Stamatellos D., Ward Thompson D., 2008, MNRAS, 384, 775

Nutter D., Ward-Thompson D., Stamatellos D., 2009, in Astronomical Society of the Pacific Conference Series, Vol. 418, T. Onaka, G. J. White, T. Nakagawa, & I. Yamamura , ed, AKARI, a Light to Illuminate the Misty Universe, p. 79

Omont A. et al., ISOGAL: A deep survey of the obscured inner Milky Way with ISO at 7 mu m and 15 mu m and with DENIS in the near-infrared, 2003, A&A, 403, 975

Ormel C. W., Shipman R. F., Ossenkopf V., Helmich F. P., The modelling of infrared dark cloud cores, 2005, A&A, 439, 613

Osorio M., Anglada G., and S. L., D'Alessio P., A Model to Test the Internal Structure of the G31.41+0.31 Hot Molecular Core, 2004, Ap&SS, 292, 369

Osorio M., Lizano S., D'Alessio P., Hot Molecular Cores and the Formation of Massive Stars, 1999, ApJ, 525, 808

Ossenkopf V., Henning T., 1994, A&A, 291, 943

Oster L., 1961, Rev. Mod Phys, 33, 525

Ott S., 2010, in Mizumoto Y., Morita K.-I., Ohishi M., ed, Astronomical Data Analysis Software and Systems XIX, ASP Conference Series

PACS Observer's Manual , 2011, PACS Consortium, HERSCHEL-DOC-0832, Version 2.2

Parsons H., Thompson M. A., Chrysostomou A., 2009, MNRAS, 399, 1506

Pearson K., 1920, Biometrika, 13, 24

Perault M. et al., 1996, A&A, 315, 165

Peretto N., Fuller G. A., 2009, A&A, 505, 405

Peretto N., Fuller G. A., A Statistical Study of the Mass and Density Structure of Infrared Dark Clouds, 2010, ApJ, 723, 555

Peretto N. et al., 2010, A&A, 518, L98

Pilbratt G. L., Riedinger J. R., Passvogel T., Crone G., Doyle D., Gageur U., Heras A. M., Jewell C., Metcalfe L., Ott S. , , Schmidt M., 2010, A&A, 518, L1

Plume R., Jaffe D. T., Evans N. J., II, A survey of CS J = 7 - 6 in regions of massive star formation, 1992, ApJS, 78, 505

Plummer H. C., The distribution of stars in globular clusters, 1915, MNRAS, 76, 107

Poglitsch A., Katterloher R. O., Hoenle R., Beeman J. W., Haller E. E., Richter H., Groezinger U., Haegel N. M., Krabbe A., 2003, in Presented at the Society of Photo-Optical Instrumentation Engineers (SPIE) Conference, Vol. 4855, T. G. Phillips & J. Zmuidzinas , ed, Society of Photo-Optical Instrumentation Engineers (SPIE) Conference Series, p. 115

Poglitsch A. et al., 2010, A&A, 518, L2

Preibisch T., Ossenkopf V., Yorke H. W., Henning T., 1993, A&A, 279, 577

Price S. D., Egan M. P., Carey S. J., Mizuno D. R., Kuchar T. A., Midcourse Space Experiment Survey of the Galactic Plane, 2001, AJ, 121, 2819

Raddick J., Lintott C. J., Schawinski K., Thomas D., Nichol R. C., Andreescu D., Bamford S., Land K. R., Murray P., Slosar A., Szalay A. S., Vandenberg J., Galaxy Zoo Team , 2007, in Bulletin of the American Astronomical Society, Vol. 38, American Astronomical Society Meeting Abstracts, p. 892

Ragan S. E., Bergin E. A., Wilner D., Very Large Array Observations of Ammonia in Infrared-dark Clouds. I. Column Density and Temperature Structure, 2011, ApJ, 736, 163

Rathborne J., Jackson J., Chambers E., Simon R., Shipman R., Frieswijk W., 2005, ApJ, 630, L181

Rathborne J., Jackson J., Simon R., 2006, ApJ, 641, 389

Rathborne J. M., Garay G., Jackson J. M., Longmore S., Zhang Q., Simon R., Hot Molecular Cores in Infrared Dark Clouds, 2011, ApJ, 741, 120

Redman M. P., Williams R. J. R., Dyson J. E., Clumpy ultracompact H II regions. II. Cores, spheres and shells from subsonic flows., 1996, MNRAS, 280, 661

Redman R., Feldman P., Wyrowski F., Cote S., Carey S., Egan M., 2003, ApJ, 586, 1127

Reid M. J., McClintock J. E., Narayan R., Gou L., Remillard R. A., Orosz J. A., The Trigonometric Parallax of Cygnus X-1, 2011, ApJ, 742, 83

Richards P. L., Bolometers for Infrared and Millimeter Waves, 1994, Journal of Applied Physics, 77, 1

Roberts W. W., Large-Scale Shock Formation in Spiral Galaxies and its Implications on Star Formation, 1969, ApJ, 158, 123

Robitaille T. P., Whitney B. A., The Present-Day Star Formation Rate of the Milky Way Determined from Spitzer-Detected Young Stellar Objects, 2010, ApJ, 710, L11

Rolffs R., Schilke P., 2011, in EAS Publications Series, Vol. 52, M. Röllig, R. Simon, V. Ossenkopf, & J. Stutzki , ed, EAS Publications Series, p. 303

Rouncefield M., Holmes P., 1993, Practical Statistics. The Macmillan Pressm Ltd

Rownd B., Bock J. J., Chattopadhyay G., Glenn J., Griffin M. J., 2003, in Presented at the Society of Photo-Optical Instrumentation Engineers (SPIE) Conference, Vol. 4855, T. G. Phillips & J. Zmuidzinas , ed, Society of Photo-Optical Instrumentation Engineers (SPIE) Conference Series, p. 510

Schieder R., Siebertz O., Gal C., Olbrich M., Schloeder F., bieber R., Schmuelling F., Tolls V., Horn J., 2002, SPIE, 4855, 313

Schroder K.-P., Connon Smith R., Distant future of the sun and earth revisited, 2008, MNRAS, 386, 155

Schuller F. et al., ATLASGAL - The APEX telescope large area survey of the galaxy at 870 μm, 2009, A&A, 504, 415

Scoville N. Z., Hersh K., Collisional growth of giant molecular clouds, 1979, ApJ, 229, 578

Sewilo M., Churchwell E., Kurtz S., Goss W., Hofner P., 2004, AAS, 36, 2574

Shannon R. R., Wyant J. C., ed, 1992, Applied Optics and Optical Engineering, Volume XI, Vol. 11

Silberg R. A., 2011, Herschel space observatory: Biggest space telescope

Simoens F., Agnese P., Béguin A., Carcey J., Cigna J.-C., Pornin J.-L., Rey P., Vandeneynde A., Rodriguez L., Boulade O., Lepennec J., Martignac J., Doumayrou E., Reveret V., Vigroux L., 2004, in Presented at the Society of Photo-Optical Instrumentation Engineers (SPIE) Conference, Vol. 5498, C. M. Bradford, P. A. R. Ade, J. E. Aguirre, J. J. Bock, M. Dragovan, L. Duband, L. Earle, J. Glenn, H. Matsuhara, B. J. Naylor, H. T. Nguyen, M. Yun, & J. Zmuidzinas , ed, Society of Photo-Optical Instrumentation Engineers (SPIE) Conference Series, p. 177

Simon R., Jackson J., Rathborne J., Chambers E., 2006a, ApJ, 639, 227

Simon R., Rathborne J., Shah R., Jackson J., Chambers E., 2006b, ApJ, 653, 1325

Smith N., Brooks K. J., A census of the Carina Nebula - II. Energy budget and global properties of the nebulosity, 2007, MNRAS, 379, 1279

SPIRE Observer's Manual , 2011, SPIRE Consortium, HERSCHEL-DOC-0798, Version 2.3

SPIRE PACS Parallel Mode Observer's Manual , 2010, SPIRE & PACS Consortia, HERSCHEL-DOC-0883, Version 2.0

Stamatellos D., 2003, Ph.D. thesis, Cardiff University

Stamatellos D., Griffin M. J., Kirk J. M., Molinari S., Sibthorpe B., Ward-Thompson D., Whitworth A. P., Wilcock L. A., Modelling Herschel observations of infrared-dark clouds in the Hi-GAL survey, 2010, MNRAS, 409, 12

Stamatellos D., Whitworth A., 2003, A&A, 407, 941

Stamatellos D., Whitworth A., 2005, A&A, 439, 159

Stamatellos D., Whitworth A., André P., Ward Thompson D., 2004, A&A, 420, 1009

Stanke T. et al., Hier ist wahrhaftig ein Loch im Himmel. The NGC 1999 dark globule is not a globule, 2010, A&A, 518, L94

Stefan J., Uber die Beziehung zwischen der Wrmestrahlung und der Temperatur, 1879, Sitzungsberichte der mathematisch-naturwissenschaftlichen Classe der kaiserlichen Akademie der Wissenschaften, 79, 391

Strömgren B., The Physical State of Interstellar Hydrogen., 1939, ApJ, 89, 526

Sutton E. C., Peng R., Danchi W. C., Jaminet P. A., Sandell G., Russell A. P. G., The distribution of molecules in the core of OMC-1, 1995, ApJS, 97, 455

Swift J. J., Two Massive, Low-Luminosity Cores Toward Infrared Dark Clouds, 2009, ApJ, 705, 1456

Swinyard B. M., Dohlen K., Ferand D., Baluteau J.-P., Pouliquen D., Dargent P., Michel G., Martignac J., Ade P. A. R., Hargrave P. C., Griffin M. J., Jennings D. E., Caldwell M. E., 2003, in Presented at the Society of Photo-Optical Instrumentation Engineers (SPIE) Conference, Vol. 4850, J. C. Mather , ed, Society of Photo-Optical Instrumentation Engineers (SPIE) Conference Series, p. 698

Tan J. C., McKee C. F., Outflow-Confined HII Regions and the Formation of Massive Stars by Accretion, 2003, ArXiv Astrophysics e-prints

Tatulli E., Benisty M., Ménard F., Varnière P., Martin-Zaïdi C., Thi W.-F., Pinte C., Massi F., Weigelt G., Hofmann K.-H., Petrov R. G., Constraining the structure of the planet-forming region in the disk of the Herbig Be star HD 100546, 2011, A&A, 531, A1

Tenorio-Tagle G., The gas dynamics of H II regions. I - The champagne model, 1979, A&A, 71, 59

Testi L., Sargent A. I., Star Formation in Clusters: A Survey of Compact Millimeter-Wave Sources in the Serpens Core, 1998, ApJ, 508, L91

Teyssier D., Hennebelle P., Perault M., 2002, A&A, 382, 624

Traficante A., Calzoletti L., Veneziani M., Ali B., de Gasperis g., Di giorgio A. M., Faustini f., Ikhenaode D., Molinari S., Natoli P., Pestalozzi M., Pezzuto S., Piacentini F., Piazzo L., Polenta G., Schisano E., 2011, MNRAS, 1373

Turner A. D., Bock J. J., Beeman J. W., Glenn J., Hargrave P. C., Hristov V. V., Nguyen H. T., Rahman F., Sethuraman S., Woodcraft A. L., Silicon nitride Micromesh Bolometer Array for Submillimeter Astrophysics, 2001, Appl. Opt., 40, 4921

van Buren D., Mac Low M.-M., Wood D. O. S., Churchwell E., Cometary compact H II regions are stellar-wind bow shocks, 1990, ApJ, 353, 570

Vasyunina T., Linz H., Henning T., Stecklum B., Klose S., Nyman L.-Å., Physical properties of Southern infrared dark clouds, 2009, A&A, 499, 149

Volk K., 2007, Chopping and Nodding For Infrared Astronomy

Walmsley M., 1995, RmxAC, 1, 137

Walsh A. J., Bertoldi F., Burton M. G., Nikola T., Mid-infrared observations of methanol maser sites and ultracompact H ii regions: signposts of high-mass star formation, 2001, MNRAS, 326, 36

Wang K.-S., Kuan Y.-J., Liu S.-Y., Huang H.-C., Charnley S. B., 2009, in Astronomical Society of the Pacific Conference Series, Vol. 420, K. J. Meech, J. V. Keane, M. J. Mumma, J. L. Siefert, & D. J. Werthimer , ed, Bioastronomy 2007: Molecules, Microbes and Extraterrestrial Life, p. 49

Ward-Thompson D., Andr'e P., 1999, in ESA Special Publication, Vol. 427, P. Cox & M. Kessler , ed, The Universe as Seen by ISO, p. 463

Ward-Thompson D., Andre P., Crutcher R. F., Johnstone D., Onishi T., Wilson C., An Observational Perspective of Low-Mass Dense Cores II - Evolution toward the IMF, 2007, Protostars and Planets V, 33

Ward-Thompson D. et al., 2010, A&A, 518, L92

Ward-Thompson D., Scott P. F., Hills R. E., Andre P., A Submillimetre Continuum Survey of Pre Protostellar Cores, 1994, MNRAS, 268, 276

Werner M., Roellig T., Low F., Rieke G., Rieke M., Hoffmann W., Young E., Houck J., Brandl B., Fazio G., Hora J., others , 2004, ApJS, 154, 25

Whitworth A. P., Bhattal A. S., Chapman S. J., Disney M. J., Turner J. A., Fragmentation of shocked interstellar gas layers., 1994, A&A, 290, 421

Whitworth A. P., Ward-Thompson D., An Empirical Model for Protostellar Collapse, 2001, ApJ, 547, 317

Wilcock L. A., Kirk J. M., Stamatellos D., Ward-Thompson D., Whitworth A., Battersby C., Brunt C., Fuller G. A., Griffin M., Molinari S., Martin P., Mottram J. C., Peretto N., Plume R., Smith H. A., Thompson M. A., The initial conditions of high-mass star formation: radiative transfer models of IRDCs seen in the Herschel Hi-GAL survey, 2011, A&A, 526, A159

Williams R. J. R., Dyson J. E., Redman M. P., Clumpy ultracompact H II regions. III. Cometary morphologies around stationary stars., 1996, MNRAS, 280, 667

Williams R. J. R., Ward Thompson D., Whitworth A. P., 2001, MNRAS, 327, 788

Woitke P., Pinte C., Tilling I., Ménard F., Kamp I., Thi W.-F., Duchêne G., Augereau J.-C., Continuum and line modelling of discs around young stars - I. 300000 disc models for HERSCHEL/GASPS, 2010, MNRAS, 405, L26

Wolf S., Henning T., Stecklum B., Multidimensional self-consistent radiative transfer simulations based on the Monte-Carlo method, 1999, A&A, 349, 839

Wood D., Churchwell E., 1989, ApJS, 69, 831

Wright M. C. H., Plambeck R. L., Wilner D. J., A Multiline Aperture Synthesis Study of Orion-KL, 1996, ApJ, 469, 216

Wyrowski F., Hofner P., Schilke P., Walmsley C. M., Wilner D. J., Wink J. E., Millimeter interferometry towards the ultra-compact H II region W3(OH)., 1997, A&A, 320, L17

Xie T., Mundy L. G., Vogel S. N., Hofner P., On Turbulent Pressure Confinement of Ultracompact H II Regions, 1996, ApJ, 473, L131

Yorke H. W., 2002, in Astronomical Society of the Pacific Conference Series, Vol. 267, P. Crowther , ed, Hot Star Workshop III: The Earliest Phases of Massive Star Birth, p. 165

Zavagno A. et al., Star formation triggered by H II regions in our Galaxy. First results for N49 from the Herschel infrared survey of the Galactic plane, 2010, A&A, 518, L101

Zhang Q., Ho P. T. P., Dynamical Collapse in W51 Massive Cores: NH 3 Observations, 1997, ApJ, 488, 241

Zhang S. B., Yang J., Xu Y., Pandian J. D., Menten K. M., Henkel C., Early Phase of Massive Star Formation: A Case Study of the Infrared Dark Cloud G084.81-01.09, 2011, ApJS, 193, 10

Zheng X. W., Ho P. T. P., Reid M. J., Schneps M. H., Molecular clouds associated with compact H II regions. II - The rapidly rotating condensation associated with ON1, 1985, ApJ, 293, 522

Zhukovska S., 2008, Ph.D. thesis, Ruperto-Carola University

Zinnecker H., Yorke H. W., Toward Understanding Massive Star Formation, 2007, ARAA, 45, 481